Model Independent Spin Determination at Hadron Colliders

Dissertation zur Erlangung des
naturwissenschaftlichen Doktorgrades
der Julius-Maximilians-Universität Würzburg

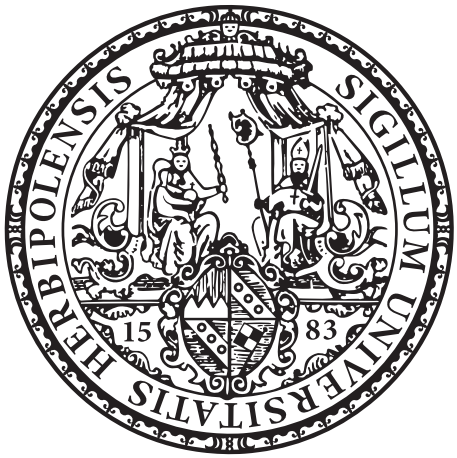

vorgelegt von

Lisa Edelhäuser

aus Rothenburg o.d.T.

Würzburg, 2011

Eingereicht am: 20.12.2011

bei der Fakultät für Physik und Astronomie

1. Gutachter: Prof. Dr. Werner Porod

2. Gutachter: Prof. Dr. Thomas Trefzger

3. Gutachter: _____

der Dissertation.

1. Prüfer Prof. Dr. Werner Porod

2. Prüfer Prof. Dr. Thomas Trefzger

3. Prüfer Prof. Dr. Thorsten Ohl

im Promotionskolloquium

Tag des Promotionskolloquiums: 25.04.2012

Doktorurkunde ausgehändigt am: _____

Zusammenfassung

Mit dem Ende des Jahres 2011 haben die beiden LHC-Experimente ATLAS und CMS jeweils ungefähr 5 inverse Femtobarn an Daten bei einer Energie von 7 TeV aufgenommen. Die bisher analysierten Daten geben nur sehr vage Hinweise auf neue Physik an der TeV-Skala. Trotzdem erwartet man, dass sich an dieser Skala neue Physik zeigt, die bekannte Probleme des Standardmodells behebt. In den letzten Jahrzehnten wurden viele Erweiterungen des Standardmodells der Teilchenphysik und ihre Phänomenologie dazu ausgearbeitet. Sobald sich neue Physik zeigt, stellt sich die Aufgabe, ihre Beschaffenheit und das zugrunde liegende Modell zu finden. Erste Hinweise können natürlich schon das Massenspektrum und die Quantenzahlen wie z.B. die elektrische und die Farbladung der neuen Teilchen liefern.

In zwei sehr bekannten und gut untersuchten Modellklassen, Supersymmetrie und Extradimensionen, haben neue Teilchen allerdings sehr ähnliche Eigenschaften an der erreichbaren Energieskala. Beide Modelle führen Partnerteilchen zu den bekannten Standardmodell-Teilchen ein, die, abgesehen von der Masse, sehr ähnliche Eigenschaften besitzen. Aus diesem Grund ist es nötig, weitere Kriterien zu ihrer Unterscheidung einzusetzen.

Ein hilfreicher Unterschied ergibt sich aus der Konstruktion beider Modelle: Während in Modellen mit Extradimensionen die Partnerteilchen gleichen Spin wie die Standardmodell-Teichen haben, ist der Spin der Partnerteilchen in supersymmetrischen Modellen um 1/2 verschieden. Dieser Unterschied hat nun interessante Auswirkungen auf die jeweilige Phänomenologie der Modelle.

Zum Beispiel kann man ausnutzen, dass die unterschiedlichen Spins die absoluten Wirkungsquerschnitte beeinflussen. Diese Methode setzt allerdings voraus, dass man die Massen und Kopplungsstärken sehr genau kennt. Eine weitere Herangehensweise nutzt aus, dass Winkelverteilungen vom Spin der involvierten Teilchen abhängen können. Eine wichtige darauf basierende Methode stellt einen Zusammenhang zwischen der invariante-Masse-Verteilung $d\Gamma/ds_{ff}$ zweier Zerfallsprodukte und dem Spin des intermediären Teilchens, über welches der Zerfall abläuft, her.

In dieser Arbeit untersuchen wir als erstes den Einfluss von Operatoren höherer Ordnung auf die Spinbestimmung in Zerfallsketten. Wir klassifizieren als erstes die relevanten Operatoren der Dimension 5 und 6. Wir berechnen die neuen Beiträge und diskutieren ihre Auswirkungen auf die Bestimmung von Kopplungen und Spin in diesen Zerfällen.

Im weiteren betrachten wir zwei Szenarien, die nicht die üblichen Zerfallsketten beinhalten:

In Dreikörperzerfällen kann die oben erwähnte Methode nicht angewendet werden, da das intermediäre Teilchen nicht auf die Massenschale gehen kann. Solche "off-shell" Zerfälle können in Szenarien wie split-Supersymmetrie oder split-"Universal Extra Dimensions" wichtig sein. Man kann hier die sogenannte "Narrow width approximation" nicht anwenden, welche eine notwendige Voraussetzung für einen einfachen Zusammenhang zwischen Spin und der invariante-Masse-Verteilung ist. Wir arbeiten eine Strategie für diese Dreikörperzerfälle aus, mittels derer man zwischen den unterschiedlichen Spinszenarien unterscheiden kann. Diese Strategie beruht darauf, dass man hier die differentielle Zerfallsbreite als globalen Phasenraumfaktor mal einem Polynom in der invarianten Masse s_{ff} schreiben kann. Die hierbei auftretenden Koeffizienten sind nur Funktionen der involvierten Massen und Kopplungen, und wir zeigen, wie beispielsweise ihre Wertebereiche und Vorzeichen dazu benutzt werden können, um den zugrunde liegenden Zerfall zu bestimmen. Am Ende testen wir diese Strategie in einer Reihe von Monte Carlo-Simulationen, und diskutieren auch den Einfluss des "off-shell" Teilchens. Im letzten Teil betrachten wir eine Topologie mit sehr kurzen Zefallsketten, in der man den oben genannten Zusammenhang zwischen Spin und invarianter Masse ebenfalls nicht anwenden kann. Wir untersuchen eine bestimmte Variable, die zur Unterscheidung von Supersymmetrie und "Universal Extra Dimensions" eingeführt wurde. Dabei nutzt man aus, dass sich das Problem im Hochenergielimes auf die zugrunde liegenden Produktionsprozesse reduziert. Wir diskutieren, wie man diese Variable auch in Szenarien anwenden kann, in denen dieser Limes keine gute Näherung darstellt. Dazu betrachten wir die möglichen Spinszenarien mit renormierbaren Kopplungen und untersuchen im Detail, wie gut diese Variable zwischen verschiedenen Spin-, Massen- und Kopplungsszenarien unterscheiden kann. Wir finden beispielsweise, dass das Spinszenario, welches den supersymmetrischen Fall beinhaltet, von den meisten anderen Spinszenarien gut unterscheidbar ist.

Abstract

By the end of the year 2011, both the CMS and ATLAS experiments at the Large Hadron Collider have recorded around 5 inverse femtobarns of data at an energy of 7 TeV. There are only vague hints from the already analysed data towards new physics at the TeV scale. However, one knows that around this scale, new physics should show up so that theoretical issues of the standard model of particle physics can be cured. During the last decades, extensions to the standard model that are supposed to solve its problems have been constructed, and the corresponding phenomenology has been worked out. As soon as new physics is discovered, one has to deal with the problem of determining the nature of the underlying model. A first hint is of course given by the mass spectrum and quantum numbers such as electric and colour charges of the new particles. However, there are two popular model classes, supersymmetric models and extradimensional models, which can exhibit almost equal properties at the accessible energy range. Both introduce partners to the standard model particles with the same charges and thus one needs an extended discrimination method. From the origin of these partners arises a relevant difference: The partners constructed in extradimensional models have the same spin as their standard model partners while in Supersymmetry they differ by spin 1/2.

These different spins have an impact on the phenomenology of the two models. For example, one can exploit the fact that the total cross sections are affected, but this requires a very good knowledge of the couplings and masses involved. Another approach uses angular distributions depending on the particle spins. A prevailing method based on this idea uses the invariant mass distribution of the visible particles in decay chains. One can relate these distributions to the spin of the particle mediating the decay since it reflects itself in the highest power of the invariant mass s_{ff} of the adjacent particles.

In this thesis we first study the influence of higher than dimension 4 operators on spin determination in such decay chains. We write down the relevant dimension 5 and 6 operators and calculate their contributions to the invariant mass distribution. We discuss how they affect the determination of spin and couplings.

We then address two scenarios which do not involve decay chains in the usual sense.

In three body decays, the method pointed out above cannot be applied since it can only be used if the mediating particle is produced on-shell. For off-shell decays, which are important e.g. in split-Supersymmetry or split-Universal Extra Dimensions, the narrow width approximation cannot be made which previously led to the simple relation between spin and the highest power of s_{ff}. We work out a strategy for these three body decays that can distinguish between the different spin scenarios. The method relies on the fact that the differential decay width $d\Gamma/ds_{ff}$ can be rewritten in this limit as a global phase space function and a polynomial in s_{ff}. The coefficients in this polynomial are functions of masses

and couplings and we show that they have distinct signs or ratios depending on the spins involved in the decay. We test the strategy in a series of Monte Carlo studies and discuss the influence of the intermediate particle's mass.
In the last part we consider a topology with very short decay chains. Again one cannot use the relation between spin and invariant mass. We investigate one variable that has been invented for the discrimination of Supersymmetry and Universal Extra Dimensions in the high energy limit which reduces the problem to the underlying production process. We show how this variable can also be used in new physics scenarios where the high energy limit is not a viable approximation. We include all possible spin scenarios with renormalizable interactions and study in detail the influence of the involved masses and couplings on the discrimination power of this variable. We find for example that the scenario containing the supersymmetric case is well distinguishable from most other spin scenarios.

Contents

1 Introduction **1**

2 BSM Models and Spin Determination **5**
2.1 Spin in BSM models 5
2.1.1 Supersymmetry 5
2.1.2 Universal Extra Dimensions 8
2.1.3 Additional gauge bosons: W' and Z' 11
2.2 Spin determination at hadron colliders 13
2.2.1 How does spin affect decays: a simple example 13
2.2.2 Spin determination in decay chains 15

3 Anomalous Couplings in Spin Determination **20**
3.1 Setup and kinematics 20
3.2 Operators 23
3.3 Influence of the dimension 5 operators 24
3.3.1 Naive expectation 24
3.3.2 Relevant decays 25
3.4 Discussion 28
3.4.1 Dimension 4 operators 28
3.4.2 Dimension 5 operators 30

4 Spin Discrimination in Three Body Decays **34**
4.1 Objective 35
4.2 Notation, setup and kinematics 36
4.2.1 Kinematics 36
4.2.2 Topologies and vertices 38
4.2.3 Polarization vectors, propagators and generic amplitudes . 43
4.3 Strategy for spin identification 44
4.3.1 Example: (S, V) 44
4.3.2 Signs of the coefficients 45
4.3.3 Decays into massless SM-fermions in case of topologies 1+2 46
4.3.4 Impact of the third topology 49
4.3.5 Special combinations of couplings 50
4.3.6 Final states containing massive SM-fermions 51
4.3.7 Influences of the mass of the intermediate particle(s) 53

4.4 Testing our strategy with Monte Carlo simulations 55
4.4.1 Fitting procedure 57
4.4.2 Variations of the fitted parameters for 10 simulations 58
4.4.3 Examples 60
4.4.4 Large sample tests 64
4.5 Summary 70

5 Spin in the Antler Diagram 71
5.1 Introduction, notation and calculation 71
5.1.1 Notation 74
5.1.2 Details on the calculation 76
5.1.3 Definition of $\mathcal{C}_B$ 78
5.1.4 Further strategy 82
5.2 Analytic results 84
5.2.1 Squared matrix elements for $2 \to 2$ 84
5.2.2 Complete squared matrix elements for $2 \to 4$ 85
5.2.3 TH results for $2 \to 4$ processes 86
5.2.4 J factors at TH 86
5.3 Fixed $\sqrt{\hat{s}}$ approach 91
5.3.1 Production process with fixed $\sqrt{\hat{s}}$ 92
5.3.2 How does the phase space depend on $\sqrt{\hat{s}}$? 95
5.3.3 The Susy case: (VSF) 96
5.3.4 Optimal δ^2 for different spin scenarios 97
5.4 Comparison of the distributions for fixed $\sqrt{\hat{s}}$ 100
5.4.1 Influence of the masses 103
5.4.2 Can one distinguish different spin scenarios? 108
5.4.3 Examples: Susy and UED 113
5.5 Summary 116

6 Conclusion 120

A Models for Monte Carlo Generators 123
A.1 Model for O'Mega/WHIZARD 123
A.2 Model for CalcHep/CompHep 127

B Analytic Results 130
B.1 Appendix to Chapter 3: Anomalous couplings 130
B.2 Appendix to Chapter 4: Three body decays 133

C Appendix to Chapter 5 137
C.1 Explicit helicity spinors 137
C.2 Figures to Section 5.4 139

Bibliography 142

Chapter 1

Introduction

Although it is a very successful and validated theory, one ingredient of the standard model (SM) of particle physics has not been confirmed so far, namely the nature of electroweak symmetry breaking. The most popular and so far the simplest mechanism to break electroweak symmetry is the Higgs Mechanism. It is one of the main objectives of the Large Hadron Collider (LHC) to clarify which mechanism is realized in nature.
Apart from this last ingredient of the SM, there are many important issues beyond the SM (BSM) that are supposed to be answered with the LHC. For example, the existence and nature of dark matter, possible solutions to the hierarchy problem, hints towards a unification of gauge couplings, existence of additional spacelike dimensions, additional gauge bosons or alternative solutions to the unitarity problem in vector boson scattering, just to mention a few. In the past decades, many models and their corresponding collider phenomenology have been worked out in detail to find solutions to these current issues beyond the SM.
There are compelling theoretical hints that new physics should show up at energies beyond 1 TeV, which is well within the reach of the LHC. As soon as new physics is detected, the underlying theory that describes the data correctly has to be understood in detail. Consequently one has to determine the mass spectrum and the quantum numbers of new particles as well as their couplings to the already known particles and among each other.
In BSM models, new particles are often organized as partners of the already known SM particles with the same gauge quantum numbers. Typically, one has the superpartners of Supersymmetry (Susy) in mind, which comprise sleptons, squarks, gauginos and so on as partners of the SM leptons, quarks and gauge bosons. However, in extradimensional models such as e.g. Universal Extra Dimensions (UED), the new particles are also arranged as partners of the SM particles. They are called Kaluza-Klein-leptons (KK), KK-quarks and KK-gauge bosons. The particle sets of the two models differ by their spin relative to the SM particles. While the supersymmetric partners differ by spin 1/2 (often called the "opposite spin" scenario in the literature), the UED partners have the same spin as the SM particles ("same spin" scenario).
Since one also wants to have a dark matter (DM) candidate, preferably a cold one, to explain current astrophysical observations, one often incorporates a parity

in the theory, implying a lightest neutral stable particle. In Susy and UED this would be R-parity and KK-parity respectively and the corresponding particle is called the lightest supersymmetric particle (LSP) and the lightest KK particle (LKP). This implies that new particles that are odd under such a parity are only produced in pairs at colliders. It also implies that the lightest stable particle is always at the end of decay chains involving new particles. Due to its properties, this LSP/LKP is supposed to leave the detector unrecorded and manifests itself as missing energy.
Consequently, the two models can have similar signatures at hadron colliders. If realized in nature, we will only be able to detect the first KK excitation and maybe some of the lighter particles of the second KK excitation within the accessible energy range of the LHC. This means that the particle spectrum is almost the same as for the minimal supersymmetric standard model, the MSSM, and both will look like a copy of the SM particles. Consequently, similar scattering and decay processes can appear.
As we have explained above, there is one crucial difference between these two scenarios: the Susy partners have opposite spin, while the KK partners have the same spin as the SM particles. This means that it is not sufficient to merely detect a new set of particles which looks like a copy of the SM particles and assign the most popular model to it, but one needs to determine the spin of newly discovered particles to be able to pin down the correct underlying model.
We thus concentrate on the important issue of model discrimination by spin determination in processes with missing energy at hadron colliders. There are mainly two methods for doing so: Firstly, via the total cross section. This method depends crucially on the masses and coupling strengths and is hence very model dependent, but in the context of specific models (fixing the couplings) it can give an early idea about the involved spin. Here, one profits from the fact that due to angular momentum conservation and different numbers of degrees of freedom, particles with different spin have distinct decay rates and cross sections. Generally, the cross section for pair production of spin-0 particles is smaller compared to spin-1/2 which is again smaller than that of spin-1 [1]. However, one needs at least a complementary method which we find by looking at distributions of certain variables constructed from the momenta of the visible particles.
Usually, this is done for long decay chains of new particles with (at least) one invisible particle where one fixes the spin of the SM particles involved and studies the invariant mass distributions of the visible particles which depend, among other things, on the spin of the invisible particles. Consider a decay chain where one heavy particle decays into an SM particle and a lighter successor. The latter is produced on-shell and decays into another SM particle and an invisible one, e.g. the DM candidate. The invariant mass distribution of the two SM particles is directly related to the spin of the intermediate particle and hence to some extent also to the spins of the invisible and the initially decaying particle.
In this thesis we address open questions which arise if one relaxes the assumptions made for the spin determination in this approach. Firstly, we want to clarify how higher dimensional operators affect the relevant distributions. Secondly, the

derivation for this relation between spin and differential decay width requires a subsequent decay of heavy particles into lighter ones. However, the condition that all intermediate particles can go on-shell, is not fulfilled in all mass scenarios. For example, quantum number conservation can forbid such a subsequent decay so that the particle can only undergo a phase space suppressed three body decay. Furthermore, the invariant mass is always derived from two SM particles which are part of one decay chain. If one has very short decay chains, this is not always possible.
Hence, we pursue the following questions:

1. What is the influence of new momentum dependent operators on spin analysis?

2. How can one determine the spin of particles if only three body decays are available and one cannot exploit the commonly used relation between invariant mass distribution and spins?

3. What can be done if the decay chain consists only of a single two body decay containing just one visible particle?

This thesis is organized as follows: In Chapter 2, we first give an overview of three important models beyond the SM which we refer to later in this thesis. We give an introduction to spin determination and a pedagogical example how spin affects distributions. The relation between invariant masses and the spin of the intermediate particle in a simple decay chain is given at the end of this chapter.
In Chapter 3, we address our first question and investigate the influence of such higher dimensional operators on the distributions. We write down the important dimension 5 and 6 operators which carry momentum dependence and point out with a simple power-counting argument, how they can in principle distort spin analysis. We then calculate the new contributions in terms of masses and generic couplings and discuss their size and the influence relative to the dimension 4 contributions. These new terms are important to consider for measurement[1] of couplings if one cannot otherwise exclude higher dimensional operators. Furthermore we calculate in detail why these contributions do not introduce any terms endangering spin determination.
In Chapter 4 we address the second question and work out a new strategy for discriminating different spin scenarios in the context of three body decays. We consider all contributing topologies for these decays and discuss the leading contributions of each. At the end of this chapter, we show the influence of mass choices on our strategy and test it in a series of Monte Carlo studies.
Chapter 5 is dedicated to a specific topology with very short decay chains. This topology is challenging since one cannot have an invariant mass distribution from a single chain, and thus the standard approach for spin determination in decay chains is not applicable. We use a variable proposed in 2005 [2] for measuring spins in this topology. We include all possible spin scenarios with renormalizable

[1] By "measurement of couplings" we mean the ratio of left and right handed coupling constants, not their absolute value.

interactions and study the influence of the masses and couplings on the discrimination power of this variable. In order to apply our results to hadron colliders, we discuss a simple scheme that can be used to disentangle PDF and spin effects. We conclude in Chapter 6. Selected analytic results, details on the implementation into Monte Carlo generators as well as additional figures are given in the Appendix.

Chapter 2

Overview of Selected BSM Models and Spin Determination

This year's model dims and fades
Last year's model is erased

(Fear Factory, "Corporate Cloning")

In this chapter, we will give a short overview of three models which we will often refer to in the following chapters. We choose Supersymmetry, Universal Extra Dimensions and additional gauge bosons. We want to put the main emphasis on the nature of the spin of the new particles. In the second part we will give a pedagogical example on how a spin affects distributions of certain variables and how spin is in principle determined in decays being present in the models above.

2.1 Spin in BSM models

2.1.1 Supersymmetry

We found [3–6] on Supersymmetry very helpful and follow their approach.
Relativistic quantum field theory (QFT) combines quantum theory and special relativity and thus invariance under Poincare symmetry plays a central role. The Poincare-algebra is a Lie-algebra and the generators of the translations P_μ and Lorentz transformations $M_{\mu\nu}$ satisfy

$$\begin{aligned}
[P_\mu, P_\nu] &= 0 \\
[P_\mu, M_{\rho\sigma}] &= i\left(g_{\mu\rho}P_\sigma - g_{\mu\sigma}P_\rho\right) \\
[M_{\mu\nu}, M_{\rho\sigma}] &= i\left(g_{\nu\rho}M_{\mu\sigma} - g_{\mu\rho}M_{\nu\sigma} + g_{\mu\sigma}M_{\nu\rho} - g_{\nu\sigma}M_{\mu\rho}\right).
\end{aligned}$$

One could now ask whether it is possible to embed the Poincare-algebra in a larger algebra. This question was answered by Coleman and Mandula in 1967 [7] with a theorem named after them, which states that, in viable QFT's, there is no

extension of the Poincare-algebra except trivial ones with generators commuting with the $M_{\mu\nu}$ and P_μ.
However, if one relaxes one of the conditions of the Coleman-Mandula theorem by including not only commutators but also anticommutators, such an extension becomes possible. Algebras which include both commuting and anticommuting objects are called graded Lie-algebras. The corresponding generators are the so-called Supersymmetry generators Q_a and the Lie-algebra is then a Supersymmetry-algebra

$$\left[Q_\alpha, Q^\dagger_{\dot\beta}\right]_+ = -2\left(\sigma^\mu\right)_{\alpha\dot\beta} P_\mu; \tag{2.1a}$$

$$[Q_\alpha, P_\mu] = \left[Q^\dagger_{\dot\alpha}, P_\mu\right] = 0; \qquad [Q_\alpha, Q_\beta]_+ = \left[Q^\dagger_{\dot\alpha}, Q^\dagger_{\dot\beta}\right]_+ = 0. \tag{2.1b}$$

This is a symmetry between fermions and bosons. In the superspace formalism, one chooses a representation of the supercharges with

$$Q_\alpha = -i\left(\partial_\alpha + i\sigma^\mu_{\alpha\dot\beta}\overline{\theta}^{\dot\beta}\partial_\mu\right); \qquad \overline{Q}^{\dot\alpha} = i\left(\partial^{\dot\alpha} + i\overline{\sigma}^{\mu\dot\alpha\beta}\theta_\beta\partial_\mu\right) \tag{2.2}$$

where $\theta, \overline{\theta}$ are Grassman-valued coordinates and transform as Weyl spinors. With these, one extends the spacetime to the so-called supercoordinates $(x^\mu, \theta^a, \overline{\theta}_{\dot a})$. They anticommute with themselves and commute with x_μ

$$\left\{\theta^a, \theta^b\right\} = \left\{\overline{\theta}_{\dot a}, \overline{\theta}_{\dot b}\right\} = \left\{\theta^a, \overline{\theta}_{\dot a}\right\} = 0; \qquad \left[x^\mu, \theta^a\right] = \left[x^\mu, \overline{\theta}_{\dot a}\right] = 0.$$

The fields in superspace now depend on the space-time coordinates x_μ and $\theta, \overline{\theta}$:

$$\mathcal{F} = f(x, \theta, \overline{\theta}).$$

Since θ are Grassman variables, all powers of θ higher than $\theta_\alpha\theta^\alpha$ vanish due to $\{\theta^\alpha, \overline{\theta}_{\dot\alpha}\} = 0$ and fields are always polynomials in the superspace coordinates

$$\begin{aligned}\mathcal{F}(x, \theta, \overline{\theta}) \quad &= f(x) + \theta\eta(x) + \overline{\theta\xi} + \theta\theta m(x) + \overline{\theta\theta}n(x) + \\ &+\theta\sigma^\mu\overline{\theta}v_\mu(x) + \theta\theta\overline{\theta\lambda}(x) + \overline{\theta\theta}\theta\psi(x) + \theta\theta\overline{\theta\theta}d(x).\end{aligned}$$

We want to emphasize here that the variables $f, m \ldots$ have so far no physical meaning. However, they have a definite transformation behaviour: f, m, n, d transform like scalars, ξ, λ, ψ, η like (left handed) Weyl spinors and v_μ like a vector field. $\mathcal{F}(x, \theta, \overline{\theta})$ is reducible with respect to the representation given in equation 2.2 and it is possible to eliminate fields by introducing one of the two constraints

$$\text{Chiral: } \overline{D}\mathcal{F} = 0 \qquad\qquad \text{Vector: } \mathcal{F}^\dagger = \mathcal{F}. \tag{2.3}$$

In the first case, one commonly renames $\mathcal{F} = \Phi$, in the second case $\mathcal{F} = V$. One can solve these constraints and, for the first case, obtains the chiral superfield (after formally shifting $x^\mu \to y^\mu = x^\mu - i\theta\sigma^\mu\overline{\theta}$)

$$\overline{D}\Phi = 0 \to \Phi(y, \theta) = \phi(y) + \sqrt{2}\theta\xi(y) + \theta\theta F(y) \tag{2.4}$$

where F is a complex auxiliary component with energy dimension 2 and thus does not have a kinetic term, leaving the complex scalar ϕ and the Weyl spinor ξ as the only dynamical fields. Solving for the second constraint given in equation 2.3, one obtains a vector superfield which, in Wess-Zumino gauge, can be written as

$$V^\dagger = V \to V_{WZ}(x,\theta) = \theta\sigma^\mu\overline{\theta}A_\mu(x) + \theta\theta\ \overline{\theta\lambda}(x) + \overline{\theta\theta}\ \theta\lambda(x) + \frac{1}{2}\theta\theta\ \overline{\theta\theta}D(x) \quad (2.5)$$

containing a vector field $A_\mu(x)$, a spinor λ and a real auxiliary field $D(x)$. Using the chiral covariant derivatives

$$\mathcal{D}_\alpha \equiv \partial_\alpha - i\sigma^\mu_{\alpha\dot{\beta}}\overline{\theta}^{\dot{\beta}}\partial_\mu; \qquad \overline{\mathcal{D}}^{\dot{\alpha}} = \overline{\partial}^{\dot{\alpha}} - i\overline{\sigma}^{\mu\dot{\alpha}\beta}\theta_\beta\partial_\mu \quad (2.6)$$

we can define the supersymmetric field strength [5]

$$W_\alpha = -\frac{1}{4}\overline{\mathcal{D}\mathcal{D}}e^{-V}\mathcal{D}_\alpha e^V. \quad (2.7)$$

Then the general supersymmetric renormalizable Lagrangian density for one non-abelian gauge group can be written as

$$\mathcal{L} = \frac{1}{16g^2k}Tr\left[\left(W^\alpha W_\alpha\right)_{\theta\theta} + h.c.\right] + \left[\Phi_i^\dagger\left(e^V\right)_{ij}\Phi_j\right]_{\theta\theta\overline{\theta\theta}} + \left(\left[\mathcal{W}(\Phi_i)\right]_{\theta\theta} + h.c.\right) \quad (2.8a)$$

$$\mathcal{W}(\phi_i) = h_i\Phi_i + \frac{1}{2}m_{ij}\Phi_i\Phi_j + \frac{1}{3!}f_{ijk}\Phi_i\Phi_j\Phi_k \quad (2.8b)$$

where $\mathcal{W}$ is the so-called superpotential. The group generators T^a are normalized as $Tr\left[T^aT^b\right] = \delta^{ab}k$.
In the Susy algebra, there is a global $U(1)$ R-symmetry. From observation and theoretical considerations it turns out that this $U(1)_R$ cannot be a continuous symmetry in nature, but a discrete symmetry can be retained which gives a discrete Z_2. Under this symmetry, one can choose the transformations as

$$\theta \to -\theta; \qquad \Phi \to (-1)^{3(B-L)}\Phi \quad (2.9)$$

for the coordinates and chiral superfields. This results in the so-called R parity

$$\mathcal{P}_R = (-1)^{3(B-L)+2S} \quad (2.10)$$

which forbids certain interactions in the superpotential which would otherwise effect proton decay. If this parity is conserved, the phenomenology of supersymmetric models is affected fundamentally. Only pair production of supersymmetric particles is possible and if those particles decay again, the decay chain has to end in a stable particle with $\mathcal{P}_R = -1$. The lightest particle with $\mathcal{P}_R = -1$ is stable and thus can act as a Dark Matter candidate.
Since no supersymmetric partner of a SM particle has been found so far, Susy must to be broken. To generate a realistic supersymmetric model like the minimal

supersymmetric SM (MSSM), one can add soft-Susy breaking terms. A concrete implementation that produces such soft-breaking terms is a hidden Susy breaking sector which is only weakly coupled to the visible sector (MSSM) and thus can avoid the problems of a direct breaking in the visible sector. There are two popular "mediation" mechanisms which connect the two sectors: (i) Gravitational mediation of Susy breaking where the two sectors are connected by gravity and (ii) Gauge mediated Susy breaking where the mediation takes place via additional chiral supermultiplets which couple on the one hand to a Susy breaking Vev and are on the other hand also charged under the SM gauge groups. These new particles are then the so-called messengers and induce soft breaking terms via loop contributions.
The simplest Susy extension of the SM, the minimal supersymmetric SM has a $\mathcal{N} = 1$ Supersymmetry with soft breaking terms. In this model, every SM particle state gets its own Susy partner and they are together in one supermultiplet. The matter fermions are in the chiral supermultiplets $L_I, e_I, Q_{\alpha I}, \overline{U}_I, \overline{D}_I$ where I is the generation index. The SM fermions therefore have scalar partners (so-called sfermions: squarks and sleptons), the SM vectors are in vectormultiplets and get fermion partners, the gauginos. The Higgs sector is represented by the chiral superfields H and $\overline{H}$ which include two Higgs doublets and their Susy partners, the higgsinos. A complex conjugated chiral multiplet is forbidden in the superpotential, and so one needs to introduce one Higgs field for the up type and one for the down type quark masses.
The superpotential (equation 2.8b) for the MSSM is

$$\mathcal{W} = -y^e_{IJ} H L_I \overline{E}_J - y^Q_{IJ} H Q_{\alpha I} \overline{D}^\alpha_J - y^U_{IJ} \overline{H} Q_{\alpha I} \overline{U}^\alpha_J - \mu \overline{H} H. \tag{2.11}$$

Since Supersymmetry is not an exact symmetry in nature, there are additional soft breaking terms. Those terms have always dimensionful couplings: Bilinear terms (gaugino mass terms, scalar mass terms) and trilinear terms (sfermions to Higgs interactions). We have summarized the particle content of the MSSM in table 2.1 where we again want to emphasize that as a consequence of being in one supermultiplet, the SM particles and their Susy partners differ by spin 1/2. If the SM particle is a boson, its Susy partner is a fermion and vice versa.

2.1.2 Universal Extra Dimensions

As an introduction to this class of models we found [8–12] useful and follow their approach. In this section we are interested in a subset of extra dimensional models with one flat extra dimension of the size $R^{-1} \sim 1$ TeV [13,14] compactified on a S_1/Z_2 orbifold where all SM particles can propagate into this single extra dimension. This propagation formally leads to a infinite number of particles, the Kaluza-Klein tower of excitations, with the same quantum numbers as the original SM fields, which is the key feature of this model. One usually denotes the 3+1 coordinates with x^μ and indices $\mu, \nu \in 0, 1, 2, 3$ and y as the extra coordinate and the indices $M, N \in 0, 1, 2, 3, 5$. Each of the 5D fields can be Fourier expanded in terms of this compactified dimension y. Since we need chiral SM model particles

	SM particles	Susy partners
	Fermions	Scalar bosons
Lepton sector	$e, \mu, \tau, \nu_e, \nu_\mu, \nu_\tau$	$\widetilde{e}_{1/2}, \widetilde{\mu}_{1/2}, \widetilde{\tau}_{1/2}$
Quark sector	u, d, c, s, t, b	$\widetilde{u}_{1/2}, \widetilde{d}_{1/2}, \widetilde{c}_{1/2}, \widetilde{s}_{1/2}, \widetilde{t}_{1/2}, \widetilde{b}_{1/2}$
	Gauge bosons	Gauginos/Higgsinos (fermions)
Gauge sector	$W^\pm, Z, \gamma;\ g^a$	$\widetilde{\chi}_1^\pm, \widetilde{\chi}_2^\pm, \widetilde{\chi}_4^0, \widetilde{\chi}_3^0, \widetilde{\chi}_2^0, \widetilde{\chi}_1^0;\ \widetilde{g}^a$
Higgs sector	$H_0, A, h_0, h^\pm$	

Table 2.1: Particle content of the MSSM.

in the zero mode of the KK tower, but chirality does not exist in 5D, one chooses the compactification with the orbifold parity $\mathcal{P}_5 : y \to -y$ which eliminates extra degrees of freedom at the zero KK level. This is equivalent to choosing boundary conditions in the 5th dimension for the component fields as e.g. for the boson field ϕ

$$\phi^+(x,y): \quad \left(\frac{\partial\ \phi(x,y)}{\partial\ y}\right)\Big|_{y=0,\pi R} = 0 \quad \text{Neuman boundary cond.} \tag{2.12a}$$

$$\phi^-(x,y): \quad \phi(x,0) = \phi(x,\pi R) = 0 \quad \text{Dirichlet boundary cond.} \tag{2.12b}$$

The two fields ϕ^+/ϕ^- are even/odd under this parity. The fourier expansion for a scalar field $\phi(x,y)$ is

$$\phi(x,y) = \frac{1}{\sqrt{2\pi R}}\left(\phi_0(x) + \sqrt{2}\sum_{n=1}^{\infty}\left(\phi_n^+(x)\cos\left(\frac{ny}{R}\right) + \phi_n^-(x)\sin\left(\frac{ny}{R}\right)\right)\right).$$

Here, $\phi_n^\pm(x)$, $\phi_0(x)$ are 4D fields and the latter one is identified with a (possible) SM scalar. The components for $n > 0$ are the KK excitations. Depending on the choice of boundary conditions, the field ϕ is then either odd or even so that either (ϕ_0 and ϕ^+) or (ϕ^-) exist. For a vector field $A_M(x,y)$ in 5D one can also assign this parity $\mathcal{P}_5$ such that the $A_\mu, \mu = 0,1,2,3$ components are the even gauge fields and the A_5 component is odd. The KK expansion is

$$A_\mu(x,y) = \frac{1}{\sqrt{\pi R}}\left(A_\mu^0(x) + \sqrt{2}\sum_{n=1}^{\infty}\left(A_\mu^n(x)\ \cos\left(\frac{ny}{R}\right)\right)\right) \tag{2.13a}$$

$$A_5(x,y) = \frac{\sqrt{2}}{\sqrt{\pi R}}\sum_{n=1}^{\infty}\left(A_5(x)\ \sin\left(\frac{ny}{R}\right)\right). \tag{2.13b}$$

The fields A_μ and A_5 obey the Neuman and Dirichlet boundary conditions respectively as in equation 2.12. In the case of fermions we need to have chiral SM fermions at the n=0 level. That leads to some complications in 5D since here chirality does not exist due to a missing 5D equivalent of the γ^5 matrix as already mentioned. Consequently, one cannot construct 5D left and right handed components coupling differently to gauge fields. Therefore one introduces two 5D fermion fields with opposite orbifold parity $\psi_{L,R}$, where the zero mode is the SM $\psi^{SM}_{L,R}$ component. In 4D, one can then set $\psi^{SM} = P_L\Psi^0_L + P_R\psi^0_R$ with the ordinary projection operators $P_{L/R} = (1 \mp \gamma^5)/2$. The decomposition for the fermion fields is then

$$\psi_R = P_R\psi^+_R + P_L\psi^-_R : \tag{2.14a}$$
$$\psi^+_R = \frac{1}{\sqrt{2\pi R}}\left(\psi^0_R(x) + \sqrt{2}\sum_{n=1}^{\infty}\psi^n_R(x)\cos\left(\frac{ny}{R}\right)\right);$$
$$\psi^-_R = \frac{1}{\sqrt{\pi R}}\left(\sum_{n=1}^{\infty}\psi^n_R(x)\sin\left(\frac{ny}{R}\right)\right);$$

$$\Psi_L = P_L\Psi^+_L + P_R\Psi^-_L : \tag{2.14b}$$
$$\Psi^+_L = \frac{1}{\sqrt{2\pi R}}\left(\Psi^0_L(x) + \sqrt{2}\sum_{n=1}^{\infty}\Psi^n_L(x)\cos\left(\frac{ny}{R}\right)\right);$$
$$\Psi^-_L = \frac{1}{\sqrt{\pi R}}\left(\sum_{n=1}^{\infty}\Psi^n_L(x)\sin\left(\frac{ny}{R}\right)\right).$$

The left handed component ψ^+_R/Ψ^+_L is even and the right handed component ψ^-_R/Ψ^-_L is odd under the orbifold symmetry $\mathcal{P}_5 : \psi \to \pm\gamma_5\psi$. The KK excitations of the right-handed SM fermion are denoted with lower case letters ψ, while those of the left-handed SM fermions are denoted with capital letters Ψ. We show the fermionic particle content of minimal UED (MUED) model in table 2.2. Since it is not for interest in this discussion, we want to refer to [9] for the full Lagrangian. We want to make a note on the mass spectra in this model. At tree level, the mass M_n of the n-th KK excitation just depends on the size of the extra dimension R and the zero KK mode mass M_0, which is the SM particle mass,

$$M_n = \sqrt{\frac{n^2}{R^2} + M_0^2} \tag{2.15}$$

which leaves us with highly degenerate masses in the first KK excitation basically forbidding decays. In [15], radiative corrections to the KK masses are calculated. The enhancement of the KK masses for the first mode for $R^{-1} = 500$ and $\Lambda R = 20$ is around 20% for the KK quark and gluon masses. These corrections originate from the bulk compactification violating 5D Lorentz invariance and from the discrete symmetry $\mathcal{P}_5$ which is also not 5D Lorentz invariant. In a non-minimal UED model, one would also allow for boundary terms at the cut-off scale Λ that affects the mass scenarios.

Let us at last say something about the KK-parity which provides a similar mechanism as in Susy for having a stable KK particle, the LKP. If one demands an additional symmetry $y \to \pi R - y$ for the Lagrangian, one has a general conservation of KK number so that a single KK mode cannot couple to two SM fields. This KK parity forces the sum of the three KK mode numbers in an interaction to be even

$$(-1)^{(k+l+m)} = 1.$$

In a three particle vertex with one SM particle with KK number 0, the other two particles in the interaction have to have the same KK number (l=m) and no single KK mode can couple to two SM particles. This KK number conservation is in UED satisfied at every vertex but is broken at loop level, so that higher KK modes can always decay into lower (lighter) ones, but the lightest particle of the lowest KK mode is stable and cannot decay further. We depict the two parities of UED in figure 2.1. Phenomenologically this is a nice feature since the lightest KK

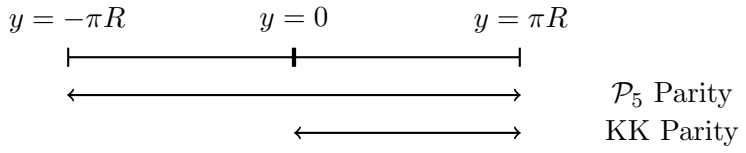

Figure 2.1: Orbifold partity $\mathcal{P}_5$ and KK parity of the extra dimension y. The orbifold parity associates the points of the complete extra dimension via $y \to -y$, the KK parity transforms the points in one half of the interval with $y \to \pi R - y$. The KK parity remains as a symmetry of the model while the orbifold parity is modded out in the compactification.

mode can serve as a Dark Matter candidate. After taking radiative corrections into account which rescind the mass degeneracy of the $n = 1$ mode, the lightest KK mode is the gauge boson B'. This particle is stable, electrically neutral and not colored and thus can serve as a DM candidate. The current preferred Dark Matter scale is around $R^{-1} = 1.3$ TeV [16] which is noticeably affected by decay channels of KK particles from the 2nd mode. A mass below 1 TeV is so far only accessible in a non-minimal model. In the following years, the LHC should be able to test for KK excitations up to a $R^{-1} \approx 1.5$ TeV [14, 17].

2.1.3 Additional gauge bosons: W' and Z'

In the models described so far, new particles would be revealed by missing energy. Due to some parity they decay into lighter ones including at least one invisible particle.
In the following we consider new vector bosons which would unveil themselves as a resonance in scattering amplitudes of two protons to W, Z pairs, leptons or jets. These new bosons are generically named W' or Z' bosons and are colour-neutral and electrically charged/neutral respectively. They are usually assumed to be gauge bosons which can come out of various BSM-models such as additional

n	Leptons		Quarks	
⋮				
1	$L^n_L = \begin{pmatrix} \nu^n_L \\ E^n_L \end{pmatrix}; L^n_R = \begin{pmatrix} \nu^n_R \\ E^n_R \end{pmatrix};$	$e^n_R,\ e^n_L$	$Q^n_L = \begin{pmatrix} U^n_L \\ D^n_L \end{pmatrix}; Q^n_R = \begin{pmatrix} U^n_R \\ D^n_R \end{pmatrix};$	$u^n_R,\ u^n_L;\ d^n_R,\ d^n_L$
0	$L^0_L = \begin{pmatrix} \nu_L \\ E_L \end{pmatrix}$	e^0_R	$Q^0_L = \begin{pmatrix} U_L \\ D_L \end{pmatrix};$	$u^0_R \qquad d^0_R$
	$SU(2)_W \times U(1)$	$U(1)$	$SU(2)_W \times U(1)$	$U(1)$

Table 2.2: Fermionic particle content for MUED. We take the notation from [9], where all right-handed SM fermions are denoted with lower case letters, and the left-handed SM fermions are denoted with capital letters.

$U(1)$ gauge groups or GUT models with exceptional groups (E6/E8). Little Higgs models provide a Higgs as a pseudo-Nambu-Goldstone boson of a broken global symmetry which can also come with new gauge bosons. Additionally, in KK-models as above, the KK-excitations of the SM Z and W bosons are also called W', Z' bosons and have similar characteristics as extra gauge bosons. However, they tend not to couple strongly to pairs of light modes in KK models.
For all of those models, one can describe their interaction with the SM fermions with a generic Lagrangian [17]

$$\begin{aligned} Z': \quad & \sum_{gen.} i\ Z'_\mu \Big(g_e^{'L}\ \overline{e}_L \gamma^\mu e_L + g_e^{'R}\ \overline{e}_R \gamma^\mu e_R + g_\nu^{'L}\ \overline{\nu}_L \gamma^\mu \nu_L \\ & \qquad + g_u^{'L}\ \overline{u}_L \gamma^\mu u_L + g_u^{'R}\ \overline{u}_R \gamma^\mu u_R + g_d^{'L}\ \overline{d}_L \gamma^\mu d_L + g_d^{'R}\ \overline{d}_R \gamma^\mu d_R \Big) \\ W': \quad & \sum_{gen.} i\ W'_\mu \left(\overline{u}_i \gamma^\mu \left(g^{'R}_{q(i,j)} P_R + g^{'L}_{q(i,j)} P_L \right) d_j + \overline{\nu}_i \gamma^\mu \left(g^{'R}_{l(i,j)} P_R + g^{'L}_{l(i,j)} P_L \right) e_j \right) \\ & \qquad + h.c. \end{aligned}$$

where u, d, e, ν are the left/right handed SM particles and the couplings g' are either free parameters or fixed by the specific models. If the bosons are sensitive to the generation, then the couplings g' depend on the generation. For the W' boson, the indices i, j label the fermion generations. Note that we have here included a right handed neutrino, which can be left out by setting the corresponding coupling $g^{'R}_{l(i,j)}$ to zero. Furthermore, additional gauge bosons cannot be introduced randomly, but have to be anomaly-free, and amplitudes with massive spin-1 particles are only unitary at high energies if they are remnants of a spontaneously broken gauge symmetry. The quantum numbers of those gauge bosons have to be chosen such that they do not violate gauge-invariance for the SM particles.
These particles were and are mainly searched for at LEP, Tevatron and the LHC as resonances in scattering amplitudes and single production such as $p\overline{p}/pp/e\overline{e} \to Z'X \to l^+l^-X$ or $p\overline{p}/pp/e\overline{e} \to Z'X \to W^+W^-X$ where X denotes missing energy. The invariant mass distributions and angular distributions of the visible particles are used to search for the resonances and, if they are found, to

determine their spin. The best current limits for sequential SM couplings are $m_{W'} > 2.15\ TeV$ for the W' [18] and $m_{Z'} > 1.83\ TeV$ for Z' [19]. Depending on the specific model, these limits can change drastically.

2.2 Spin determination at hadron colliders

In the second part of this chapter we turn our interest to the question how the spin of the particles involved in the decay affects distributions.
In the following we will look at a pedagogical example of a particle decaying into two fermions and a third particle, and see how the spin and the helicity affect the angular distribution of the visible particles, in our case the two fermions. Since angles are frame-dependent, we choose as the observable the invariant mass of the two fermions. We will sometimes refer to the angle θ which is then the angle between the two fermions in the rest frame of the decaying particle.

2.2.1 How does spin affect decays: a simple example

Let us look at decays of the form

$$X(p_X, m_X) \to f(p_f, m_f)\ \overline{f}(p_{\overline{f}}, m_f)\ \ Y(p_Y, m_Y) \quad \text{with } X, Y \in S, V. \tag{2.16}$$

were S, V stand for scalar and vector respectively. We investigate the differential decay rate as a function of the invariant mass $s_{ff} = (p_f + p_{\overline{f}})^2$. To simplify the discussion, we take the fermions as massless and the intermediate particle as heavy so that we can neglect the momentum dependent part of the fermion propagator. In the rest frame of the decaying particle, s_{ff} (for massless fermions) is a function of the angle between the two fermions: $s_{ff} = E_1 E_2 \cdot (1 - \cos\theta_{f\overline{f}})$. Thus, for $s_{ff} = 0$ the angle between the two fermions is $\theta_{f\overline{f}} = 0°$, and $s_{ff} = s_{max}$ corresponds to the maximal angle between the two fermions, $\theta_{f\overline{f}} = 180°$. In the first case, both fermions move in the same direction, while in the second case, they are back to back in the centre of mass frame. Let us understand the individual cases in the following.
• $S \to f\overline{f}S$: In this case, we have a decaying spin 0 particle and a spin 0 daughter particle. From spin conservation we only have one possible helicity assignment for the fermions if they are collinear, i.e. parallel or back to back. They have to have a spin projected onto the quantization axis of $+1/2$ and $-1/2$ respectively to give a total spin of 0 along this axis. One can see this from the matrix element $\mathcal{M}_{fi}$ which for this decay reads

$$\mathcal{M}_{fi} = \overline{u}_f\ (g_r P_R + g_l P_L) S_I (n_l^* P_L + n_r^* P_R) v_f \simeq \frac{1}{M_I} \overline{u}_f (g_r n_l^* P_R + g_l n_r^* P_L) v_f$$

since in the limit of a very heavy intermediate particle the corresponding propagator reduces to $S_I = 1/(\not{p} - M_I) \simeq 1/M_I$. We can now consider the extreme cases sketched in figures 2.2 and 2.3. In the first one, the spin projected onto the quantization axis has the same value for both fermions. The configuration on the right hand side of figure 2.2 vanishes due to the helicity structure in the matrix

element ($P_L P_R$) while the process on the left hand side is in principle allowed. However, since we have a scalar decaying into massless fermions and a scalar, the squared matrix element is proportional to s_{ff}, and nevertheless vanishes for $s_{ff} = 0$. In the case of figure 2.3 we have two fermions with opposite spins with respect to the quantization axis. The right side in this figure shows the allowed helicities for $s_{ff} = s_{max}$. Since the squared matrix element is again proportional to s_{ff}, we have a contribution on this side. For $s_{ff} = 0$ the amplitude vanishes already on matrix element level. The resulting distribution is shown in figure 2.4 (green/large dashed).

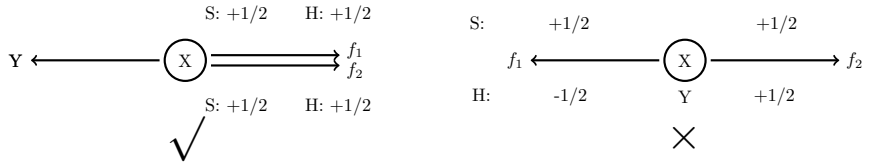

Figure 2.2: Forbidden process for scalar decay. Due to spin conservation, this process is forbidden. For $s_{ff} = s_{max}$ the amplitude is 0 due to the helicities of the fermions. For $s_{ff} = 0$ the amplitude, which is proportional to s_{ff}, is also zero.

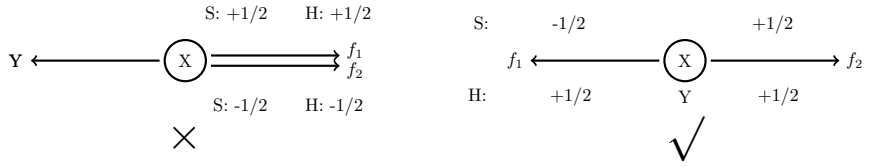

Figure 2.3: Allowed scalar decay for $s_{ff} = 0$ (left side) and $s_{ff} = s_{max}$. The distribution is shown in figure 2.4 (green/large dashed).

• $S \to f\overline{f}V$: Since the vector can have polarization $\pm 1, 0$, this process has a more involved structure. However, one can at least explain the trend. The matrix element reads:

$$\begin{aligned}\mathcal{M}_{fi} &= \overline{u}_f \ (g_r P_R + g_l P_L) S_I \gamma_\mu (n_l^* P_L + n_r^* P_R) v_f \epsilon_Y^\mu \\ &\simeq \frac{1}{M_I} \overline{u}_f \ \gamma_\mu (g_r n_r^* P_L + g_l n_l^* P_R) v_f \epsilon_Y^\mu .\end{aligned}$$

We can thus either have the two fermions back to back, in which case they have to have the same spin projected on the quantization axis, or they are in the same direction, in which case they have to have opposite spin. This corresponds to a polarization for the vector of either ± 1 which gives a transversal vector (for $s = s_{max}$), or polarization $= 0$ which is the longitudinal polarization. Thus, for both $s_{ff} = 0$ and $s_{ff} = s_{max}$ we have a contribution, and in the limit $s_{ff} \to 0$ and $s_{ff} \to s_{max}$ the amplitudes are proportional to $((m_X/m_Y)^2 - 1)$ and $(m_X^2 - m_Y^2)$. The first one is larger and diverges as $m_Y \to 0$ which reflects the massive polarization sum which was taken for this vector. This can be nicely seen in the blue/small dashed distribution in figure 2.4.

• $V \to f\overline{f}S$: In this case, we start with a spin 1 boson. We can follow a similar reasoning as above but end up with the opposite result, namely that there is a maximal contribution $s_{ff} = s_{max}$. This distribution we can see in the pink/small dashed line in figure 2.4.
• $V \to f\overline{f}V$: There are several limiting cases to be considered for this decay. The matrix element is given by

$$\begin{aligned}\mathcal{M}_{fi} &= \overline{u}_f \ \gamma_\mu(g_r P_R + g_l P_L) S_I \gamma_\nu (n_l^* P_L + n_r^* P_R) v_f \epsilon_Y^\mu \epsilon_X^{\mu *} \\ &\simeq \frac{1}{M_I} \overline{u}_f \ \gamma_\mu \gamma_\nu (g_r n_l^* P_L + g_l n_r^* P_R) v_f \epsilon_Y^\nu \epsilon_X^{\mu *} . \end{aligned} \tag{2.17}$$

In this decay we have several combinations of fermion helicities and their orientation with respect to the decaying vector. Consequently, on can now in principle get a non-vanishing matrix element squared for all s_{ff} in contrast to $S \to f\overline{f}S$, which has an equivalent chirality structure. For the special combination of couplings $g_R = g_L = n_L = n_R$ as shown in figure 2.4 (cyan/dot-dashed) one has the specific case where the matrix element vanishes for $s_{ff} = 0$.
Obviously, these simple results change if one considers fermion masses and a massive propagator.

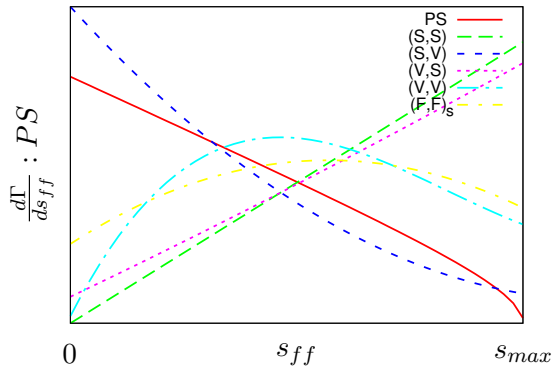

Figure 2.4: Invariant mass distribution for the decays $X \to f\overline{f}Y$, with $X, Y \in S, V$ from equation 2.16. The letters in parentheses denote the decays with particles (X, Y). We have chosen $m_f = 0$ and $m_X/m_Y = 0.1$. In order to disentangle spin effects from phase space contributions, the differential decay rate is divided by the global phase space factor.

2.2.2 Spin determination in decay chains

Let us now look at expected signatures from the decays of BSM particles at a hadron collider. As we have seen, both (M)UED and Susy can have a parity that predicts pair production of some BSM particles and a stable, probably undetectable particle. We have also seen that the partner particles in Susy are organized as opposite spin partners, and in UED as same spin partners to the SM, which is due their respective origin from supermultiplets or KK-towers.

A decay in these models thus looks similar: a new unstable heavy particle X is produced at a hadron collider which will subsequently decay into lighter particles $A, B, \ldots, K, L$ and a bunch of SM particles or jets, and a stable, undetectable particle Y which is usually the Dark Matter candidate of the respective model. Such a decay chain is sketched in figure 2.5 where SM_i, $i = 1, 2, 3, 4$ should denote the SM particles/jets and $X, A, B \ldots$ are the new particles.

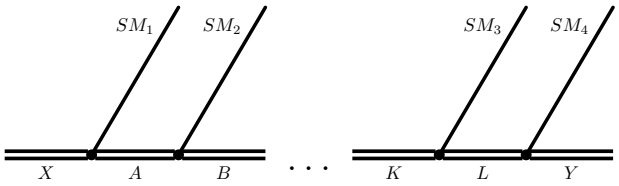

Figure 2.5: Example of a decay chain of a heavy particle X into SM particles and BSM particles $A, B \ldots$ and a stable BSM particle Y which remains undetected.

To contrast Susy and UED in such a decay chain, let us look at a simple example with a short chain of subsequent decays

$$X(p) \to f(q_1)I(p_I) \to \overline{f}(q_2)Y(q_3). \tag{2.18}$$

In UED, the decaying particle can be a KK-excitation of a gluon (vector) whereas in Susy, the corresponding particle would be a Majorana gluino, both depicted in figure 2.6. Both particles decay, assuming the squarks/ KK-quarks are lighter than the gluino, into squarks/ KK-quarks and finally in a neutralino/B'. The visible particles are SM model fermions $f, \overline{f}$ from which we reconstruct the invariant mass distribution $s_{ff} = (q_1 + q_2)^2$. Since we want to know which is the model realized in nature, we have to determine the spins of the particles $A, B \ldots$ in figure 2.5, which in our example corresponds to the bosonic/fermionic nature of squarks/quark' in figure 2.6.

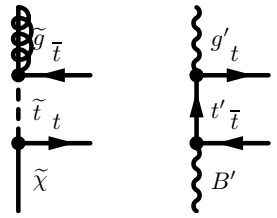

Figure 2.6: Decays with the same signature (two SM-fermions and missing energy) in Susy (left) and UED (right) scenario. The spin of the BSM particles is different: The decaying and the invisible particles in Susy are Majorana fermions while they are vector particles in UED.

For decay chains involving more than or at least two visible decay products one can build one or more invariant mass distributions of different visible particles. From reconstructing these, we can investigate two properties of the underlying model:
The endpoints of these distributions depend on the masses of the involved particles and these "kinematic edges" can be used to reconstruct the masses even

of the invisible particles. For a detailed review on this topic investigating different models see [20] with references therein, for new studies concentrating on parameter determination in Susy models see e.g. [21].
While these endpoints are fixed by kinematics, the shape of the differential distribution is sensitive to the spin of the decay products. Each spin and coupling scenario has its specific signature as we have illustrated in the simple example in Section 2.2.1 for off-shell decays. In the case of subsequent decays, this property has been studied widely and discussed for various decay chains [2, 20, 22–37] where in many cases model dependent assumptions have been made. In [38–42] s-channel resonances have been investigated. One can also get information on the spin from cross section measurements [1].
Complications of these methods are among other things that one needs to know or guess which particles belong to which decay chain (if there are two-sided decay chains, as can be present in Susy/UED with a parity), and also the assignment of near and far lepton or quark in a decay chain with at least three particles. This alters the distribution and washes out the effects.

We are interested in the invariant mass of two SM particles which come out of a decay chain as above. Here one can get the spin of the intermediate particle as in figure 2.6 via the specific dependence of the differential decay rate on the invariant mass.
In subsequent decays, this method relies on plane wave decomposition of a matrix element depending on the energy s and two angles θ, ϕ into a reduced matrix element and spherical harmonics [43],

$$\mathcal{M}(s,\theta,\phi) = \sum_{l=0}^{\infty} \sum_{m=-l}^{l} \mathcal{M}(s)_{l,m} Y_{l,m}(\theta,\phi).$$

The spherical harmonics can be expressed with the Wigner-d/D rotation matrices or the reduced Wigner rotation matrix d [43, 44]

$$Y_{l,m}(\theta,\phi) = \sqrt{\frac{2l+1}{4\pi}} D^{l*}_{m0}(\phi,\theta,-\phi); \quad D^{j}_{m,m'}(\theta,\phi,\gamma) = e^{-im'\theta} d^{j}_{m'm}(\theta) e^{-im\gamma}$$

where ϕ, θ, γ are the three Euler angles. One can now make use of this expansion and thus the helicity amplitude for the decay of an unstable particle with orbital momentum J, and its projection on the z-axis M, $(J,M) \to (j_1,\lambda_1),(j_2,\lambda_2)$ is given by

$$\begin{aligned}\mathcal{M}^{(J,M)}_{(j_1,\lambda_1),(j_2,\lambda_2)} &= \sqrt{\frac{2J+1}{4\pi}} D^{J*}_{M,\lambda}(\phi,\theta,-\phi) \mathcal{M}^{J}_{\lambda_1,\lambda_2} \\ &= \sqrt{\frac{2J+1}{4\pi}} e^{i(M-\lambda)\phi} d^{J}_{M,\lambda}(\theta) \mathcal{M}^{J}_{\lambda_1,\lambda_2}\end{aligned}$$

with $\lambda = \lambda_1 - \lambda_2$. If we go to the rest frame of this decaying particle, we can replace $J = S$ since all orbital momentum vanishes and we have

$$\mathcal{M}^{(S,M)}_{(j_1,\lambda_1),(j_2,\lambda_2)} = \sqrt{\frac{2S+1}{4\pi}} D^{S*}_{M,\lambda}(\phi,\theta,-\phi) \mathcal{M}^{S}_{\lambda_1,\lambda_2}$$

$$= \sqrt{\frac{2S+1}{4\pi}} e^{i(M-\lambda)\phi} d^S_{M,\lambda}(\theta) \mathcal{M}^S_{\lambda_1,\lambda_2}.$$

The angle θ is now the angle of one of the decay products with respect to some quantization axis e.g. of the initial particle's spin, and ϕ is the azimuthal angle around this axis. The spin information of the initial particle S is now purely contained in the rotation matrices $d^S_{M,\lambda}$ which can be expressed as [45, 46]

$$d^J_{M,\lambda}(\theta) = \sum_k (-1)^k \left[\frac{\sqrt{(J+\lambda)!(J-\lambda)!(J+M)!(J-M)!}}{k!(J-\lambda-k)!(J+M-k)!(k+\lambda-M)!} \right] \times \left(\cos\frac{\theta}{2}\right)^{2(J-k)+M-\lambda} \left(\sin\frac{\theta}{2}\right)^{(2k+\lambda-M)} \tag{2.19}$$

where one sums over all k guaranteeing positive factorials. In the rest frame of the decaying particle, $J = S$, and the differential decay rate is

$$\frac{d\Gamma}{d\Omega} = \frac{p_f}{32\pi^2 m^2} \left| \mathcal{M}^{(S,M)}_{\lambda_1\lambda_2} \right|^2,$$

and is hence quadratic in $d^S_{M,\lambda}$, leading to a polynomial in $\cos\theta$ with maximal degree $2S$ according to equation 2.19.
For an amplitude of a scattering process $a(\lambda_a) + b(\lambda_b) \to i(J, M) \to c(\lambda_c) + d(\lambda_d)$ the helicity amplitude in the rest frame of the particle i reads [43]

$$\mathcal{M}^{\lambda_a\lambda_b}_{\lambda_c\lambda_d}(S, \theta_{bc}, \phi) = (2S+1) d^S_{\lambda_i,\lambda_f}(\theta_{bc}) e^{i\phi(\lambda_i-\lambda_f)} \mathcal{M}^S_{\lambda_i,\lambda_f} \tag{2.20}$$

where θ_{bc} is the scattering angle of the process. Note that $\mathcal{M}^S_{\lambda_i\lambda_f}$ is the reduced matrix element and thus does not depend on the angles θ, ϕ. Using crossing symmetries, this can be rewritten as the decay $a(\lambda_a) \to b(\lambda_b) + c(\lambda_c) + d(\lambda_d)$ [47]

$$\mathcal{M}^{\lambda_a}_{\lambda_b\lambda_c\lambda_d}(S, \theta_{bc}, \phi) = (2S+1)\ d^S_{\lambda_i,\lambda_f}(\theta_{bc}) e^{i(\lambda_i-\lambda_f)\phi} \mathcal{M}^S_{\lambda_i\lambda_f}$$

with $\lambda_i = (\lambda_a - \lambda_b), \lambda_f = (\lambda_c - \lambda_d)$ and the scattering angle of two of the products θ_{bc}. The Wigner-d/D rotation matrices $d^S_{M,\lambda}$ are a polynomial in $\cos\theta_{bc}/2$ of degree $2S$ (as given in equation 2.19). After squaring, this leads to a polynomial in $\cos\theta_{bc}$ of degree $2S$

$$\sum_{pols.} |\mathcal{M}|^2 = a_0 + \ldots + a_{2S-1}\ \cos_{bc}\theta^{(2S-1)} + a_{2S}\ \cos_{bc}\theta^{2S}$$
$$= \sum_i^{2S} a_i\ \cos(\theta_{bc})^i. \tag{2.21}$$

Since we want to study frame-independent variables, we rewrite equation 2.21 in terms of the invariant mass $s_{ff} = (q_1 + q_2)^2$ of two of the decay products, and the $\cos\theta_{bc}$ dependence of the squared matrix element translates into [1]

$$d\,\Gamma(X \to f\overline{f}Y) = ds_{ff} \sum_i^{2S} b_i\ s^i_{ff}. \tag{2.22}$$

[1] $s_{ff} \propto E_1E_2 - ||\vec{q_1}||\vec{q_2}|\cos\theta_{bc}$ with q_1, q_2, E_1, E_2 being momenta and energies of the decay products.

The differential decay rate for the amplitude of equation 2.18 has now maximal degree $2S$ where S is the spin of the intermediate particle I and b_i are the coefficients of the polynomial which are only functions of the masses and the coupling strengths.
From this distribution, one can hence reconstruct the polynomial that is needed to explain the data and to find via the highest power $2S$, the spin S of the intermediate particle. Depending on whether the visible SM particles SM_1, $SM_2, \ldots$ in figure 2.5 are fermions or bosons, one can also determine the fermion line(s). For a detailed study see e.g. [35, 43].
In figure 2.7 we show such distributions for decays where the intermediate particle is a scalar (black dashed), a vector particle (grey dotted) and a fermion (black solid). The distribution for an intermediate scalar is just a constant as expected from equation 2.22, the one for fermion is of order s^1_{ff} and the scalar has a parabolic distribution of order s^2_{ff}. In the literature, most of these distributions are shown for m_{ff} with $m^2_{ff} = s_{ff}$ which gives a Jacobian factor. Although the kinematical edges for mass determination are more obvious using this variable, we find that for spin determination the shape is better reflected for the distribution over s_{ff}.
These properties are widely investigated and will be used to discriminate various spin scenarios as soon as there are data of such decay chains with missing energy. As we have already pointed out in the introduction on page 3, there are some interesting cases where the simple relation given in equation 2.22 cannot be applied. The next three chapters are dedicated to these problems and their discussion and solution.

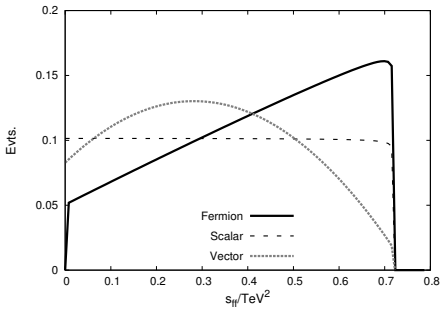

Figure 2.7: Invariant mass distribution of two fermions in a decay $X \to f\overline{f}Y$ with SM particles $f, \overline{f}$ for intermediate fermion, scalar and vector. The events are arbitrarily normalized. For intermediate scalar, the distribution is $\propto s^0_{ff}$, for fermion $\propto s^1_{ff}$ and for intermediate vector $\propto s^2_{ff}$ according to equation 2.22. The kinematic edges are usually displayed as $\mathrm{d}\Gamma/\mathrm{d}m_{ff}$ with $m^2_{ff} = s_{ff}$ which gives a better impression for mass studies. The influence of the spin is however more obvious to see in the terms of s_{ff}.

Chapter 3

Anomalous Couplings in Spin Determination

In this chapter we investigate the influence of non-renormalizable momentum dependent operators on decay chains. We calculate the contributions of these operators to the differential decay width and give the results for generic couplings. Their influence is important with regard to two aspects: Firstly, from a simple power counting argument, these higher dimension operators can in principle contribute a higher order in s_{ff} in equation 2.22 and distort spin analysis with this method. Secondly, these operators can have an effect on the measurement of the couplings [1] and one has to take their contributions into account in addition to the dimension 4 operators which are discussed in [33]. In this chapter, we first summarize the set-up and give the power counting argument why new operators can in principle distort spin determination. We derive the corresponding decays with momentum dependent dimension 5 operators and give the modified coefficients b_i appearing in equation 2.22 as functions of the original and the new couplings and the masses involved. We discuss explicitly how contributions of momentum dependent operators to misleading powers of s_{ff} vanish.

3.1 Setup and kinematics

We investigate the decay chain

$$X(p, m_X) \to f(q_1, m_f)\overline{f}(q_2, m_f)Y(q_3, m_Y) \tag{3.1}$$

where X, Y can be scalars, vectors or spin 1/2 fermions. We summarize the notation in figure 3.1. We define the Mandelstam variables as

$$s_{ff} := s = (q_1 + q_2)^2 = (p - q_3)^2; \qquad u = (q_1 + q_3)^2 = (p - q_2)^2; \tag{3.2a}$$

$$t = (q_2 + q_3)^2 = (p - q_1)^2 \tag{3.2b}$$

where s_{ff} is the invariant mass of the two visible SM fermions and the variable we are interested in. For the calculation of the differential decay rate $\mathrm{d}\Gamma/\mathrm{d}s_{ff}$

[1] By "measurement of couplings" we mean the ratio of left and right handed coupling constants, not their absolute value.

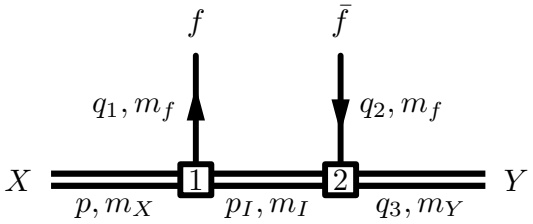

Figure 3.1: Notation for decay in equation 3.1. The double lines denote the particles with unknown spin and the boxes stand for dim. 4 and dim. 5 couplings. In the following we refer to the vertex with "1" as the first and the vertex with "2" as the second vertex and we denote the corresponding coupling $\Gamma_{1S,V}$.

one usually replaces one of the variables, e.g. u, via Mandelstam's relation

$$u = 2\ m_f^2 + m_X^2 + m_Y^2 - t - s_{ff} \tag{3.3}$$

and integrates out the remaining invisible invariant mass, (in this case t) for which the upper and lower bounds are

$$t_\pm = \left(m_f^2 + m_X^2 + m_Y^2 - s_{ff}\right) \pm \frac{\sqrt{s_{ff}\left(-4m_f^2 + s_{ff}\right)\left(m_X^4 + \left(m_Y^2 - s_{ff}\right)^2 - 2m_X^2\left(m_Y^2 + s_{ff}\right)\right)}}{2s_{ff}}.$$

The other remaining visible invariant mass s_{ff} has then the kinematical bounds[2]

$$s_{ff_} = (2m_f)^2; \qquad s_{ff_+} = (m_X - m_Y)^2. \tag{3.4}$$

For the sake of completeness we also give the propagators and polarization sum used (here without NWA). The fermion propagator, the scalar propagator and the vector propagator (unitary gauge) are respectively

$$\not{F}_{p_I} = \frac{i\left(\not{p}_I + m_I\right)}{p_I^2 - m_I^2 + im_I\Gamma}; \tag{3.5a}$$

$$W_{p_I,s} = \frac{i}{p_I^2 - m_I^2 + im_I\Gamma}; \quad W_{p_I,v} = \frac{-i\left(g^{\mu\nu} - p_I^\mu p_I^\nu/m_I^2\right)}{p_I^2 - m_I^2 + im_I\Gamma} \tag{3.5b}$$

and the polarization sums for external vector bosons are

$$\sum_s \epsilon(k)^{s\mu} \cdot \epsilon(k)^{s\nu *} = \frac{k^\mu k^\nu}{k^2} - g^{\mu\nu}; \tag{3.6a}$$

$$\sum_s u^s(k)\bar{u}^s(k) = \not{k} + m; \quad \sum_s v^s(k)\bar{v}^s(k) = \not{k} - m. \tag{3.6b}$$

[2]From $s_{ff} = (q_1 + q_2)^2 = (m_1^2 + m_2^2 + 2(E_1 \cdot E_2 - \cos\theta|\vec{p}_1||\vec{p}_2|)) = (m_1^2 + m_2^2)^2$, with the condition for the lower bound (fermion 1 and 2 get minimal energy) $E_1 = E_2 = 0, \cos\theta = 0$ and hence $|q_i| = m_i$, analogous for the upper bound where the fermion 1 and 2 get maximal energy and hence the other two particles minimal energy ($E_x = E_y = 0$): $s_{ff} = (p - q_3)^2 = (m_X^2 + m_Y^2 + 2(E_x E_y - \cos\theta|\vec{p}||\vec{q}_3|))^2 = (m_X - m_Y)^2$.

If we want to make use of the spin-argument in Section 2.2, we need to have the mass hierarchy $m_X > m_I > m_Y$ so that the intermediate particle I is on-shell and the decay is then

$$X(p, m_X) \to f(q_1, m_f) + I(p_I, m_I) \to f(q_1, m_f) + \overline{f}(q_2, m_f) + Y(q_3, m_Y) \quad (3.7)$$

where we have explicitly introduced the intermediate particle I with momentum p_I and mass m_I. This decay will normally take place if the subsequent decay is possible from conservation of quantum numbers or colour flows since the produced particles only decay into lighter ones. Three body decays as considered in the next chapter are always suppressed by phase space and the mass of the mediating particle.
One usually makes in this case the narrow width approximation (NWA) where one assumes that the width of the particle Γ_I is small compared to its mass (see e.g. [43] or [48]).
We use NWA to calculate the (differential) decay width and replace the propagator of the intermediate particle with its width and a delta function that fixes the invariant mass to the on-shell mass of the particle

$$\frac{1}{(s_{ff} - m_I^2)^2 + m_I^2\Gamma_I^2} \approx \frac{\pi}{m_I\Gamma_I}\delta(s_{ff} - m_I^2). \quad (3.8)$$

In this approach, one usually calculates the separate decays for this process and multiplies them together with this factor instead of using the full propagator. The complete decay rate is then given by

$$\Gamma_{2\to n} = \Gamma_{2\to n-1}\frac{\Gamma_{1\to 2}}{\Gamma_{total}} \quad (3.9)$$

where Γ_{total} is the total width of this particle. Since the NWA approach treats the spin of the particles by averaging over the initial polarizations and summing over the final particles' polarizations, one does not keep helicity and spin information properly. Since we are explicitly interested in the spin information, we need to include these effects. There are two possibilities: one can either use helicity density matrix methods or calculate the full process and afterwards take the limit. Since this decay with the full propagator has a clear and simple structure, we will use the second method. However, for the first method we refer the reader to Section 5.1.2 where we derive the cross section for a more involved topology by using helicity density matrix methods.
The decay width is given by

$$\mathrm{d}\Gamma = \frac{1}{(2\pi)^3}\frac{1}{32m_X^3}\sum_{pol.}|\mathcal{M}|^2_{(X,Y)}\ \mathrm{d}s\ \mathrm{d}t \quad (3.10)$$

where we sum over the initial and average over the final polarizations. We first replace all Mandelstam-u-parameters with the Mandelstam relation from equation 3.3 and then set the intermediate particle on-shell with $t = (q_2 + q_3)^2 = m_I^2$

so that we effectively integrate out t. The Mandelstam variables become in this limit

$$t = (p - q_1)^2 = (q_2 + q_3)^2 = m_I^2 \tag{3.11a}$$
$$u = (q_1 + q_3)^2 = (p - q_2)^2 = 2m_f^2 + m_X^2 + m_Y^2 - s_{ff} - m_I^2. \tag{3.11b}$$

After using NWA, the endpoints of the invariant mass distribution s_{ff} differ from equation 3.4 due to the kinematics altered, and are given by [17]

$$s_{ff_-} = (2m_f)^2 \qquad s_{ff_+} = \frac{(m_X^2 - m_I^2)(m_I^2 - m_Y^2)}{m_I^2}. \tag{3.12}$$

In this approach, we do not need to worry about the wrong treatment of the polarizations of the intermediate particle since we automatically include all spin effects by using the full propagator for the intermediate particle.

3.2 Operators

The basic operator structures are given in [49] which, however, involves only the SM fields as external particles. In our examples new particles are allowed including additional gauge interactions with covariant derivatives $D_\mu = \partial_\mu - iA_\mu$ and field strengths $F_{\mu\nu} = (\partial_\mu A_\nu - \partial_\nu A_\mu + \ldots)$. We assume that these additional gauge groups are broken at a scale as a new scalar ϕ gets a vacuum expectation value (VeV) v_ϕ inducing a dim. 5 and dim. 6 operator via

$$\frac{\phi}{\Lambda^2} \to \frac{v_\phi}{\Lambda^2} = \frac{1}{\Lambda_{eff}}. \tag{3.13}$$

We get two classes of momentum dependent operators: fermion-fermion-vector (f-f-V) interactions and fermion-fermion-scalar (f-f-S). For the (f-f-V) interactions we have

$$\mathcal{L}_{D4}^g = (A_\mu \overline{\psi_1} \gamma^\mu \left(g_l P_L + g_r P_R\right) \psi_2 + h.c.) \tag{3.14a}$$
$$\mathcal{L}_{D5}^a = \frac{1}{\Lambda_a} \left(\overline{\psi_1} \sigma^{\mu\nu} \left(a_l P_L + a_r P_R\right) \psi_2 F_{\mu\nu} + h.c.\right) \tag{3.14b}$$
$$\mathcal{L}_{D6} = \frac{1}{\Lambda^2} \left(\overline{(D_\mu \psi_1)} \left(b_l P_L + b_r P_R\right) \psi_2 D^\mu \phi + h.c.\right)$$
$$\to \mathcal{L}_{D5}^b = \frac{1}{\Lambda_b} \left(\overline{(\partial_\mu \psi_1)} \left(b_l P_L + b_r P_R\right) \psi_2 (-iA^\mu) + h.c.\right) \tag{3.14c}$$
$$\mathcal{L}_{D6} = \frac{1}{\Lambda^2} \left(\overline{\psi_1} \left(c_l P_L + c_r P_R\right) D_\mu \psi_2 D^\mu \phi + h.c.\right)$$
$$\to \mathcal{L}_{D5}^c = \frac{1}{\Lambda_c} \left(\overline{\psi_1} \left(c_l P_L + c_r P_R\right) \partial_\mu \psi_2 (-iA^\mu) + h.c.\right) \tag{3.14d}$$

and for (f-f-S) interactions

$$\mathcal{L}_{D4}^n = \left(\phi \overline{\psi_1} \left(n_l P_L + n_r P_R\right) \psi_2 + h.c.\right) \tag{3.15a}$$

$$\mathcal{L}^x_{D5} = \frac{1}{\Lambda_x}\left(\overline{\psi_1}\gamma^\mu\left(x_l P_L + x_r P_R\right)\psi_2 D^\mu\phi + h.c.\right) \tag{3.15b}$$

$$\mathcal{L}^y_{D5} = \frac{1}{\Lambda_y}\left(\overline{(D_\mu\psi_1)}\gamma^\mu\left(y_l P_L + y_r P_R\right)\psi_2\phi + h.c.\right) \tag{3.15c}$$

$$\mathcal{L}^z_{D5} = \frac{1}{\Lambda_z}\left(\overline{\psi_1}\gamma^\mu\left(z_l P_L + z_r P_R\right)(D_\mu\psi_2)\phi + h.c.\right). \tag{3.15d}$$

We can see that for both (f-f-V) and (f-f-S) interactions there is a new covariant derivative acting on each of the fields in one interaction which then gives the momentum dependence. Obviously, not all are independent, e.g. by partial integration one can transfer one of the derivatives to the other two fields. In principle one could also consider dim. 6 operators for the (f-f-S) case but as we will discuss below, no new features will arise in such a case.

3.3 Influence of the dimension 5 operators

In the following we give a simple power counting argument why the interactions considered here can in principle give a new contribution. Then we have a look at the relevant decays and give further examples.

3.3.1 Naive expectation

Let us investigate a simple example: In the case of X, Y being fermions and an intermediate scalar I, the matrix element for dim. 4 vertices reads

$$\mathcal{M}_{D4,D5} \propto (\overline{u}(f)(1+\lambda_1 \not{k}_1)u(X))\left(\overline{u}(Y)(1+\lambda_2\not{k}_2)v(\bar{f})\right)$$
$$|\mathcal{M}|^2_{D4,D5} \propto Tr\left[\not{q}_1(1+\lambda_1\not{k}_1)\not{p}(1+\lambda_1\not{k}_1)\right] \times Tr\left[\not{q}_3(1+\lambda_2\not{k}_2)\not{q}_2(1+\lambda_2\not{k}_2)\right].$$

For showing what happens, we have restricted ourselves to pure scalar couplings and set the axial couplings to zero in this discussion. Furthermore we have introduced λ_i which is just the (mass dependent) ratio of the dim. 4 to the dim. 5 coupling strength. The momenta $p, q_1 \ldots$ are chosen as introduced in equation 3.1. The part of the coupling with "1" is the normal dim. 4 coupling, the term with $\lambda_i \not{k}_i$ is the anomalous part with a momentum dependence k_i. The momentum k_i is a momentum or a combination of momenta which can appear in the interactions given in equation 3.15 and is not specified further here since it is not important for our example.
The first Dirac trace for the dim. 4 interaction in NWA is just $\propto p \cdot q_1 = t + const. = m_I^2 + const.$, the second one is $\propto q_2 \cdot q_3 = t + const. = m_I^2 + const.$ and both are independent of s_{ff}. In the case of an intermediate scalar I, the decay rate is therefore constant and does not depend on s_{ff}.
However we see that for the $\lambda_i \not{k}_i$ terms, the trace is affected and new scalar products and hence new momentum combinations show up which could give a new dependence on s_{ff} depending on the specific form of k_i. This could then distort the spin analysis with the approach given in equation 2.22.

3.3.2 Relevant decays

We have to consider only those processes where the two external SM fermion are connected via the intermediate particle I. The topology, where the two SM fermions couple directly to the mediating one at one single vertex gives just a mass peak in the invariant mass distribution at the intermediate particle's mass m_I.
For all six decays we find that after calculating the complete decays and taking the NWA as described in Section 3.1, none of the anomalous couplings give a contribution to a new power in s_{ff} and thus equation 2.22 holds also in the presence of anomalous couplings. The specific form of the coefficients in this equation however changes but this is at least suppressed with the scale $1/\Lambda_i$ of the corresponding operator.
For intermediate fermions, we have the following processes which we denote with the short forms in the parentheses

$$S \to f\bar{f}S \quad (S,S); \quad S \to f\bar{f}V \quad (S,V); \quad V \to f\bar{f}S \quad (V,S); \quad V \to f\bar{f}V \quad (V,V)$$

and we calculate the differential decay rate

$$\frac{\mathrm{d}\,\Gamma}{\mathrm{d}s_{ff}} = A \cdot s_{ff}^0 + B \cdot s_{ff}^1 \tag{3.16}$$

where A, B are the coefficients of the polynomial and just depend on the masses and coupling strengths involved. The Feynman graphs for the corresponding decays are the first four in figure 3.2. The explicit analytic results are shown in the Appendix B.1. We give the full result for (S,S), whereas for readability we reduce the analytic results for (S,V), (V,S), (V,V) to the case with an overall scale $\Lambda_x = \Lambda_y = \ldots = \Lambda$ and show it only up to order $1/\Lambda^2$. Note here, that the lowest order interference terms of an anomalous coupling and the dimension 4 interaction always vanish and the leading contribution is already of order $1/\Lambda^2$. Consequently, the contribution of the dimension 5 operators is highly suppressed. The higher order contributions such as $1/\Lambda^3, 1/\Lambda^4 \ldots$ are interference terms of two anomalous couplings.

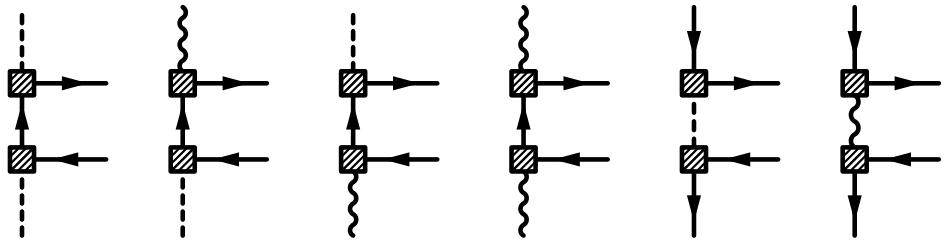

Figure 3.2: Feynman diagrams for the decays involving intermediate fermions and a scalar/vector boson. The boxes denote the dim. 5 couplings. In comparison to the diagram in figure 3.1, the diagrams are rotated clockwise for $\pi/2$ so that the upper line denotes the decaying particle X.

The relevant decays with intermediate bosons are

$$(F,F)_S \qquad F \xrightarrow{S} f\bar{f}F \qquad \frac{\mathrm{d}\,\Gamma}{\mathrm{d}s_{ff}} = A \cdot s_{ff}^0 \tag{3.17a}$$

$$(F,F)_V \qquad F \xrightarrow{V} f\bar{f}F \qquad \frac{\mathrm{d}\,\Gamma}{\mathrm{d}s_{ff}} = A \cdot s_{ff}^0 + B \cdot s_{ff}^1 + C \cdot s_{ff}^2. \tag{3.17b}$$

A, B, C are again functions of the couplings and the masses involved. The Feynman graphs for these decays are the last two in figure 3.2. In Appendix B.1 we give the explicit results simplified with $\Lambda_x = \Lambda_y = \ldots = \Lambda$ as above. We see that the lowest order interference terms again vanish and the leading contribution is of order $1/\Lambda^2$. Since the differential decay width $(F,F)_S$ is a constant in s_{ff}, we do not show it separately.

To illustrate how these contributions of the dim. 5 operators affect the differential decay rates, we show the differential decay distributions for all six decays in figure 3.3. The masses and the couplings are chosen as

$$m_X = 1 \text{ TeV} \qquad m_Y = 0.15 \text{ TeV} \qquad m_f = m_{\bar{f}} = 0 \text{ TeV} \tag{3.18a}$$

$$m_I = 0.4 \text{ TeV} \qquad \lambda = 3 \text{ TeV} \tag{3.18b}$$

$$n_l = 1, n_r = 0.1; \qquad g_l = 1, g_r = 0.1; \tag{3.18c}$$

$$a_l = 1, a_r = 0.3; \qquad b_l = 0.4, b_r = 0.5; \qquad c_l = 0.8, c_r = 0.7; \tag{3.18d}$$

$$x_l = 0.4, x_r = 0.3; \qquad y_l = 0.5, y_r = 0.3; \qquad z_l = 1, z_r = 0.1; \tag{3.18e}$$

where the couplings are given in equations 3.14 and 3.15 with values chosen randomly between [0,1].
We show the complete dim. 4 (black dashed) and dim. 5 distribution (red solid) for each decay and just for comparison include the NWA (dim. 4, NWA: black dotted; dim. 5, NWA: grey solid) result. For all decays, the NWA result is a very good approximation to the complete decays including the full propagator. The only difference is at the kinematic edges where the approximation does not take the possible off-shellness of the intermediate particle into account. The NWA result obviously yields only a line/parabola and not the smooth edges of the complete result. The influence of the dim. 5 operators in this mass/coupling scenario is the largest in the $(F,F)_V$ followed by the (V,S) decay. The first one is clear since here, the polynomial for this decay in equation 2.22 is the longest and thus there are 3 coefficients (minus the relative normalization) which can be influenced while in the decays via fermions, the polynomial has only two coefficients (minus the relative normalization). In the $(F,F)_S$ decay, the influence of the anomalous coupling is not present since the decay rate is constant in NWA. There is also a tiny effect for the other decays including vector particle $(V,V), (S,V), (V,S)$ since here one gets a stronger mass dependent relative shift of the coefficients via the vector polarization sum(s) in comparison to the decay (S,S).
In reasonable scenarios, the mass of the decaying particle, which is the highest scale in the decay, satisfies $m_X < \Lambda$. Due to the fact that the leading term is already of order $1/\Lambda^2$, the contribution from the anomalous interactions is of order $(m_X/\Lambda)^2$ and thus tiny.

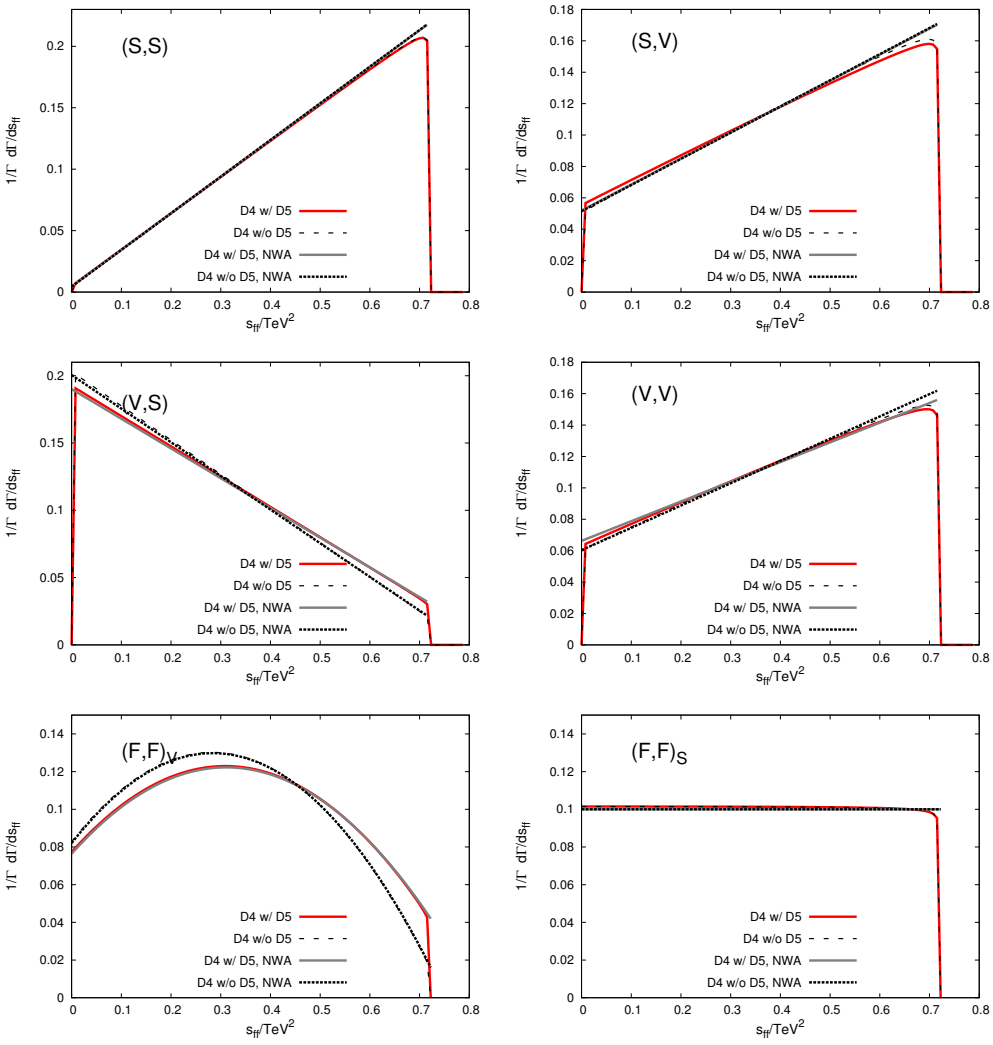

Figure 3.3: Differential decay rate over the invariant mass s_{ff} for the dim. 4 (black) and the dim. 5 (red/grey) couplings for intermediate fermions/bosons (first two row/last row). We show the exact results (solid/dashed) and NWA results (solid/dotted). The masses and couplings are chosen as in equation 3.18. The effects of the anomalous coupling are very weak and are stronger when there is a vector particle due to the momentum dependence of the polarization sum and the vector propagator.

3.4 Discussion

In the beginning of Section 3.3 we have given a simple power counting argument, why higher dimension operators are in principle capable of introducing new powers of s_{ff} to equation 2.22. In the following we discuss in detail how these additional terms cancel.
We concentrate here on the following four decays since for (S,V) and (V,S) the same arguments apply as for (V,V) or (S,S). The amplitudes for these decays include dim. 4 and dim. 5 interactions given in equations 3.14 and 3.15

$$\mathcal{M}_{(S,S)} = \overline{u}(q_1)\left(\Gamma^{D4}_{1\ S} + \Gamma^{D5}_{1\ S}\right)\left(\frac{\not{p} - \not{q_1} + m_I}{(p_I^2 - m_I^2)}\right)\left(\Gamma^{D4*}_{2\ S} + \Gamma^{D5*}_{2\ S}\right)v(q_2) \tag{3.19a}$$

$$\mathcal{M}_{(V,V)} = \epsilon^{\mu}(p)\epsilon^{\nu *}(q_3)\overline{u}(q_1)\left(\Gamma^{D4}_{1\ S} + \Gamma^{D5}_{1\ S}\right)_{\mu}\left(\frac{\not{p} - \not{q_1} + m_I}{(p_I^2 - m_I^2)}\right) \times \left(\Gamma^{D4*}_{2\ S} + \Gamma^{D5*}_{2\ S}\right)_{\nu} v(q_2) \tag{3.19b}$$

$$\mathcal{M}_{(F,F)_S} = \left(\overline{u}(q_1)\left(\Gamma^{D4}_{1S} + \Gamma^{D5}_{1S}\right)u(p)\right)\cdot\left(\overline{u}(q_3)\left(\Gamma^{D4}_{2S} + \Gamma^{D5}_{2S}\right)v(q_2)\right) \tag{3.19c}$$

$$\mathcal{M}_{(F,F)_V} = \left(\overline{u}(q_1)\left(\Gamma^{D4}_{1V} + \Gamma^{D5}_{1V}\right)_{\mu}u(p)\right)\cdot\left(\overline{u}(q_3)\left(\Gamma^{D4}_{2V} + \Gamma^{D5}_{2V}\right)_{\nu}v(q_2)\right) \times \left(\frac{g^{\mu\nu} - p_I^{\mu}p_I^{\nu}/m_I^2}{p_I^2 - m_I^2}\right). \tag{3.19d}$$

We denote which couplings carry Lorentz indices by writing down the couplings with $\left(\Gamma^{D4}_{1V} + \Gamma^{D5}_{1V}\right)_{\mu}$ to emphasize the contractions. The indices "1,2" in the couplings denote the first or the second vertex of the decay.

3.4.1 Dimension 4 operators

Let us first investigate decay 3.19a with renormalizable dim. 4 couplings $\Gamma^{D4}_{1\ S}$ ($\Gamma^{D5}_{1\ S} = 0$) to see how the highest power of s_{ff} arises. These term must come from the part in the propagator which is momentum dependent since the massive part m_I just gives a constant (=massive) contribution. The same is the case for the polarization sum $u(p)^s\bar{u}(p)^s = \sum_s \not{p} + m$ after squaring the matrix element and summing over all polarizations. Thus we neglect the massive/constant part of the amplitude in the following. Furthermore we suppress the left/right handed projectors since they are irrelevant for the general discussion (in this decay, we will just leave out the couplings $\Gamma_{1S,2S}$ since they do not carry Lorentz nor spinor indices). Whenever we make such a simplification, we use the symbol '$\sim$' to emphasize that in this step in the calculation all unimportant non-leading orders (masses etc.) are dropped and we concentrate only on the maximal contribution of the momenta. The matrix element is then given by

$$\sum_{pols}|\mathcal{M}_{(S,S),D4}| \sim \sum_{pols}\left(\overline{u}(q_1)\not{p}_I v(q_2)\right)\left(\overline{v}(q_2)\not{p}_I u(q_1)\right) \sim Tr\left[\not{q_1}\not{p}_I\not{q_2}\not{p}_I\right]$$
$$\sim \left(8\underbrace{(p\cdot q_1 - q_1^2)}_{(1)}p\cdot q_2 + 4\underbrace{(q_1^2 - p^2)}_{(2)}q_1\cdot q_2\right). \tag{3.20}$$

From the Mandelstam variables in the NWA limit given in equation 3.11 we only get a s_{ff} term from the scalar products

$$p \cdot q_2 \to s_{ff} + const.; \qquad q_1 \cdot q_3 \to s_{ff} + const. \tag{3.21a}$$

$$q_1 \cdot q_2 \to s_{ff} + const. \qquad p \cdot q_3 \to s_{ff} + const. \tag{3.21b}$$

while the remaining scalar products just give a mass and hence a constant contribution

$$p \cdot q_1 \to const.; \qquad q_2 \cdot q_3 \to const. \tag{3.22}$$

Consequently, the first bracket (1) in equation 3.20 gives just a mass term times $(p \cdot q_2)$, which can only contribute with one power of s_{ff} according to equation 3.21. The second bracket (2) gives again a mass term, while $(q_1 \cdot q_2)$ is again only one power of s_{ff}. This means that the whole expression has the maximal order of $\mathcal{O}(s_{ff}^1)$:

$$\sum_{pols} |\mathcal{M}|^2_{(S,S)} \sim \mathcal{O}({s_{ff}}^1) \sim \mathcal{O}({s_{ff}}^{2 \cdot 1/2}) \tag{3.23}$$

which is exactly what we would expect from the discussion in Section 2.2 for an intermediate fermion.
For the decay with two external vector bosons in equation 3.19b we derive the squared amplitude

$$\begin{aligned}\sum_{pols} |\mathcal{M}_{(V,V),D4}|^2 &\sim \sum_{pols} \left(\overline{u}(q_1)\gamma_\mu \not{p}_I \gamma_\nu v(q_2)\right)\left(\overline{v}\gamma_{\nu'}(q_2)\not{p}_I\gamma_{\mu'}u(q_1)\right) \cdot \epsilon^\mu(p)\epsilon^{\nu *}(q_3) \\ &\sim Tr\left[\not{q_1}\gamma_\mu \not{p}_I \gamma_\nu \not{q_2}\gamma_{\nu'}\not{p}_I\gamma_{\mu'}\right] \cdot \frac{p^\mu p^{\mu'}}{m_X^2} \cdot \frac{q_3^\nu q_3^{\nu'}}{m_Y^2} \\ &\sim 4\left(2p\cdot q_1 - m_X^2\right)^2 (2p\cdot q_1 \; p\cdot q_2 - m_X^2 q_1 \cdot q_2). \end{aligned} \tag{3.24}$$

The scalar product $(p \cdot q_1)$ is just a mass term, while the scalar products in the second bracket give a contribution to $\mathcal{O}(s_{ff}^1)$, but no higher terms according to equation 3.11.
We now turn to the decays with intermediate bosons, starting with equation 3.19c where we expect a constant matrix element squared. In contrast to the decays above, we have two fermion lines here

$$\begin{aligned}\sum_{pols} |\mathcal{M}_{(F,F)_S,D4}|^2 &\sim \sum_{pols} \left(\overline{u}(q_1)u(p)\overline{u}(p)u(q_1)\right)\left(\overline{u}(q_3)v(q_2)\overline{v}(q_2)u(q_3)\right) \\ &\sim Tr\left[\not{q_1}\not{p}\right] Tr\left[\not{q_2}\not{q_3}\right] \sim (q_1 \cdot p) \;\; (q_2 \cdot q_3) \end{aligned} \tag{3.25}$$

which in NWA give just the mass of the intermediate particle and no s_{ff} contribution which is intuitively clear since the numerator of the scalar propagator is independent of a momentum. Hence there is no connection between the fermions with momentum q_2 and q_3 which could give and s_{ff} dependence.

In the case of the intermediate vector boson, we have

$$\begin{aligned}\sum_{pols}|\mathcal{M}_{(F,F)_V,D4}|^2 &\sim \sum_{pols}\left(\overline{u}(q_1)\gamma_\mu u(p)\overline{u}(p)\gamma_\nu u(q_1)\right)\left(\overline{u}(q_3)\gamma_{\nu'}v(q_2)\overline{v}(q_2)\gamma_{\mu'}u(q_3)\right)\\ &\quad\times(g^{\mu\nu}-\frac{p_I^\mu p_I^\nu}{m_I^2})(g^{\mu'\nu'}-\frac{p_I^{\mu'}p_I^{\nu'}}{m_I^2})\\ &\sim Tr\left[\not{q}_1\gamma_\mu\not{p}\gamma_\nu\right]Tr\left[\not{q}_2\gamma_{\nu'}\not{q}_3\gamma_{\mu'}\right]\cdot(g^{\mu\nu}-\frac{p_I^\mu p_I^\nu}{m_I^2})(g^{\mu'\nu'}-\frac{p_I^{\mu'}p_I^{\nu'}}{m_I^2})\\ &\sim 16(-g^{\mu\mu'}p\cdot q_1+p^\mu q_1^{\mu'}+p^\mu q_1^{\mu'})(-g^{\nu\nu'}q_2\cdot q_3+q_2^\nu q_3^{\nu'}+q_2^\nu q_3^{\nu'})\\ &\quad\times(g^{\mu\nu}-\frac{p_I^\mu p_I^\nu}{m_I^2})(g^{\mu'\nu'}-\frac{p_I^{\mu'}p_I^{\nu'}}{m_I^2}).\end{aligned}\tag{3.26}$$

In comparison to equation 3.25, we have the additional contributions of $p^\mu q_1^{\mu'}\ldots$ which can then be contracted with the momenta of the trace of the second fermion line. These contractions give new momentum combinations and one can see that terms of the form $(q_1\cdot q_2)\ (p\cdot q_3)$ arise which according to equation 3.21 give a $\mathcal{O}(s_{ff}^2)$ contribution characteristic for intermediate vector bosons.

3.4.2 Dimension 5 operators

Now we generalize the discussion to dimension 5 operators. We focus here on the leading powers of s_{ff} and thus of the momenta, and show explicitly why they vanish. Analogous to above, we will therefore only investigate the $\frac{k^\mu k^\nu}{m^2}$ term of the propagator or polarization sum for vector bosons, and only the $\not{k}$ part in fermionic propagators. As before, we denote these steps in the calculation with "$\sim$". Recall that only the specific momentum combinations in equation 3.21 can give a term proportional to s_{ff}, all others give just a massive (constant) contribution.

We start with the decay $(F,F)_S$ from equation 3.19c including the anomalous dim. 5 couplings Γ_S^{D5}. To see what happens, we abbreviate the dim. 5 couplings for the first and the second vertex with

$$\Gamma_{1S}^{D5}=A_1\cdot\not{p}+B_1\cdot\not{q}_1+C_1\cdot p_I;\qquad \Gamma_{2S}^{D5}=A_2\cdot\not{q}_2+B_2\cdot\not{q}_3+C_2\cdot p_I\tag{3.27}$$

where A_i, B_i, C_i include the chiral couplings for the first and the second vertex which are not relevant for the following arguments and have therefore been abbreviated for better legibility. The amplitude for the dim. 5 couplings then is

$$\begin{aligned}\mathcal{M}_{(F,F)_S,D5}&\sim\left\{\overline{u}(q_1)\left(A\cdot\not{p}+B\cdot\not{q}_1+C\cdot p_I\right)u(p)\right\}\\ &\quad\times\left\{\overline{u}(q_3)\left(A_2\cdot\not{q}_2+B_2\cdot\not{q}_3+C_2\cdot p_I\right)u(p)\right\}.\end{aligned}\tag{3.28}$$

By using the Dirac equation

$$\not{p}u(p)=m_p\ u(p);\qquad\qquad \overline{u}(p)\not{p}=\overline{u}(p)\ m_p\tag{3.29}$$

for all parts with momenta given in equation 3.28, we see that all these contributions are proportional to m_X, m_Y, m_f[3]. Nevertheless, the coefficients in equation

[3]Since $p_I=(p-q_1)=(q_2+q_3)$.

2.22 are changed due to these new terms, but no new power of s_{ff} appears.
In the case of the decay $(F,F)_V$ give in equation 3.19d we have the following anomalous coupling

$$\Gamma_{1V}^{D5\mu} = A_1 \cdot \sigma^{\mu\alpha} p_{I\ \alpha} + B_1\ q_1^\mu + C_1 \cdot p^\mu; \tag{3.30a}$$
$$\Gamma_{2V}^{D5\mu} = A_2 \cdot \sigma^{\mu\alpha} p_{I\ \alpha} + B_2\ q_2^\mu + C_2 \cdot q_3^\mu. \tag{3.30b}$$

and with the matrix element in equation 3.19d we see that the index μ is always contracted with the momentum $p_I^\mu = (p-q_1)^\mu = (q_2+q_3)^\mu$ from the propagator. This leads to the contractions

$$\sigma^{\mu\alpha} p_{I\ \alpha} p_{I\ \mu}; \qquad (p-q_1)^\mu q_{1\ \mu}; \qquad (p-q_1)^\mu p_\mu \tag{3.31a}$$

at the first vertex and

$$\sigma^{\mu\alpha} p_{I\ \alpha} p_{I\ \mu}; \qquad (q_2+q_3)^\mu q_{2\ \mu}; \qquad (q_2+q_3)^\mu q_{3\ \mu} \tag{3.31b}$$

at the second vertex. The contractions with the antisymmetric $\sigma^{\mu\alpha}$ matrix give zero, the other terms give a mass dependence and either a scalar product $(p \cdot q_1)$ or $(q_2 \cdot q_3)$. In NWA these are just proportional to the mass of the intermediate particle m_I and do not give a new s_{ff} dependence according to equation 3.22. All other contractions are of the same order of s_{ff} as the terms arising from dim. 4 couplings.
Let us now consider the decays with intermediate fermions, starting with the decay (V,V) of equation 3.19b. We shorten the couplings analogous to above with

$$\Gamma_{1V}^{D5\mu} = A_1 \sigma^{\mu\alpha} p_\alpha + B_1 p_I^\mu + C_1 q_1^\mu; \quad \Gamma_{2V}^{D5\mu} = A_2 \sigma^{\nu\alpha} q_{3\ \alpha} + B_1 p_I^\nu + C_1 q_2^\nu \tag{3.32}$$

where we have again summarized the chiral parts of the couplings in the coefficients A_i, B_i, C_i with $i = 1,2$ for the first and the second vertex. The momenta of the anomalous couplings are contracted with the polarization vectors of the external vector bosons. The squared matrix element is given by

$$\begin{aligned}
&\sum_{pols} |\mathcal{M}_{VV\ D5}|^2 \sim \\
&\sim \left(\overline{u}(q_1)(A_1\sigma^{\mu\alpha}p_\alpha + B_1 p_I^\mu + C_1 q_1^\mu)\not{p}_I(A_2\sigma^{\nu\alpha}q_{3\ \alpha} + B_1 p_I^\nu + C_1 q_2^\nu)v(q_2)\right) \\
&\times \left(\overline{u}(q_1)(A_1\sigma^{\mu'\alpha}p_\alpha + B_1 p_I^{\mu'} + C_1 q_1^{\mu'})\not{p}_I(A_2\sigma^{\mu'\alpha}q_{3\ \alpha} + B_1 p_I^{\mu'} + C_1 q_2^{\mu'})v(q_2)\right)^\dagger \\
&\cdot \underbrace{\epsilon_\mu(p)\epsilon_{\mu'}(p)^*\epsilon_\nu(q_3)\epsilon_{\nu'}(q_3)^*}_{\frac{(p^\mu p^{\mu'})}{m_X^2}\frac{(q_3^\nu q_3^{\nu'})}{m_Y^2}}.
\end{aligned} \tag{3.33}$$

We know from the transversality condition that

$$\epsilon(k) \cdot k = 0 \tag{3.34}$$

so that the parts of equation 3.33 where $p_I^\mu = (p-q_1)^\mu = (q_2+q_3)^\mu$ is contracted to the polarization vector are zero. From these we only have the remaining momenta q_1 and q_2 from the first and the second vertex respectively. They are now in the polarization sum contracted to either p (for the first vertex) or q_3 (for the second vertex) which is again in NWA proportional to m_I^2 and gives no s_{ff} contribution. The remaining part is the term with the antisymmetric σ matrices which give 0 since they always contract the same vector's momentum.
The last decay we have to investigate is the one of equation 3.19a. We again abbreviate the couplings with

$$\Gamma_{1S}^{D5} = A_1 \not{p} + B_1 \not{q}_1 + C_1 \not{p}_I; \qquad \Gamma_{2S}^{D5} = A_2 \not{q}_2 + B_2 \not{q}_3 + C_2 \not{p}_I$$

and the matrix element reads

$$\mathcal{M}_{SS\ D5} \sim \left(\overline{u}(q_1)(A_1 \not{p} + B_1 \not{q}_1 + C_1 \not{p}_I)(\not{p}_I + m_I)(A_2 \not{q}_2 + B_2 \not{q}_3 + C_2 \not{p}_I) v(q_2)\right).$$

We can again use the Dirac equation given in equation 3.29 and get rid of the parts with $\not{q}_1$ and $\not{q}_2$. Since we use NWA we can replace the propagator backwards by the spinor sum $\sum_{pols} u(p_I)\overline{u}(p_I) = (\not{p}_I + m_I)$ so that we can also reduce $p_I u(p_I) = m_I u(p_I)$ and hence get rid of the remaining momenta. The complete amplitude then has no remaining momenta and gives a constant like the dim. 4 amplitude.
Since one can apply the same arguments for the remaining decays (S, V) and (V, S) we will not go through the explicit argumentation for these decays.

The main reasons why higher dimension operators do not change the overall lepton and quark invariant mass spectra of the decays can be summarized as follows

1. Additional s_{ff} dependence, which is equivalent to additional $\cos\theta$ dependence, can only arise through the following products (which are not independent!): $(q_1 \cdot q_3)$, $(p \cdot q_2)$, $(p \cdot q_3)$, $(q_1 \cdot q_2)$. All other ($(p \cdot q_1)$ and $(q_2 \cdot q_3)$) give in NWA sums of masses squared, see e.g. equation 3.22.

2. The antisymmetric part, e.g. the $\sigma^{\mu\nu}$ part, of the (f-f-V) interaction gets always contracted with the same momentum of the vector boson due to the polarization sum/propagator and hence gives zero.

3. The momentum dependent parts in the (f-f-V) coupling k^μ relate only momenta within a given vertex. In NWA the momentum conservation at a given vertex implies that all scalar products of momenta can be expressed either as masses squared or as $t = m_I^2$.

4. Momenta contracted with γ matrices yield only masses after using the Dirac equation.

5. Transversality condition for the (f-f-V) vertex with external vector bosons.

We have checked that the same reasoning also applies for dim. 6 operators. Higher than dim. 6 operators should play no role as at this stage higher order corrections due to emission of gluons and photons become important.
It should be emphasized here that these arguments are also true not only for (eff.) dim. 5 operators as written down in the Section 3.2 but also for all higher order operators. Their structure is again a linear combination of the three (or two) momenta appearing in the vertex and the arguments are again valid in NWA.

In conclusion, new dimension 5 operators alone have no effect on spin determination in decay chains. However, they distort measurements of the couplings as e.g. proposed in [33] where only dimension 4 operators are assumed. Nevertheless, those contributions are suppressed by a factor of $1/\Lambda^2$ and are, as we have also seen in a numerical example, very small and most likely smaller than the statistical uncertainty. These results show, how anomalous interactions in principle influence spin analysis. Based on the analytic expressions given in this chapter, detailed studies of the impact on measurements of couplings are possible and an interesting subject for future research.

Chapter 4

Spin Discrimination in Three Body Decays

In the 1950's, C. Bouchiat and L. Michel [50] [51] were able to pin down the electroweak $(V-A)$ interaction of the W boson with leptons and neutrinos with the help of the muon decay. The calculations back then were done without prior knowledge of the existence of the W boson and the decay was treated in this Fermi theory as an effective four fermion interaction. This type of decay where the mediating particle is rather heavy compared to the other particles involved is called three body decay.
In this chapter we will have a closer look at three body decays in the context of model discrimination with particle decays at the LHC. Little attention is paid to this topic in the literature, since the effects of those decays are suppressed with the mass of the heavy intermediate particle. However, if the subsequent two body decay is forbidden kinematically and is only possible via a heavier particle than the mother particle (as in the muon decay), one has to pay attention to these important decays. The spin of the mediating particle cannot be determined with equation 2.22 any more, since it is not valid in the context of a three body decay as we have elaborated in Section 2.2.
In contrast to model dependent approaches [34, 52], we develop a bottom-up approach which can be used for all models with heavy intermediate particles and renormalizable operators.
We organize this chapter as follows: We first formulate the problem and sketch the objective. Then we introduce our notation, the relevant topologies and vertices and show afterwards, that the invariant mass contains enough spin information to extract the spins of the unknown particles in such a decay scenario. We will present the strategy including a discussion of the impact of different decay topologies, discuss the influence of the mass of the off-shell particle and conclude with a test of our strategy in a series of Monte Carlo examples.

4.1 Objective

We investigate decays of a directly produced particle X decaying via a three body decay

$$X(p, m_X) \to f(q_1, m_f)\bar{f}(q_2, m_f)Y(q_3, m_Y) \tag{4.1}$$

into two SM-fermions $f, \bar{f}$ and a new invisible particle Y, which escapes detection. The p, q_i, $i = 1, 2, 3$ are the four momenta of our particles, and m_i, $i = X, f, Y$ are the masses. The particles X and Y can either be scalars (S) (spin-0), vectors (V) (spin-1) or Majorana/Dirac fermions (F) (spin-1/2)[1] and we abbreviate the decays with $S \to f\bar{f}S$, $S \to f\bar{f}V$, $V \to f\bar{f}S$, $V \to f\bar{f}V$, $F \to f\bar{f}F$ by (S, S), (S, V), (V, S), (V, V), (F, F) respectively. We assume that Y is a colour singlet as it should serve as a potential dark matter candidate.
We assume that all 2-body decays of X are either kinematically forbidden or at least loop-suppressed compared to this tree level three body decay. In these decays, all particles mediating them, which are collectively denoted by I with mass m_I, are very heavy compared to the decaying one, X, so $m_I \gg m_X$. An example is e.g. split-Susy [53] where the squarks are heavier than the gluino; or split-UED [54]. Usually, the masses in one KK level are degenerate at tree level due to equation 2.15, but with the introduction of specific boundary terms, one can split the degeneration such that the KK partner to the gluon is lighter then the KK partners to the quarks. Both scenarios are a very good example for the similarity of mass spectra of Susy and UED at the TeV range. Also, in higgsless supersymmetric models, such three body decays can be present [55].
Since we want to treat the spin information of equation 4.1 as general as possible, we take the most generic Lagrangian with arbitrary couplings of the same order $\mathcal{O}(1)$ and dimension 4 operators in contrast to the last chapter. From this we calculate the widths for the decays of X assigning different spins to X and Y, respectively.
We integrate over the momentum of the escaping particle Y so that we are left with the invariant mass distribution s of the two observable fermions. In the case of a mediating on-shell particle one derives the decay in NWA and ends up with the simple relation in equation 2.22 for the discrimination of spins.
Since our mediating particle is off-shell, we can obviously not take this approach and hence cannot use this relation so that we have no indications of the mediating particle's spin. The question arises, whether one can find a similar, model independent argumentation for the distinction of different spin scenarios.
We discuss in this chapter, that there is enough spin information in three body decays with one invisible particle, but the correlation between the degree of the polynomial and the spin of the mediating particle is not as simple as in equation 2.22. Instead, we give the resulting expressions as a phase space factor times a Laurent series (actually polynomials in most cases) of a dimensionless variable $\hat{s}$

[1] In the following we denote with "fermions" only spin-1/2 particles, although in general, fermions are of course all particles with half-integer spin. Since we consider only renormalizable interactions, we restrict ourselves to spin-1/2 fermions.

which is derived from the invariant mass $s_{ff} = (q_1 + q_2)^2$ where q_1 and q_2 are the four momenta of the SM-fermions. Our approach for the distinction of the various spin scenarios does not rely on the degree of s_{ff} (because there is no unique correlation) but on the coefficients of this Laurent series. They depend only on the couplings and masses of the particles involved and the question arises, if and how one gets information on the spins without knowing these quantities explicitly. As it turns out, we have to assume in our approach that the mass of Y and the mass difference $(m_X - m_Y)$ are known within a given uncertainty but in general we do not need any information about the underlying couplings.
So the basic idea is that different spin assignments lead to different relations between these coefficients which can be exploited to discriminate between the spin scenarios unambiguously. There is however one obstacle: one cannot exclude on logical grounds that there is a 'conspiracy' between the couplings suppressing the dominant terms in the expansion. This complicates life somewhat but even in that case relations between the coefficients are maintained as discussed below.
In the first discussion, we will consider the decays of a particle X charged under $SU(3)_C$ into two massless quarks and Y which is a colour singlet. Considering coloured particles in the first place is motivated by the fact that they in general have sizeable cross sections at the LHC. Moreover, due to gauge invariance only a subset of all topologies are allowed which simplifies the obtained expressions considerably. The additional features of either taking X as an $SU(3)$ singlet and/or the case that the SM-fermions are massive (i.e. top quarks) will be discussed afterwards.
In general the new particle X will be pair-produced in the production process and one has to worry about how to distinguish the products of the two decaying particles for each side of the two branches of such a symmetric production. In practice one can avoid this problems as in general several decay channels will be open, e.g. a supersymmetric gluino can either decay according to $\tilde{g} \to \bar{q}q\tilde{\chi}_1^0$ with q being a light quark of the first two generations or $\tilde{g} \to \bar{b}b\tilde{\chi}_1^0$. Therefore, one has to take events where two different final states can be observed. Although this will reduce the statistics to some extent, it will also allow to use the techniques proposed below on several final states and thus cross-checks of the results are possible.

4.2 Notation, setup and kinematics

4.2.1 Kinematics

We have already introduced the notation for the masses and the momenta of the particles involved in this decay in equation 4.1. In contrast to a NWA approach where the mediating particle is on-shell, one has to consider here also interference terms of all possible topologies leading to three final state particles. There are three topologies in this case and their Feynman graphs are shown in figure 4.1. We will later discuss the contribution of each one which explicitly depends on the propagator of the mediating particle.

We use the Mandelstam variables

$$s_{ff} = (p - q_3)^2 = (q_1 + q_2)^2 \; ; \; t = (p - q_2)^2 = (q_1 + q_3)^2$$
$$\text{and} \qquad u = (p - q_1)^2 = (q_2 + q_3)^2 = -s - t + m_X^2 + m_Y^2 + 2m_f^2$$

and we introduce the dimensionless parameters τ_i and $\hat{s}$

$$\hat{s} = \frac{\left(4\tau_f^2 + (\tau_Y - 1)^2\right) - \frac{2s_{ff}}{m_X^2}}{\left(4\tau_f^2 - (\tau_Y - 1)^2\right)} \; ; \; \tau_Y = \frac{m_Y}{m_X} \; ; \; \tau_f = \frac{m_f}{m_X} \; ; \; \tau_C = \frac{M_C}{m_X} \tag{4.2}$$

where M_C denotes dimensionful couplings, e.g. as they appear in the ZZH vertex or the trilinear soft Susy breaking parameters A_i. The invariant mass $\hat{s}$ is chosen such that $\hat{s}_{min} = -1$ and $\hat{s}_{max} = 1$ which turns out to be useful in the context of the fitting procedure later on.

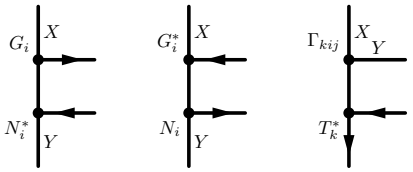

Figure 4.1: Topologies for three body decay.

Instead of the on-shell limit for the mediating particle, we take the limit on the far side of the mass range, where $m_I \gg m_X$. We therefore expand the matrix elements squared in powers of

$$\epsilon = \frac{m_X}{m_I}. \tag{4.3}$$

Now, we can perform the integration over t so that we integrate over the momentum of the unobserved particle Y. For the t-integration we have the bounds in terms of the variables defined in equation 4.2

$$\begin{aligned} t_\pm =& \frac{1}{4} m_X^2 \Bigg((\tau_Y + 1)^2 + \hat{s}\left(4\tau_f^2 - (\tau_Y - 1)^2\right) \\ & \pm \left((\tau_Y - 1)^2 - 4\tau_f^2\right) \times \sqrt{\frac{(1 - \hat{s}^2)\left((1 - \hat{s})((\tau_Y - 1)^2 - 4\tau_f^2) + 8\tau_Y\right)}{4\tau_f^2 + (\tau_Y - 1)^2 + \hat{s}\left((\tau_Y - 1)^2 - 4\tau_f^2\right)}} \Bigg) \end{aligned} \tag{4.4a}$$

and we define the variable

$$\begin{aligned} PS =& \int_{t_-}^{t_+} dt \\ =& \left((\tau_Y - 1)^2 - 4\tau_f^2\right) \frac{m_X^2}{2} \sqrt{\frac{(1 - \hat{s}^2)\left((1 - \hat{s})((\tau_Y - 1)^2 - 4\tau_f^2) + 8\tau_Y\right)}{4\tau_f^2 + (\tau_Y - 1)^2 + \hat{s}\left((\tau_Y - 1)^2 - 4\tau_f^2\right)}} \end{aligned} \tag{4.4b}$$

and will refer to this function as the "phase space" PS. As we can see here, this function is the integral of 1 dt and shows up globally for all decays. Since we exemplify the main features for massless SM-fermions, we display equation 4.4 for this massless case:

$$t_\pm = \frac{1}{4}m_X^2\left((\tau_Y+1)^2 - \hat{s}(\tau_Y-1)^2 \right. \\ \left. \pm(1-\tau_Y)\sqrt{(1-\hat{s})\left((1-\hat{s})(\tau_Y-1)^2+8\tau_Y\right)}\right) \tag{4.5a}$$

$$PS = \frac{1}{2}m_X^2(1-\tau_Y)\sqrt{(1-\hat{s})\left((1-\hat{s})(\tau_Y-1)^2+8\tau_Y\right)}. \tag{4.5b}$$

After expanding in ϵ given in equation 4.3, the differential decay rate can now be expressed as

$$\frac{d\Gamma}{d\hat{s}} = \frac{PS}{(2\pi)^3\ 256\ m_X}\left(\frac{Z}{(a\hat{s}+b)^2}+\frac{A}{a\hat{s}+b}+B+C\cdot\hat{s}+D\cdot\hat{s}^2+E\cdot\hat{s}^3+F\cdot\hat{s}^4\right) \tag{4.6}$$

where $a = \left((\tau_Y-1)^2-4\tau_f^2\right)$ and $b = \left((\tau_Y-1)^2+4\tau_f^2\right)$. The prefactors $Z, A, \ldots, F$ are functions of ϵ, the τ_i and the couplings. Note that Z and F only appear in the case of the decay (V,V).

4.2.2 Topologies and vertices

We want to be as general as possible and use a bottom up approach. There are 22 possibilities to assign different spins to the three topologies in figure 4.1. We show them in table 4.1, grouped by the underlying topology and hence sorted by the propagator. For the underlying interactions, we write down the most general renormalizable Lagrangian leading to the corresponding couplings. We use an unconventional style of writing, where we denote the fields of the particles with their names, e.g. X_S for a scalar field, if X is a scalar or $f, \bar{f}$ for the SM fermions. The couplings are denoted by "$\widetilde{G}_i/\widetilde{N}_i/\widetilde{T}_i$" and the index i is then either scalar (S) or vector (V). If possible, we keep generic left and right handed couplings denoted with $g(r/l, s/v)$ or $n(r/l, s/v)$ for scalar/vector-like couplings. The coupling notation g is for the first vertex coupling X to the intermediate particle, and n is for the Y particle coupling as shown in figure 4.1. In the case of a three boson interaction, we can have various couplings which are either momentum dependent or dimensionful via a mass scale M_C.

Bosonic decays

The effective Lagrangian density which we need for the bosonic decays is

$$\mathcal{L}_{i,j,k} = X_i\overline{I}_f\widetilde{G}_i f + Y_i\overline{I}_f\widetilde{N}_i f + I_i\overline{f}\widetilde{T}_i f + I_iX_jY_k\widetilde{\Gamma}_{ijk} + h.c. \tag{4.7}$$

where $i,j,k = s,v$ and I_i is the intermediate off-shell particle which is either bosonic (3rd topology) or fermionic (top. 1+2). The first two terms give the

interactions for the topology 1+2, the latter two for the interactions of topology 3, where the two SM fermions are directly coupled. The generic couplings are given by

$$\begin{array}{lll} \widetilde{G}_i: & G_s = (g(r,s)P_R + g(l,s)P_L)\,; & G_v = \gamma^\mu\,(g(r,v)P_R + g(l,v)P_L) \\ \widetilde{N}_i: & N_s = (n(r,s)P_R + n(l,s)P_L)\,; & N_v = \gamma^\mu\,(n(r,v)P_R + n(l,v)P_L) \\ \widetilde{T}_i: & T_s = (s(r)P_R + s(l)P_L)\,; & T_v = \gamma^\mu\,(v(r)P_R + v(l)P_L) \end{array} \tag{4.8}$$

and for $\widetilde{\Gamma}_{ijk}$

$$\begin{array}{ll} \Gamma_{sss} & = c(s)M_C; \\ \Gamma_{vvs} & = \Gamma_{vsv} = \Gamma(v^\mu, v^\nu, s) = c(v)M_C g^{\mu\nu} \\ \Gamma_{svv} & = \Gamma(s, v^\mu, v^\nu) = c(s)M_C g^{\mu\nu}; \\ \Gamma_{vs_1s_2} & = \Gamma(v^\mu, s_1, s_2) = c(v)(p_{s_2} - p_{s_1})^\mu \\ \Gamma_{s_1s_2v} & = \Gamma_{s_1vs_2} = \Gamma(s_1, s_2, v^\mu) = c(s)(p_{s_2} - p_{s_1})^\mu \\ \Gamma_{v_1v_2v_3} & = \Gamma(v_1^\nu, v_2^\rho, v_3^\mu) = c(v)\,((p_{v_1} - p_{v_2})^\mu g^{\nu\rho} + (p_{v_2} - p_{v_3})^\nu g^{\mu\rho} \\ & \quad + (p_{v_3} - p_{v_1})^\rho g^{\mu\nu}) \end{array} \tag{4.9}$$

where the indices of the vertex expressions Γ_{ijk} correspond to those of the Lagrangian in equation 4.7. $P_{L/R}$ are the left/right handed projectors $P_{L/R} = (1 \mp \gamma^5)$. Since we use the same definition as in O'Mega/WHIZARD [56, 57], we drop the ordinary factor of 1/2 in this definition.

Fermionic decays

In the case of fermionic decays, the generic Lagrangian is given by

$$\mathcal{L}_i \;=\; I_i\overline{f}G_iM_x + I_i\overline{f}N_iM_y + I_i\overline{M_y}\Gamma_iM_x + I_i\overline{f}T_if + h.c. \tag{4.10}$$

where $M_{x,y}$ denote the spinors of the new fermions and $i = s, v$ denotes whether the exchanged particle is a scalar or a vector boson. The couplings are the same as in equation 4.8 and 4.9 and we have additionally

$$\begin{array}{ll} i = s: & \Gamma_s = (d(s,r)P_R + d(s,l)P_L) \\ i = v: & \Gamma_v = \gamma^\mu\,(d(v,r)P_R + d(v,l)P_L)\,. \end{array} \tag{4.11}$$

Topologies

Depending on which colour structure and which topologies we allow, the results and thus the strategy for spin determination simplifies pretty much. In the first considerations, we take only the decays of a coloured particle X into two SM quarks and a colour singlet Y into account, which come with topology 1+2 and are motivated by the comparison of Susy or UED. However, we want to look at the spin determination for these decays without prejudice, so we include also topology 3 in a follow-up discussion. Due to gauge invariance reasons, one cannot write down interactions for all of the decays in table 4.1. Thus, in a third step

Decay	Top. 1	Top. 2	Top. 3(s/v)	
(S,S)	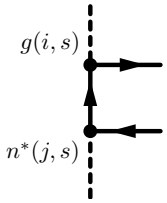	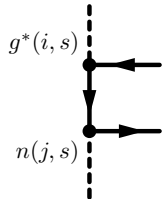	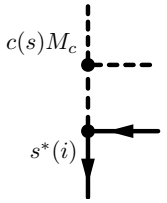	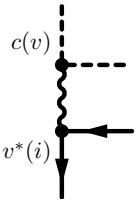
(S,V)	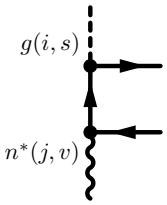	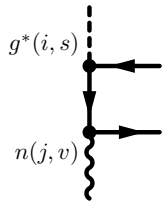	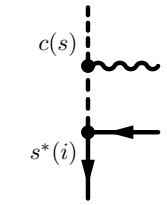	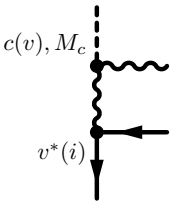
(V,S)	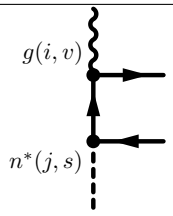	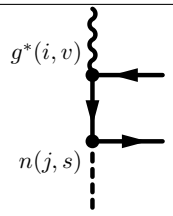	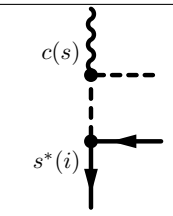	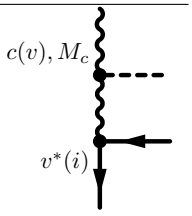
(V,V)	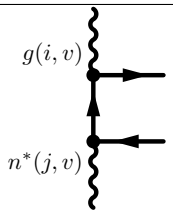	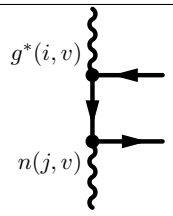	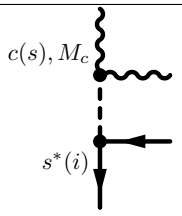	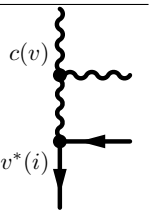

Top. 1 (s)	Top. 2 (s)	Top. 3 (s)	Top. 1 (v)	Top. 2 (v)	Top. 3 (v)
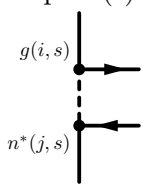	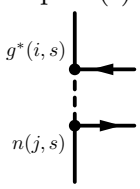	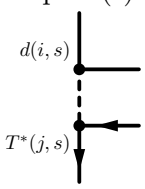	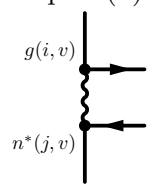	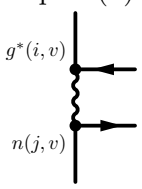	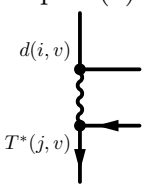

Table 4.1: Topologies for the decays of bosons $X \to f\bar{f}Y$ (top) and fermions (F,F) (bottom) with $i,j \in \{l,r\}$ (see also equation 4.8, 4.9 and 4.11).

we add the third scenario where we allow all three topologies, which corresponds to the case that the particle X is uncoloured.
Thus, we can divide our investigations into three cases:

(I) Most common: all particles uncoloured

(II) Top. 1+2+3: all coloured

(III) Top. 1+2 only: all coloured.

Let us first have a look at the three-boson vertices of table 4.1 that can occur. The only terms in agreement with gauge theories are

$$\mathcal{L} = \phi_1^a \phi_{2,a}, \phi_3 \phi_4; \qquad \phi_4 \quad \text{aquires a VeV} \tag{4.12a}$$

$$\mathcal{L} = F^a_{\mu\nu} F_a^{\mu\nu}; \qquad F^a_{\mu\nu} = \partial_\mu A^a_\nu - \partial_\nu A^a_\mu + g f^{abc} A^b_\mu A^c_\nu \tag{4.12b}$$

$$\mathcal{L} = (D_\mu \phi)^\dagger_a \, (D^\mu \phi)^a \, ; \qquad (D_\mu \phi)_a = \partial_\mu \phi_a - i g f^{abc} A_{\mu,b} \phi_c. \tag{4.12c}$$

All interactions for the topology 3 in table 4.1 are calculated from these Lagrangian densities. We mark the particles in the Feynman graphs in the following with '8' or '0' for colour octet or singlet. The first vertex from topology 3 of table 4.1 is

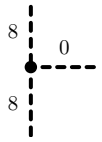

(4.13)

and the corresponding Feynman interaction is derived from the Lagrangian density with the colour contractions

$$\mathcal{L} = (\phi_1^a \ \phi_{2,a}) \ (\phi_3 \phi_4)$$

where $a = 1 \ldots 8$ is the colour index which connects the intermediate particle, e.g. ϕ_2 and the decaying particle ϕ_1, whereas the colour singlet ϕ_4 has a VeV and therefore allows the three scalar vertex 4.13.
The second vertex for the decay (S, S) is

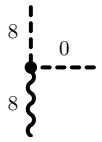

(4.14)

which can only arise from a term $(D_\mu \phi)_a = \left(\partial_\mu \phi^a - i g f^{abc} A_{\mu,b} \phi_c\right)$ which has an open colour index a. However, there is no possibility to contract this term with a colour singlet ϕ, so this operator is not considered in the coloured decays, as well as

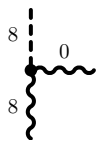

(4.15)

which faces the same problem. For one of the interactions present in the (S, V) decay,

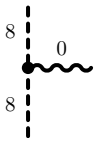

(4.16)

one can derive the interaction from

$$\mathcal{L} = (D_\mu \phi_a)^\dagger (D^\mu \phi_a) \tag{4.17}$$

with the covariant derivative $D_\mu = \partial_\mu - igA_\mu + \ldots$ where "..." means that here one can have additional gauge bosons which do not play a role in this consideration. This operator is therefore considered in the following.
In the two vertices including two vectors and one colour octet scalar which are needed for (V, S) and (V, V), we have

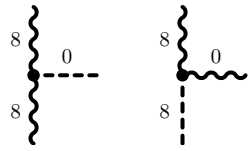

(4.18)

and we have in principle the possibility to write down the corresponding operator $\left(\partial_\mu \phi^a - igf^{abc} A_{\mu\, b} \phi_c\right)^\dagger \left(\partial^\mu \phi_a - igf_{ade} A^{\mu\, d} \phi^e\right)$. Nevertheless, the only possibility to have two vector fields and one scalar is to give a VeV to the other scalar which would break the colour gauge symmetry. For the same reasoning

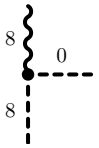

(4.19)

is not considered in the following. The remaining vertex is the three vector vertex of the (V, V) decay,

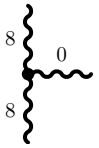

(4.20)

which can only have its origin in $F^a_{\mu\nu} F^{\mu\nu}_a$ with all three/four vectors being charged under colour and is therefore not considered in the following.
Thus, the only considered operators in addition to the first two topologies in the case of a coloured decay are those of vertices 4.13 and 4.16 for the third topology.

4.2.3 Polarization vectors, propagators and generic amplitudes

We define 'polarization' vectors in such a way that we are able to write down a general bosonic decay

$$\epsilon_s = \mathbb{1}; \qquad \epsilon_v = \widetilde{\epsilon}^{\mu}$$

and we use the fermion and boson propagators as in equation 3.5 where we neglect the width Γ.
These three propagators affect the decay rate differently. As we have mentioned in Section 4.2.1, equation 4.3, we expand the amplitudes in the dimensionless parameter $\epsilon = m_X/m_I$ to derive the off-shell limit. As is clear from the propagator structure in the equation 3.5b, the leading degree of ϵ is different for the topologies 1+2 vs. 3, and the leading order in ϵ of the decay width is distinct

$$\text{Fermionic propagator:} \qquad \frac{d\Gamma}{ds} \sim \epsilon^2 + \mathcal{O}(\epsilon^3) \tag{4.21a}$$

$$\text{Bosonic propagator:} \qquad \frac{d\Gamma}{ds} \sim \epsilon^4 + \mathcal{O}(\epsilon^5) \tag{4.21b}$$

so that, taking all three topologies into account, the interference terms are of order ϵ^3 and higher. We take all contributions up to the order of ϵ^4 into account and will come back later to this expansion for cases, where either the leading order, ϵ^2, vanishes, and only the ϵ^4 order shows up, or alternatively where the ϵ^4 order can "fake" the leading order by carrying a dimensionful coupling as in the vertex of 4.13.

Matrix elements for bosonic and fermionic decays

We are now ready to write down generic matrix elements for those decays. The bosonic decays are calculated with

$$\begin{aligned}\mathcal{M}_{i,j} \;=\; & \overline{u}(q_1, m_f) G_i \not{F}_p \;\gamma^0 N_j^\dagger \gamma^0 \; v(q_2, m_f) \epsilon_i(p) \epsilon_j(q_3) \\ & + \overline{u}(q_1, m_f) N_j \not{F}_p \;\gamma^0 G_i^\dagger \gamma^0 \; v(q_2, m_f) \epsilon_i(p) \epsilon_j(q_3) \\ & + \sum_{k=s,v} \Gamma_{kij} W_{P,i} \overline{u}(q_1, m_f) \gamma^0 T_k^\dagger \gamma^0 v(q_2, m_f)\end{aligned} \tag{4.22}$$

and the matrix elements for fermionic decays are

$$\begin{aligned}\mathcal{M}_i \;=\; & \Big[\overline{u}(q_1, m_f) G_i u(p, m_X)\Big] \; W_{p,i} \; \Big[\overline{u}(q_3, m_Y) \gamma^0 N_i^\dagger \gamma^0 v(q_2, m_f)\Big] \\ & + \Big[\overline{u}(q_1, m_f) N_i v(q_3, m_Y)\Big] \; W_{p,i} \; \Big[\overline{v}(p, m_X) \gamma^0 G_i^\dagger \gamma^0 v(q_2, m_f)\Big] \\ & + \Big[\overline{u}(q_3, m_Y) \Gamma_i u(p, m_X)\Big] \; W_{p,i} \; \Big[\overline{u}(q_1, m_f) \gamma^0 T_i^\dagger \gamma^0 v(q_2, m_f)\Big] .\end{aligned} \tag{4.23}$$

For the fermionic decays we use generalized Fierz identities [58] to derive all spinor chains in equation 4.23.

Our main focus here lies on the case of massless fermions as this is already sufficient to get the required information as we will see in the next chapter. Hence we discuss the massless case first in the next chapter. Besides the specific form of the terms, our strategy works as well in the massive case with minor changes to specific values used in the strategy. To illustrate our results we give the differential decay width for the massless case up to order ϵ^2 in the Appendix B.2.

4.3 Strategy for spin identification

With the explicit results in the Appendix B.2 for the boson and fermion decays, we can now work out a strategy for discriminating the spins assigned to the particles X and Y in these various decay scenarios.
In the case where we assume the SM fermions to be massless, the differential decay rate from equation 4.6 immediately simplifies since some of the coefficients for the differential width are zero, and we obtain

$$\frac{d\Gamma}{d\hat{s}} = \frac{PS}{(2\pi)^3\ 256\ m_X}\big(B + C\hat{s} + D\hat{s}^2 + E\hat{s}^3 + F\hat{s}^4\big). \tag{4.24}$$

The main procedure is to find suitable relations or to determine the signs of the different coefficients $Z, A, \ldots, F$ without prior knowledge of the couplings. We will show this with one example here and refer to the next section for the remaining decays.

4.3.1 Example: (S, V)

We pick the decay (S, V). According to Section B.2, equation B.7, some coefficients of the polynomial of the decay rate,

$$\frac{d\Gamma}{d\hat{s}} = \frac{PS}{(2\pi)^3\ 256\ m_X}\left(\frac{Z}{(a\hat{s}+b)^2} + \frac{A}{a\hat{s}+b} + B + C\cdot\hat{s} + D\cdot\hat{s}^2 + E\cdot\hat{s}^3 + F\cdot\hat{s}^4\right)$$

vanish, in particular $Z, A, E, F = 0$. The remaining coefficients, in the leading order of ϵ^2, are

$$B = \frac{64}{3\tau_Y^2}\left(g(r,s)^2 n(l,v)^2 + g(l,s)^2 n(r,v)^2\right)(\tau_Y - 1)^2\left(25\tau_Y^2 + 6\tau_Y + 1\right) \tag{4.25a}$$

$$C = \frac{128}{3\tau_Y^2}\left(g(r,s)^2 n(l,v)^2 + g(l,s)^2 n(r,v)^2\right)(\tau_Y - 1)^2\left(11\tau_Y^2 - 2\tau_Y - 1\right) \tag{4.25b}$$

$$D = \frac{64}{3\tau_Y^2}\left(g(r,s)^2 n(l,v)^2 + g(l,s)^2 n(r,v)^2\right)(\tau_Y - 1)^4. \tag{4.25c}$$

Remember that the coefficient τ_Y is the mass ratio of m_Y/m_X and due to energy conservation can only be in the interval [0,1]. One can immediately see, that the B and D coefficients are both positive, completely independent from this mass ratio

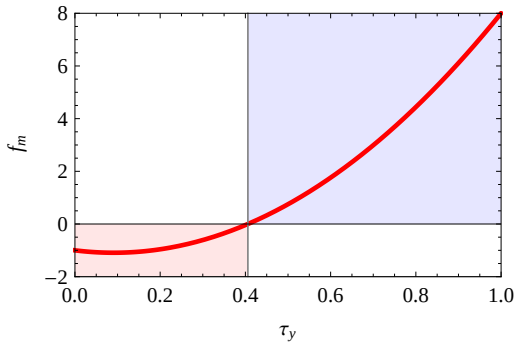

Figure 4.2: Sign flip for the mass-dependent function f_m of equation 4.25b. In the red shaded area (left), f_m is negative and thus, C of equation 4.25b is negative. In the blue (right) shaded area, f_m has the opposite sign, and the coefficient C also flips sign.

or the specific couplings strengths $g(r/l)$ and $n(r/l)$. For the C coefficient in equation 4.25b, we are less lucky: In this case, the mass factor $f_m = \left(11\tau_Y^2 - 2\tau_Y - 1\right)$ can flip sign (as shown in figure 4.2) for values $\tau_y \lessgtr (1 - 2\sqrt{3})/11)$.
However, we also see that the dependence on the couplings is the same for each coefficient, which is only the case in some decays. But here, we can derive the possible ratios of the coefficients $C/D, C/B, D/B$ and vary the mass ratio τ_Y in its valid interval [0,1]. The ratios of the coefficients are limited to specific ranges originating from the mass-dependent function f_m. As it turns out, for most of the decays, it is sufficient to determine the degree of the polynomial and the sign of the coefficients, but for the two spin assignments (S, V) and (V, S) it is not enough and one has to pin down these ranges for the coefficient ratios. We have plotted the ratios in figure 4.3 for those two decays, and will later come back to them. So far, we only want to draw attention to the blue/solid line, which gives characteristic regions for all three possible ratios of (S, V).

4.3.2 Signs of the coefficients

In the same manner as before, we can now classify all 5 decays. We start by summarizing the signs of the different coefficients sorted by the underlying decay, the order in ϵ and the three cases of page 41, I-III.
We collect the signs of the different coefficients for all decays of bosons in table 4.2 where we have expanded the coefficients in powers of ϵ, e.g.

$$B = \sum_{k=2}^{4} B_k \epsilon^k \tag{4.26}$$

Most of the signs in table 4.2 are obtained analytically but several (for the (F, F) decays below) are obtained numerically by scanning and inserting random couplings in the range $[-1, 1]$ since the analytic function is to involved and one cannot disentangle in a simple way the mass and the coupling dependence, as e.g. in equation 4.25.

There are some coefficients where the sign cannot be determined without prior knowledge of the mass ratios or the couplings which are marked by "±", as e.g. the C coefficient of equation 4.25b. If the coefficient in question vanishes, we have put a 0.
The signs in table 4.2 for the boson decays are sorted as in the cases of page 41 from the most general to the most restricted one

(I) Column "s": X is an $SU(3)$ singlet, where all topologies of table 4.1 contribute.

(II) Column "c": X is an $SU(3)$ colour octet and all allowed contributions are taken into account.

(III) Column "1+2": X is an $SU(3)$ colour octet and only topologies 1+2 contribute.

In the case of fermion decays (F, F), it turns out that the result does neither depend on the spin of the exchanged particle nor on the topology, e.g. it does not matter if all topologies are taken or only a subset. Since we have only bosonic propagators there are only the $\mathcal{O}(\epsilon^4)$ contributions and we find:

$$\text{sign}(B_4) = + \; ; \quad \text{sign}(C_4) = \pm \; ; \quad \text{sign}(D_4) = - \; ; \quad \text{sign}(E_4) = 0 \; . \tag{4.27}$$

In the subsequent sections, we discuss these cases in reverse order, starting with the simplest case which is motivated by scenarios such as UED and Susy. We will primarily focus on the terms of order ϵ^2, however, we will also discuss scenarios, where this leading order is zero which is the case for some special coupling arrangements discussed in section 4.3.5.

4.3.3 Decays into massless SM-fermions in case of topologies 1+2

Let us assume that we have measured the differential decay width of a new particle and determined the coefficients introduced above accurately in a fit. A realistic fit is naturally affected by finite statistic, but we assume for now, that the coefficients could be determined perfectly. The next section, 4.4, will be dedicated to the application of the following strategy in a "realistic" world by discussing various Monte Carlo studies at parton level where we also review the obtainable accuracy. We want to point out that such problems obviously also arise in the on-shell case, e.g. that finite statistics can also render the determination of the highest degree in s difficult.
However, the strategy elaborated in the following can be used to determine the spins of the new particles or at least to exclude certain possibilities. The main strategy is summarised in figure 4.4 and explained in some more detail below.
Let's start with the E term which is only non-zero in the (V, V) case. This immediately implies that (V, V) is preferred once the 'measured' E term is significantly larger than 0. For consistency we check that $B > 0$. The next step is to look at the D term as for $D \neq 0$ and $E = 0$ the sign of D determines whether one is

	(S,S)			(S,V)		(V,S)		(V,V)	
ϵ^2	s	c	1+2	s	c/1+2	s	c/1+2	s	c/1+2
B_2	+	+	+	+	+	+	+	±	±
C_2	+	+	+	±	±	+	+	±	±
D_2	0	0	0	+	+	+	+	±	±
E_2	0	0	0	0	0	0	0	+	+
ϵ^3									
B_3	±	±	0	±	0	±	0	±	0
C_3	±	±	0	±	0	±	0	±	0
D_3	0	0	0	±	0	±	0	±	0
E_3	0	0	0	0	0	0	0	±	0
ϵ^4									
B_4	+	+	+	+	+	+	+	+	+
C_4	±	+	+	±	±	±	±	±	±
D_4	±	−	−	±	±	±	±	±	±
E_4	0	0	0	±	±	±	±	±	±
F_4	0	0	0	0	0	0	0	±	±

Table 4.2: Signs of the coefficients for the case of a boson decaying into another boson and massless SM-fermions in the final state. The rows correspond to the following cases: (case (III) of page 46, *s*): X is an $SU(3)$ singlet, (case (II) of page 46, *c*:) X is charged under $SU(3)$ taking all possible topologies into account and (case (I) of page 46, 1 + 2:) X is charged under $SU(3)$ taking topologies 1+2 into account. The ± marks the cases where the sign cannot be determined without knowing the masses/couplings and 0 marks the cases with a vanishing coefficient.

dealing with fermions ($D < 0$) or bosons ($D \geq 0$) where the latter case includes (S,S), (S,V) and (V,S). In case of $D = 0$ only the case (S,S) remains.
The discrimination between (S,V) and (V,S) needs to be worked out via the ratios of coefficients, since in these cases, the couplings can cancel out (see Appendix, equation B.7 and B.8). We can build three different ratios for each of the decays, namely

$$(S,V): \quad D/C = \frac{(\tau_Y - 1)^2}{22\tau_Y^2 - 4\tau_Y - 2} \qquad \in [-\infty, -\frac{1}{3}] \cup [0, \infty] \tag{4.28a}$$

$$(V,S): \quad D/C = -\frac{(\tau_Y - 1)^2}{2(\tau_Y(\tau_Y + 2) - 11)} \qquad \in [0, \frac{1}{22}] \tag{4.28b}$$

$$(S,V): \quad C/B = \frac{22\tau_Y^2 - 4\tau_Y - 2}{\tau_Y(25\tau_Y + 6) + 1} \qquad \in [-2, \frac{1}{2}] \tag{4.28c}$$

$$(V,S): \quad C/B = \frac{8(\tau_Y + 9)}{\tau_Y(\tau_Y + 6) + 25} - 2 \qquad \in [\frac{1}{2}, \frac{22}{25}] \tag{4.28d}$$

$$(S,V): \quad D/B = \frac{(\tau_Y - 1)^2}{\tau_Y(25\tau_Y + 6) + 1} \qquad \in [0, 1] \tag{4.28e}$$

$$(V,S): \qquad D/B = \frac{(\tau_Y - 1)^2}{\tau_Y(\tau_Y + 6) + 25} \qquad \in [0, \frac{1}{25}] \qquad (4.28f)$$

We show these ratios in figure 4.3 and mark the important regions by shading. In the left figure of 4.3, we show the ratio D/C. The dotted red line is the ratio for (S,V). The range of this ratio excludes the green shaded region. The blue solid line is the ratio of the same coefficients for (V,S) and is limited to a small but overlapping area from eq. 4.28a and 4.28b. However, if the value determined from the fit is in the red area, it must be (V,S). If it is in the green area, it is neither one of both, which will be important for the fitting strategy in the next chapter.
The figure in the centre shows the ratio C/B, and again, the blue/solid line is the (V,S) result, and the red/dashed line is the (S,V) result. The corresponding values for the ratios are shaded in blue/red respectively and we see that the areas have no overlap and hence this is the best suited ratio to distinguish between (S,V) and (V,S).
The figure on the right side shows the ratio for D/B with the same colour code as above, but we see that there is an overlap of the two spin scenarios. However, the region of the shaded red area belongs entirely to (S,V) since these values cannot be reached from (V,S).
So, the D/B and D/C ratios seem to be less useful since the intervals overlap, but except for $\tau_Y = 1$ but they are never equal. In the range where τ_Y is close to one, the SM-fermions become very soft and this part will be excluded because a lower cut on their energies is put in practice.
However, we can still make use of the regions for the exclusion of one of the two scenarios.

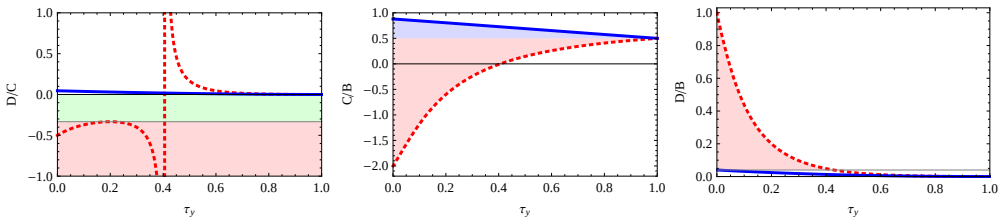

Figure 4.3: Ratios of coefficients over the range of τ_y. The solid/blue line shows the result for the decay (V,S), the dashed/red line is the ratio for (S,V). The green (upper) shaded area in the left plot shows the region that is forbidden in both decays (S,V) and (V,S). The red (lower) shaded region is only allowed by (S,V). In the middle plot, the allowed regions are completely distinct, the red region contains the values for (S,V), the blue the values for (V,S). In the right plot, only the red shaded area from [1/25,1] is solely allowed for (S,V).

Last but not least we note, that the decay (S,S) can be further checked by the requirement that $B/C = 1$ as can be seen from equation B.4. This will later on again play an important role for the exclusion of this scenario.
Colloquial, we can state, that independently of the mass ratios or the specific values of the couplings, all those five cases can be discriminated from each other.

We depict this strategy for a perfect fit in the flow chart in figure 4.4 where one can see, that each one of the decays can be uniquely determined using the characteristics worked out here.

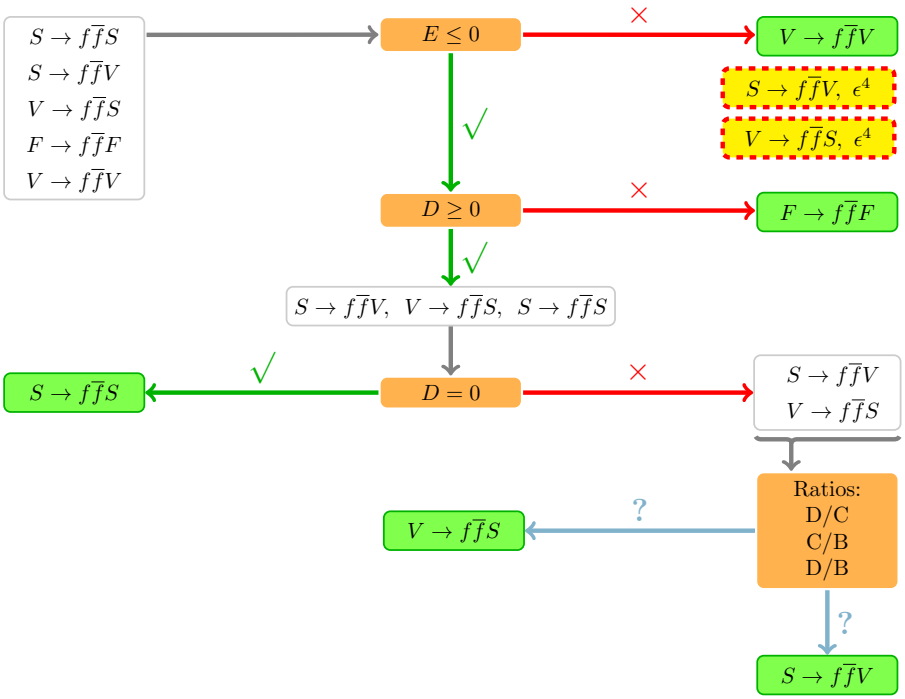

Figure 4.4: Flowchart for the strategy to discriminate different spin assignments for $m_f = 0$ using the signs of the coefficients given in section 4.3.2. Green (solid frame) boxes are for the case of taking only the leading order into account. Impact or dominance of higher order terms is given by the yellow (dashed frame) boxes, see text for details.

4.3.4 Impact of the third topology

In the cases (II) and (III), we also take the third topology into account. The dominant contributions stem from topologies 1 and 2 of table 4.1 in the case of decays of bosons. This is due to the fact that the third topology generally contributes at $\mathcal{O}(\epsilon^4)$ as we have seen on page 43. Note, that in case of new fermions, higher orders in ϵ have no impact and, thus, we restrict the discussion here to decays of bosons.

One might ask if one of the dimensionful couplings of the three-boson vertices in the diagrams of the third topology can become so large to disturb the above strategy, e.g. the VeV in the coupling 4.13 on page 41.

Let us first consider the case that X is in a non-trivial $SU(3)$ representation. Here only (S, S) can have a potentially dangerous contribution because the trilinear scalar coupling can in principle be of order m_I and thus can change the order of

ϵ^4 to ϵ^2.
However, from the specific term in the Appendix, equation B.4, we see that only the equality $B = C$ gets broken, and the D-term will only get a tiny contribution, and thus the general strategy should still work.
In case of the scalar exchange in the third topology of the (S, V) case with the coupling in equation 4.16, the coupling is momentum dependent and is of order m_X and one is safe again.
In the case where X is a colour singlet, all diagrams for the third topology in table 4.1 contribute in principle. Here one has to distinguish two cases: (i) there are no new vector bosons or the new vector bosons do not belong to a new gauge group. In this case a detailed inspection of the diagrams shows that one arrives at the same conclusions as above, because all dimensionful couplings, which had not been considered before, have to be of the order m_X due to $SU(2)_L$ gauge invariance. (ii) There is a new gauge group at higher energies to which the intermediate vector bosons belong. In this case the SVV coupling as well as the masses of the vector boson will be of the same order of magnitude and thus our assumption that the intermediate particle is much heavier than the decaying one does not hold in this case.
To conclude, we find that one is on the safe side for both of these cases.

4.3.5 Special combinations of couplings

Up to now we have considered only the leading terms in case of decays of new bosons. However, it can happen that for special helicity assignments, the leading order ϵ^2 becomes zero. An example is the (S, S) case as can be seen in equation B.4 and B.5 where the leading order is proportional to $(g(r, s)n(l, s) + g(l, s)n(r, s))^2$ which is 0 in the case of e.g. $g(l, s) = n(r, s) = 0$. In such cases the momentum dependent part of the fermion propagator, $\not{p}/m_I^2$, becomes important which contributes only at $\mathcal{O}(\epsilon^4)$. The question arises now if these terms can distort our strategy from Section 4.3.3 such that we arrive at the wrong conclusion.
Therefore we choose the specific coefficients were the order ϵ^2 contribution vanishes and derive the new coefficients of order ϵ^4. Note that if order ϵ^2 vanishes, also order ϵ^3 is zero and the leading order is ϵ^4. We summarize again the sign of the coefficients, but of the order ϵ^4 and collect them in table 4.3. We need to compare those now with the order ϵ^2 coefficients of table 4.2 to see whether they can lead to wrong conclusions.
We start with the case where X is charged under $SU(3)$, so only topology 1+2 are contributing. One immediately sees that the cases (S, S) and (V, V) are not affected since the signs are the same. The problematic ones are (S, V) and (V, S) which now get a positive E as is the case of (V, V) in the leading order of table 4.1. Unfortunately, ratios of the other coefficients do not help if one has no further information about couplings and/or masses of the intermediate particles. We have marked this possibility in figure 4.4 with the yellow boxes surrounded by red dashed lines. However, we want to stress that this requires fine-tuning

	(S,S)			(S,V)		(V,S)		(V,V)	
ϵ^4	s	c	1+2	s	$c/$ 1+2	s	c/1+2	s	c/1+2
B_4	+	+	0	+	+	+	+	+	+
C_4	±	+	0	±	±	±	−	±	±
D_4	+	0	0	±	−	±	±	−	−
E_4	0	0	0	+	+	+	+	+	+
F_4	0	0	0	0	0	0	0	+	+

Table 4.3: ϵ^4 coefficients for the case that ϵ^2, and thus also ϵ^3, are fine-tuned to vanish; $m_f = 0$.

between different couplings which, although being unlikely, cannot be excluded on logical grounds.
In the case that X is an $SU(3)$ singlet the situation gets even a little bit more complicated because now the D coefficient is non-zero also in case for (S,S). However, it is still positive and thus it can for sure not be confused with the case of a new fermion decaying. In the (V,V) case on the other hand we get in principle even more information as now also the F is non-zero which immediately tells us that there is a special combination of couplings.

4.3.6 Final states containing massive SM-fermions

So far, our investigations are only for the massless SM-fermions. For completeness, we want to work out a strategy, for the case of massive SM-fermions, which in practice only is important for top-quarks. It turns out that the strategy hardly changes besides for the fact that one has to determine more coefficients by fitting, since we now have to take the full polynomial into account

$$\frac{d\Gamma}{d\hat{s}} = \frac{PS}{(2\pi)^3\ 256\ m_X}\left(\frac{Z}{(a\hat{s}+b)^2} + \frac{A}{a\hat{s}+b} + B + C\cdot\hat{s} + D\cdot\hat{s}^2 + E\cdot\hat{s}^3 + F\cdot\hat{s}^4\right).$$

We again summarize the coefficients for the specific decays for the order of ϵ^2, ϵ^3 and ϵ^4 in table 4.4 with the same notation and naming as before, e.g. on page 47.
Comparing tables 4.2 and 4.4, we see that we can use the same strategy in principle. However, for distinguishing between the (S,V) and (V,S) cases the ranges for the ratios of the coefficients change. As it turns out, the coefficients do not disentangle into coupling strength parts and mass-depending functions as well as in the massless example. In difference to e.g. the case of the coefficients in equation B.7 they now have a more involved structure. This implies that the ratios of coefficients do not necessarily have to be independent of the coupling strengths as in the massless case. It turns out, that only the ratio D/C is independent of the coupling strengths and we find

$$(S,V): \quad D/C = \frac{(\tau_Y-1)^2 - 4\tau_f^2}{12\tau_f^2 + 22\tau_Y^2 - 4\tau_Y - 2} \in [-\infty, -\frac{1}{3}] \cup [0,\infty] \quad (4.29a)$$

	(S,S)		(S,V)		(V,S)		(V,V)	
ϵ^2	s	$c/1{+}2$	s	$c/\ 1{+}2$	s	$c/1{+}2$	s	$c/1{+}2$
A_2	0	0	$+$	$+$	$+$	$+$	$+$	$+$
B_2	$\pm$	$\pm$	$\pm$	$\pm$	$\pm$	$\pm$	$\pm$	$\pm$
C_2	$\pm$	$\pm$	$\pm$	$\pm$	$+$	$+$	$\pm$	$\pm$
D_2	0	0	$\pm$	$\pm$	$+$	$+$	$\pm$	$\pm$
E_2	0	0	0	0	0	0	$+$	$+$
ϵ^3								
A_3	0	0	$\pm$	$\pm$	$\pm$	$\pm$	$\pm$	$\pm$
B_3	$\pm$	$\pm$	$\pm$	$\pm$	$\pm$	$\pm$	$\pm$	$\pm$
C_3	$\pm$	$\pm$	$\pm$	$\pm$	$\pm$	$\pm$	$\pm$	$\pm$
D_3	0	0	$\pm$	$\pm$	$\pm$	$\pm$	$\pm$	$\pm$
E_3	0	0	0	0	0	0	$\pm$	$\pm$
ϵ^4								
Z_4	0	0	0	0	0	0	$-$	$-$
A_4	$+$	0	$+$	$+$	$+$	$+$	$+$	$+$
B_4	$\pm$	$+$	$\pm$	$\pm$	$\pm$	$\pm$	$\pm$	$\pm$
C_4	$\pm$	$+$	$\pm$	$\pm$	$\pm$	$\pm$	$\pm$	$\pm$
D_4	$\pm$	$-$	$\pm$	$\pm$	$\pm$	$\pm$	$\pm$	$\pm$
E_4	0	0	$\pm$	$\pm$	$\pm$	$\pm$	$\pm$	$\pm$
F_4	0	0	0	0	0	0	$\pm$	$\pm$

Table 4.4: Same as table 4.2 but for massive SM-fermions.

$$(V,S): \quad D/C = \frac{(\tau_Y-1)^2-4\tau_f^2}{2\left(6\tau\mathrm{f}^2-\tau_Y(\tau_Y+2)+11\right)} \qquad \in \ [0,\frac{1}{22}]. \quad (4.29b)$$

For the intervals, we have used that the mass ratios τ_y and τ_f are limited due to energy and momentum conservation by

$$1 \geq \tau_Y + 2\tau_f. \quad (4.30)$$

As in the case of massless SM-fermions, the overlap region of the two intervals is only for the case $\tau_Y \to 1-2\tau_f$, e.g. the kinematical limit, where all particles are practically at rest in the centre of mass system of X.
In general, for the (S,V) decay the ratio D/C will be either negative or much larger than $1/2$. Note that we have $A=0$ for the (S,S) case which can be used as a criterion to confirm this scenario. Also in case of a new fermion we arrive at the same conclusions because

$$\begin{aligned} &\mathrm{sign}(A_4)=+; && \mathrm{sign}(B_4)=\pm; && \mathrm{sign}(C_4)=\pm; \\ &\mathrm{sign}(D_4)=-; && \mathrm{sign}(E_4)=0. \end{aligned} \quad (4.31)$$

The only exception is where this decay is mediated solely by scalars in the third topology as in this case $A_4=0$.

	(S,S)			(S,V)		(V,S)		(V,V)	
ϵ^4	s	c	1+2	s	c/1+2	s	c/1+2	s	c/1+2
Z_4	0	0	0	0	0	0	0	$-$	$-$
A_4	$+$	0	0	$+$	$+$	$+$	$+$	$+$	$+$
B_4	$\pm$	$+$	$+$	$\pm$	$\pm$	$\pm$	$+$	$\pm$	$\pm$
C_4	$\pm$	$+$	$+$	$\pm$	$\pm$	$\pm$	$-$	$\pm$	$\pm$
D_4	$+$	0	0	$\pm$	$\pm$	$\pm$	$\pm$	$\pm$	$\pm$
E_4	0	0	0	$\pm$	$+$	$+$	$+$	$\pm$	$+$
F_4	0	0	0	0	0	0	0	$+$	$+$

Table 4.5: Same as table 4.3 but $m_f \neq 0$.

For completeness, we also give in table 4.5 the results for the case that the leading orders vanish in decays of bosons. It turns out that this case is almost the same as for the case of massless SM-fermions discussed above except that now in general also A will be non-zero.

4.3.7 Influences of the mass of the intermediate particle(s)

We now address the question to what extent the expansion in ϵ works and how the neglected terms from the propagator influence the values of the coefficients. Therefore we choose two different scenarios and look at the deviation of the differential distribution for the correct result and the expanded result depending on the mediating particle's mass m_I. In a second part, we investigate the values of the fitted coefficients depending on the mass range of m_I.
We choose for these considerations two coupling scenarios

(I) $g(r) = g(l) = n(r) = n(l) = 1$: leading order dominates

(II) $g(l) = n(l) = 0$: leading order vanishes in case of bosonic decays

where in the second scenario, the sub-leading terms become dominant. Note that in case of new fermions we did not find a combination where the leading order vanishes.
In all cases we have taken $m_X = 1\ TeV$, $m_Y = 100\ GeV$ and $m_f = 0$. We have checked that our results do not depend crucially on these values except for the cases where m_Y gets close to m_X which would imply soft SM fermions and experimental difficulties to observe the decay.

Relative deviation of $m_I \to \infty$ and fixed ϵ

First we derive the relative deviation from the differential width Γ_ϵ for a given ϵ in the limit where $m_I \to \infty$

$$R = \frac{d\Gamma_\epsilon - d\Gamma_H}{d\Gamma_H} \quad \text{with} \quad d\Gamma_i = \frac{1}{\Gamma_i}\frac{d\Gamma_i}{d\hat{s}} \,. \tag{4.32}$$

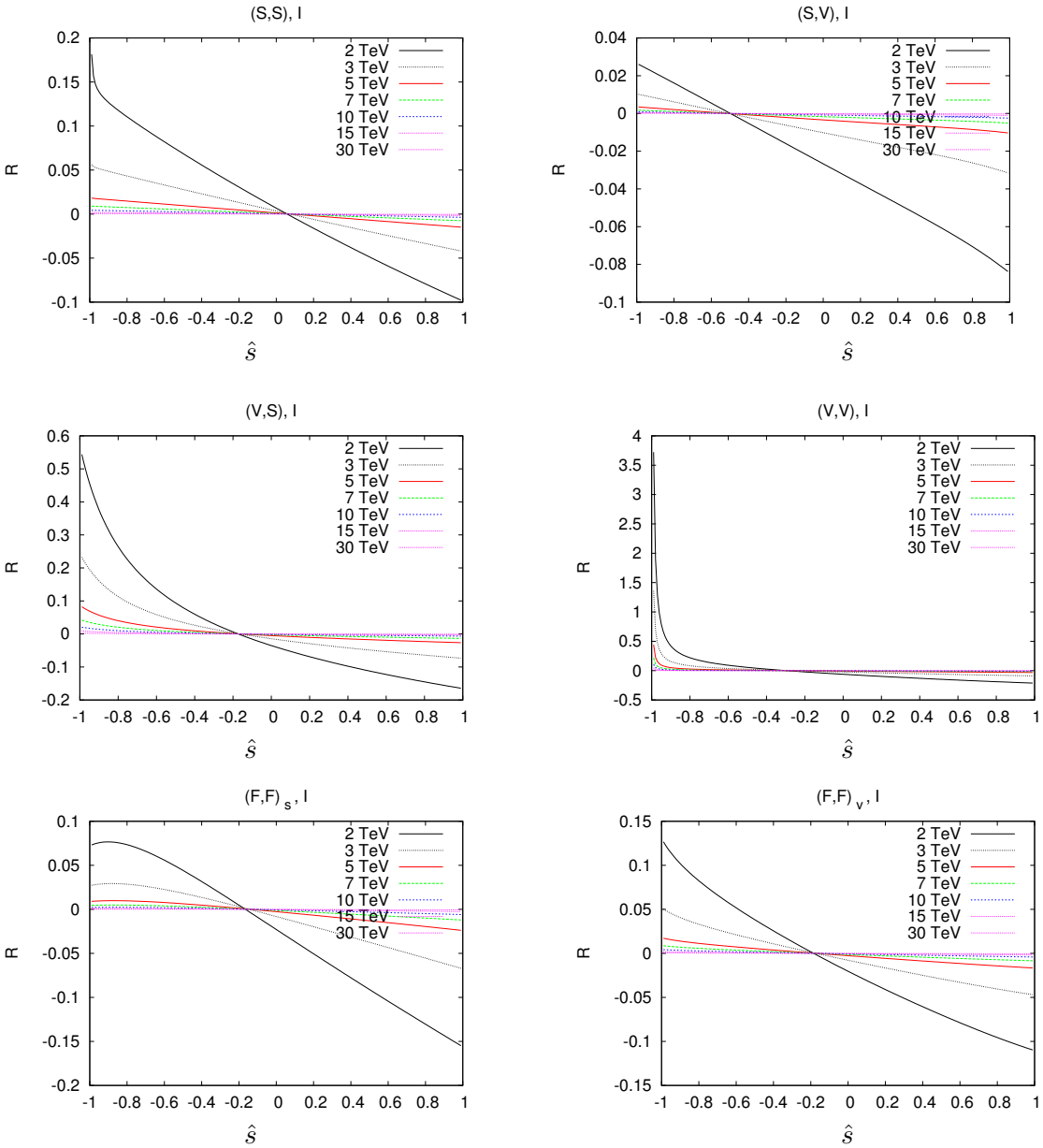

Figure 4.5: Ratio R for the processes $X \to f\bar{f}Y$ for scenario (I) taking $m_X = 1\,TeV$, $m_f = 0$, $m_Y = 0.1\,TeV$. We have calculated the decay width for the following masses of the intermediate particle: $m_I = 2, 3, 5, 7, 10, 15, 30\,TeV$.

We show this relative deviation in figures 4.5 and 4.6. The smaller this deviation is, the less is the differential distribution affected by the expansion.
We find that for a decaying scalar and for a decaying fermion the deviation is always below 20%. In case of a decaying vector particle the situation is more difficult and only for $\epsilon \leq 1/5$ we get $R \lesssim 0.2$ for all values of $\hat{s}$. The reason for these large deviations for $|\hat{s}|$ close to one is, that here the differential widths becomes zero and the rise/fall at the ends of the interval gets steeper the smaller ϵ is. This also implies, that in the corresponding intervals for $\hat{s}$ one will observe only a few events. The situation improves for the decay of a vector boson if the sub-leading terms become dominant as in figure 4.6.

Dependence of coefficients on the mediating particle's mass

Moreover, we show the dependence of the coefficients on the intermediate mass in figure 4.7 to investigate the quality on our conditions needed for the decision-making. For this we have fitted the decay rates for different intermediate masses m_I to the polynomial in equation 4.24 and normalized them with respect to $B = 1$. Note that we have always this freedom as this amounts to a rescaling of the unknown couplings.
We see that all our statements in equation 4.28 and in the strategy flowchart of figure 4.4 are fulfilled within the above claimed range of validity. Note that the only potential problem, namely $D < 0$ in case of (V, S), only occurs for $m_I \lesssim 2.5$ TeV or equivalently $\epsilon > 0.4$ and thus outside the range of validity for vector bosons.
We can sum our observations up by stating that our strategy should work well for all decays if the mass ratio $\epsilon = m_X/m_I$ is below 1/5, in cases of scalar particles or spin 1/2 fermion $\epsilon = 1/2$ is already a reasonable value. This is for example a natural value for gluino decays in supersymmetric models.

4.4 Testing our strategy with Monte Carlo simulations

Now we want to test our strategy from figure 4.4 with Monte Carlo simulations at parton level. We want to be independent of already implemented models, also because sometimes they cannot support all spin assignments or coupling structures we want to discriminate. This is why we chose to write a generic model file for O'Mega/WHIZARD [56, 57] which is explained in the appendix, Section A.1. We give an overview of the supported particles, couplings, the implementation and usage. This model file allows us to consider every decay with arbitrary (renormalizable) couplings.
With the help of this, we have created data sets and tried in a "blinded test" to find out the spin-assignments without any prior knowledge but m_Y and $(m_X - m_Y)$ and their uncertainties. We presume that the first mass of the invisible particle Y is given by an independent source with a precision of 10% and the

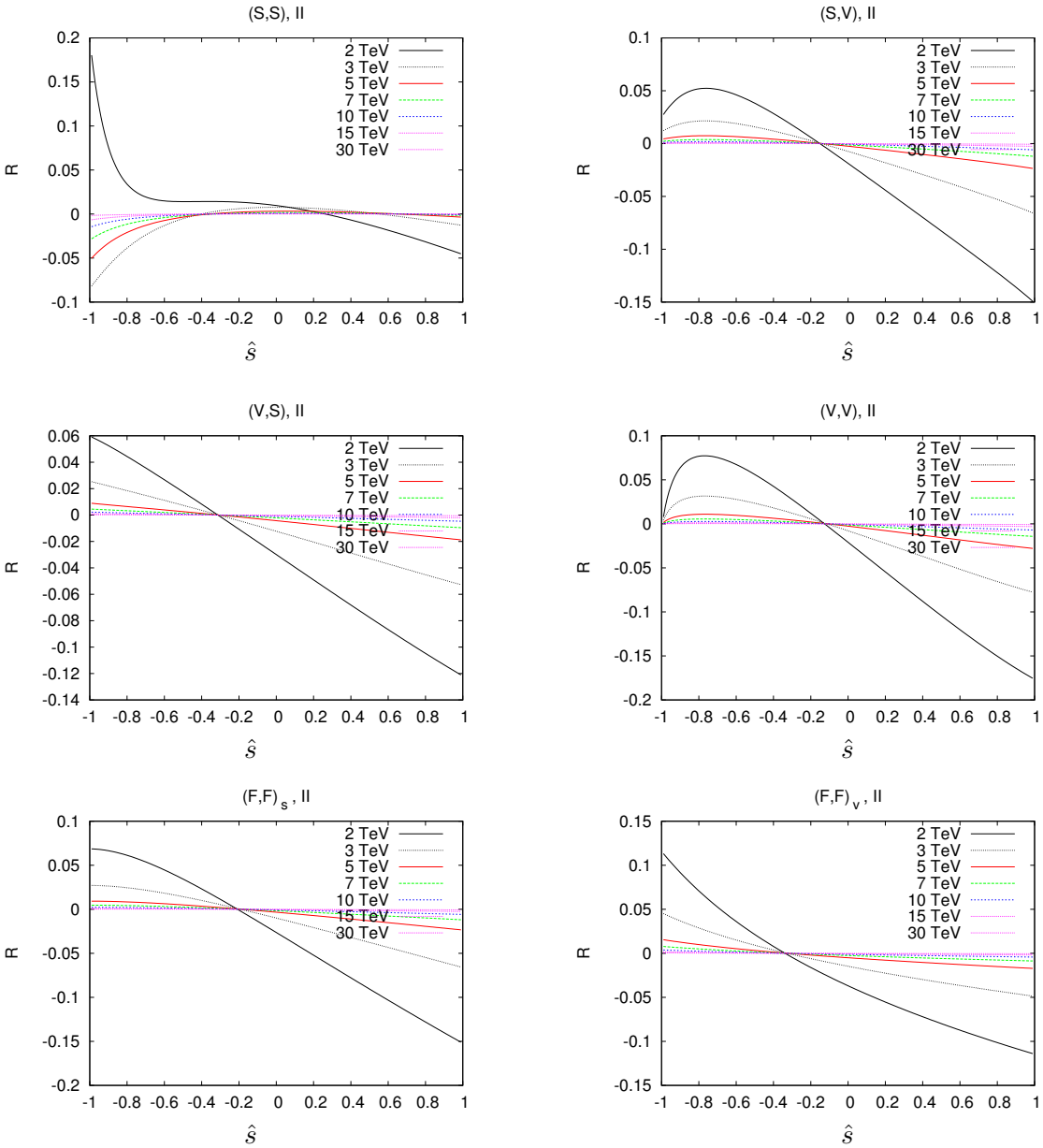

Figure 4.6: Relative deviation for differential decay width the processes $X \to f\bar{f}Y$ with couplings (II).

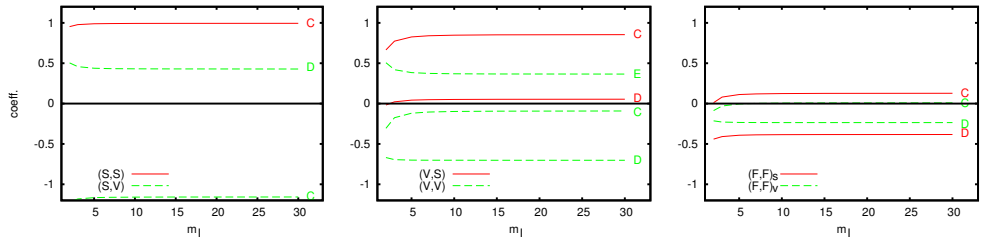

Figure 4.7: Normalized fitted coefficients, e.g. C/B, D/B and E/B, for different masses m_I and mass scen. (I).

second one with a precision of 3%, see e.g. [59–61] and references therein[2].
For definiteness we have taken $m_X = 1\ TeV$, $m_Y = 100\ GeV$ and $m_f = 0$. In the following we will denote by (B, C), (B, C, D), (B, C, D, E) and (B, C, D, E, F) the differential width in equation 4.24 where all but the given coefficients are zero.
We first frame our fitting procedure, and then explain the strategy for specific decays. After that we perform a large sample test.

4.4.1 Fitting procedure

In practice one will not have $\frac{d\Gamma}{d\hat{s}}(\hat{s})$ but one will have the total number of events for a given intervall $[\hat{s}_i, \hat{s}_i + \Delta\hat{s}]$. For this reason we actually fit "distributions" of the form

$$\sum_{i=1}^{n} \int_{-1+(i-1)\Delta\hat{s}}^{-1+i\Delta\hat{s}} \frac{d\Gamma}{d\hat{s}} d\hat{s} \tag{4.33}$$

where $\Delta\hat{s} = 2/n$, n is the number of bins considered and $\frac{d\Gamma}{d\hat{s}}$ is given in equation 4.24. For the creation of the "data" we have used our O'Mega/WHIZARD model file A.1 for generic particles and couplings. For fitting we hence use a linear least squares approach as described e.g. in [62] and references therein. We will exemplify this for the case of the polynomial with coefficients (B, C, D):

$$\begin{pmatrix} x_1 & x_1^2 & x_1^3 \\ x_2 & x_2^2 & x_2^3 \\ & \vdots & \\ x_n & x_n^2 & x_n^3 \end{pmatrix} \cdot \begin{pmatrix} B \\ C \\ D \end{pmatrix} = \hat{X} \cdot \begin{pmatrix} B \\ C \\ D \end{pmatrix} = \begin{pmatrix} \text{data}_1 \\ \text{data}_2 \\ \vdots \\ \text{data}_n \end{pmatrix} \tag{4.34}$$

where the first $3 \times n$ matrix represents the powers of x_i for each bin, $(B, C, D)^T$ are the coefficients which we want to know, and the last n -dimensional vector contains the data entries of n bins. For arbitrary coefficients, this equation reads $\hat{X} \cdot \vec{c} = \vec{d}$ where $\hat{X}$ is the matrix containing the powers of x_i in equation 4.34, $\vec{c}$ is the coefficient vector, and $\vec{d}$ contains the "measured" data of the differential

[2] In case of supersymmetric models the uncertainty on the mass on the lightest neutralino can be smaller, e.g. 5%.

width integrated over intervals of length $\Delta\hat{s}$. This equation can not be solved in general. Therefore one solves for

$$(\hat{X})^T\hat{X}\cdot\vec{c} = (\hat{X})^T\vec{d} \tag{4.35}$$

which optimizes $||\hat{X}\cdot\vec{c}-\vec{d}||$. There are various methods to solve equation 4.35, e.g. QR-decomposition. It can be shown that one obtains a viable fit if the matrix $\hat{X}$ is well-conditioned, so that the eigenvalues of $(\hat{X})^T\hat{X}$ are of comparable magnitude. This is the reason for shifting the variable s to $\hat{s}$ in equation 4.2 on page 37. As it turned out, for the unshifted s values, those eigenvalues differ by 15 orders of magnitude while after shifting the s variable to the interval $[-1,1]$, the eigenvalues differ only by a factor of $\mathcal{O}(10^2)$. This manifests itself in the quality of the fitted coefficients which greatly improved compared to the unshifted fit. So for higher powers of s, they become very small and hard to determine in the fit, although one had very clean data or just smooth test functions. The reason for this is that in the first place, we consider dimensionful coefficients, which became naturally very small for higher degrees of s. After shifting, both $\hat{s}$ and the coefficients are dimensionless so that they still have a hierarchy, but not as strong as before and not depending on the mass.
We solve the equation 4.35 and calculate the corresponding χ^2 with

$$\chi^2 \;=\; \frac{1}{n-j}\sum_i \frac{(\text{Expected}_i - \text{Observed}_i)^2}{\left(\text{Expected}_i + \epsilon^4\cdot\text{Expected}_i^2\right)} \tag{4.36}$$

where n is the number of bins (= number of data points) and j the degrees of freedom (in this case the number of coefficients) of the fit function. Noisy data are always represented better by a polynomial with higher degree which thus will lead to a better χ^2 for larger polynomials. Since we want to reduce this effect, we punish the χ^2 value by multiplying the factor $1/(n-j)$ which is small for large number of j (degrees of freedom) and vice versa.
The theoretical uncertainty from the expansion in ϵ can be estimated in the following way: we have seen in the previous section that in the case of decays of a boson, one obtains qualitative new features only in the 4th order of the ϵ expansion leading to a relative uncertainty of ϵ^2. This in turn leads to a total uncertainty of $\epsilon^2 N$ where N is the number of events. We estimate the error for the coefficients by adding a Poisson noise to the data and determine the corresponding confidence interval after fitting.
In the next subsection, we investigate simulated decays for 10k, 100k and 1M events and investigate the influence of the binning size on the fit in order to get a feeling for the best set-up.

4.4.2 Variations of the fitted parameters for 10 simulations

For all decays we use generic particles with masses: $m_X = 1$ TeV, $m_Y = 0.1$ TeV, $m_f = 0$ which corresponds to the massless cases. The couplings are randomly chosen between -1 and 1 and are displayed in table 4.6. Since we only want to test

our method, these masses and also the couplings do not correspond to a realistic or existing model[3].

(S,S)	g(l,s) = 0.4	g(r,s) = -0.6	n(l,s) = 0.8,	n(r,s) = 0.7
(S,V)	g(l,s) = 0.93	g(r,s) = -0.16	n(l,v) = -0.05	n(r,v) = 0.75
(V,S)	g(l,v) = 0.3	g(r,v) = -0.8	n(l,s) = -0.1	n(r,s) = 0.5
(V,V)	g(l,v) = 0.5	g(r,v) = -0.2,	n(l,v)= -0.1	n(r,v) = 0.9

Table 4.6: Random couplings used in this section.

We have simulated the generic decay (S, V) 10 times with a different number of events (each 2× of 10k, 100k, 1M) and than fitted our four possible polynomials (BC),(BCD), $(BCDE)$ and $(BCDEF)$ to the data using a different amount of bins (10 and 50 bins). We have averaged over the 10 simulations to obtain a mean χ^2 displayed in table 4.7 where the scenarios are listed.

#bins	10			50		
#events	10k	100k	1M	10k	100k	1M
Scen.	1	2	3	4	5	6
(BC)	44.498	207.047	2082.186	30.899	23.020	237.426
(BCD)	1.282	1.628	1.173	1.115	1.1083	0.934
(BCDE)	2.991	1.766	0.965	1.845	1.1288	0.892
(BCDEF)	1.650	1.333	1.0749	1.249	1.0547	0.9005

Table 4.7: Mean χ^2 for different bin sizes and events for 10 simulations of (S,V) decay after fitting them to polynomials with coefficients (BC),... (BCDEF). We have used here the common definition of χ^2 with ϵ=0 since the influence of the mass m_I is here negligible.

Furthermore we calculate the ratios of fitted values for (BCD) in table 4.8 in comparison to the analytic ones. In figure 4.8 we show the deviation

$$\text{Dev.} \quad = \quad \frac{C_{\text{analy.}} - C_{\text{fit}}}{C_{\text{analy.}}} \tag{4.37}$$

and the analogous value for the D coefficient. For all scenarios #1-10, the deviation from the analytic value is smaller the 25% which means in particular that even if the fitted values are not that good, their deviation from the analytic values is much smaller then 100% so that it is unlikely that they change their sign. This is sufficient since we are not interested in the specific value of the coefficients, but only in their existence and their sign.
As one can see, almost every χ^2 for all scenarios is best for the (BCD) fit, which is the polynomial of the underlying process. However, for scenario 3 and 6 the algorithm would prefer the $(BCDE)$ fit, although the χ^2 are very close. The scen.

[3]Except for the (F, F) result where we have taken the SPS 2 [63] masses M_X = 809 GeV, M_X = 121 GeV, $m_f = m_u = 0$ and $M_I = m_{\tilde{u}_1}$ = 3026 GeV and the corresponding MSSM couplings.

Scen.	1	2	3	4	5	6	Analytic
D/C	-0.373	-0.370	-0.375	-0.374	-0.367	-0.374	-0.372
C/B	-1.177	-1.181	-1.181	-1.175	-1.182	-1.181	-1.178
D/B	0.439	0.437	0.443	0.440	0.433	0.442	0.438

Table 4.8: Ratios for different bin sizes and events for the (BCD) fit for (S, V).

6 case can be understood by looking at the calculation of the χ^2. Obviously, a function with a higher order polynomial will always fit better to data with noise. As already discussed on page 58 we try to control this effect by introducing the additional factor j in equation 4.36. The impact of this factor j depends however on the total number of data points (=number of bins) since we divide by $(n-j)$. Thus for a higher number of bins (here: 50), j has a smaller impact and so higher polynomials are not as strongly disfavoured as for a small number of bins.

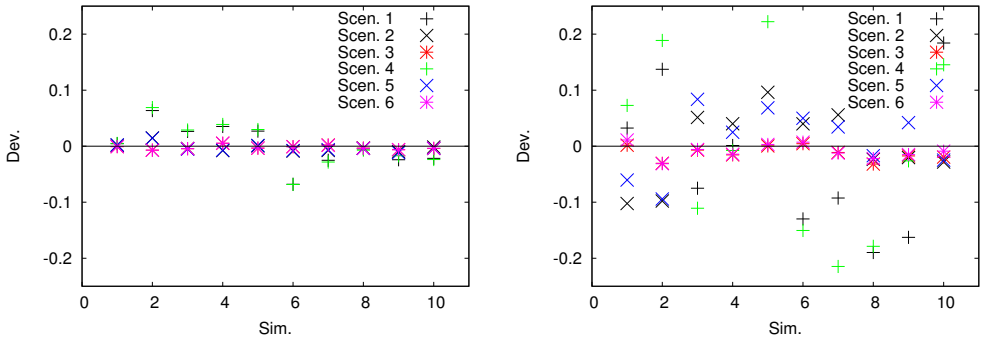

Figure 4.8: Deviation for the C (left) and D (right) coefficient from their analytic value for 10 different MC simulations (on the x axis) and scenarios 1-6 with different number of bins and events. As one can see, the relative deviations are under 25 % for each simulation for each of our secenario which implies that even if the fit is not that good, the coefficient will not change sign.

The question is in the a case, where two orders have a χ^2 around 1, if it is not compelling to always choose the smaller polynomial if it is not in conflict with the analytic constraints on signs and ratios.
For the following discussion we therefore take 10 and 50 bins with 10 k events. We want to demonstrate this way that our method also works with a low production rate of a very massive X particle.

4.4.3 Examples

Here we will show with five examples how our strategy works. We will do the analysis for (S, S), (S, V), (V, S), (V, V) and a "realistic" (F, F)-Susy (SPS2) example. We fit (BC), (BCD), $(BCDE)$ and $(BCDEF)$ to a corresponding MC data set with 10 k (in the (F, F) case also for 2k events) events for 10 and 50 bins and look at the best χ^2. If not denoted otherwise, we use the masses

$m_X = 1000 \pm 150$ GeV, $m_Y = 100 \pm 15$ GeV and m_I=15 TeV. The standard deviation is $3\sigma = 99.7\%$.

• (S, S) Decay
The fit results are shown in table 4.9, top. The χ^2 for all four model fits are very close together. For 10 bins, the χ^2 favours the (BCD), for 50 bins, the (BC) model is favoured. In comparison to some other χ^2, those values are all very good, so we have to have a closer look at the coefficients according to our strategy. In this case one can definitely decide that for both number of bins, the (BC) model is favoured since the fitted value for B and C is the same within the error bars and exactly corresponds to what we found as an analytic constraint for the (BC) model. The error bars of the E and F coefficients of model $(BCDE)$ and $(BCDEF)$ let us assume that those coefficients are zero. So for both bin numbers, (BC) and so (S, S) is compelling which was the original process simulated in O'Mega/WHIZARD.

Model	Coef	χ^2	$(S,S)_{10}$	χ^2	$(S,S)_{50}$	$(S,S)_{an}$
(BC)	C	0.91	1.004 ± 0.0277	0.85	1.004 ± 0.027	1
(BCD)	C	0.87	0.991 ± 0.093	0.89	0.986 ± 0.090	
	D		-0.020 ± 0.110		-0.026 ± 0.110	
(BCDE)	C	0.98	0.994 ± 0.099	0.87	0.989 ± 0.086	
	D		-0.027 ± 0.180		-0.032 ± 0.182	
	E		-0.013 ± 0.182		-0.010 ± 0.186	
(BCDEF)	C	0.85	1.036 ± 0.148	5.43	1.020 ± 0.149	
	D		0.076 ± 0.298		0.037 ± 0.285	
	E		-0.100 ± 0.260		-0.077 ± 0.284	
	F		-0.169 ± 0.384		-0.116 ± 0.362	

Model	Coef	χ^2	$(S,V)_{10}$	χ^2	$(S,V)_{50}$	$(S,V)_{an}$
(BC)	C	69.3	-1.308 ± 0.120	24.48	-1.306 ± 0.126	
(BCD)	C	1.16	-1.173 ± 0.101	0.99	-1.173 ± 0.100	-1.178
	D		0.424 ± 0.237		0.406 ± 0.227	0.438
(BCDE)	C	1.76	-1.249 ± 0.227	1.06	-1.262 ± 0.237	
	D		0.514 ± 0.200		0.517 ± 0.198	
	E		0.157 ± 0.388		0.186 ± 0.393	
(BCDEF)	C	6.19	-1.137 ± 0.206	2.11	-1.143 ± 0.195	
	D		0.940 ± 0.746		0.893 ± 0.608	
	E		-0.188 ± 0.394		-0.164 ± 0.413	
	F		-0.678 ± 0.933		-0.616 ± 0.829	

Table 4.9: Fit results for spin scenarios (S,S) (top) and (S,V) (bottom).

• (S, V) Decay
The fit results are shown in table 4.9, bottom. Here the χ^2 and the ratio of B/C definitely exclude the (S, S) model. The smallest χ^2 is (BCD). The large error

bars of the E and F coefficients include the 0. The ratios for (BCD) model are $D/C = -0.361$, $C/B = -1.173$, $D/B = 0.424$ and suggest (S,V) with equation 4.28.

• (V,S) Decay

The fit results are shown in table 4.10, top. For this data set, the χ^2 is again not very significant since all χ^2 values are very good. The values $F = 0$ and $E = 0$ are again compatible with the error bars. The (S,S) model is not supported, since $B \neq C$ in the range of the error bar. The D coefficient from the (BCD) model is in the range of the error bars also 0, but the value is already analytically very small. The ratios for (BCD) are $D/C = 0.042$, $C/B = 0.851$, $D/B = 0.036$ and suggest (V,S) with equation 4.28.

• (V,V) Decay

The fit results are shown in table 4.10, bottom. Here the χ^2 is significant for the 10 bin case which obviously favours the (V,V) case, while the 50 bin results are less characteristic. But a closer look at the fitted coefficients unveils the underlying result. The (BC) fit is impossible since the C term is negative and not the same as B. The χ^2 for the (BCD) model is extremely large for 10 bins. (V,S) can be excluded due to the wrong interval for C/B. Furthermore $F = 0$ for the $(BCDEF)$ model in the range of the error bars and $(BCDEF)$ has quite a large χ^2. The remaining process is $(BCDE)$, although the values for D and E could also be zero (within the error bars).

A supersymmetric example: (F,F) decay

As a "realistic" test we choose a supersymmetric example and study a focus point scenario which is inspired by SPS2 [63]: $m_0 = 3 \cdot 10^3$ GeV, $m_{1/2} = 3 \cdot 10^2$, $A_0 = 0$, $\tan\beta = 10$ and $\mathrm{sign}(\mu) > 0$. We simulate for the gluino decay 2k and 10k events and also study the effect of different binning sizes, namely 10 and 50 bins. Afterwards we fit the resulting distribution to all possible cases. Here we have assumed that the following information on the masses is given: $(m_X - m_Y) = 688 \pm 23\ GeV$, $m_Y = 121 \pm 12\ GeV$ with a Gaussian distribution. The results are summarised in table 4.11. As one knows neither the absolute values of the couplings nor the intermediate masses, one has the freedom to normalise B to 1 and, thus, only the other coefficients and their uncertainties are given. The χ^2 slightly favours the (B,C,D) polynomial for both 10 and 50 bins. However, if higher powers in $\hat{s}$ are included, one still obtains a good fit and the χ^2 will not be sufficient to discriminate between the different possibilities. This is a quite generic feature because usually there is a hierarchy between the non-zero coefficients: $|B|, |C| \gg |E|, |F|$. The (B,C) case can be ruled out since $B = C$ is not compatible with the range of the error bars. The smallness of the parameters and the large errors in the E and F coefficients of the (B,C,D,E) and (B,C,D,E,F) models suggest that those values are zero. The remaining model is (B,C,D) with negative D which suggests (F,F). We find it encouraging that already for 2000 events one gets first information, including that the (S,S) case can be excluded.

Model	Coef	χ^2	$(V,S)_{10}$	χ^2	$(V,S)_{50}$	$(V,S)_{an}$
(BC)	C	0.34	0.828 ± 0.038	0.82	0.827 ± 0.037	1
(BCD)	C	0.27	0.851 ± 0.090	0.82	0.852 ± 0.094	0.843
	D		0.036 ± 0.116		0.038 ± 0.110	0.032
(BCDE)	C	0.29	0.856 ± 0.108	0.84	0.852 ± 0.110	
	D		0.0264 ± 0.159		0.037 ± 0.167	
	E		-0.017 ± 0.210		-0.003 ± 0.182	
(BCDEF)	C	0.24	0.881 ± 0.172	0.83	0.883 ± 0.163	
	D		0.090 ± 0.3452		0.105 ± 0.304	
	E		-0.071 ± 0.323		-0.069 ± 0.286	
	F		-0.104 ± 0.465		-0.115 ± 0.394	

Model	Coef	χ^2	$(V,V)_{10}$	χ^2	$(V,V)_{50}$	$(V,V)_{an}$
(BC)	C	2.48	-0.844 ± 0.116	1.04	-0.850 ± 0.112	1
(BCD)	C	7.11	-0.882 ± 0.089	1.91	-0.886 ± 0.0911	
	D		-0.096 ± 0.177		-0.091 ± 0.117	
(BCDE)	C	1.93	-0.986 ± 0.214	0.92	-0.982 ± 0.231	-0.917
	D		0.022 ± 0.182		0.025 ± 0.176	0.026
	E		0.227 ± 0.353		0.212 ± 0.351	0.139
(BCDEF)	C	2.48	-0.974 ± 0.179	0.95	-0.973 ± 0.196	
	D		0.061 ± 0.527		0.052 ± 0.509	
	E		0.195 ± 0.318		0.187 ± 0.361	
	F		-0.063 ± 0.690		-0.045 ± 0.641	

Table 4.10: Fit results for spin scenarios (V,S) (top) and (V,V) (bottom).

Coef.	χ^2	$(F,F)_{10}$	χ^2	$(F,F)_{50}$	χ^2	$(F,F)_{10,2k}$
C	1.37	0.210 ± 0.061	0.81	0.208 ± 0.071	0.79	0.208 ± 0.126
C	0.08	0.089 ± 0.077	0.30	0.089 ± 0.076	0.76	0.089 ± 0.155
D		-0.232 ± 0.106		-0.227 ± 0.110		-0.227 ± 0.252
C	0.09	0.079 ± 0.141	0.31	0.067 ± 0.128	0.97	0.067 ± 0.300
D		-0.218 ± 0.150		-0.197 ± 0.139		-0.197 ± 0.322
E		0.028 ± 0.227		0.060 ± 0.228		0.060 ± 0.536
C	0.11	0.080 ± 0.149	0.31	0.077 ± 0.160	0.55	0.077 ± 0.401
D		-0.215 ± 0.456		-0.169 ± 0.340		-0.169 ± 1.108
E		0.025 ± 0.260		0.035 ± 0.311		0.035 ± 0.738
F		-0.006 ± 0.516		-0.046 ± 0.443		-0.046 ± 1.315

Table 4.11: Testing of the Susy focus point taking 10 bins in case of 2k events and 10 and 50 bins for 10k events. Input for the fit is: $(m_X - m_Y) = 688 \pm 23$ GeV, $m_Y = 121 \pm 12$ GeV with gaussian distribution, $m_I = 3026$ GeV. The coefficients are normalised such that $B = 1$ and the uncertainties are at 3σ. The analytic values for the coefficients are $B = 1$, $C = 0.123$, $D = -0.188$.

We have also checked how things change if the errors on the $m_X - m_Y$ and m_Y are increased. As a first step we have doubled the mass uncertainties and we find that the central values remain stable. The uncertainty on C (D) in case of (B, C) and (B, C, D) fits increases by about 50 (few) per cent. In case higher polynomials are included the uncertainty of C increases by about 30 per cent whereas the uncertainties of the other parameters change again only in the few per cent range. This is roughly speaking the border-line where one can make reliable statements in this case. We have also increased the mass uncertainties by a factor three and find that the uncertainties of the coefficients C and D are close to 100 per cent and thus that no reliable statement can be made.

The (S, S) and (F, F) processes with all possible fits for 50 bins are shown in figure 4.9 where one can see the analytic results and the data for 10k events. For the (S,S) result, the data points can apparently also be fitted well with higher polynomials, and the resulting curves coincide. With the (F,F) result, we can see that for the (BC) model the fit and the analytic result differ a lot for small $\hat{s}$.

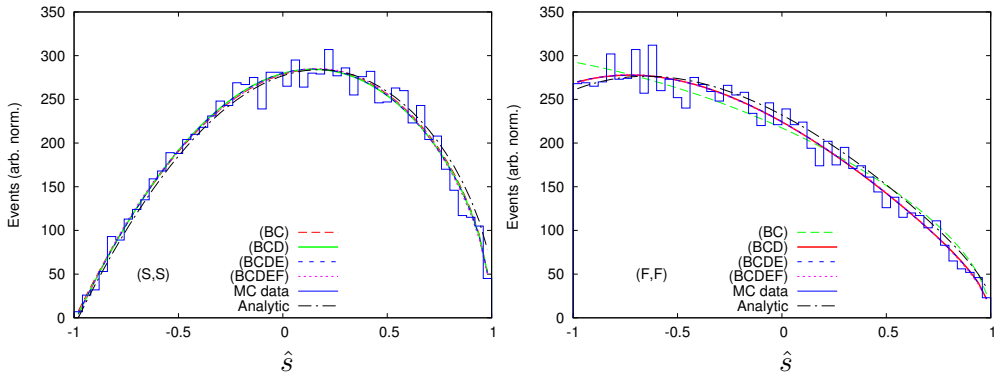

Figure 4.9: Comparison of different fits with the analytic result and the MC data. Left: (S,S), right: (F,F). The normalization of the y-axes is arbitrary.

4.4.4 Large sample tests

In the second step we have tested our strategy for a large set of random couplings, fixing however the kinematics to $m_X = 1$ TeV, $m_Y = 100$ GeV and all $m_I = 5$ TeV. The latter number is not crucial as long as it is above 5 TeV (2 TeV) in case of decaying vector bosons (decaying scalars and fermions). In an ideal world one could use the strategy depicted in figure 4.4 without any problems, since each path is unique in this flowchart. In reality there will be some smearing of the data from the measurement itself as well as from the background subtraction and we have to adjust our strategy to that. This is why one may not end up with on specific spin assignment to a data set, but only with an exclusion list and two or three possible underlying spin scenarios.
Let us initially discuss an important feature for the decision making process which we stumbled upon when performing the first large sample tests.

Initially, we wanted to fit the data to the largest polynomial possible (B, C, D, E, F) and expected to get e.g. E and F close to zero for data sets from generated scenarios, e.g. (S, V), where the true value is zero. However, after taking noisy data into account, we realized that noisy data would always prefer a larger polynomial, and that all coefficients get values independent from their true values.
However, by taking a χ^2 test into account which punishes larger polynomials as in equation 4.36, a distortion of the decision by this effect could be avoided. But those ill-fitted coefficients, e.g. E to a small value, of course also have an impact on the fitted values for the other actually non vanishing coefficients. We thus might not be able to apply the part of our strategy in which we take the specific values, e.g. ratios of coefficients, into account. This is why we choose to vary the decision-making in the following way

1. Fit data to all possible polynomials (B, C), (B, C, D), (B, C, D, E), (B, C, D, E, F) [4] (by solving the equation 4.35)
2. Calculate χ^2 from equation 4.36
3. Go through necessary requirements for each spin assignment (listed below) which are derived from the decision tree shown in figure 4.4
4. In the case of disagreement, throw out the corresponding decay in the model list in equation 4.38 (shown below) which includes all possible decay scenarios.

In this approach, we are as sure as possible not to falsely exclude the correct model. We apply steps 1-4 to the model list

$$\{(S, S), (S, V), (V, S), (F, F), (V, V), (V, V)_4\} \tag{4.38}$$

and the corresponding differential widths. $(V, V)_4$ denotes the case where only the 4th order in ϵ of (V,V) remains which is a polynomial with coefficients $(BCDEF)$. The criteria which we worked out in the strategy are summarized in the following list

1. $B \neq C \rightarrow$ remove (S, S)
2. $D > 0 \rightarrow$ remove (F, F); $D < 0 \rightarrow$ remove $(S, V), (V, S)$
3. C/B in (S,V) interval $\rightarrow$ if not, remove (S, V)
4. C/B in (V,S) interval $\rightarrow$ if not, remove (V, S)
5. D/B in (S,V) interval $\rightarrow$ if not, remove (S, V)
6. D/B in (V,S) interval $\rightarrow$ if not, remove (V, S)
7. D/C in (S,V) interval $\rightarrow$ if not, remove (S, V)

[4] We choose here not only to include the three polynomials for the leading order of ϵ^2 but also a fourth polynomial which can show up in the case where the leading terms are zero.

8. D/C in (V,S) interval $\rightarrow$ if not, remove (V,S)
9. if $E<0$ in $(V,V)/(V,V)_4$, $\rightarrow$ remove $(V,V)/(V,V)_4$
10. if $F<0$ in $(V,V)_4$, $\rightarrow$ remove $(V,V)_4$
11. *Optional*: Remove all models with $\chi^2>3$ (here: $\epsilon=1/5$)
12. *Optional*: Remove $(V,V)/(V,V)_4$ if $E,\ F<0.001$ respectively.

The last two criteria are only optional, which means that we will first discuss the basic criteria 1 to 10 and in a second step, we also include the last two criteria separately. They are distinct from the others because the values needed for these criteria are subjective.

Basic criteria

We have generated 100 different data sets with random couplings for each of the decays (S,S), (S,V), (V,S), (V,V) and (F,F) with 10^4, 10^5 and 10^6 events for each set of couplings. Now we apply steps 1-4 of page 65 to it and every time one criterion could be applied and not fulfilled within the range of the error bars, the corresponding model was cancelled from the list in equation 4.38 at page 65.
The results for all the different Monte Carlo data sets are summarized in table 4.12 after going through the criteria. The table is structured as follows: The first row lists the tested models, while the first column lists the true underlying decays. For example, the numbers in the first row were obtained as follows: We started with 100 different data sets for the (S,S) decay, apply our criteria 1 to 8, and after that, 97 (S,S) models remain, 0 of (S,V), 24 of (V,S), 99 of (F,F) and so on. This means that the test could correctly exclude 100% of the (S,V) decays, more than 3/4 of the (V,S) decays and so on. Note that there were no data sets were all models were excluded except one single wrong one.
From these numbers, we can draw the following conclusion:

1. It is easier to fit data originating from a polynomial which has low powers of $\hat{s}$ by a higher order polynomial if there is smearing than vice versa.
2. The number of criteria depends on the decay mode, e.g. it is easier to exclude (S,V) where 3 criteria are at hand than (V,V) where only one exists. Additionally, some criteria (like B=C) are strong while others are weaker (e.g. $E>0$) which affects the number of excluded (S,S) underlying models (ideally always 100%).
3. The modulus of the coefficients E and F is usually up to two orders of magnitude smaller than the modulus of the other coefficients but the absolute uncertainty is roughly the same for all coefficients. Although the error bars always include the 0, the models can not be cancelled out using this argument, since in the correct (V,V) models, the error bars also include the 0 (as can be seen in table 4.10 e.g.; however, the absolute value of the

	(S,S)	(S,V)	(V,S)	(F,F)	(V,V)	(V,V_4)
10^4 events:						
(S,S):	**97**	0	24	99	100	100
(S,V):	0	**100**	0	3	100	100
(V,S):	0	0	**100**	100	99	100
(F,F):	0	1	0	**100**	100	100
(V,V):	0	67	0	78	**100**	100
10^5 events:						
(S,S):	**99**	0	0	100	100	100
(S,V):	0	**95**	0	3	100	100
(V,S):	0	1	**99**	100	100	100
(F,F):	0	0	0	**100**	100	100
(V,V):	0	17	0	60	**100**	100
10^6 events:						
(S,S):	**96**	0	0	100	100	100
(S,V):	0	**87**	0	6	100	100
(V,S):	0	1	**99**	100	100	100
(F,F):	0	0	0	**100**	100	99
(V,V):	0	2	0	57	**100**	99

Table 4.12: The number of remaining models for 100 input models each where the various criteria are applied using 3σ uncertainties on the coefficients. The masses are chosen as $m_Y = 100 \pm 10\ GeV$ and the mass difference $(m_X - m_Y) = 900 \pm 30\ GeV$. The bold numbers are the correct model fits.

correctly-fitted E value is much larger than the ill-fitted value for the wrong model).

4. A higher number of wrongly excluded models for 10^6 events (e.g. for the (S, V) model (87)) is due to the high statistics which make the influence of the expansion visible.

In particular the third item implies that it will be rather difficult to exclude a positive E and F in practice if only one decay channel is considered! However, one should keep in mind, that these criteria are for generic decays, and no restrictions have been made for the coupling structure or the masses. If one has a hint towards some specific model, one can then work out more model-specific criteria and those can be used to check if the data still fulfil those.

Additional criteria

So far, we have not used our knowledge about the χ^2. One can of course always remove the models with the largest χ^2. However, this is not a strict criterion and thus we applied such test such as criterion 11.
From the test-fits in Chapter 4.4.3, we could see that in the cases where (V, V) is not the underlying model and the decay can be described with a polynomial like (BC) or (BCD), the values for coefficients E and F are very tiny. Although this is a common feature in this type of decays (which we saw also in the large sample tests above), we do not make use of it in the criteria 1 to 8. The point is that the errors are large and include of course the 0 as expected, but the same happens in the case of the true (V, V) decay. Here, the E coefficient in table 4.10 has a much larger value compared to e.g. the E coefficient for the (S, V) decay in table 4.9. So both error bars include the 0 and if that would be the criterion, it would remove the wrong as well as the correct model.
This is why we have introduced the optional criteria 11 and 12 separately, the first includes the χ^2 of the fit, the second one gets rid of very tiny coefficients and thus the wrong model. Since the value for these criteria is not straightforward, we have tested different values to see which one throws out most models correctly but none or only few of the correct models. We give the resulting numbers in table 4.13 which is organized as table 4.12 but with two numbers, the first one taking only criteria 1 to 8 and 11 into account, the second one also applying 12: The first number of 99/100 (as e.g. in the (S, S) case) denotes the number remaining after applying the χ^2 criterion, the second number the same with the small E, F criterion. The results are

1. the $\chi^2 > 3$ criterion is most useful if the underlying decay is $(V, V)/(V, V)_4$, since the polynomials with a lower order have a large χ^2. This is e.g. reflected in the (V, V) decay with 10k events, and the fitted (S, V) and (F, F) polynomials. Here the number of remaining processes is reduced by applying the χ^2 test from 67 ((S, V), table 4.12) to 56 (table 4.13) and for (F, F) from 78 to 48.

	(S,S)	(S,V)	(V,S)	(F,F)	(V,V)	(V,V_4)
10^4 events:						
(S,S):	**97/97**	0/0	24/24	99/99	99/82	99/84
(S,V):	0/0	**96/100**	0/0	1/3	95/94	97/87
(V,S):	0/0	0/0	**100/100**	100/100	99/94	100/87
(F,F):	0/0	1/1	0/0	**100/100**	99/97	100/87
(V,V):	0/0	56/67	0/0	48/78	**98/96**	99/95
10^5 events:						
(S,S):	**99/99**	0/0	0/0	100/100	100/60	100/68
(S,V):	0/0	**94/95**	0/0	0/3	100/88	99/70
(V,S):	0/0	1/1	**99/99**	100/100	100/56	100/73
(F,F):	0/0	0/0	0/0	**100/100**	100/72	100/70
(V,V):	0/0	2/17	0/0	1/60	**99/97**	97/87
10^6 events:						
(S,S):	**96/96**	0/0	0/0	100/100	100/13	100/20
(S,V):	0/0	**87/87**	0/0	0/6	100/54	100/42
(V,S):	0/0	1/1	**99/99**	100/100	100/17	100/30
(F,F):	0/0	0/0	0/0	**100/100**	100/31	100/27
(V,V):	0/0	0/2	0/0	0/57	**100/100**	99/66

Table 4.13: Same as table 4.12 but taking into account either the optional criterion 11 (exclude $\chi^2 > 3$) or criterion 12 (small E,F) corresponding to the first/second number in each entry.

2. The criterion for small $E,\ F$ works very well for high statistics since the fit gives values that are close to 0. This is reflected in the last row of table 4.13, where the underlying process is (F, F). After application of the common criteria, 100 of (V, V) and 99 of $(V, V)_4$ models remain (see table 4.12). However, after additionally applying the criterion 12 this number is reduced to 31 (V, V) and 27 $(V, V)_4$.

However, the same argument does not remove any of the (V, V) models, if (V, V) is the underlying process. For a smaller number of events, there are only a few coefficients $E,\ F$ smaller then 0.001 so only a smaller number of models are removed as e.g. in table 4.13 for 10k events, 94/87 remaining $(V, V)/(V, V)_4$ models for the underlying (V, S) process.
As in the case of the supersymmetric example in Section 4.4.3 we have also used larger uncertainties on m_Y and $m_X - m_Y$ and come to the same conclusions.

4.5 Summary

We have worked out a detailed strategy for spin determination in three body decays where ordinary spin determination via the degree of the polynomial for the differential decay width cannot be applied.
Our approach is based on the fact that the differential decay width can be written as a polynomial times a global function after we take the off-shell limit and expand in $\epsilon = m_X/m_I$. In contrast to the on-shell spin determination approach, knowing the degrees of polynomials is not enough to be able to distinguish between the different intermediate particles[5]. We found that all five different spin assignments can be discriminated uniquely from each other, and that in a perfect fit the underlying spin assignment can be perfectly reconstructed. However, in data suffering from statistical fluctuations, we saw by investigating large Monte Carlo data samples, that some criteria can better be applied than others and that for some models there are more criteria then for others making the former easier to exclude.
In summary one can say that the strategy yields unique results from its construction but suffers, as do all other methods, from low statistics. In our approach this leads to a strategy that excludes models if the data do not fulfil the characteristic criteria of a certain decay. This has the consequence that one might be left with more then one model after applying our decision-making strategy, while reducing the risk of falsely excluding the correct underlying model.

[5]It should be mentioned that for on-shell decays, the degree of the polynomial also only gives information about the mediating particle's spin, not that of the external particles, which we are also able to analyse with this strategy.

Chapter 5

Spin in an s-Channel Diagram With Very Short Decay Chains

We dedicate this chapter to spin determination in the case of very short decay chains. We investigate the s-channel diagram where two intermediate particles decay into four final state particles, including two invisible ones. We take all possible spin scenarios with renormalizable interactions into account and study the influence of the masses and couplings on the discrimination power of a specific variable that has been proposed in the literature. In order to apply our results to hadron colliders, we discuss a simple scheme that can be used to disentangle PDF and spin effects.

5.1 Introduction, notation and calculation

In this chapter we investigate a scattering process with a certain topology denoted in [64] as the antler topology, with

$$p, p \to B, \overline{B} \to C\overline{C}, l\bar{l} \tag{5.1}$$

where $C, \overline{C}$ are invisible particles and $l, \bar{l}$ are SM leptons. The "antler" can be seen in figure 5.1, if one rotates the Feynman diagram counter clockwise by $\pi/2$. There is one invisible particle on each branch, and only the invariant mass distribution which can be build from the visible leptons is observable. The methods discussed in the chapters before can therefore not be used because the decay chains are too short in this scattering process. This topology was discussed in the literature (see, e.g. [14, 65–69]). It is very interesting since it appears in many models of new physics and, due to the shortness of the decay chains, can be treated in a model independent way. Unfortunately, this antler topology introduces a lot of problems. The cross section of uncoloured processes are significantly smaller than coloured ones. This lowers the number of events in the process in question and reduces the statistics. Furthermore, more thought has to be given to mass measurement since the endpoint of the invariant mass distribution of the two leptons depends on the total energy. There are several techniques available for mass measurement, such as [64] where the masses can be determined from cusps in the invariant mass distribution if the particle A in figure 5.1 is resonant. In

[70], the "Cambridge Variable" M_{T2} was introduced that works by a minimizing-maximizing event-by-event analysis of the missing transverse energy. In [71], the "contransverse mass" M_{CT} was introduced while [72] investigates the projected contransverse mass M_{CTx}.

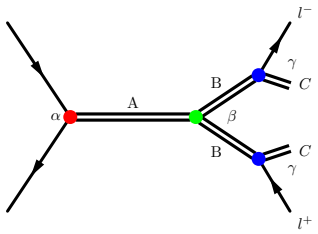

Figure 5.1: Notation for the antler diagram. The undetectable particles are C, while $l^{\pm}$ are SM leptons (massless). The couplings are denoted here generically by α, β, γ. They are specified for each process in table 5.2. The double lines mark the particles with unknown spin.

Besides uncertainties in the mass determination, one can also have t-channel contributions. Since we restrict ourselves only to leptons in the final states and not jets, this topolgy would however imply leptoquarks, and we leave this subject for later study.
Since we are considering processes for a hadron collider, we are only interested in observables that are boost invariant along the beam axis (z-axis). We have investigated different observables which are z-boost invariant, including the invariant mass of the two visible leptons, the contransverse mass of the two leptons M_{CT}, the projected contransverse mass M_{CTx} and the difference of the pseudorapidities of the two visible leptons which we denote in the following with $\mathcal{C}_B$. Most of them have their origin in mass measurement as mentioned above.
Since the last variable showed the most spin dependence in our investigations, we study this variable in the following and see how suitable it is for spin determination. It is related to the angle of the particles B in figure 5.1 in the centre of mass (CoM)[1] frame and is hence sensitive to the spin of the particles in the production process. It has been of much interest (see e.g. [73] [74] [69]) in the recent years for the discrimination of Susy and UED. We investigate if and how this discrimination power depends on the couplings, mass and spin scenarios.
Let us first have a look at the appealing properties of this variable. Therefore we only consider the production level of the process in figure 5.1 which corresponds to slepton production in Susy and KK-lepton production in UED. The dependence of the cross section on the production angle $\cos\theta^*$ (the angle between one of the B particles and the beam axis) is crucially different for Susy and UED in the CoM frame

$$SUSY: \quad \frac{d\sigma}{d\cos\theta^*} \propto 1 - \cos^2\theta^* \tag{5.2a}$$

[1] In order to avoid confusion with the LHC experiment CMS, we use the short form "CoM" for centre of mass.

$$UED: \quad \frac{d\sigma}{d\cos\theta^*} \propto 1 + \frac{1-x}{1+x}\cos^2\theta^* \tag{5.2b}$$

where $x = (2M_B)^2/\hat{s}$ and $\hat{s} = (p_B + p_{\overline{B}})^2$ is the CoM energy[2]. The distributions are shown in the left plot of figure 5.2. If one turns on PDFs, this effect gets washed out, since the $\cos\theta^*$ angle is no longer measured in the CoM frame, but in the Lab frame. If we could measure the sleptons/ KK-leptons directly, we could reconstruct the CoM distribution and determine the underlying spins of the particles involved. Since sleptons or KK-leptons are assumed to decay into a lepton and an invisible particle, we do not have the necessary information about the z-boost to go back into the CoM frame from the Lab frame.
The variable $\mathcal{C}_B$ is z-boost invariant and is related to $\cos\theta^*$ such that for high energies it approaches the $\cos\theta^*$ distribution of the parents B in the CoM frame. This is due to the fact that in this high energy (HE) limit, the C particles are boosted in the direction of the parents.

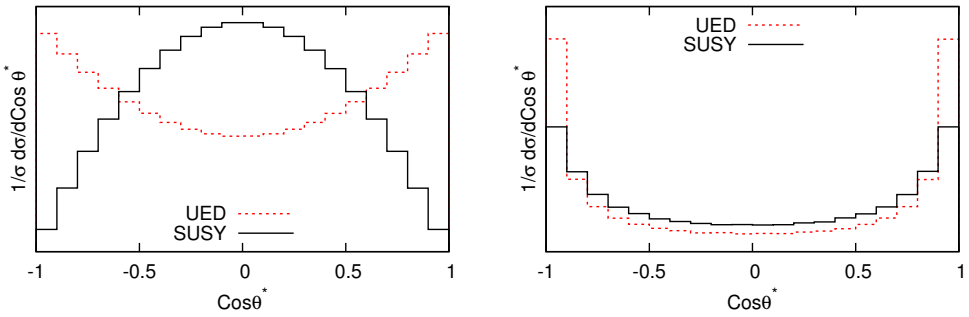

Figure 5.2: In the left plot, we see the $\cos\theta^*$ distribution in the CoM frame for Susy and UED which shows a significant difference between the two models Susy and UED. If one includes PDFs as done in the right plot, the B particles, here sleptons or lepton', are boosted along the z direction and hence the effect is washed out.

We turn our attention here to the threshold (TH) limit where the particles B are produced almost at rest. In this limit one cannot apply equation 5.2. This is the case for heavy particles B where the HE limit is not a good approximation since the boost of the C particle is smaller. In the following we will investigate, whether there is a comparably simple dependence as in equation 5.2 in this case as well.
In the HE limit, the $\cos\theta^*$ distribution "loses" all information about the spin or the mass of the C particle. However, in the TH limit, the spin, mass and chiral couplings of particles C, which are e.g. neutralinos or B', play an important role so that the dependence is not as simple as that of equations 5.2 but crucially depends on these values.
We therefore organize this chapter as follows: We will first specify our notation, and make some remarks about the calculation. Then we will define the variable

[2]Note here, that we use $\hat{s}$ in this chapter differently from the one in the last chapter. Since the investigated topologies are different, there is no danger of confusion.

of interest, $\mathcal{C}_B$. In Section 5.2 we give the analytic results for the full matrix elements squared of all investigated processes as well as the TH results.
In Section 5.3 we explain our fixed $\sqrt{\hat{s}}$ approach which helps us disentangle spin effects from smearing of the energy due to the parton distribution functions (PDFs).
In Section 5.4 we go through the possible spin scenarios and investigate for which coupling set or mass range the discrimination of two scenarios is possible and in which cases one has to be careful not to misidentify or mix up spin scenarios.

5.1.1 Notation

We investigate the scattering process in equation 5.1 depicted in figure 5.1. We assume that the C particles are invisible so that they can serve as a dark matter candidate in the models of interest. The two visible SM particles are leptons $l, \bar{l}$. The masses are denoted with M_A, M_B, M_C for the particles A, B, C respectively. The double lines in figure 5.1 denote the (BSM) particles which have unknown spin. If we assign all possible spins up to spin 1, we end up with 8 different spin assignments

$$(ABC) = (SSF);\ (SVF);\ (VSF);\ (VVF);\ (SFS);\ (VFS);\ (SFV);\ (VFV); \tag{5.3}$$

where (ABC) denote the particles as shown in figure 5.1. As in the previous chapters, S, V, F stands for scalar, vector or spin-1/2 fermion. The production processes $p, p \to B, \overline{B}$ are denoted in the same manner with

$$(AB) = (SS);\ (SV);\ (VS);\ (VV);\ (SF);\ (VF). \tag{5.4}$$

We give all 8 spin assignments for this topology in table 5.1, and the generic interactions we consider in the following are summarized in table 5.2. For chiral couplings, we use the notation

$$\tau_c = \left(\frac{M_C}{M_B}\right)^2; \qquad x = \frac{(2M_B)^2}{\hat{s}}; \tag{5.5a}$$

$$\alpha = \frac{a_l^2 - a_r^2}{a_l^2 + a_r^2}; \qquad \beta = \frac{b_l^2 - b_r^2}{b_l^2 + b_r^2}; \qquad \gamma = \frac{c_l^2 - c_r^2}{c_l^2 + c_r^2} \tag{5.5b}$$

and for $a^s, b^s, c^s, \widetilde{c}^s, \widetilde{c}$ accordingly.
We choose to derive the components of the amplitudes in three different reference frames. The decay parts are calculated in the CoM frame of the decaying particles B respectively. On the one hand this simplifies the decay calculations since we can express the momenta of the particles of each decay in the reference frame of the decaying particle, while on the other it introduces Jacobian factors to the phase space integral when we rewrite it in terms of $\mathcal{C}_B$. We use the following notation

$$\text{Production:} \quad p, \overline{p} \to B, \overline{B} \tag{5.6a}$$

$$\text{Decay 1:} \quad B(p_1, M_B) \to l(p_2, 0), C(p_3, M_C) \tag{5.6b}$$

B/A	S		V	
S	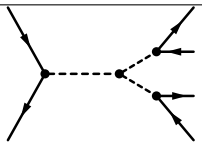	$H\widetilde{\chi}_2^0\widetilde{\chi}_2^0$	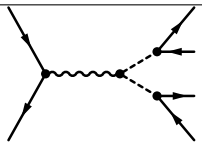	Susy; Z'+Susy
V	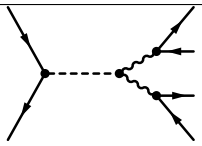	Higgs+WW	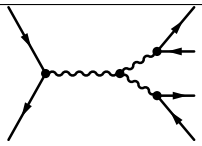	
F, C=S	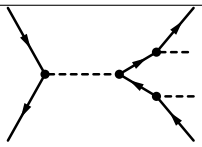	LHT [75]	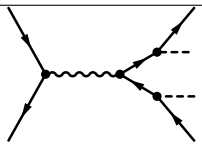	
F, C=V	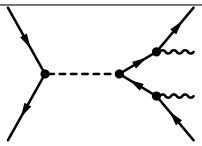	LHT	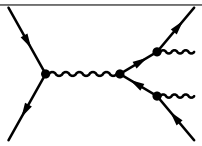	UED

Table 5.1: All 8 different spin assignments for $q\overline{q} \to l\bar{l}, CC$ and examples of different theoretical models corresponding to some of them.

Pos.	Vertex/Lagrangian			
$\alpha:$		$\overline{\psi}_q \left(a_l^s P_L + a_r^s P_R\right) \psi_q$		$\overline{\psi}_q \gamma^\mu \left(a_l P_L + a_r P_R\right) \psi_q A_A^\mu$
$\beta:$ 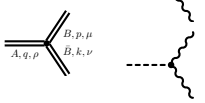		$\overline{\psi}_B \gamma^\mu \left(b_l P_L + b_r P_R\right) \psi_B A_A^\mu$ $b_1 \cdot f^{abc} A_\mu^a \partial^\mu A_\nu^b A^{\nu\ c}$ $b_3 \cdot A_B^\mu A_{\mu,B} \phi_A$		$\overline{\psi}_q \left(b_l^s P_L + b_r^s P_R\right) \psi_q$ $b_2 \cdot (D_\mu \phi_B)^\dagger (D^\mu \phi_B)$ $b_4 \cdot \phi_B \phi_B^\dagger \phi_A$
$\gamma:$		$\overline{\psi}_l \gamma^\mu \left(c_l P_L + c_r P_R\right) \psi_B A_C^\mu + hc.$ $\overline{\psi}_l \gamma^\mu \left(\widetilde{c}_l P_L + \widetilde{c}_r P_R\right) \psi_C A_B^\mu + hc.$		$\overline{\psi}_l \left(c_l^s P_L + c_r^s P_R\right) \psi_B \phi_C + hc.$ $\overline{\psi}_l \left(\widetilde{c}_l^s P_L + \widetilde{c}_r^s P_R\right) \psi_C \phi_C + hc.$

Table 5.2: Summary of the vertices and Lagrangians for generic interactions used in this chapter.

$$\text{Decay 2:} \quad \overline{B}(p_1', M_B) \to \bar{l}(p_2', 0), C(p_3', M_C). \tag{5.6c}$$

The phase space integrals are

$$\mathrm{d}\Omega = \mathrm{d}\cos\theta^* \mathrm{d}\phi^* \qquad \mathrm{d}\Omega_1 = \mathrm{d}\cos\theta_1 \mathrm{d}\phi_1 \qquad \mathrm{d}\Omega_2 = \mathrm{d}\cos\theta_2 \mathrm{d}\phi_2 \tag{5.7}$$

where θ_i, θ^* are in the CoM frame of the decaying particles and the production CoM frame respectively.

5.1.2 Details on the calculation

In the calculation we use narrow width approximation (NWA) for the particle B. Since we are particularly interested in the influence of the particles' spin in the process, we use an extended version of common NWA called helicity method which we illustrate in the following. We found [43] and [76] very useful in this topic and follow their approach.

Helicity method

Common NWA is used to calculate typical high energy processes in which two particles collide, producing other particles which then decay in various decay chains. Working in NWA means assuming that the width of the unstable particle is small compared to its mass m so that its propagator can be approximated by a delta function

$$\frac{1}{(s-m^2)^2 + m^2\Gamma^2} \approx \frac{\pi}{m\Gamma}\delta(s-m^2).$$

The total cross section for $2 \to n$ can then be calculated from

$$\sigma_{2\to n} \approx \sigma_{2\to k} \frac{\Gamma_{1\to m}}{\Gamma}; \quad n = k + m - 1$$

where Γ is the total width of the decaying particle, and $\Gamma_{1\to m}$ the remaining $1 \to m$ process. If the initial particles are unpolarized, one would average over the initial particle helicities and sum over the final state ones for each total cross section. This treatment does not take into account possible helicity correlation effects between the production and the decay processes. If the decaying particles have non-zero spin, we have interference effects which are commonly calculated by using density matrices. In our case we have the production and decay processes as in equation 5.6. We denote the matrix element of the production with $\mathcal{M}_{\lambda(B),\mu(\overline{B})}$ with the particles $B, \overline{B}$ and their helicities $\lambda(B), \mu(\overline{B})$ and the matrix elements of the corresponding decays with $\mathcal{N}_{\lambda(B)}$, $\mathcal{N}_{\mu(\overline{B})}$.
The density matrix for the production and decay is then calculated in the following way. We keep the helicity of the particle B as λ, λ' and calculate the production and decay density matrix by averaging/summing over the the initial/final state particles:

$$\rho^{prod}_{\lambda\lambda',\mu\mu'} = \sum_{init.\ pols.} \mathcal{M}_{\lambda\mu}\mathcal{M}^*_{\lambda'\mu'};$$

$$\rho^{decay\ B}_{\lambda\lambda'} = \sum_{fin.\ pols.} \mathcal{N}_\lambda \mathcal{N}^*_{\lambda'}; \qquad \rho^{decay\ \overline{B}}_{\mu\mu'} = \sum_{fin.\ pols.} \mathcal{N}_\mu \mathcal{N}^*_{\mu'}$$

where we denote the helicity of B with λ, λ' and the helicity of $\overline{B}$ with μ, μ'. The total cross section is then calculated from

$$\sum_{ext.\ pols.} |\mathcal{M}|^2_{\text{total}} = \sum_{\lambda,\mu,\lambda',\mu'.} \rho^{prod}_{\lambda\lambda',\mu\mu'} \rho^{decay\ B}_{\lambda'\lambda} \rho^{decay\ \overline{B}}_{\mu'\mu}.$$

In short, this means that in our process with two decays we have to sum over all possible helicities of the intermediate particles, then square the amplitudes and sum/average over the final/initial particles' helicities:

$$\sum_{ext.\ pols.} |\mathcal{M}|^2_{q\overline{q}\to l\overline{X}\,\bar{l}X} = \delta\left(s_{l\overline{X}} - M_B^2\right)\delta\left(s_{\bar{l}X} - M_B^2\right) \cdot \left(\frac{\pi}{M_B\Gamma_B}\right)^2 \times \sum_{\lambda(q,\overline{q},l,\bar{l},X,\overline{X})} \left| \sum_{\lambda(B),\mu(\overline{B})} \mathcal{M}_{q\overline{q}\to B\overline{B}}\, \mathcal{N}_{B\to l\overline{X}} \mathcal{N}_{\overline{B}\to \bar{l}X} \right|^2 \tag{5.8}$$

where $\lambda(\ldots)$ denote the helicities of the particular particle we sum over. Here one can see that interference terms are entering the calculation, giving us the correct treatment of polarization effects.

Calculation with explicit helicity spinors

For the calculation of the production and decays we use explicit helicity spinors and we follow the notations and definitions in [43,76,77] for our calculation which we summarize in appendix C.1. As a representative example, we will show the calculation and the corresponding density matrices for the example (SFS). Let us start with the production process (SF). The scalar coupling implies that we only have the possibility for the initial quarks to be both either left (ll) or right (rr) handed. The (lr) or (rl) combinations vanish[3]. We have the matrix elements

$$\mathcal{M}_{ll,\lambda(B)\mu(\overline{B})} = 2iA_l \begin{pmatrix} B^- - B^+\sqrt{1-x} & 0 \\ 0 & B^- + B^+\sqrt{1-x} \end{pmatrix} \tag{5.9a}$$

$$\mathcal{M}_{rr,\lambda(B)\mu(\overline{B})} = -2iA_r \begin{pmatrix} B^- - B^+\sqrt{1-x} & 0 \\ 0 & B^- + B^+\sqrt{1-x} \end{pmatrix} \tag{5.9b}$$

$$\mathcal{M}_{lr} = 0; \quad \mathcal{M}_{rl} = 0; \tag{5.9c}$$

where we use $B^- = (b_l - b_r)$ and $B^+ = (b_l + b_r)$. The decays are

$$\mathcal{N}(B \to l^- S)_{(\lambda(B),\lambda(l^-))} = r \cdot \begin{pmatrix} \cos\left(\frac{\theta_1}{2}\right) & \frac{c_l}{c_r}\sin\left(\frac{\theta_1}{2}\right) \\ -e^{i\phi_1}\sin\left(\frac{\theta_1}{2}\right) & \frac{c_l}{c_r}e^{i\phi_1}\cos\left(\frac{\theta_1}{2}\right) \end{pmatrix} \tag{5.10}$$

[3] In the (VF) process, it is the other way around, since here we do not have a sign flip of the hermitian conjugated process due to the vector-like coupling.

$$\mathcal{N}(\overline{B} \to l^+ S)_{(\mu(\overline{B}),\lambda(l^+))} = r \cdot \begin{pmatrix} -e^{i\phi_2}\cos\left(\frac{\theta_2}{2}\right) & -\frac{c_l}{c_r}e^{i\phi_2}\sin\left(\frac{\theta_2}{2}\right) \\ \sin\left(\frac{\theta_2}{2}\right) & -\frac{c_l}{c_r}\cos\left(\frac{\theta_2}{2}\right) \end{pmatrix} \tag{5.11}$$

with $r = c_r e^{-\frac{i\phi_1}{2}} M_B\sqrt{1-y}$. The entries for both are

$$\left(\begin{array}{c|c} B_L\ l_L & B_L\ l_R \\ \hline B_R\ l_L & B_R\ l_R \end{array}\right). \tag{5.12}$$

Now we have to first sum over the B particles' polarization, as in equation 5.8 and after squaring, one can also sum over the external polarizations. In this case, we have only (ll) and (rr) for the quark helicities, but in general one has also to sum over the C particles' polarization.
Depending on which particle is the intermediate one, the dimension of the matrix in equation 5.9 is either 1×1 (scalar), 2×2 (fermion) or 3×3 (massive vector). The density matrix for the two decaying fermions involved has 2×2 entries for each decay, while for the vector boson we have $3{\times}3$ possibilities. We show the full summed and squared result for (SFS) together with the other spin scenarios in Section 5.2.

5.1.3 Definition of $\mathcal{C}_B$

A. Barr's variable $\mathcal{C}_B$ is defined as [2]

$$\mathcal{C}_B := \tanh\left(\frac{\eta_1 - \eta_2}{2}\right) \tag{5.13}$$

where η_i are the pseudorapidities of the two leptons in the Lab frame. Since we take the difference of these two rapidities, $\mathcal{C}_B$ in this definition is z-boost invariant since $\eta_i \to \eta_i + \eta_z$ and the two η_z cancel in the sum. In the rest frame of particle B, the pseudorapidites of C are defined as

$$\eta_i = \frac{1}{2}\log\left(\frac{E^i + p_z^i}{E^i - p_z^i}\right) = \frac{1}{2}\log\left(\frac{1+\cos\theta_i}{1-\cos\theta_i}\right). \tag{5.14}$$

After boosting and rotating them into the Lab frame they are

$$\eta_1 = \frac{1}{2} \times \log\left(\frac{\sinh\lambda(\cos\theta_1 + \cos\theta^*) + \cosh\lambda(1 + \cos\theta_1\cos\theta^*) - \sin\theta_1\sin\theta^*\cos\varphi_1}{\sinh\lambda(\cos\theta_1 - \cos\theta^*) + \cosh\lambda(1 - \cos\theta_1\cos\theta^*) + \sin\theta_1\sin\theta^*\cos\varphi_1}\right)$$

$$\eta_2 = \frac{1}{2} \times \log\left(\frac{\sinh\lambda(\cos\theta_2 + \cos\theta^*) - \cosh\lambda(\cos\theta_2\cos\theta^* + 1) + \sin\theta_2\sin\theta^*\cos\varphi_2}{\sinh\lambda(\cos\theta_2 - \cos\theta^*) + \cosh\lambda(\cos\theta_2\cos\theta^* - 1) - \sin\theta_2\sin\theta^*\cos\varphi_2}\right)$$

where we express the variable in terms of θ_i, ϕ_i, θ^* and ϕ^* as they are defined in equation 5.7 and $\cosh\lambda$ is the boost of the particle B

$$\cosh\lambda = \frac{\sqrt{\hat{s}}}{2M_B}. \tag{5.15}$$

We denote the energy squared of the incoming partons with $\hat{s}$ whereas the total hadronic energy squared is s. In the specific frames of equation 5.7, the variable becomes

$$\mathcal{C}_B = \frac{\sqrt{f_2 - 1} - \sqrt{f_1 - 1}}{\sqrt{f_2 - 1} + \sqrt{f_1 - 1}} \tag{5.16a}$$

$$f_1 = \frac{2\cosh(\eta_2 - \lambda)}{\cosh(\eta_2 - \lambda) + \cos\phi_2 \sin\theta^* - \cos\theta^* \sinh(\eta_2 - \lambda)} \tag{5.16b}$$

$$f_2 = \frac{2\cosh(\eta_1 + \lambda)}{\cosh(\eta_1 + \lambda) + \cos\phi_1 \sin\theta^* - \cos\theta^* \sinh(\eta_1 + \lambda)}. \tag{5.16c}$$

In the case where the boost $\cosh\lambda = 1$, and $\sqrt{\hat{s}} = 2M_B$, the particles B are produced at TH and $\mathcal{C}_B$ simplifies to

$$\mathcal{C}_B^{TH} = \tanh\left(\frac{\eta_1^{TH} - \eta_2^{TH}}{2}\right). \tag{5.17}$$

where the rapidities are

$$\eta_i^{TH} = \frac{1}{2}\log\left[\cot^2\left(\frac{\theta_i}{2}\right)\right]; \quad i = 1, 2 \tag{5.18}$$

and where we have used that the definition of $\mathcal{C}_B$ is independent of θ^* at TH.
In the high energy limit however, the expression in equation 5.13 becomes the angle of the parents in the CoM frame

$$\mathcal{C}_B^{HE} \to \cos\theta^*. \tag{5.19}$$

This property can be used to distinguish Susy and UED at the LHC if the energy $\sqrt{\hat{s}}$ is high enough in comparison to the involved particles' masses [2,73] in which case we recover the shapes as in equation 5.2, depicted in the left side of figure 5.2.
We are instead interested in the case where the B particles are not sufficiently light so that s= 7...14 TeV does not play the role of the high energy limit where the $\mathcal{C}_B$ distribution approaches $\cos\theta^*$ as in equation 5.19. We discuss the correlation of $\mathcal{C}_B$ and $\cos\theta^*$ for the simple phase space (PS) distribution where the matrix element is just 1 (so no spin effects) in order to study the transition from the TH limit to the high energy limit.
In figure 5.3 we show this correlation for four different parton energies $\sqrt{\hat{s}}$ and a particle mass $M_B = 150$ GeV. The highest correlation is achieved when all events are on the bisector. The first plot shows the correlation at $\sqrt{\hat{s}} = 1$ TeV, where there is already a good correlation present between $\cos\theta^*$ and $\mathcal{C}_B$. For slightly higher energies, the correlation becomes even better which is visible by the shrinking of the blue oval region. At $\sqrt{\hat{s}} \to \infty$ case, all events are on the bisector.
In figure 5.4 we show this correlation for a particle with higher mass $M_B = 500$ GeV. The first plot shows again the correlation at $\sqrt{\hat{s}} = 1$ TeV which is in this

case the TH limit. Here there is no correlation present between $\cos\theta^*$ and $\mathcal{C}_B$. For slightly higher energies, the correlation becomes a little better which is visible by the shrinking of the blue region to an oval. However, only at $\sqrt{\hat{s}} > 5$ TeV, a good correlation is achieved and for the $\sqrt{\hat{s}} \to \infty$ case, all events are on the bisector.
We see that the correlation at reasonable energies is much better for small masses since the energy/mass ratio is larger. Only at a partonic energy of $\sqrt{\hat{s}} > 5$ TeV in the case of $M_B = 500$ GeV, the correlation is comparable to the correlation for the low mass M_B at 1 TeV. We therefore want to emphasize that the energy/mass ratio determines the correlation and that for higher masses, one cannot simply anticipate the HE result as in equation 5.2.

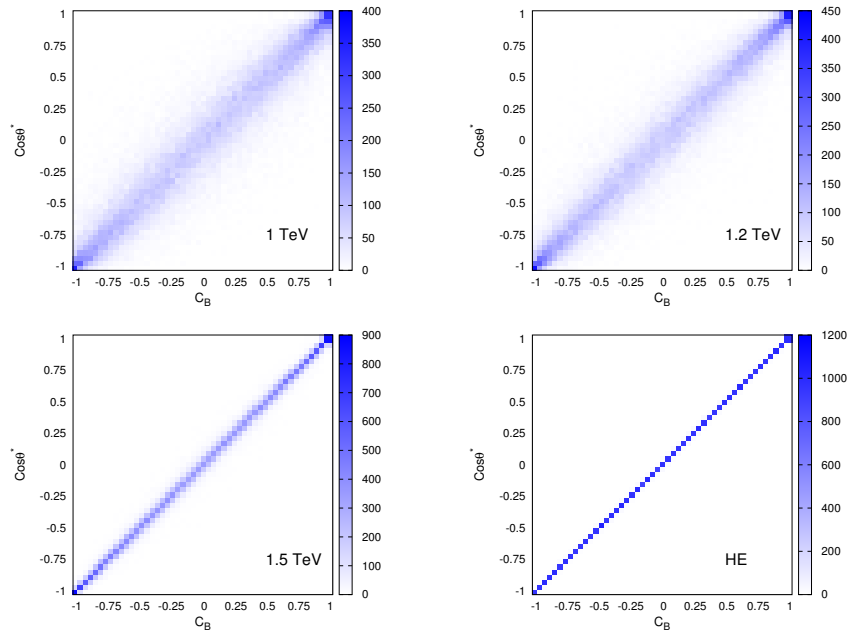

Figure 5.3: Correlation between $\cos\theta^*$ and $\mathcal{C}_B$ for different parton energies $\sqrt{\hat{s}}$. We choose $\sqrt{\hat{s}} = 1,\ 1.2,\ 1.5$ TeV and $\sqrt{\hat{s}} \to \infty$. These plots are done for $M_B = 0.15$ TeV with 50000 events for pure phase space without spin effects. The highest correlation is achieved when all events are on the bisector.

Changing integration variables

For completeness we will give our notation for rewriting the full phase space integral in terms of $\mathcal{C}_B$. We therefore introduce a $1 = \int d\mathcal{C}_B\ \delta(\mathcal{C}_B - \mathcal{C}_B[\theta^*, \phi^*, \theta_i, \phi_i])$ in the phase space integral where $\mathcal{C}_B[\ldots]$ stands for the definition of the $\mathcal{C}_B$ in equation 5.16 with rapidities expressed in angles. By integrating out the angular

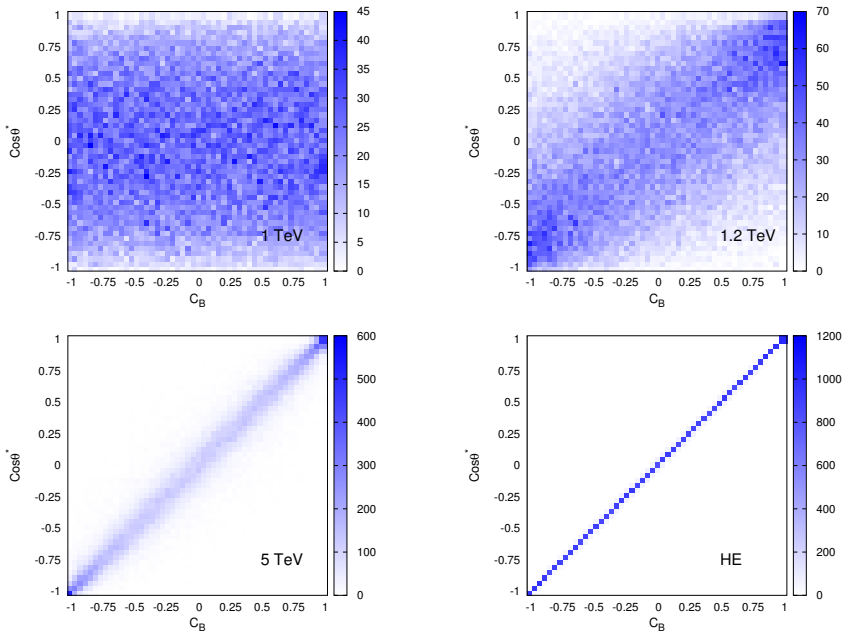

Figure 5.4: Correlation between $\cos\theta^*$ and $\mathcal{C}_B$ for different parton energies $\sqrt{\hat{s}}$. We choose the TH limit ($\sqrt{\hat{s}} = 2 \cdot M_B$), at the energy defined at the peak mass (1.2 TeV), at intermediate energy ($\sqrt{\hat{s}} = 5$ TeV) and at $\sqrt{\hat{s}} \to \infty$. These plots are done for $M_B = 0.5$ TeV with 50000 events for pure phase space without spin effects.

components we can express the phase space integral in terms of the $\mathcal{C}_B$

$$\begin{aligned} \mathrm{d}\Gamma &= \underbrace{\int \mathrm{d}\Omega_1 \; \mathrm{d}\Omega_2 \; \mathrm{d}\Omega}_{:=\mathrm{d}\Omega_c} \int \mathrm{d}\mathcal{C}_B \; \delta(\mathcal{C}_B - \mathcal{C}_B[\theta^*, \phi^*, \theta_i, \phi_i]) \sum_i C_i \cdot A_i \\ &= \int \mathrm{d}\mathcal{C}_B \quad C_i \cdot J_i \end{aligned} \tag{5.20}$$

Here we have split each term of the squared matrix element into a part A_i depending solely on angles, and a part C_i solely depending on masses and couplings. Integrating out all remaining angles and rewriting the angular distributions in terms of $\mathcal{C}_B$ leads us to characteristic Jacobian factors J_i.

$\mathcal{C}_B$ at high energies

We will show here that the $\cos\theta^*$ distribution of the parent particles B can be recovered by $\mathcal{C}_B$ at high energies $\sqrt{s} \to \infty$. Let us rewrite $\mathcal{C}_B$ of equation 5.16 in terms of the angles θ_i

$$\begin{aligned} \mathcal{C}_B(\lambda) &= \tanh \left\{ \frac{1}{4} \times \right. \\ &\times \left(\log \left[\frac{(1 + \cos\theta_1 \cos\theta^*) \cosh\lambda + \cos\varphi_1 \sin\theta_1 \sin\theta^* - (\cos\theta_1 + \cos\theta^*) \sinh\lambda}{(\cos\theta_1 \cos\theta^* - 1) \cosh\lambda - \cos\varphi_1 \sin\theta_1 \sin\theta^* + (\cos\theta^* - \cos\theta_1) \sinh\lambda} \right] - \right. \end{aligned}$$

$$- \log \left[\frac{(1 + \cos\theta_2 \cos\theta^*) \cosh\lambda - \cos\varphi_2 \sin\theta_2 \sin\theta^* - (\cos\theta_2 + \cos\theta^*) \sinh\lambda}{(\cos\theta_2 \cos\theta^* - 1) \cosh\lambda + \cos\varphi_2 \sin\theta_2 \sin\theta^* - (\cos\theta_2 - \cos\theta^*) \sinh\lambda} \right] \Bigg) \Bigg\} .$$

We set $\cosh\lambda = \sqrt{\hat{s}}/(2M_B)$ and since $\hat{s} \gg (2M_B)^2$, we estimate $\cosh\lambda = \sinh\lambda = 1/\epsilon$ with $\epsilon \to 0$ when $\sqrt{\hat{s}} \to \infty$. The definition of $\mathcal{C}_B$ then simplifies to

$$\mathcal{C}_B(\epsilon) = \tanh \left\{ \frac{1}{4} \left(\log \left[-1 - \frac{2(1 + \cos\theta_1)}{(1 + \cos\theta_1)(-1 + \cos\theta^*) - \epsilon \cos\varphi_1 \sin\theta_1 \sin\theta^*} \right] \right.$$
$$\left. - \log \left[-1 + \frac{2(\cos\theta_2 - 1)}{(-1 + \cos\theta_2)(\cos\theta^* + 1) - \epsilon \cos\varphi_2 \sin\theta_2 \sin\theta^*} \right] \right) \Bigg\} \qquad (5.21)$$

For $\epsilon \to 0$, we see that the terms in the denominator vanish and we are left with

$$\mathcal{C}_B^{HE} = \tanh \left\{ \frac{1}{4} \left(\log \left[\frac{1 + \cos\theta^*}{1 - \cos\theta^*} \right] - \log \left[\frac{1 - \cos\theta^*}{1 + \cos\theta^*} \right] \right) \right\} = \cos\theta^* \qquad (5.22)$$

which is just the angle between one of the parents and the beam axis. This angle is sensitive to the spin of the particles A and B and hence, in this limit, $\mathcal{C}_B$ can in principle be used to determine those particles' spin.

5.1.4 Further strategy

We saw in figure 5.4, that for a heavy B particle, the correlation of $\mathcal{C}_B$ and $\cos\theta^*$ is not as promising as investigated in the literature and therefore is not as useful as assumed for distinguishing between Susy and UED. This is why we will pursue the question whether there is a similar simple dependence as in equations 5.2 of the differential distributions of $\mathcal{C}_B$ for lower energies that we find more suitable for an LHC process. Since we can now calculate the $\mathcal{C}_B$ distribution for phase space (PS), we also know that everything which deviates from this form has to be a spin effect.
Our central questions are

1. Are there spin dependences of the $\mathcal{C}_B$ distributions for heavier particles B, in which case we cannot take the limit $\mathcal{C}_B = \cos\theta^*$ (HE limit)?

2. Is there a similar simple dependence for the $\mathcal{C}_B$ distributions as in the HE limit in equations 5.2?

3. How do different mass and coupling choices affect the distributions?

4. Can different spin scenarios look alike and fake each other?

To answer these questions we have to split the problem into several sub-problems.
• Fixed $\sqrt{\hat{s}}$ approach
As we saw in the discussion on equation 5.2, the HE limit is simply obtained by taking $s \to \infty$ so that the results in these equations are just the $2 \to 2$ results. In the low energy region, we also have the influence of the final particles l, C. Since already the PS distribution depends on $\sqrt{\hat{s}}$, we need to know or at least estimate the energy at which the process takes place. Since we are dealing with a

hadron collider, the energy $\sqrt{\hat{s}}$ is solely dictated by the PDFs. We therefore need to disentangle the PDF and thus the energy dependence of the $\mathcal{C}_B$ distribution from the spin effect.
The approximation is motivated by the fact that for heavier B particles in the case of an off-shell s-channel particle A (e.g. a Z or a Higgs boson), the main production takes place at energies slightly above TH. Therefore we take a suitable fixed $\sqrt{\hat{s}}$ as the energy of the main production. This means we mimic the full PDF result by choosing an appropriate fixed energy. We will dedicate Section 5.3.1 to this topic. Once we have a good estimate for fixed $\sqrt{\hat{s}}$, we can investigate the influences of masses and couplings on the distributions at this particular energy and how well the $\mathcal{C}_B$ discriminates between different spin scenarios at this fixed $\sqrt{\hat{s}}$.
• TH limit
As it turns out, it is not possible to derive analytically a full $\mathcal{C}_B$ distribution by performing the integration of equation 5.20 viable for all energies $\sqrt{\hat{s}}$ as one would have hoped. Let us first see what we need to do in order to derive the integral in equation 5.20. We have the integral

$$\int d\cos\theta^* \; d\phi^* \; d\cos\theta_1 \; d\phi_1 \; d\cos\theta_2 \; d\phi_2 \;\; \delta(\mathcal{C}_B - \mathcal{C}_B[\phi^*, \theta^*, \phi_1, \theta_1, \phi_2, \theta_2]). \quad (5.23)$$

We integrate over the angles $d\cos\theta^* d\phi^*$, $d\cos\theta_1 d\phi_1$, $d\cos\theta_2 d\phi_2$ so that we are left with the integral $d\mathcal{C}_B$. This is usually done by rewriting the δ distribution using

$$\int_{-\infty}^{+\infty} dx \; f(x) \; \delta(g(x)) = \sum_i \int_{-\infty}^{+\infty} dx f(x) \frac{\delta(x - x_i)}{|g'(x_i)|} = \sum_i \frac{f(x_i)}{|g'(x_i)|}, \quad (5.24)$$

where $g(x) = \mathcal{C}_B - \mathcal{C}_B[\phi^*, \theta^*, \phi_1, \theta_1, \phi_2, \theta_2]$. We have to sum over all zeros x_i of the function $g(x)$. The integration variable x stands for any of the angles $\phi^*, \theta^*, \phi_1, \theta_1, \phi_2, \theta_2$. One has to solve equation 5.16 for one of the angles in order to perform the rest of the integrals which could not be done analytically due to the involved structure of the terms. However, it is possible investigate the analytic forms in the limit where $x = (2M_B)^2/\hat{s} \approx 1$, close to threshold (TH) where we can perform this integration and determine analytically the Jacobian factors of equation 5.20. Since we are not completely at TH, we will expand the full results around TH to see how the influence of masses and couplings changes at higher orders.

In the next section we will summarize our analytic results for

- $2 \to 2$: production processes
- $2 \to 4$: full squared matrix elements (only short results)
- $2 \to 4$: squared matrix elements in the TH limit
- Jacobian factors of the $\mathcal{C}_B$ at TH

- $2 \to 4$ differential distributions in terms of $\mathcal{C}_B$ at TH
- $2 \to 4$ differential distributions in terms of $\mathcal{C}_B$ expanded around TH.

In the penultimate section, 5.4, we compare for the fixed $\sqrt{\hat{s}}$ approach the different spin scenarios in different mass ranges and coupling ranges and test the discrimination power of $\mathcal{C}_B$.
We want to be able to compare the distributions from our calculation fast and independently with the simulated CalcHep/CompHep [78, 79] results including PDFs. Therefore we have to calculate the integral in equation 5.20. We do this via Monte Carlo integration since methods which use an explicit δ-distribution as one would do for an analytic result are not reliable enough. Since we want to use the squared matrix elements derived before, we integrate out this δ-distribution via a Monte Carlo method. We start by randomly choosing values for $\phi^*, \cos\theta^*, \phi_1, \cos\theta_1, \phi_2, \cos\theta_2$ in their particular ranges and calculate at this point $\mathcal{C}_B$ corresponding to these random values. If we are interested in the pure phase space, we just have to write this "event" in a histogram and repeat the procedure. For the integration of the squared matrix elements, we weight the events filled in the histogram with the value of the squared matrix element. Alternatively, one can enter the event into a histogram with a probability proportional to this weight.

5.2 Analytic results

We summarize here the analytic results which we will investigate later and which we have derived as explained in the previous section. First we will show the $2 \to 2$ squared matrix elements of the production, which are important if one wants to see what the distribution looks like at high energies. Then we show, if expressible in a short form, the full $2 \to 4$ squared matrix elements followed by the $2 \to 4$ matrix elements at TH. After that we derive the Jacobians from equation 5.20 in the TH limit and give the corresponding TH results for the $2 \to 4$ processes.

5.2.1 Squared matrix elements for $2 \to 2$

We summarize here the squared matrix elements for the $2 \to 2$ processes which depend on the $\cos\theta^*$. Since we are only interested in the angular dependences, we leave out global normalization factors:

$$|\mathcal{M}|^2_{(SS)} \propto 1 \tag{5.25a}$$

$$|\mathcal{M}|^2_{(SV)} \propto 1 \tag{5.25b}$$

$$|\mathcal{M}|^2_{(SF)} \propto 1 \tag{5.25c}$$

$$|\mathcal{M}|^2_{(VS)} \propto 1 - \cos^2\theta^* \tag{5.25d}$$

$$|\mathcal{M}|^2_{(VF)} \propto 1 + 2\alpha\beta\frac{\sqrt{1-x}}{x\sqrt{1-\beta^2}+1}\cos\theta^* + \frac{1-x}{x\sqrt{1-\beta^2}+1}\cos^2\theta^* \tag{5.25e}$$

$$|\mathcal{M}|^2_{(VV)} \propto 1 + \left(-1 + \frac{16x}{4+3x(4+x)}\right)\cos^2\theta^* \tag{5.25f}$$

where $x = (2M_B)^2/\hat{s}$. We see that (VS), which is the Susy case, has its characteristic $\sin^2\theta^*$ form while UED (VF) has $1 + const\cdot\cos^2\theta^*$ for fixed $\hat{s}$. However, we also see that the first three distributions are all PS (here: constant) due to the s-channel scalar and that (VV) also has a $1 + const\cdot\cos^2\theta^*$ distribution for fixed $\hat{s}$. Depending on these constants which are functions of mass, energy and/or coupling strength, (VV) and (VF) can look alike. This shows, that although the Susy (VS) and UED (VF) cases have distinct shapes, they could still be mimicked by the others.

5.2.2 Complete squared matrix elements for $2 \to 4$

The squared matrix elements for the full $2 \to 4$ processes (including NWA via helicity methods) are

$$\begin{aligned}
|\mathcal{M}|^2_{(SFS)} \propto\ & 2 - x\left(1+\sqrt{1-\beta^2}\right) + 2\sqrt{1-x}\beta\gamma(\cos\theta_1+\cos\theta_2) \\
& + \left(x - 2\sqrt{1-\beta^2} + x\sqrt{1-\beta^2}\right)\gamma^2\cos(\phi_1-\phi_2)\sin\theta_1\sin\theta_2 \\
& - \left(x - 2 + x\sqrt{1-\beta^2}\right)\gamma^2\cos\theta_1\cos\theta_2
\end{aligned} \tag{5.26a}$$

$$|\mathcal{M}|^2_{(VSF)} \propto 1 - \cos^2\theta^* \tag{5.26b}$$

$$|\mathcal{M}|^2_{(VFS)} \propto 1 + \alpha\gamma(\cos\theta_1 - \cos\theta_2) - \gamma^2\cos\theta_1\cos\theta_2 \tag{5.26c}$$

$$\begin{aligned}
|\mathcal{M}|^2_{(SVF)} \propto\ & 128\left(\cos^2\theta_1+\cos^2\theta_2\right)(1-x)(1-\tau_c)^3 \\
& - (32(\tau_c-1)^2(4+x(x-4+2x\tau_c))) \\
& - (32\cos\theta_1^2\cos\theta_2^2(x-2)^2(1-\tau_c)^4) \\
& + x^2 64\cos\theta_1\cos\theta_2(1-\tau_c)^2\gamma^2 - 32\cos\phi_{12}^2(1-\tau_c)^4\sin^2\theta_1\sin^2\theta_2 \\
& - x(64\cos\phi_{12}(x-2)(1-\tau_c)^2\left((1-\tau_c)^2\cos\theta_1\cos\theta_2-\gamma^2\right)\sin\theta_1\sin\theta_2)
\end{aligned} \tag{5.26d}$$

$$|\mathcal{M}|^2_{(SSF)} \propto 1 \tag{5.26e}$$

$$\begin{aligned}
|\mathcal{M}|^2_{(SFV)} \propto\ & 32\cos\theta_1\cos\theta_2(1-2\tau_c)^2(1-\tau_c)\left(-2+x+x\sqrt{1-\beta^2}\right)\gamma^2 \\
& + \frac{32(\tau_c-1)}{\sqrt{1-\beta}}\left(\left(2(\beta-1)\sqrt{1+\beta} + x\left(\sqrt{1-\beta}+(1-\beta)\sqrt{1+\beta}\right)\right)\right. \\
& \left.\times\gamma^2(1-2\tau_c)^2\cos(\phi_1-\phi_2)\sin\theta_1\sin\theta_2\right) \\
& + 32(1-\tau_c)(1+2\tau_c)^2\left(x-2+x\sqrt{1-\beta^2}\right) \\
& + 64(\cos\theta_1+\cos\theta_2)\sqrt{1-x}(1-\tau_c)(1-4\tau_c^2)\beta\gamma
\end{aligned} \tag{5.26f}$$

with $\phi_{12} = \phi_1 + \phi_2$. We do not show the results for (VVF) and (VFV) since their form is long and is not very useful for clarification. Every term that has an angular dependence is a deviation from PS and thus gives us spin effects. We see that the impact of these spin effects depends on the masses τ_c and the couplings

β, γ from equation 5.5. E.g. for the case of equation 5.26e, there is no spin structure at all. The (VSF) case in equation 5.26b has already here the $cos^2\theta^*$ dependence of equation 5.25d.

5.2.3 TH results for $2 \to 4$ processes

We summarize here the results for $2 \to 4$ at TH:

$$|\mathcal{M}|^{2\ TH}_{(SFS)} \propto 1 + \gamma^2(\cos\theta_1 \cos\theta_2 + \cos(\phi_1 - \phi_2) \sin\theta_1 \sin\theta_2) \tag{5.27a}$$

$$|\mathcal{M}|^{2\ TH}_{(SFV)} \propto 1 + \gamma^2 \frac{(1-2\tau_c)^2}{(1+2\tau_c)^2} (\cos(\phi_1 - \phi_2) \sin\theta_1 \sin\theta_2 + \cos\theta_1 \cos\theta_2) \tag{5.27b}$$

$$|\mathcal{M}|^{2\ TH}_{(VFS)} \propto 1 + \alpha\gamma(\cos\theta_1 - \cos\theta_2) - \gamma^2 \cos\theta_1 \cos\theta_2 \tag{5.27c}$$

$$|\mathcal{M}|^{2\ TH}_{(VFV)} \propto 1 - \cos\theta_1 \cos\theta_2 \frac{(1-2\tau_c)^2}{(1+2\tau_c)^2} - \alpha\gamma\,(\cos\theta_2 - \cos\theta_1)\,\frac{(1-2\tau_c)}{(1+2\tau_c)} \tag{5.27d}$$

$$|\mathcal{M}|^{2\ TH}_{(SSF)} \propto 1 \tag{5.27e}$$

$$|\mathcal{M}|^{2\ TH}_{(VSF)} \propto 1 \tag{5.27f}$$

$$\begin{aligned} |\mathcal{M}|^{2\ TH}_{(SVF)} \propto\ & 1 + \frac{2\gamma^2}{1+2\tau_c} (\cos\theta_1 \cos\theta_2 - \cos(\phi_1 + \phi_2) \sin\theta_1 \sin\theta_2) \\ & + \frac{(1-\tau_c)^2}{1+2\tau_c} (\cos\theta_1 \cos\theta_2 - \cos(\phi_1 + \phi_2) \sin\theta_1 \sin\theta_2)^2 \end{aligned} \tag{5.27g}$$

$$\begin{aligned} |\mathcal{M}|^{2\ TH}_{(VVF)} \propto\ & \frac{2(1+\tau_c)}{\tau_c} - (1-\tau_c)(\cos^2\theta_1 + \cos^2\theta_2) \\ & - \frac{2(1-\tau_c)^2}{\tau_c} \cos^2\theta_1 \cos^2\theta_2 \\ & + \frac{2\alpha\gamma}{\tau_c} (\cos\theta_1 + \cos\theta_2)\,(1 - \cos\theta_1 \cos\theta_2(1-\tau_c)) \end{aligned} \tag{5.27h}$$

5.2.4 J factors at TH

From equations 5.27 we see that the investigated matrix elements at TH are only functions of certain angular combinations,

$$\begin{aligned} |\mathcal{M}|^2 = \{ & C_0 + C_1\,(\cos\theta_1 - \cos\theta_2) + C_2 \cos\theta_1 \cos\theta_2 \\ & + C_3 \sin\theta_1 \sin\theta_2 \cos(\phi_1 - \phi_2) + C_4 f_{\theta_1\theta_2\phi} + C_5 \cos^2\theta_1 \cos^2\theta_2 \\ & + C_6 f^2_{\theta_1\theta_2\phi} + C_7(\cos^2\theta_1 + \cos^2\theta_2) \\ & + C_8(\cos\theta_1 + \cos\theta_2)(1 - a \cdot \cos\theta_1 \cos\theta_2)\} \end{aligned} \tag{5.28}$$

with

$$f_{\theta_1\theta_2\phi} = (\cos\theta_1 \cos\theta_2 - \cos\phi_{12} \sin\theta_1 \sin\theta_2). \tag{5.29}$$

The "a" in the last line of equation 5.28 stands for a process dependent prefactor which is not important at this point since the angular dependence belonging to C_8 vanishes after being rewritten in $\mathcal{C}_B$. The prefactors C_i are only functions of

the masses and the couplings as can be seen in equations 5.27. The coefficients $C_{4/5}$ only appear in the context of (SVF) where all other coefficients except for C_0 are 0. We can now rewrite the phase space integral for these single factors A_i in terms of $\mathcal{C}_B$ by introducing the delta function $\delta(\mathcal{C}_B - \mathcal{C}_B[\theta^*, \phi^*, \theta_i, \phi_i])$ with the definition of $\mathcal{C}_B$ at TH in equation 5.17. By integrating out the angular components which are not in the TH definition of $\mathcal{C}_B$ given in equation 5.17 we can express the phase space integral in terms of $\mathcal{C}_B$

$$\begin{aligned}\sigma^{TH} &= \underbrace{\int \mathrm{d}\Omega_1 \; \mathrm{d}\Omega_2 \; \mathrm{d}\Omega}_{:=\mathrm{d}\Omega_c} \; \mathrm{d}\mathcal{C}_B^{TH} \; \delta(\mathcal{C}_B^{TH} - \mathcal{C}_B^{TH}[\theta_i]) \sum_i C_i^{TH} \cdot A_i^{TH} \\ &= \int \mathrm{d}\mathcal{C}_B^{TH} \quad C_i^{TH} \cdot J_i^{TH}. \end{aligned} \tag{5.30}$$

The ϕ_i angles can be integrated out independently since the $\mathcal{C}_B$ in equation 5.17 does not depend explicitely on them. The remaining angles θ_1, θ_2 are rewritten in terms of the rapidities η_1, η_2 (equation 5.14)

$$\mathrm{d}\theta_i \sin\theta_i = \mathrm{d}\eta_i \; \mathrm{sech}^2\eta_i \tag{5.31}$$

and are now integrated out so that we can calculate the Jacobian factors J_i^{TH} from equation 5.30. We will show this in the following for some angular functions and then, starting from those, define normalized Jacobian factors and rewrite the differential cross section as a function of $\mathcal{C}_B$.
Depending on the angular combinations, we get different Jacobian factors J_i^{TH} which we show in the following. We have normalized J_0^N with $\int_{-1}^{1} d\mathcal{C}_B J_0^N = 1$. We will in the following denote with J_i^N the normalized TH Jacobian factors and suppress the additional index "TH" for simplicity. Consequently, the coefficients C_i of equations 5.27 have to be divided by a factor of 4 and the integrals of the non-vanishing Jacobians are then

$$\int_{-1}^{1} d\mathcal{C}_B \; J_2^N = 0; \quad \int_{-1}^{1} d\mathcal{C}_B \; J_5^N = 4/9; \quad \int_{-1}^{1} d\mathcal{C}_B \; J_6^N = 4/3; \quad \int_{-1}^{1} d\mathcal{C}_B \; J_7^N = 8/3.$$

We will make some comments on the calculation of particular terms in the following. The J_1 term which belongs to $(\cos\theta_1 - \cos\theta_2)$ is

$$J_1 = \frac{(1-\mathcal{C}_B^2)}{4\mathcal{C}_B^4}\left(-12(\mathcal{C}_B^3 + \mathcal{C}_B) + 2(3\mathcal{C}_B^4 + 2\mathcal{C}_B^2 + 3) \cdot \log\left(\frac{1+\mathcal{C}_B}{1-\mathcal{C}_B}\right)\right).$$

However, this result is antisymmetric for $\mathcal{C}_B \to -\mathcal{C}_B$ and thus after symmetrizing, this contribution vanishes and $J_1 = 0$. This means that, although the matrix element can have a contribution proportional to $(\cos\theta_1 - \cos\theta_2)$, it does not contribute in terms of $\mathcal{C}_B$. J_3 is automatically 0 after integrating out the ϕ_i angles

$$J_3 = \int \mathrm{d}\Omega_c \; \mathrm{d}\mathcal{C}_B^{TH} \; \delta(\mathcal{C}_B^{TH} - \mathcal{C}_B^{TH}[\theta_i])(\cos(\phi_1 - \phi_2)\sin\theta_1 \sin\theta_2) = 0.$$

For the integration of $A_4 = f_{\theta_1\theta_2\phi}$ we have

$$\begin{aligned} J_4 &= \int \mathrm{d}\Omega_c \; \mathrm{d}\mathcal{C}_B^{TH} \; \delta(\mathcal{C}_B^{TH} - \mathcal{C}_B^{TH}[\theta_i])(\cos\theta_1\cos\theta_2 - \cos\phi_{12}\sin\theta_1\sin\theta_2) \\ &= \int \mathrm{d}\Omega_c \; \mathrm{d}\mathcal{C}_B \; \delta(\mathcal{C}_B^{TH} - \mathcal{C}_B^{TH}[\theta_i])(\cos\theta_1\cos\theta_2) = J_2 \end{aligned}$$

since again the ϕ_i integration gives 0 and the first term is just the same as J_2. For J_6 we also have to rewrite the angular dependence $A_6 = f^2_{\theta_1\theta_2\phi}$:

$$\begin{aligned} \mathrm{d}\Omega_c A_6 &= \int \mathrm{d}\Omega_c(\cos\theta_1\cos\theta_2 - \cos\phi_{12}\sin\theta_1\sin\theta_2)^2 \\ &= \int \mathrm{d}\Omega_c \cos^2\theta_1\cos^2\theta_2 - 2\cos\theta_1\cos\theta_2\cos(\phi_1-\phi_2)\sin\theta_1\sin\theta_2 \\ &\quad + (\cos\phi_{12}\sin\theta_1\sin\theta_2)^2 \\ &= \int \mathrm{d}\Omega_c \left(\cos^2\theta_1\cos^2\theta_2 + (\cos\phi_{12}\sin\theta_1\sin\theta_2)^2\right) \\ &= \int \mathrm{d}\eta_1\mathrm{d}\eta_2 \mathrm{sech}^2\eta_1\mathrm{sech}^2\eta_2 \left(2\sinh^2\eta_1\sinh^2\eta_2 + \cosh^2\eta_2\cosh^2\eta_2\right) \\ J_6^N &= \frac{1-\mathcal{C}_B^2}{48\mathcal{C}_B^7}\left(-2\mathcal{C}_B(45\mathcal{C}_B^8 + 22\mathcal{C}_B^4 + 45)\right. \\ &\quad \left. +3(15\mathcal{C}_B^{10} - 5\mathcal{C}_B^8 + 6\mathcal{C}_B^6 + 6\mathcal{C}_B^4 - 5\mathcal{C}_B^2 + 15)\log\left(\frac{1+\mathcal{C}_B}{1-\mathcal{C}_B}\right)\right). \end{aligned}$$

We can now summarize all factors which are normalized as discussed above

$$J_0^N = \frac{1-\mathcal{C}_B^2}{4\mathcal{C}_B^3}\left(-2\mathcal{C}_B + (1+\mathcal{C}_B^2)\log\left(\frac{1+\mathcal{C}_B}{1-\mathcal{C}_B}\right)\right) \tag{5.32a}$$

$$J_1 = J_3 = J_8 = 0 \tag{5.32b}$$

$$\begin{aligned} J_2^N = \frac{1-\mathcal{C}_B^2}{4\mathcal{C}_B^5}&\left(2\mathcal{C}_B(3\mathcal{C}_B^4 + 2\mathcal{C}_B^2 + 3)\right. \\ &\left. -(3\mathcal{C}_B^6 + \mathcal{C}_B^4 + \mathcal{C}_B^2 + 3)\log\left(\frac{1+\mathcal{C}_B}{1-\mathcal{C}_B}\right)\right) = J_4^N \end{aligned} \tag{5.32c}$$

$$\begin{aligned} J_5^N = \frac{1-\mathcal{C}_B^2}{24\mathcal{C}_B^7}&\left(-2\mathcal{C}_B(15\mathcal{C}_B^8 + 8\mathcal{C}_B^6 + 10\mathcal{C}_B^4 + 8\mathcal{C}_B^2 + 15)\right. \\ &\left. +3(5\mathcal{C}_B^{10} + \mathcal{C}_B^8 + 2\mathcal{C}_B^6 + 2\mathcal{C}_B^4 + \mathcal{C}_B^2 + 5)\log\left(\frac{1+\mathcal{C}_B}{1-\mathcal{C}_B}\right)\right) \end{aligned} \tag{5.32d}$$

$$\begin{aligned} J_6^N = \frac{1-\mathcal{C}_B^2}{48\mathcal{C}_B^7}&\left(-2\mathcal{C}_B(45\mathcal{C}_B^8 + 22\mathcal{C}_B^4 + 45)\right. \\ &\left. +3(15\mathcal{C}_B^{10} - 5\mathcal{C}_B^8 + 6\mathcal{C}_B^6 + 6\mathcal{C}_B^4 - 5\mathcal{C}_B^2 + 15)\log\left(\frac{1+\mathcal{C}_B}{1-\mathcal{C}_B}\right)\right) \end{aligned} \tag{5.32e}$$

$$J_7^N = \frac{1}{3\mathcal{C}_B^5}\left(2\mathcal{C}_B(3\mathcal{C}_B^6 + \mathcal{C}_B^4 - \mathcal{C}_B^2 - 3) + 3(1-\mathcal{C}_B^8)\log\left(\frac{1+\mathcal{C}_B}{1-\mathcal{C}_B}\right)\right). \tag{5.32f}$$

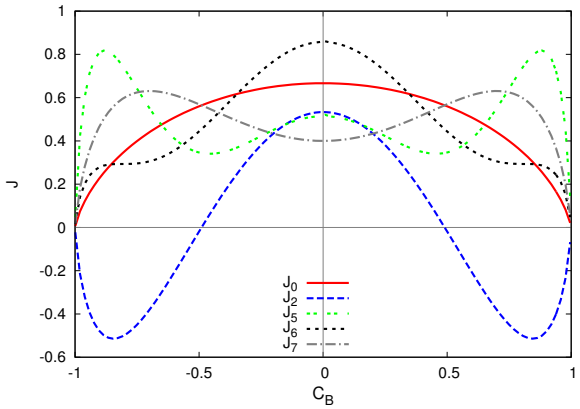

Figure 5.5: Plot of the J functions given in equation 5.32. The red/solid line is phase space at TH. Except for J_2, all functions are positive.

Note that $J_4^N = J_2^N$ and $J_1 = J_3 = J_8 = 0$. We plot these functions in figure 5.5. With the help of the Jacobians, we can now express the results for each process at TH in terms of the $\mathcal{C}_B$

$$\frac{1}{\sigma^{TH}} \frac{d\,\sigma_{TH}^{(VSF)}}{d\,\mathcal{C}_B} = J_0^N \tag{5.33a}$$

$$\frac{1}{\sigma^{TH}} \frac{d\,\sigma_{TH}^{(SFS)}}{d\,\mathcal{C}_B} = J_0^N + \frac{\gamma^2}{4} J_2^N \tag{5.33b}$$

$$\frac{1}{\sigma^{TH}} \frac{d\,\sigma_{TH}^{(SFV)}}{d\,\mathcal{C}_B} = J_0^N + \frac{\gamma^2}{4} \left(\frac{1-2\tau_c}{1+2\tau_c}\right)^2 J_2^N \tag{5.33c}$$

$$\frac{1}{\sigma^{TH}} \frac{d\,\sigma_{TH}^{(VFS)}}{d\,\mathcal{C}_B} = J_0^N - \frac{\gamma^2}{4} J_2^N \tag{5.33d}$$

$$\frac{1}{\sigma^{TH}} \frac{d\,\sigma_{TH}^{(VFV)}}{d\,\mathcal{C}_B} = J_0^N - \frac{\gamma^2}{4} \left(\frac{1-2\tau_c}{1+2\tau_c}\right)^2 J_2^N \tag{5.33e}$$

$$\frac{1}{\sigma^{TH}} \frac{d\,\sigma_{TH}^{(SSF)}}{d\,\mathcal{C}_B} = J_0^N \tag{5.33f}$$

$$\frac{1}{\sigma^{TH}} \frac{d\,\sigma_{TH}^{(SVF)}}{d\,\mathcal{C}_B} = \frac{3(2\tau_c+1)}{(\tau_c+2)^2} \left(J_0^N - \frac{\gamma^2}{2(1+2\tau_c)} J_2^N + \frac{(1-\tau_c)^2}{4(1+2\tau_c)} J_6^N\right) \tag{5.33g}$$

$$\frac{1}{\sigma^{TH}} \frac{d\,\sigma_{TH}^{(VVF)}}{d\,\mathcal{C}_B} = \frac{9(\tau_c+1)}{2(\tau_c+2)^2} \left(J_0^N - \frac{\tau_c(1-\tau_c)}{8(\tau_c+1)} J_7^N - \frac{(1-\tau_c)^2}{4(1+\tau_c)} J_5^N\right) \tag{5.33h}$$

where we have chosen the prefactors such that the integrals are normalized to 1. Note that these results are not depending on the specific form of the couplings α, β which turn out to be just overall factors. J_0^N is the analytic PS distribution of $\mathcal{C}_B$ at TH since it stems from the angle independent matrix element 1.
In Section 5.4 we will compare the full distributions with each other and investigate the influences of masses and couplings. As it turns out, we can identify the

corresponding behaviour of the distributions there to these TH formulas. However, one might assume that, if one leaves TH and turns on $\sqrt{\hat{s}} > (2M_B)^2$, the distributions might change rapidly. As it turns out, they do not behave like this and instead, the TH formulas are good enough to give us an impression of the dependence on the masses and couplings. To see this analytically, we now expand the full results around δ with

$$\hat{s} = (2M_B)^2(1+\delta^2)^2. \tag{5.34}$$

The full expansion up to power δ^2 is

$$\sum_{i=0}^{8}(C_i^{TH}\cdot J_i^N + C_i^{TH}\cdot \widetilde{J}_i + C_i^{\delta^2}\cdot J_i^N) + \mathcal{O}(\delta^3) \tag{5.35}$$

where $C_i^{\delta^2}, \widetilde{J}_i$ mean the δ^2 order of the full C_i, J_i. Thus we have a new contribution from the expanded Jacobian factors with the power δ^2, $\tilde{J}_i$ and we have the expanded coefficients $C_i^{\delta^2}$. We do not show the results of the $\tilde{J}_i$ here, since they have a long and involved structure and are not important for the sake of the argument. However, the important contribution to which we turn our attention to, comes from the new $C_i^{\delta^2}$ coefficients. As we can see in the following equations, they are the same up to prefactors as the leading order C_i^{TH} terms in the equations 5.33. We show here only the order δ^2 contribution of the $C_i^{\delta^2}\cdot J_i^N$,

$$\frac{1}{\sigma^{TH}}\frac{d\,\sigma_{TH}^{(VSF)}}{d\,\mathcal{C}_B}\bigg|_{\delta^2} = 0 \tag{5.36a}$$

$$\frac{1}{\sigma^{TH}}\frac{d\,\sigma_{TH}^{(SFS)}}{d\,\mathcal{C}_B}\bigg|_{\delta^2} = 2\cdot\frac{\left(3-\sqrt{1-\beta^2}\right)}{1-\sqrt{1-\beta^2}}\left(J_0^N+\frac{\gamma^2}{4}J_2^N\right) \tag{5.36b}$$

$$\frac{1}{\sigma^{TH}}\frac{d\,\sigma_{TH}^{(SFV)}}{d\,\mathcal{C}_B}\bigg|_{\delta^2} = 2\cdot\frac{\left(3-\sqrt{1-\beta^2}\right)}{1-\sqrt{1-\beta^2}}\left(J_0^N+\frac{\gamma^2}{4}\left(\frac{1-2\tau_c}{1+2\tau_c}\right)^2 J_2^N\right) \tag{5.36c}$$

$$\frac{1}{\sigma^{TH}}\frac{d\,\sigma_{TH}^{(VFS)}}{d\,\mathcal{C}_B}\bigg|_{\delta^2} = 0 \tag{5.36d}$$

$$\begin{aligned}\frac{1}{\sigma^{TH}}\frac{d\,\sigma_{TH}^{(VFV)}}{d\,\mathcal{C}_B}\bigg|_{\delta^2} &= \left(\frac{1}{4\beta^2}((1+\beta^2)-2\sqrt{1-\beta^2})\right)\cdot J_0^N \\ &\quad -\frac{\gamma^2}{2}\left(\frac{1-2\tau_c}{1+2\tau_c}\right)^2\frac{\sqrt{1-\beta^2}+3}{\sqrt{1-\beta^2}+1}J_2^N\end{aligned} \tag{5.36e}$$

$$\frac{1}{\sigma^{TH}}\frac{d\,\sigma_{TH}^{(SSF)}}{d\,\mathcal{C}_B}\bigg|_{\delta^2} = 0 \tag{5.36f}$$

$$\frac{1}{\sigma^{TH}}\frac{d\,\sigma_{TH}^{(SVF)}}{d\,\mathcal{C}_B}\bigg|_{\delta^2} = \frac{3(2\tau_c+1)}{(\tau_c+2)^2}\left(J_0^N\cdot\frac{(5+2\tau_c)}{4(1+2\tau_c)}-\frac{\gamma^2}{(1+2\tau_c)}J_2^N\right.$$

$$+\left(\frac{(1-\tau_c)^2}{2(1+2\tau_c)}\right)J_6^N+\frac{2(\tau_c-1)^2}{2\tau_c+1}\cdot J_5^N-\frac{2(1-\tau_c)}{2\tau_c+1}\cdot J_7^N\Bigg) \tag{5.36g}$$

$$\frac{1}{\sigma^{TH}}\frac{d\,\sigma_{TH}^{(VVF)}}{d\,\mathcal{C}_B}\bigg|_{\delta^2}=\frac{9(\tau_c+1)}{4(\tau_c+2)^2}\left(J_0^N-\frac{3\tau_c(1-\tau_c)}{8(\tau_c+1)}J_7^N-\frac{3(1-\tau_c)^2}{4(1+\tau_c)}J_5^N\right). \tag{5.36h}$$

As we can see, we have similar dependences on $J_0^N, J_2^N \ldots$, but no other Jacobian factors appear. There are two main points we want to stress here. First, the relative ratios between the J_0^N and J_2^N can change, e.g. an additional relative factor of 3 in the case of equation 5.36h in comparison to 5.33h. Furthermore these higher order contributions come with prefactors as a whole that give an additional factor relative to the "leading" order. In addition, in the case of (SVF), two more Jacobians J_5^N, J_6^N appear, and in the case of (VFV) we have an additional influence of β.
The question arises, why we do not use the TH formulas to investigate the influence of the couplings and $\sqrt{\tau_c}$. As we can see in the expansion, the order of δ^2 in the expansion contributes with the same prefactor $C_i^{\delta^2}$ as in the TH formulas, but there come in additional coefficients which give a different weight induced by the numerical factors to each of the Jacobians. It turns out that these weights have a constant impact on the distribution for one spin scenario. We have therefore decided to use the full result which is Monte Carlo integrated as explained in Section 5.1.4 for the study on the influences of masses and couplings. The point we want to stress here is that the mass and coupling dependent prefactors have a similar influence on the full result as on the TH distributions. If the prefactor C_i vanishes or is maximal, the complete term belonging to C_i vanishes or is maximal, independent of its specific weight.

5.3 Fixed $\sqrt{\hat{s}}$ approach

As we have seen in the last section, the $\mathcal{C}_B$ distributions depend on $\sqrt{\hat{s}}$, the spin of the particles, masses and couplings. As pointed out before, we want to disentangle those effects in the following discussion. First, we investigate the pure phase space function and see how it depends on the energy $\sqrt{\hat{s}}$.
Since we are considering processes for a hadron collider, we need to include PDF effects. We want to disentangle the effects from the PDFs, which induce a non fixed $\sqrt{\hat{s}}$ value, from the spin, coupling and mass effects by choosing a suitable fixed $\sqrt{\hat{s}}$ which approximates the PDF result.
In the following we estimate this fixed $\sqrt{\hat{s}}$. First we will have a look at the underlying production processes $q, \bar{q} \to B\bar{B}$ and determine which is the dominant invariant mass region in the total production cross section. This depends on the underlying spin structure which we will discuss first. Then we will take the full $2 \to 4$ processes into account, since the nature of the particle C also plays a role and influences the value of the optimal fixed $\sqrt{\hat{s}}$.

5.3.1 Production process with fixed $\sqrt{\hat{s}}$

We consider the case $M_A < 2 \cdot M_B$. The $\sqrt{\hat{s}}$ distribution of the two particles B in the production process with PDFs has an initial point which is given by the mass of the two particles $2M_B$ (TH limit). The distribution has a peak directly after the initial point at $(2 + \mu_{Prod}) \times M_B$ where μ_{Prod} depends on the overall energy, the particles produced and their couplings and masses. In the fixed $\sqrt{\hat{s}}$ case, we want to make use of this peak to approximate the PDF effects via setting the CoM energy $\sqrt{\hat{s}}$ to a value close to which most of the events are produced, i.e. close to this peak. Since this peak is relatively close to TH, we also want to make use of the TH functions to make statements about the discrimination power of $\mathcal{C}_B$ for the different spin scenarios.
We have to estimate μ_{Prod} in order to see how close we are in the approximation at the realistic PDF result. To get a qualitative idea about the size of this deviation, we investigate (a) the maximum of the produced events (Peak: μ_P, $\sqrt{\hat{s}} = 2 \cdot M_P$) (b) the mean/average value of the produced events (Mean/Average: μ_A, $\sqrt{\hat{s}} = 2 \cdot M_{Av}$) and (c) the Median which gives the median mass (μ_M, $\sqrt{\hat{s}} = 2 \cdot M_M$) where half of the events are at smaller energies and half at higher. We derive the relative deviation from the true mass M_B for the peak, mean and median value

$$\begin{aligned} \mu_P &= \frac{(M_P/2 - M_B)}{M_B} \\ \mu_A &= \frac{(M_{Av}/2 - M_B)}{M_B} \\ \mu_M &= \frac{M_M}{2M_B} \text{ where } \frac{1}{N_{tot}} \sum_{0}^{M_M} Evts = \frac{1}{2} \text{ and } \frac{1}{N_{tot}} \sum_{M_M+1}^{N_{tot}} Evts = \frac{1}{2} \end{aligned} \tag{5.37}$$

where M_B is the intermediate particles' mass and M_P, M_{Av}, M_M is the "peak mass" and "mean mass/average mass" and "median mass" respectively. Since we work with binned data, we use a sum over the events instead of an integral.
In figure 5.6 we show the invariant mass $\sqrt{\hat{s}}$ distributions of the two particles B for $\sqrt{s} = 7$ TeV. Shown are the production processes (SS) and (VV) for different masses of M_B. These two plots are exemplary for an s- and p-wave mediated process. The vertical lines indicate the peak, average and mean mass. The rise of the distribution originates in the cross section. However, with increasing energy, the production gets suppressed due to the decrease of the PDFs and the off-shellness of the particle A.
We show the corresponding deviations in figure 5.7 for $\sqrt{s} = 7$ and 14 TeV. In case of (SS) we see that for low energies the values for μ_M and μ_A cross each other. This is an effect that has its origin in the binning of the data. It appears whenever the distributions are very narrow as e.g. in the left plot of figure 5.6.
As we see, depending on the spin of the intermediate and final particles, the peak is shifted more or less to higher energies. First, we have a suppression via the phase space, so beyond $\hat{s} < (2M_B)^2$, there is not enough energy available for an on-shell production. As soon as $\hat{s} \geq (2M_B)^2$, the process is kinematically allowed

and is now only suppressed by a phase space factor of β_B^2 with

$$\beta_B = \sqrt{1 - \frac{(2M_B)^2}{\hat{s}}} \tag{5.38}$$

and potential additional suppression factors of β_B coming from the squared matrix element. For the 6 different spin scenarios we find these suppression factors in terms of the boost

$$(SS), (SV), (VF) \propto 1 + \mathcal{O}(\beta_B) \tag{5.39a}$$
$$(SF) \propto 1 + \mathcal{O}(\beta_B) \text{ if } b_l \neq b_r \tag{5.39b}$$
$$(VS), (VV) \propto \beta_B^2 + \mathcal{O}(\beta_B^3) \tag{5.39c}$$
$$(SF) \propto \beta_B^2 + \mathcal{O}(\beta_B^3) \text{ if } b_l = b_r \tag{5.39d}$$

where $b_{r/l}$ are the corresponding couplings in this scenario as defined in table 5.2. The non-suppressed processes can be mediated via s-wave, while the suppressed ones can only be mediated via p-wave. As we can see in figure 5.7 and as expected, the mean and median deviations μ_A, μ_M for 14 TeV are larger than for the corresponding 7 TeV deviations since the average energy per parton is higher. The peak values μ_P are roughly the same for both energy ranges. The peak deviation is the smallest for (SS), (VF) and (SV) as expected from equation 5.39a. The additional suppression factor of β^2 induces a broadening of the distributions of p-wave processes in comparison to the s-wave processes.

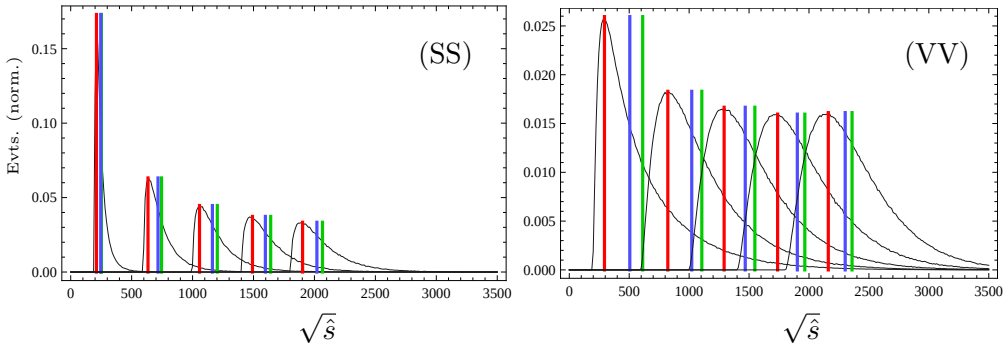

Figure 5.6: Two example plots for s (left) and p (right) wave production processes. Shown is the di-lepton invariant mass distribution for masses M_B =100, 300, 500, 700, 900 GeV. The orange/blue/green vertical lines indicate the respective peak/mean/median mass. The number of events is normalized arbitrarily.

Let us assume an exponential decrease of the PDFs with $\exp(-\hat{s}/\lambda)$ where λ is a dimensionful parameter that can be fitted from the PDFs. For fixed $\hat{s}$, the PDFs decrease with higher energies $\hat{s}$ roughly as $(\hat{s}-(2M_B)^2)e^{-\hat{s}/\lambda}$ where the TH factor is $(\hat{s}-(2M_B)^2)$. The maximum of this function is given for $e^{-\hat{s}/\lambda}(4M_B^2-\hat{s}+\lambda) = 0$ at $\hat{s} = (2M_B)^2 + \lambda$ so that the maximum of the deviation $\mu^2 = \hat{s}/(2M_B^2) = \lambda/(2M_B^2)+2$. Therefore, μ decreases with higher masses of the produced particle and therefore we see in figure 5.7 that the relative deviation is larger for smaller masses.

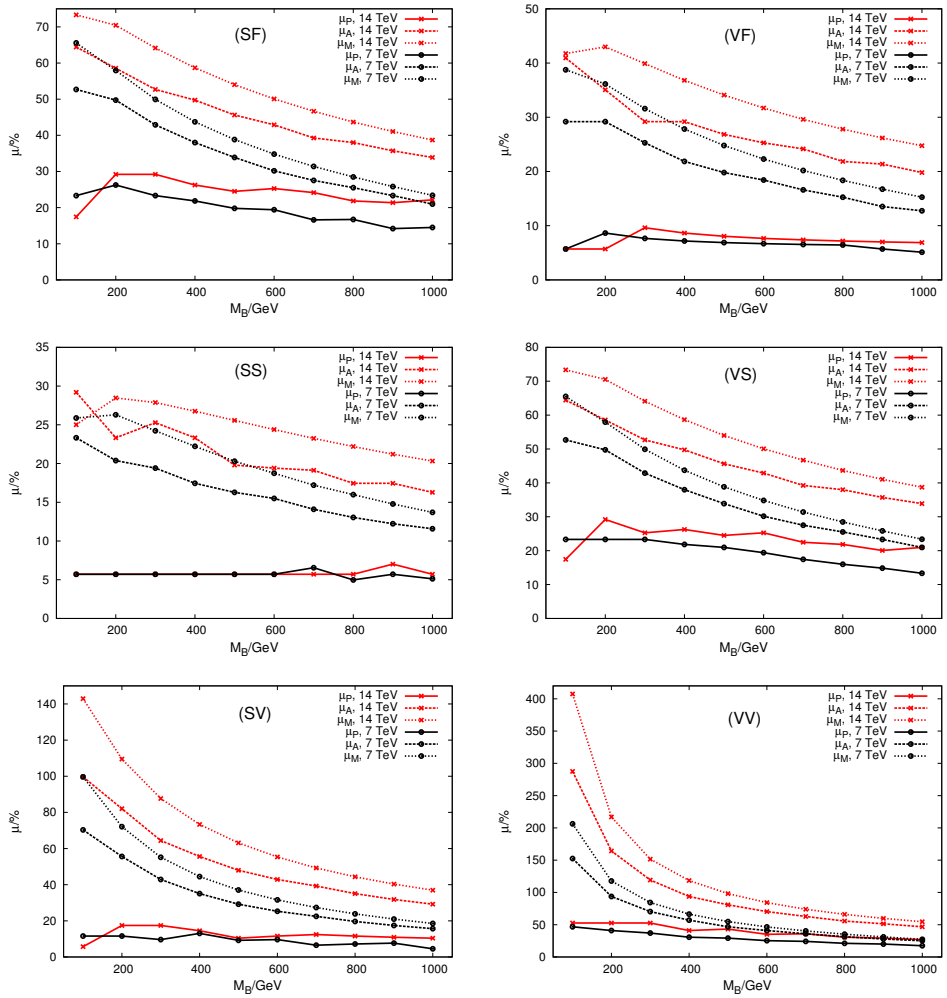

Figure 5.7: Relative deviation of peak and mean and average/median mass from the original mass M_B for all 6 spin scenarios. M_A=100 GeV, PDF set: CTEQ5M.

We have seen how the spin influences the peak for the production process with final on-shell particles. Next, we want to turn our attention to the full $2 \to 4$ process and see how the PS distribution changes with energy, and which fixed $\sqrt{\hat{s}}$ is thus best for estimating the PS with PDFs.

5.3.2 How does the phase space depend on $\sqrt{\hat{s}}$?

As before, we call the distribution which carries only kinematic information but no spin information, the phase space distribution (PS). We will first look at the PS distribution including PDFs simulated with CalcHep for $\sqrt{s} = 7$ and 14 TeV and then compare these distributions with a χ^2-function with our fixed $\sqrt{\hat{s}}$ formula.
In the following, we will compare CalcHep/CompHep distributions to the analytical ones. For this purpose, we have implemented a model in CalcHep capable of simulating generic processes. We have also implemented $\mathcal{C}_B$ as a variable. We summarize both in the Appendix A.2.
We define a δ^2 in terms of the relative [4] deviation of $\sqrt{\hat{s}}$ from $2M_B$,

$$\hat{s} = (2M_B)^2(1+\delta^2)^2. \tag{5.40}$$

We use the rescaled χ^2 between PS and the CalcHep simulation (CH) as

$$\chi^2(CH;PS) = \sum_i^n \frac{(CH(\mathcal{C}_{B\ i}) - PS(\mathcal{C}_{B\ i}))^2}{CH(\mathcal{C}_{B\ i})} \tag{5.41}$$

where we normalize the distributions such that the sum of all bins is 1,

$$\sum_i^n CH(\mathcal{C}_{B\ i}) = 1; \qquad \sum_i^n PS(\mathcal{C}_{B\ i}) = 1.$$

Due to this normalization, the absolute value of the χ^2 in equation 5.41 is rather small. For N events we can recover the standard definition of χ^2 from $\chi^2 \to N/(n-j)\cdot\chi^2$ with the number of degrees of freedom j and the number of bins n. We fit the optimal δ^2 value by minimizing the χ^2 in equation 5.41.
Since we cannot simulate the pure PS distribution with CalcHep, we test two different processes where we know that the matrix element is independent of angles. The first process is the spin scenario (SSF) which we also want to investigate later. The second process is (SSS) which was additionally implemented for CalcHep. Here we have substituted the SM-lepton by an additional scalar that is also massless. We simulate those for both 7 TeV and 14 TeV and for two mass scenarios which we will refer to as M_1 and M_2 given by

$$M_1: \qquad M_B = 500 \text{ GeV}, \quad M_C = 100 \text{ GeV} \tag{5.42a}$$
$$M_2: \qquad M_B = 500 \text{ GeV}, \quad M_C = 490 \text{ GeV}. \tag{5.42b}$$

[4] Note here that we choose δ quadratically compared to the peak, mean and medium μ. Their relationship thus is $\delta^2 \sim \mu_A, \mu_M, \mu_P$.

We have chosen two extreme mass ratios $\tau_c = (M_C/M_B)^2$. In the first one, the C particle is light, while in the second one, the masses are almost degenerate as e.g. in most UED mass scenarios. We have chosen the mass of $M_A = 100$ GeV. We have checked that the results do not crucially dependent on this value and have chosen it such that it is between the Z boson mass and a typical value for a light Higgs boson mass.
Both spin scenarios yield coinciding results in this χ^2 based fit and we find that the value for δ^2 has to be chosen around 0.2. The optimal values for δ^2 in both spin scenarios are of equal size,

$$14\ TeV,\ M_1: \quad \delta^2_{min} = 0.23 \qquad 14\ TeV,\ M_2: \quad \delta^2_{min} = 0.21 \tag{5.43a}$$

$$7\ TeV,\ M_1: \quad \delta^2_{min} = 0.19 \qquad 7\ TeV,\ M_2: \quad \delta^2_{min} = 0.16 \tag{5.43b}$$

which is not surprising since both matrix elements squared are constant and what we actually see is the PS distribution as expected. If we now compare these numbers to figure 5.7, we see that the δ^2 from the full process is comparable to that of the production process at the average/median mass μ_A. We also see that the estimation only considering the production process does of course not take the mass of the particle C into account. In equation 5.43 we see that this mass affects the best δ^2. Therefore, we will determine in Section 5.3.4 the optimal δ^2 for different masses and couplings for each of the 8 processes.

5.3.3 The Susy case: (VSF)

This case is different from the other scenarios, since here, the distribution remains the same over a large energy range. The PS at TH and the result for (VSF), $(1 - \cos^2\theta^*)$ (which is also the high energy result) are very similar and thus the shape does not change drastically.
In figure 5.8 we show the χ^2 for (VSF) in comparison to the high energy (HE) analytic distribution (blue) and to the threshold (TH) distribution (red) depending on the CoM energy which was varied over a wide range $\sqrt{s}$=7, 14, $7 \cdot 10^2$, 10^5, 10^7 TeV where we include for the argument the unrealistic energies > 14 TeV. We show the χ^2 result for the two different mass scenarios M_1 (dashed) and M_2 (solid) from equation 5.42. We see in this plot that for realistic energies of 7 and 14 TeV, the (VSF) distribution is much closer to the TH distribution than in the HE case. Only at very high energies, the HE limit formula is good enough to resemble the actual distribution and the TH limit becomes worse.
To emphasize this point, we show the actual distributions for $7, 14$ TeV (black solid/dashed) and the unrealistic, but high energy case with 10^7 TeV (blue solid) for the mass scenario M_1 and M_2 in figure 5.9 and compare it there to the PS result at threshold ($\delta \sim 0$, red solid). Only at very high energies, the (SV) distribution (HE limit) is reached which goes as $(1 - \cos^2\theta^*)$, while at realistic energies, it is basically the PS at TH distribution. Thus, the approximation is only valid at non-achievable energies but however looks very similar to the HE result. Nevertheless, this is not a disadvantage, since we now have the PS at TH

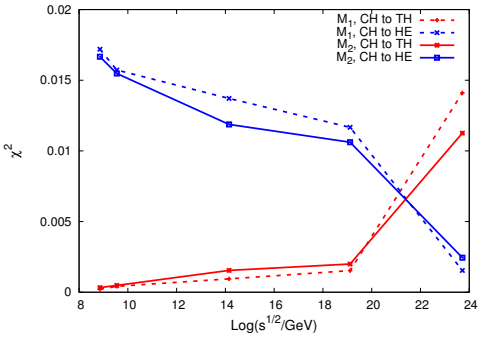

Figure 5.8: Correlation plot for the CH result in comparison to the PS at TH formula and the HE formula for the two mass scenarios M_1 and M_2 (dashed/solid). We see that the HE limit is only a good approximation at unrealistic high energies and the TH limit is the better choice at realistic energies.

formula and know that independently of the mass of the particle C, this formula is valid even if we have PDFs.

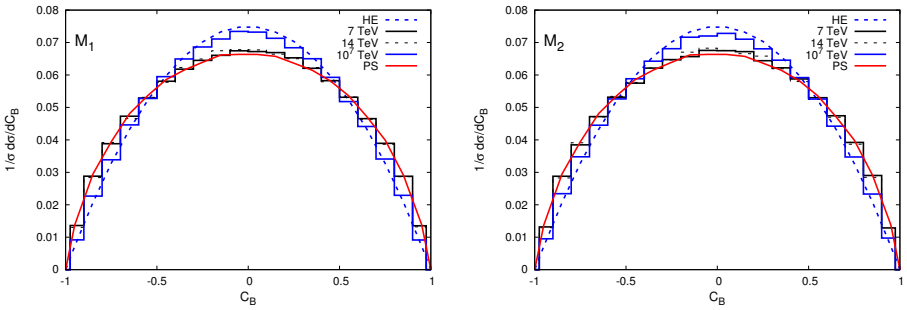

Figure 5.9: The PS and the HE distribution of (VSF) and the corresponding CH distributions for the different energies in the two mass scenarios M_1 and M_2. We see that the HE result, which approaches the (SV) process, is only achieved at very high energies which are not relevant at a collider.

5.3.4 Optimal δ^2 for different spin scenarios

Now we determine the optimal fixed energy $\sqrt{\hat{s}}$ for the full $2 \to 4$ process in terms of δ^2 of equation 5.40 which represents best the energy distribution due to the PDFs. Of course, we will find a similar effect as in the $2 \to 2$ processes, but we will now also investigate the influence of the couplings and mass M_C of the particle C.
Therefore we simulate all 8 processes for two CoM energies (7 TeV and 14 TeV) with each of the two coupling sets C_1 and C_2 and mass scenarios M_1 and M_2 from equation 5.42. We have chosen the coupling sets C_1 for all scenarios as

$$a_l = 1 \qquad a_r = 1; \qquad b_l = 1 \qquad b_r = 1; \qquad c_l = 1 \qquad c_r = 1 \qquad (5.44)$$

so that all couplings to fermions are pure vector/scalar like. Since the distributions are normalized, the results are independent of the size of the three boson vertex. We choose the second coupling set C_2 with chiral couplings for each process differently such that the chosen coupling set gives the maximal deviation from PS for the corresponding spin scenario. We will give the specific couplings for each process below.
We compare the simulation from CalcHep $CH(\mathcal{C}_B)$ now with the analytic results $A(\mathcal{C}_B)$ from Section 5.2 where we scan $\hat{s}$ in terms of δ^2 by equation 5.40 and determine for each δ^2 a χ^2 which we define here with

$$\chi^2(CH;A) = \sum_i^n \frac{(CH(\mathcal{C}_{B\ i}) - A(\mathcal{C}_{B\ i}))^2}{CH(\mathcal{C}_{B\ i})} \tag{5.45}$$

and sum over all bins i. We have calculated the $\mathcal{C}_B$ distribution of the analytic results $A(\mathcal{C}_B)$ with the help of the Monte Carlo integration as explained in Section 5.1.4. Note here, that we have normalized both distributions with

$$\sum_i^n CH(\mathcal{C}_{B\ i}) = 1; \qquad \sum_i^n A(\mathcal{C}_{B\ i}) = 1 \tag{5.46}$$

where i is the bin number corresponding to $\mathcal{C}_B \in [-1,1]$. Due to this, the absolute determined values of χ^2 are naturally small as already noted on page 95.
By doing this we get the optimal fixed $\sqrt{\hat{s}}$ value for each of the processes and what we will do later is to choose this specific δ^2 to investigate the influences of the masses and the couplings on the distributions.
We already know that for (VSF), $\delta^2 = 0$ gives us the full PDF result for 7 and 14 TeV. For (SSF), we have also the best δ^2 already determined for the two mass scenarios. We show some of our results for the discussed study points in figure 5.10. We show in these figures the χ^2 as defined in equation 5.45 as a function of δ^2 for different mass and spin (left: C_1 and right: C_2) scenarios for different energies which are given in the respective legends. The optimal values for δ^2 for all spin scenarios depending on the mass and energies are summarized in table 5.3.
We summarize the optimal values for δ^2 in table 5.3, and we see there that the trend discussed in Section 5.3.1 remains the same. The processes being suppressed by an additional factor of β^2 from the matrix element given in equation 5.39 have a larger optimal δ^2 (such as (VVF) and (SFX) for C_1) than those without the additional suppression factor (such as (SSX), (SFX) for C_2 and (SVF)). X stands here for either S or V.
In the following we will have some notes on the distributions of the different spin scenarios. To get an impression of the various distributions and their different shapes, we show some interesting cases in figures 5.11 and 5.12. We show the simulated CalcHep distribution (in solid/red with boxes), the PS distribution in dashed-dotted/green, the best-δ result in solid/black, the distributions for $\delta = 0$ in dotted/black and the $\delta = 1$ in blue/dotted[5].

[5]For black-and-white printouts, please note that green translates into bright grey and blue into dark grey.

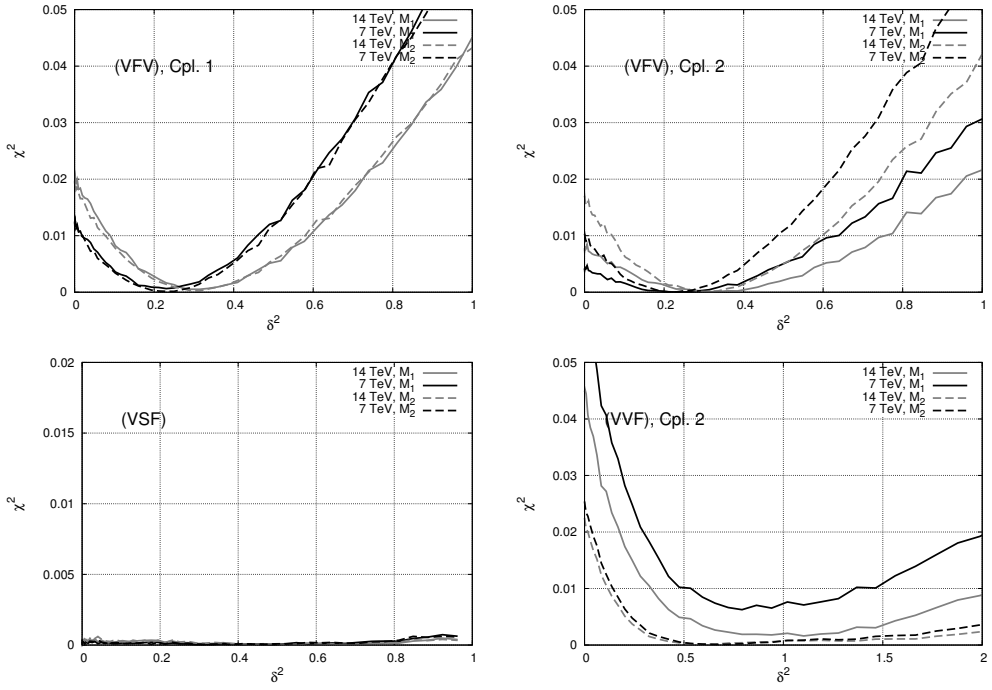

Figure 5.10: Selected interesting cases for the δ^2 scans. Top: (VFV) case (UED) for two coupling sets, bottom: (VSF) case (SUSY, left) and (VVF), right.

• (VFV) We show the δ^2-scans in figure 5.10 (top) and the corresponding distributions in figure 5.11(a). The coupling set C_2 is chosen with $a_l = a_r = b_l = b_r = c_r = 1;\ c_l = 0$. We can already note that for C_1, (VFV) resembles PS while for C_2, the distribution shows a dependence on mass. This is what we would have expected from the TH formula in equation 5.33e. The mass influence is larger for M_1 since in this case the prefactor of J_2^N in equation 5.33e is larger than for M_2.

• (VSF) We show the δ^2-scans in figure 5.10 (lower left) and the corresponding distributions in figure 5.11(b). From the δ^2-scan in figure 5.10 we see that the distribution for 7 and 14 TeV look like TH at PS for all energies, so that we can take $\delta^2 = 0$ for all cases. A second coupling set C_2 has no influence on the distribution (as we can see in equation 5.26b) and gives just an overall factor. Therefore we show only the distribution for C_1.

• (SFS) The coupling set C_2 is chosen with $a_l = a_r = b_l = b_r = c_r = 1;\ c_l = 0$. For both scenarios, there is a deviation from PS, which is stronger for C_2, and the results are independent of the mass scenario as one would have assumed from equation 5.33b. This can be seen in figure 5.11(c) where we have a larger deviation of (SFS) (black/solid) from the PS (green dashed-dotted) for C_2 than for C_1.

• (VFS) The coupling set C_2 is chosen with $a_l = b_l = b_r = c_r = 1;\ a_r = c_l = 0$. The distributions using C_1 resemble PS while C_2 shows spin dependence which one can again expect from equation 5.33d and which can be seen in the corre-

sponding distributions in figure 5.11(d).

• (SVF) The coupling set C_2 is chosen with $c_l = 1;\ c_r = 0$. For C_1 we can explain the distribution shown in figure 5.12(a) from the TH formula in equation 5.33g. Here we have $\gamma = 0$ and for $M_1, \sqrt{\tau}_c \approx 0$, the spin-dependent factor of equation 5.33g in front of J_6^N is maximal, while for M_2 where $\sqrt{\tau_c} \approx 1$, this factor vanishes and we see only PS. For C_2, both influences are rather small since the influences of both Jacobian factors J_2^N and J_6^N approximately cancel due to the different relative sign as can be seen in in equation 5.33g.

• (VVF) We show the δ^2-scans in figure 5.10 (lower right) and distributions for M_1 and M_2 in figure 5.12(b). The coupling set C_2 is chosen with $c_l = 1;\ a_r = c_r = 0$. Here we have the problem, that the result for $M_1,\ C_2$ at 7 TeV does not coincide for any δ^2. We investigated this effect further in CalcHep by fixing the energy and comparing it directly to our analytic distributions for the same $\sqrt{\hat{s}}$. We found that at higher energies $\sqrt{\hat{s}} > 800$ GeV both distribution are the same and differ only for smaller energies. We attribute this to the fact that (VV) has a strong spin suppression as can be seen in figure 5.7 resulting in dominant off-shell decays of the particles B in the significantly lighter C particles for energies below the median mass. These off-shell decays have a different $\mathcal{C}_B$ dependence and can consequently not be reconstructed with the analytic results. The distributions for 7 TeV are less affected by this then the distributions at 14 TeV.
We also see that this effect is absent in the distributions with M_2. Here the off-shell process is basically not allowed, since the C particle has approximately the same mass as the B particle. Consequently, the off-shell decay is absent and does not disturb the distributions at 7 nor 14 TeV as we can see in figure 5.12(b). We will however investigate the influence of masses and compare it to the rest of the distributions since this effect is only present for smaller masses.

• (SFV) We show the corresponding distributions in figure 5.12(c). The coupling set C_2 is chosen with $a_l = a_r = b_l = c_l = 1; b_r = c_r = 0$. There are spin and mass influences whereas the spin influences are stronger for C_2 and with the same reasoning as for (VFV) stronger for M_1.
We have determined here the best δ^2 for the 8 spin scenarios and found that the nature of the C particle influences the value of δ^2. In the following we will work with the values given in table 5.3. We use those as fixed $\sqrt{\hat{s}}$ to study how the distributions change for different mass and coupling scenarios.

5.4 Comparison of the distributions for fixed $\sqrt{\hat{s}}$

In this section, rather than using PDFs, we fix the $\sqrt{\hat{s}}$ by taking the δ^2 as defined in equation 5.40, $\sqrt{\hat{s}} = (2M_B)(1+\delta^2)$, which we have determined for each process separately in the last section. We will have a look at the influences of the masses and the couplings on the distribution at this fixed $\sqrt{\hat{s}}$. We interpolate the δ^2 for the mass scans linearly between the two mass scenarios M_1 and M_2. We use again the two coupling sets C_1 and C_2 as in the section before.

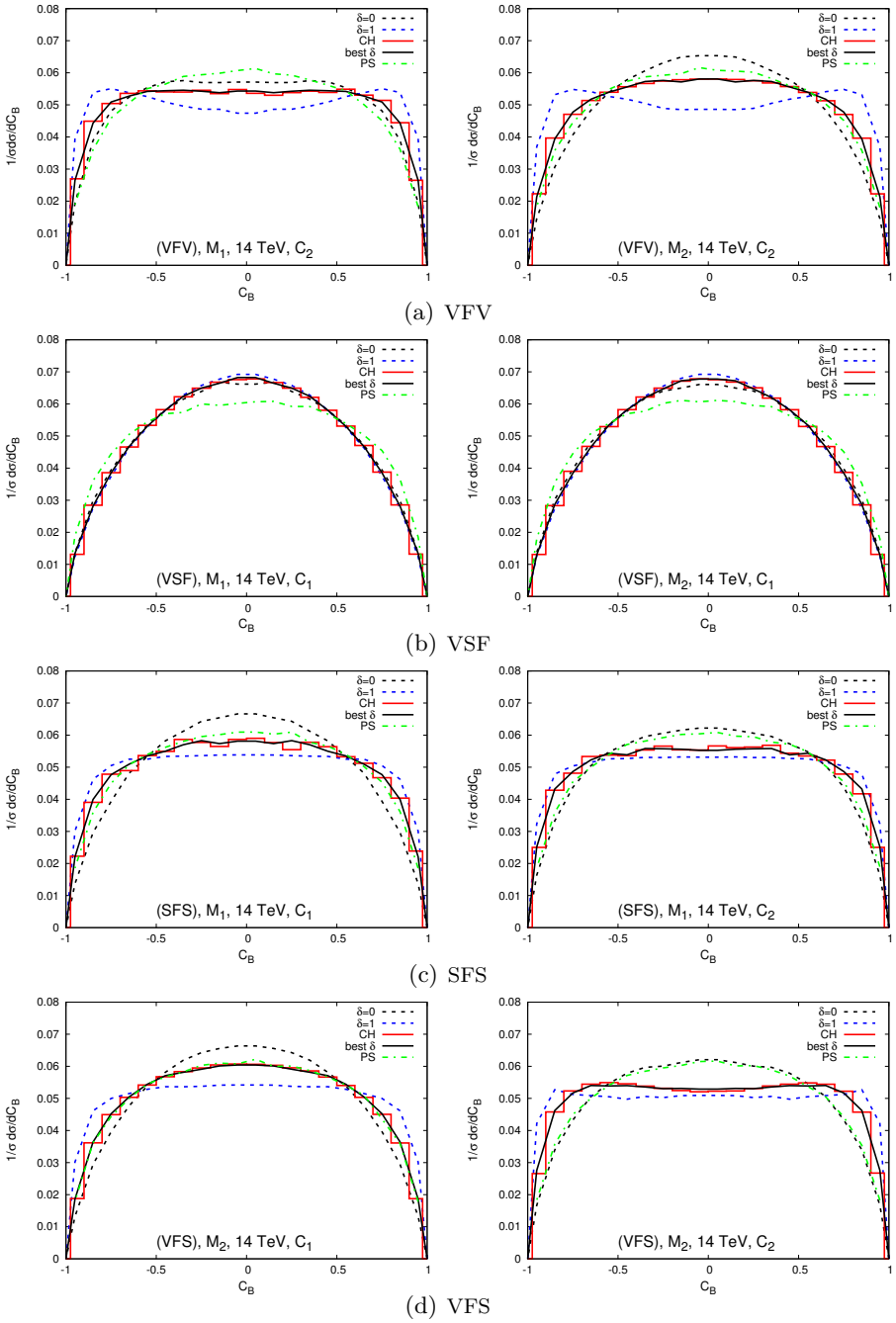

(a) VFV

(b) VSF

(c) SFS

(d) VFS

Figure 5.11: Some interesting distributions. We show the simulated CalcHep distribution (in solid/red with boxes), the PS distribution in dashed-dotted/green, the best-δ result in solid/black, the distributions for $\delta = 0$ in dotted/black and the $\delta = 1$ in dotted/blue.

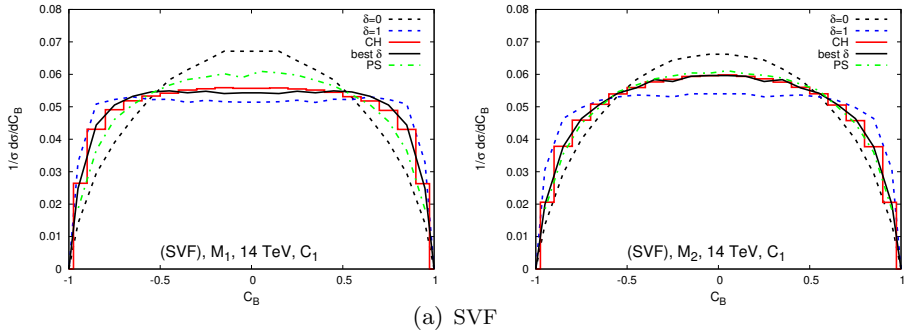

(a) SVF

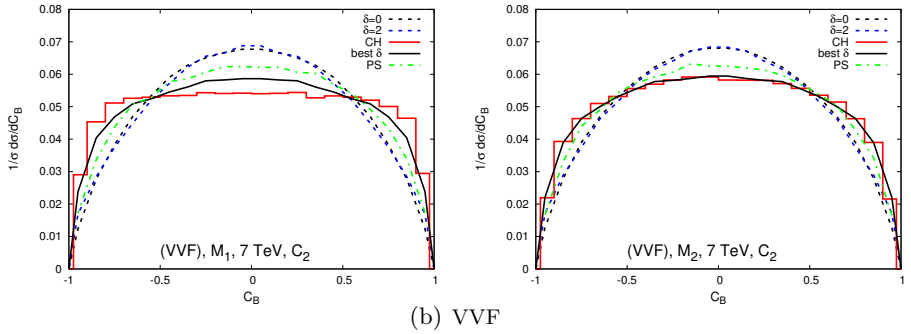

(b) VVF

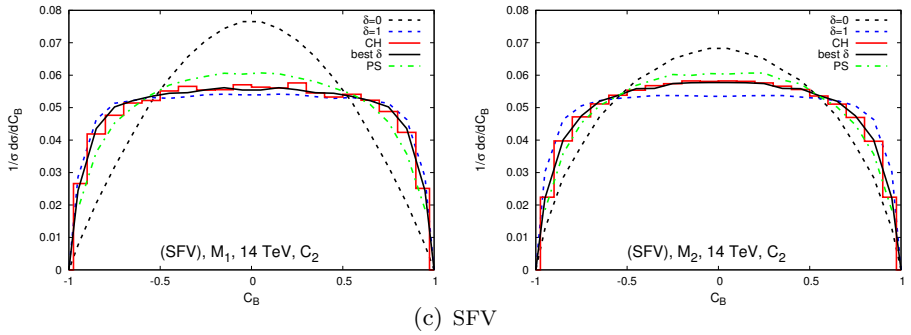

(c) SFV

Figure 5.12: Same as figure 5.11.

δ^2 for C_1	(SSF)	(VSF)	(VFV)	(VFS)	(SFS)	(VVF)	(SVF)	(SFV)
7 TeV, M_1	0.19	0	0.23	0.28	0.35	0.5	0.30	0.40
14 TeV, M_1	0.23	0	0.31	0.37	0.42	0.9	0.48	0.48
7 TeV, M_2	0.16	0	0.25	0.17	0.48	0.35	0.18	0.48
14 TeV, M_2	0.21	0	0.31	0.24	0.59	0.35	0.30	0.59

δ^2 for C_2	(SSF)	(VSF)	(VFV)	(VFS)	(SFS)	(VVF)	(SVF)	(SFV)
7 TeV, M_1	0.19	0	0.23	0.20	0.26	(0.79)	0.24	0.59
14 TeV, M_1	0.23	0	0.31	0.24	0.48	(1.10)	0.40	0.72
7 TeV, M_2	0.16	0	0.23	0.17	0.45	0.66	0.17	0.32
14 TeV, M_2	0.21	0	0.29	0.20	0.59	0.59	0.32	0.45

Table 5.3: Optimal values of δ^2 for the two mass scenarios M_1 and M_2 and the two coupling scenarios C_1 and C_2 at 7 and 14 TeV. We use these values in the next section.

5.4.1 Influence of the masses

We investigate the influence of the mass ratios $\sqrt{\tau}_c = (M_C/M_B) \in [0,1]$ on the distributions for a fixed $\sqrt{\hat{s}}$. To be able to use the same δ^2, we just vary M_C and leave M_B untouched.
We show two kinds of deviations. The first one is a density plot where, with the help of a certain measure, we compare each mass point with the other possible mass points in this particular spin scenario. We will refer to this kind of plot as a "self-comparison plot". The second plot shows the deviation from phase space as a function of $\sqrt{\tau}_c$ at 7 and 14 TeV for both coupling sets. The first kind of plot tells us how the distribution depends on the chosen mass scenario, the second one tells us how well the spin information is visible at the mass points and how large the deviation from PS is.
Since we now compare two distributions with each other in the self-comparison plot we need a measure that treats both on equal footing. We choose a measure called the symmetrized Kullback-Leibler distance $KL(f,g)$ [80]

$$\Delta(f,g) = \frac{1}{2}\left\{KL(f,g) + KL(g,f)\right\} \tag{5.47a}$$

$$KL(f,g) = \sum_i^n f(x_i) \log \frac{f(x_i)}{g(x_i)} \tag{5.47b}$$

where x_i is the corresponding variable and i sums over all bins. The distance measure KL can be used to disfavour a specific model based on data (or in this case, Monte Carlo results). It furthermore gives us a tool to estimate the minimum number of events needed to discriminate between two theoretical models [24,81]. For our purpose we symmetrize the distance as also proposed in [80] and estimate in Section 5.4.2 the minimum number of events with the equation

$$\frac{1}{R} \sim \frac{1}{2}\left\{\exp[-\mathrm{N}\cdot KL(f,g)] + \exp[-\mathrm{N}\cdot KL(g,f)]\right\}. \tag{5.48}$$

The R factor is the ratio of the likelihoods of two competing models disfavouring each other. We choose $R = 1/1000$ to simplify a comparison with the existing literature [24,69,81]. This corresponds to approximately 97% confidence level.
We show the differences of the PS to the different spin scenarios in figures 5.13. Note that the bumpy structure is due to Monte Carlo uncertainties. We have picked $\sqrt{\tau}_c$ that yield the minimal and maximal deviation and show them together with the PS distribution in the Appendix C.2, figures C.2 and C.3. The values for $\sqrt{\tau_c}$ for minimal and maximal KL distances are collected in table 5.4.
In the following we will discuss each of the scenarios. We will see that we can trace back the influences to the TH formulas in equation 5.33 similarly to the discussion about the deviation from PS in the last section. Since the production energy is close to TH, the expansion in δ^2 works very well. We show as an example two interesting self-comparison plots in the figure 5.15.

• (VFV) We see in figure 5.13(a) that for the C_1 coupling, the Δ indicates no deviation from PS. For C_2 we see that for small $\sqrt{\tau_c}$ the deviation is maximal

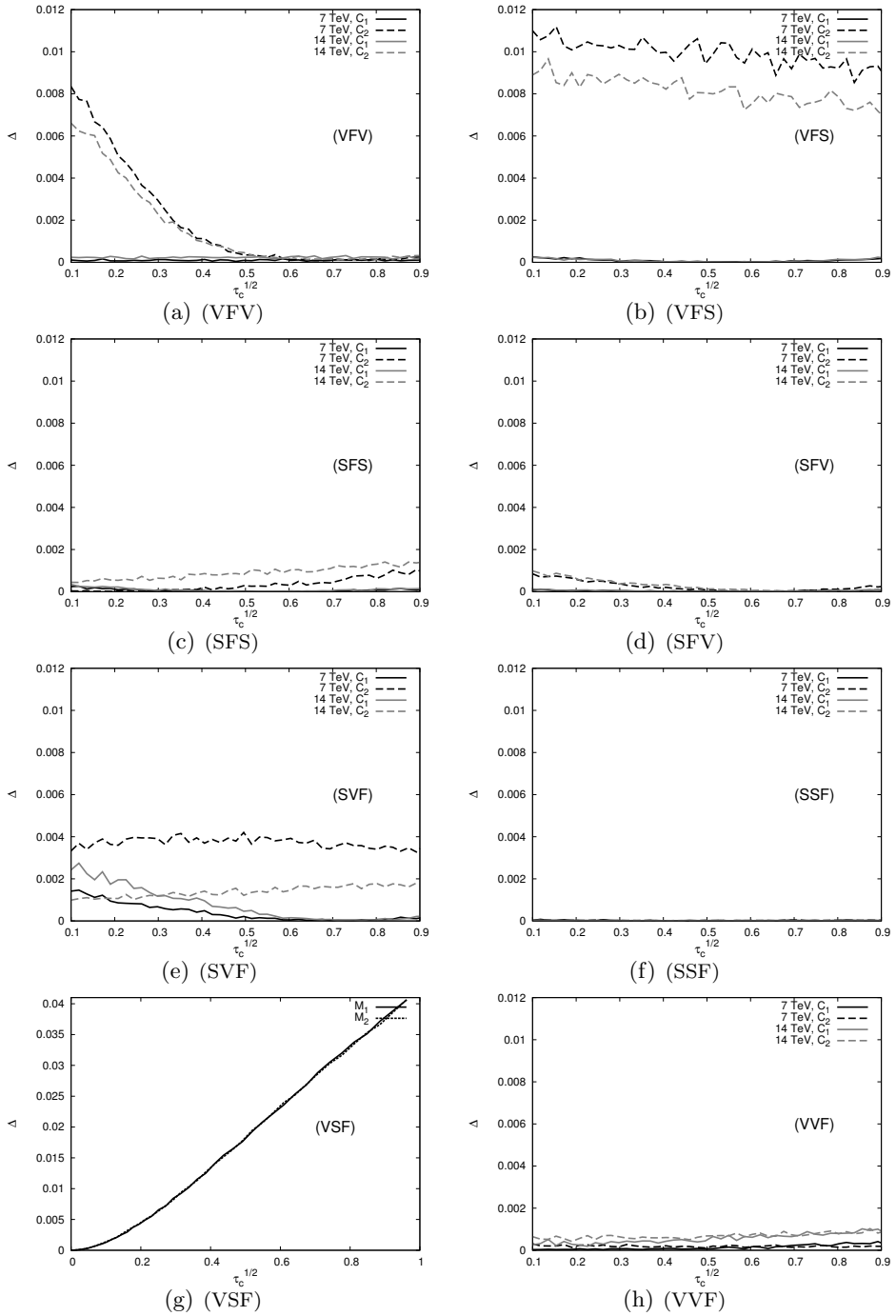

(a) (VFV) (b) (VFS)

(c) (SFS) (d) (SFV)

(e) (SVF) (f) (SSF)

(g) (VSF) (h) (VVF)

Figure 5.13: Deviation of spin scenarios from PS as a function of the mass ratio $\sqrt{\tau}_c$.

	Scen.	C_1	7 TeV	14 TeV	C_2	7 TeV	14 TeV
(VFV)	Min		0.48	0.84		0.66	0.73
	Max		0.59	0.73		0.10	0.10
(SFV)	Min		0.59	0.53		0.59	0.68
	Max		0.12	0.10		0.10	0.10
(SFS)	Min		0.59	0.50		0.19	0.12
	Max		0.12	0.10		0.95	0.94
(VFS)	Min		0.48	0.60		0.84	0.91
	Max		0.10	0.96		0.15	0.14
(SVF)	Min		0.69	0.71		0.93	0.10
	Max		0.12	0.12		0.50	0.96
(VVF)	Min		0.96	0.96		0.50	0.19
	Max		0.89	0.86		0.10	0.93

Table 5.4: Summary for the values of $\sqrt{\tau}_c$ giving the largest and smallest KL-distance with respect to PS (Min. and Max. deviation). We do not show (VSF) and (SSF) since the results do not depend on $\sqrt{\tau}_c$.

and for higher $\sqrt{\tau_c} > 1/\sqrt{2}$, the distributions coincides with the PS distribution at these energies. For C_2, the minimal Δ is at $\sqrt{\tau_c} = 0.66$ for 7 TeV and at $\sqrt{\tau_c} = 0.84$ for 14 TeV. This is close to the minimal value for $\sqrt{\tau_c} = \sqrt{1/2}$ in the TH formulas where $(1-2\tau_c)^2(1+2\tau_c)^2 = 0$ in equation 5.33e. In figure 5.14 we show the different mass dependences of the TH formulas given in equation 5.33. The red/solid line shows the functions appearing in the (VFV) case. We see that the relatively small deviation from 0 for $1/\sqrt{2} \leq \sqrt{\tau_c} \leq 1$ is the reason for the deviation in figure 5.13(a). This shows that, although we are not explicitly at TH, the TH formulas represent the behaviour of the distributions close to TH very well. (VFV) is independent from $\sqrt{\tau_c}$ for the C_1 couplings. The self-comparison plot for C_2 in the right side of figure 5.15 reflects the results from figure 5.13(a): The deviation from PS is larger for small mass ratios while around $\sqrt{\tau_c} = 1/\sqrt{2}$, the distribution is just PS. That means that one can discriminate different mass scenarios from each other best at small masses and around $\sqrt{\tau_c} = 1/\sqrt{2}$ which corresponds to the blue/dark area in this figure.

• (VSF) We see in figure 5.13(g) that at $\sqrt{\tau_c} = 0$, (VSF) and PS have the minimal relative deviation. As we have already mentioned, (VSF) is the same as PS at TH for all energies. The deviation from PS comes just from the energy dependence of the actual PS distribution and in contrast to this, the nearly constant distribution of (VSF). We can see from equation 5.26b and 5.33a that the distribution is independent of the choice of couplings and masses, which is why we do not show the self-comparison plots.

• (SFS) In figure 5.13(c) we see that for both C_1 and C_2 there is only a very small dependence on the mass ratio $\sqrt{\tau_c}$. For C_1, the distribution is extremely close to PS, while for C_2 we have a deviation from PS which is stronger for 14 TeV than for 7 TeV. This comes of course from the factor of γ^2 in equation 5.33b. However,

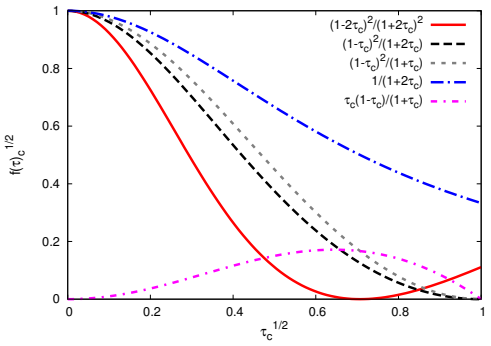

Figure 5.14: The different mass dependent prefactors of equation 5.33.

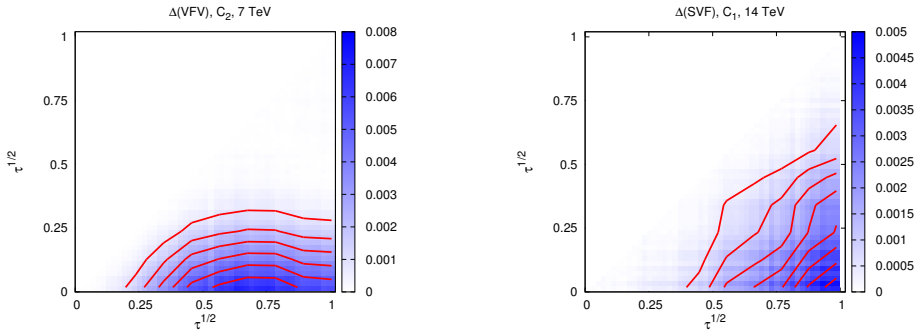

Figure 5.15: Self-comparison plots for the masscan for two interesting spin scenarios with KL-distance Δ. The red lines indicate the steps of the legend on the right hand side of the plots.

the tiny rise in the deviation with increasing $\sqrt{\tau_c}$ is not obvious from the equation 5.33b or 5.26a since both do not depend on this mass ratio explicitly. Since the deviation from PS doesn't show this rise for 14 TeV as much as for 7 TeV, we assume that this deviation comes from an effect not originating in the squared matrix element and is hence no spin effect which we can control.

• (SSF) As we can see in equation 5.26e and as we have already discussed, this process is just PS and has only a normalization that depends on the masses and coupling strength. In contrast to (VSF) in figure 5.13(g) the energy dependence is hence also the same as that of the PS.

• (VFS) This is an interesting case concerning the coupling structure. For C_1, the distribution is PS. The TH result for the distribution in equation 5.33d depends only on the γ^2 coupling which gives a contribution only for C_2. This is reflected by the mass independent deviation in figure 5.13(b). However, the self-comparison plots are constant so that we do not show them. The deviation from PS for all values of $\sqrt{\tau_c}$ (in contrast to e.g. (VFV) where the difference vanishes for suitable $\sqrt{\tau_c}$) is important for the discrimination for the rest of the spin scenarios.

• (SVF) This scenario shows interesting effects in the deviation from PS in figure 5.13(e). We see that C_1 depends strongly on $\sqrt{\tau_c}$. The TH result in equation 5.33g shows that for C_1, where $\gamma^2 = 0$, there is also a dependence on J_6^N besides the Jacobian factor for PS, J_0^N, which is has a mass-dependent coefficient $(1 - \sqrt{\tau_c})^2/(1 + 2\sqrt{\tau_c})$. We show this function with the black/long-dashed line in figure 5.14. For C_2, this factor is also there, but relatively smaller due to the normalization factor in 5.33g. However, in this case, the prefactor of the Jacobian J_2^N gives a contribution with the prefactor $1/(1 + 2\sqrt{\tau_c})$ which is also shown in figure 5.14 (blue/long dashed-dotted). This function decreases with increasing $\sqrt{\tau_c}$ like the previous one. Since there is a relative sign in equation 5.33g, these two mass dependences approximately cancel so that we get a nearly constant deviation from PS for C_2. This implies also that in the self-comparison plots, we have a constant Δ for C_2 and a variation for C_1 shown in figure 5.15. The deviation is the smallest for $\sqrt{\tau_c} \to 1$ and largest for $\sqrt{\tau_c} = 0$, and thus we see in figure 5.15 the most deviation in the right lower corner, decreasing to the other two corners.

• (SFV) In figure 5.13(d) we can see that the distribution for C_1 is basically PS. For C_2 we have a slight dependence on $\sqrt{\tau_c}$. However, the dependence of the J_2^N coefficient on the mass is shown in figure 5.14 with the red/solid line. Altogether, the deviation is very tiny. Surprisingly, (VFV) has the same mass-dependent factor $((1-2\tau_c)/(1+2\tau_c))^2$ but with the opposite sign in front. If we look at the J_2^N and J_0^N functions in figure 5.5, we see that by subtracting the two functions, the resulting function as it appears in (VFV) becomes typically broader in contrast to (SFV) where the two functions are added. This results in a smaller total deviation Δ for (SFV) as for (VFV). Comparing the plots directly, one sees that 5.13(d) shows indeed 1/8 of the total deviation of 5.13(a) for $\sqrt{\tau_c} \to 0$.

• (VVF) In this scenario we see a constant deviation from PS. The mass-dependent

prefactors of equation 5.33h are depicted in figure 5.14 by the pink/short-dashed-dotted line and by grey/short-dashed line. With the normalization factor for both, these two dependences approximately cancel and we get a constant deviation from PS that is slightly stronger for C_2. Since the deviation is constant over $\sqrt{\tau_c}$, we do not see any structure in the comparison plots and thus we do not show them.

5.4.2 Can one distinguish different spin scenarios?

After the detailed discussion of the individual scenarios, we now want to study the discrimination power of the variable $\mathcal{C}_B$ between pairs of scenarios. Therefore, we show for interesting cases pairwise comparison plots for the 8 spin scenarios. We summarize the minimal and maximal deviation together with the masses and an estimated minimal number of events needed to distinguish between both scenarios in the tables 5.6 and 5.5 at the end of this section. The minimal number of events is estimated from the Kullback-Leibler distance given in equation 5.47 and 5.48. This number is of course only a lower bound and can be enhanced by cuts, smearing or detector effects.
We will start with scenario (VFV) and go through all possible pairings with the other scenarios.

• (VFV) $\leftrightarrow$ (SFS) For C_1, both (VFV) and (SFS) do not depend strongly on $\sqrt{\tau_c}$. Both are close to the PS distribution and therefore, one cannot discriminate between both scenarios. In the coupling scenario where both show the most deviation, C_2, the situation improves, since here, (SFS) is still rather similar to PS and deviates little with increasing $\sqrt{\tau_c}$, an effect that is even stronger for higher energies, while (VFV) deviates very much from PS for $\sqrt{\tau_c} \leq 1/\sqrt{2}$. This is shown in the comparison plot in figure 5.16 where a darker region means larger Δ. We therefore find two regions with good discrimination power: One is where (VFV) resembles PS at $\sqrt{\tau_c} \geq 1/\sqrt{2}$ and where (SFS) shows most deviation, namely at high $\sqrt{\tau_c}$. The situation in the other region is reversed: (VFV) shows the largest deviation from PS for small $\sqrt{\tau_c} \to 0$ and (SFS) resembles PS for small $\sqrt{\tau_c}$. The effect for the first region is stronger for 14 TeV since here, the deviation from PS is stronger for higher energies and a little weaker for (VFV) at small $\sqrt{\tau_c} \sim 0$ as can be seen in figure 5.13(a) and 5.13(c). In the best case, the number of events is estimated with ~ 1595.

• (VFV) $\leftrightarrow$ (VSF) This is an important and interesting scenario because it represents the generalization of the comparison between Susy and UED. In the coupling scenario C_1, (VFV) and (VSF) are constant with respect to $\sqrt{\tau_c}$ and we have approximately a constant Δ measure between $5 \ldots 10 \cdot 10^{-3}$. The estimated number of events in the best case is around ~ 1102 (7 TeV) and ~ 660 (14 TeV). The difference here comes from the fact that (VFV) is close to PS and changes with energy $\sqrt{\hat{s}}$ but (VSF) remains constant. In the scenarios C_2, the differences are best for small $\sqrt{\tau_c}$ in the (VFV) scenario which means a large difference between the masses M_B and M_C where (VFV) deviates most from PS as shown in figure 5.13. The corresponding comparison plot is shown in figure 5.16. Unfortunately,

in most UED scenarios, the masses of the lepton' and the B' which are masses M_B and M_C respectively, are degenerate and only differ via radiative corrections in the minimal UED model. However, for this model, the assumption is made, that all boundary terms vanish at a certain scale Λ. This is a rather arbitrary choice, and in extended models this constraint is loosened and the degeneracy is lifted. The minimum events are estimated with 283 (7 TeV) and 256 (14 TeV). One can also see that even in the case of minimal Δ distance, the number of events is close to the numbers for largest Δ which implies that we have a good discrimination power for all mass scenarios.

• (VFV) $\leftrightarrow$ (SFV) C_1 yields an almost PS-like distribution for both mass scenarios, and Δ is small. There are two optimal points for discrimination, the first[6] one around $\sqrt{\tau_c}(SFV) \to 1$ and small $\sqrt{\tau_c}(VFV)$ because here, (VFV) has biggest deviation from PS. The other region is at small $\sqrt{\tau_c}(SFV)$ where (SFV) is most distinguishable from PS but (VFV) is basically PS. A comparison plot is shown in figure 5.16 and the maximal deviation is $\Delta = 5.1 \cdot 10^{-3}$ (7 TeV) and $3.64 \cdot 10^{-3}$ (14 TeV) in the first region corresponding to 1358 and 1868 events.

• (VFV) $\leftrightarrow$ (VFS) Both distributions are PS for C_1, so they show only a tiny difference. For C_2, (VFS) shows a large constant difference from PS and so the discrimination power from (VFV) is best for $\sqrt{\tau_c}(VFV) \to 1$ where (VFV) resembles PS. A comparison plot is shown in figure 5.16. Since the mass influence is stronger at lower energies, the discrimination power is stronger for smaller $\sqrt{s}$ with ~ 705 minimum events.

• (VFV) $\leftrightarrow$ (SVF) For the (SVF) scenario with C_1 we have a $\sqrt{\tau_c}(SVF)$ dependent distribution as seen in figure 5.13(e). Therefore, we have a large Δ at small $\sqrt{\tau_c}(SVF)$, since here the deviation is maximal from (VFV) which resembles PS in this coupling scenario. Since the deviation for (SVF) from PS is stronger for large $\sqrt{s}$, the effect is even stronger for 14 TeV than for 7 TeV and the minimal number of events is around 2100 for 14 TeV. For C_2, both distributions have a large deviation from PS and also between each other, as we can see in figure 5.16. For (SVF) we have a constant deviation for all mass scenarios while for (VFV) the deviation is larger for small $\sqrt{\tau_c}$. Thus we have a very distinct distribution in this region ranging from $\Delta = 23 \cdot 10^{-3}$ corresponding to 310 events (7 TeV) to $\Delta = 11.8 \cdot 10^{-3}$ corresponding to 595 events.

• (VFV) $\leftrightarrow$ (VVF) For C_1 both scenarios resemble PS and so the Δ measure is tiny. For C_2, (VVF) shows a constant deviation from PS so that for all ranges of $\sqrt{\tau_c}$ in both spin scenarios, we have always a non-zero Δ. We can see that also in the TH formulas in equation 5.33h and 5.33e. Independently of the specific prefactors C_i, the Jacobian factors are distinct for both scenarios (J_7^N and J_5^N vs. J_2^N), so that, if they give a contribution, it is distinct. Compare this situation e.g. to (VFS) in equation 5.33d where the spin dependent part with the Jacobian factors can give the same contribution as in (VFV), which cannot be the case for (VFV) and (VVF). The deviation is maximal for small $\sqrt{\tau_c}(VFV)$ with $\Delta = 4.37 \cdot 10^{-3}$

[6] $\sqrt{\tau_c}(X)$ denotes the $\sqrt{\tau_c}$ of the specific spin scenario X.

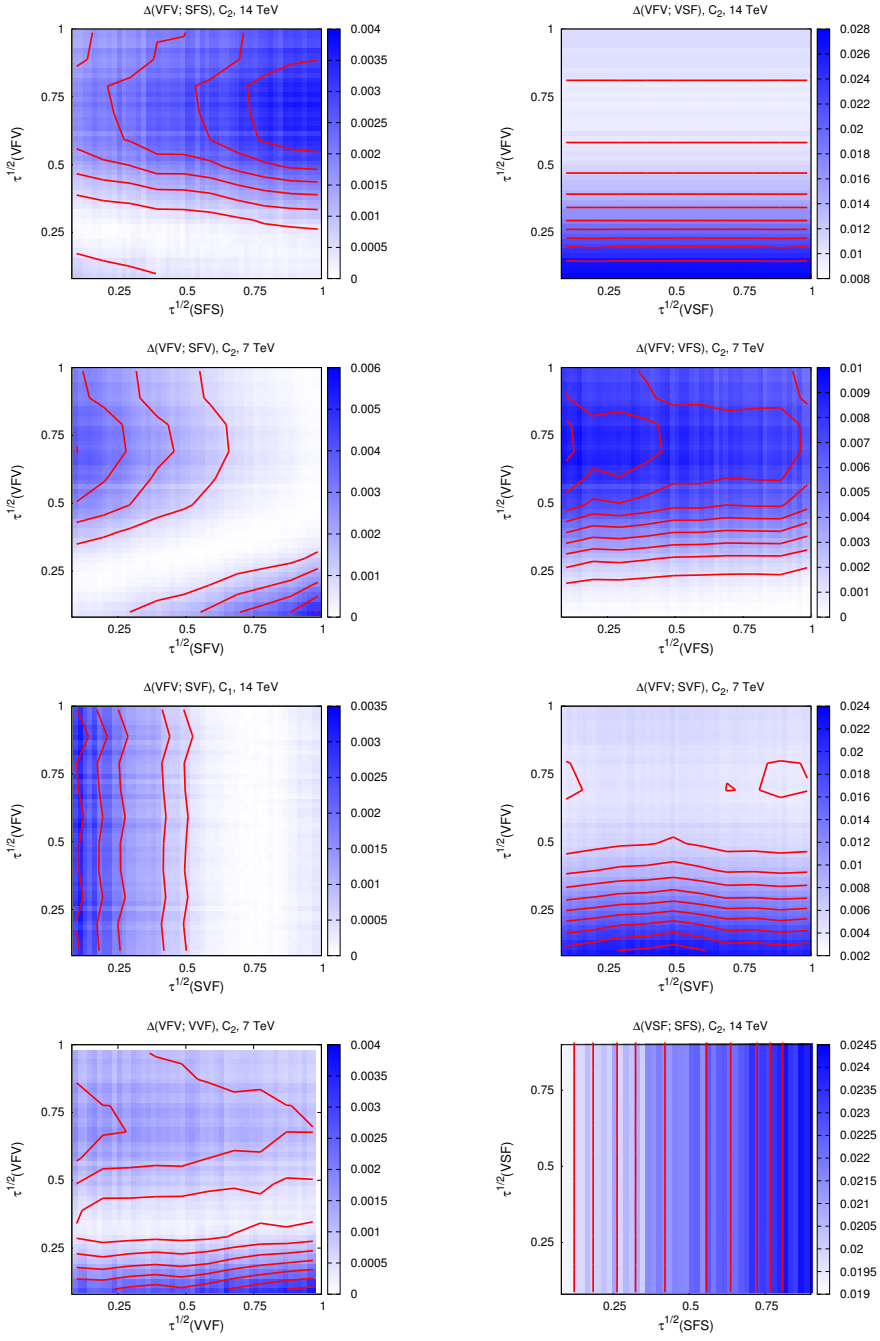

Figure 5.16: Comparison plots for different spin scenarios.

(corresponding to 1588 events). A comparison plot is shown in 5.16. Note that the large Δ values for C_1 come from the limit where $\sqrt{\tau_c}(VVF) = 1$.

• (VSF) $\leftrightarrow$ (SFS) The discrimination power here is very good, since for energies above TH, the (VSF) distribution still has its characteristic PS at TH form, while the (SFS) distribution deviates very much from this form. Since the (VSF) remains constant for all masses/couplings, it does not change at all and we are basically looking at the deviation of (SFS) from the PS at TH distribution. It becomes more obvious if we directly compare the figures 5.11(c) and 5.11(b). A comparison plot is shown in figure 5.16. The maximal deviation between the scenarios at 7 TeV is $\Delta = 19.4 \cdot 10^{-3}$ (C_2) but their minimal deviation $\Delta = 10.3 \cdot 10^{-3}$ is very large as well and we estimate the corresponding minimum number of events between 348 and 658. At 14 TeV, the minimal number for C_2 is even a mere 279 events.

• (VSF) $\leftrightarrow$ (SFV) For C_1 we have a constant deviation around $\Delta \sim 11 \cdot 10^{-3}$. For C_2 we have a large deviation for $\sqrt{\tau_c}(SFV) \leq 1/\sqrt{2}$. In this region, the J_2^N factor comes in and flattens the distribution while the (VSF) has still its original shape as in figure 5.11(c). A comparison plot is shown in figure 5.17. The minimal number of events is between 281 and 665 depending on the scenario and energy.

• (VSF) $\leftrightarrow$ (VFS) For both coupling scenarios we have a large $\Delta = 29.8 \cdot 10^{-3}$ ($33.7 \cdot 10^{-3}$) for C_2 for 7 (14) TeV and around $6.68 \cdot 10^{-3}$ ($10.0 \cdot 10^{-3}$) for C_1. Since we have constant deviations for all $\sqrt{\tau_c}$ regions, we get an approximately constant deviation in all cases. The constant deviation in the C_2 case for (VFS) has its origin in the J_2^N factor which has only a coupling dependent prefactor that is maximal for C_2. The minimum number of events is $\sim$ 200 for the best scenario.

• (VSF) $\leftrightarrow$ (VVF) As in the other cases, the distinction power is again very good since (VVF) shows either no spin dependence in the C_1 case or constant deviation from PS. The Δ is around $7.6 \ldots 16 \cdot 10^{-3}$ corresponding to a minimal number of 493...900 events.

• (VSF) $\leftrightarrow$ (SVF) Besides the case for C_2 at 7 TeV, all distributions have a Δ that is between $\Delta = 3.1 \ldots 23.9 \cdot 10^{-3}$ for small $\sqrt{\tau_c}(SVF)$ corresponding to 220-283 events. For C_2 and 7 TeV, Δ is extremely small. A direct comparison of distributions shows that in the (SVF) case, the distribution is steeper than the PS distribution whereas in most other cases, the spin influence flattens the distribution e.g through the influence of J_2^N. Since both distributions (VSF) and (SVF) are steeper then PS, they have a small Δ value. For higher energy, the distribution flattens again and the PS is above the actual distribution so that Δ increases. So far, this is the only case where we have agreement of (VSF) with another scenario besides some ranges in the (VFV) case. A comparison plot is shown in figure 5.17.

• (SVF) $\leftrightarrow$ (SFS) For C_2, the deviation is the largest for large $\sqrt{\tau_c}(SFS)$, namely up to $\Delta = 17.9 \cdot 10^{-3}$ (7 TeV) and $9.5 \cdot 10^{-3}$ (14 TeV) corresponding to a min-

imum number of events of 376 and 713 respectively. As we can see in equation 5.33g and 5.33b, we have no dependence on $\sqrt{\tau_c}$ in the (SFS) case but the prefactor of J_2^N maximizes in this coupling scenario. We see that the same prefactor for J_2^N in equation 5.33g can be achieved if $\sqrt{\tau_c}(SVF) \to 1/\sqrt{2}$ so that the only difference between both distributions comes from the J_6^N Jacobian and its prefactor from (SVF). This is why we see a non-zero deviation also for small $\sqrt{\tau_c}(SFS)$. For C_1, (SFS) has only a slight dependence on $\sqrt{\tau_c}$ but resembles PS while (SVF) has still the mass-dependent prefactor of J_6^N that influences the comparison in the C_1 plots. However, the discrimination is best for C_2 and large $\sqrt{\tau_c}(SVF)$ since here, the J_2^N of (SVF) has the most influence. A comparison plot is shown in figure 5.17.

• (SVF) $\leftrightarrow$ (SFV) Here we have a similar scenario as before. For C_1, the difference comes from the J_6^N factor of equation 5.33g which is absent in equation 5.33c. For C_2, we have two mass-dependent prefactors of J_2^N, $(1-2\tau_c)^2/(1+2\tau_c)^2$ (SFV) and $1/(1+2\tau_c)$ (SVF). They differ by a sign so that the sum of the distributions is maximized with the difference of the corresponding functions, which is the case for $\sqrt{\tau_c} = 0$. The functions are shown in figure 5.14 with the red/solid and the blue/long dashed-dotted line. A comparison plot is shown in figure 5.17.

• (SVF) $\leftrightarrow$ (VFS) For large $\sqrt{\tau_c}$, the mass prefactor of J_6^N of equation 5.33g vanishes so that for C_1, both distributions resemble PS and the discrimination power is small but increases with decreasing $\sqrt{\tau_c}$. The distributions are more distinguishable for large $\sqrt{\tau}_c$ of (VFS) and small $\sqrt{\tau_c}$ of (SVF). In the coupling scenario C_2 we have a large deviation of around $\Delta = (20.8 \ldots 27.7) \cdot 10^{-3}$ (7 TeV) and $\Delta = (7.48 \ldots 15.4) \cdot 10^{-3}$ (14 TeV) from the same reasoning as before. (VFS) has its characteristic flat form and can be discriminated well from (SVF) which changes only little with $\sqrt{\tau_c}$. Thus the minimum number of events in the best case is 243.

• (SVF) $\leftrightarrow$ (VVF) For C_1, we see that the maximal difference is at $\sqrt{\tau_c}(SVF) \sim 1$ and $\sqrt{\tau_c}(VVF) \sim 0$. This is the case where in the TH formulas we have for (VFV) a maximal contribution from the prefactors of J_7^N and J_5^N but a vanishing prefactor of J_2^N and J_6^N in (SVF). For C_2 we have a large deviation for all $\sqrt{\tau_c}$ with $\Delta = (7.66 \ldots 12.2) \cdot 10^{-3}$ (7 TeV) and $\Delta = (1.8 \ldots 3.8) \cdot 10^{-3}$ (14 TeV) translating to a minimum number of 553 and 1284 events. Since we have four contributing Jacobians for these processes, we have a non vanishing difference everywhere. A comparison plot is shown in figure 5.17.

• (SFV) $\leftrightarrow$ (SFS) The deviation between these two spin scenarios is rather small. As we can see in figures 5.13(d) and 5.13(c), both scenarios have a small deviation from PS. While these differences are stronger in some other cases, here we have both depending similarly on J_2^N. Since we have chosen a different δ^2, the difference is largest for both $\sqrt{\tau_c}(SFS) \sim 0$ or $\sqrt{\tau_c}(SFV) \sim 1$. The minimum number of events in the best case is 2456.

• (SFV) $\leftrightarrow$ (VFS) The deviation here is minimal at C_2 for $\sqrt{\tau_c}(SFV) \sim 0$. The prefactor of J_2^N in equation 5.33c is 1 and so both 5.33d and 5.33c have the same

dependence on J_2^N. In the case of C_1, we have a small deviation that maximizes in the case of $\sqrt{\tau_c}(SFV) \sim 1$ with $\Delta = 7.3 \cdot 10^{-3}$ (939 events) for C_2, 7 TeV. A comparison plot is shown in figure 5.17.

• (SFV) $\leftrightarrow$ (VVF) In this case, all deviations are rather small. For C_1, we have the largest deviation in the region where both $\sqrt{\tau_c} \sim 1$, but for C_2, it is maximal for $\sqrt{\tau_c}(VVF) \sim 1$ and in the low region for $\sqrt{\tau_c}(SFV) \sim 0$. In this region, (SFV) has the most deviation from PS for C_2. The largest Δ is at C_2 for 14 TeV with $\Delta = 2.8 \cdot 10^{-3}$ corresponding to 2504 events.

• (VVF) $\leftrightarrow$ (SFS) For C_1, (SFS) does not show a large $\sqrt{\tau_c}$ dependence and also (VVF) has only small deviation from PS over the range of $\sqrt{\tau_c}$, and thus we find a rather constant deviation for C_1 with $\Delta \sim 1 \cdot 10^{-3}$. In the case of C_2, we have a constant deviation from PS for both distributions, which results in a deviation from each other since three different Jacobian factors J_2^N, J_5^N, J_6^N contribute. We get a maximal deviation of $\Delta = 2.9 \cdot 10^{-3}$ ($\sim$ 2370 events) for C_2, 14 TeV and both $\sqrt{\tau_c}$ maximized.

• (VVF) $\leftrightarrow$ (VFS) Between these two scenarios we have a larger deviation in C_2. We have the same prefactors and Jacobians contributing as in the last case. However, the sign of J_2^N in (VFS) is flipped which has a stronger effect on the comparison of these two spin scenarios. The maximum is for large $\sqrt{\tau_c}(VVF) \sim 1$ with $\Delta = 3.35 \cdot 10^{-3}$ (C_1) and $\Delta = 5.4 \cdot 10^{-3}$ (C_2) corresponding to 1269 and 994 events respectively.

• (VFS) $\leftrightarrow$ (SFS) Two comparison plots are shown in figure 5.17. In the case of C_1, there is good discrimination power for $\sqrt{\tau_c} \sim 1$ for both energies, with the maximal deviation of $\Delta = 4.5(4.2) \cdot 10^{-3}$ (7/14 TeV) corresponding to 1528/1631 events. Here, both spin scenarios show only a slight mass dependence and resemble PS in this coupling scenario. The comparably large Δ comes from the fact that the δ^2 is very different for both scenarios and the interpolation function even has a different sign. For C_2, we have a constant deviation from PS for (VFS) and only a slight deviation for (SFS). The maximal $\Delta = 5.07/2.17 \cdot 10^{-3}$ (7/14 TeV) (corresponding to 1377/3191 events) is in a region of small $\sqrt{\tau_c}(SFS)$.

We summarize the KL distances and the corresponding events in the tables 5.6 and 5.5 for all minimal and maximal deviations.

5.4.3 Examples: Susy and UED

We want to close this chapter by showing the distributions with PDFs for a complete UED and Susy scenario in comparison to the fixed $\sqrt{\hat{s}}$ distributions. In both scenarios we discuss di-lepton production in association with two respective DM candidates.
For the UED example, we choose a study point with $\Lambda R = 20$, $R^{-1} = 500$ GeV. The resulting masses for the B' in MUED are $m_{e'_R} = 505$ GeV, $m_{e'_L} = 515$ GeV and $m_{B'} = 500$ GeV ($\tau_c = 0.98$). For the analytic distribution with which we compare the model (VFV), we choose δ^2 according to table 5.3 as 0.23 (7 TeV) and 0.29 (14 TeV). We show the corresponding distributions on the left side of

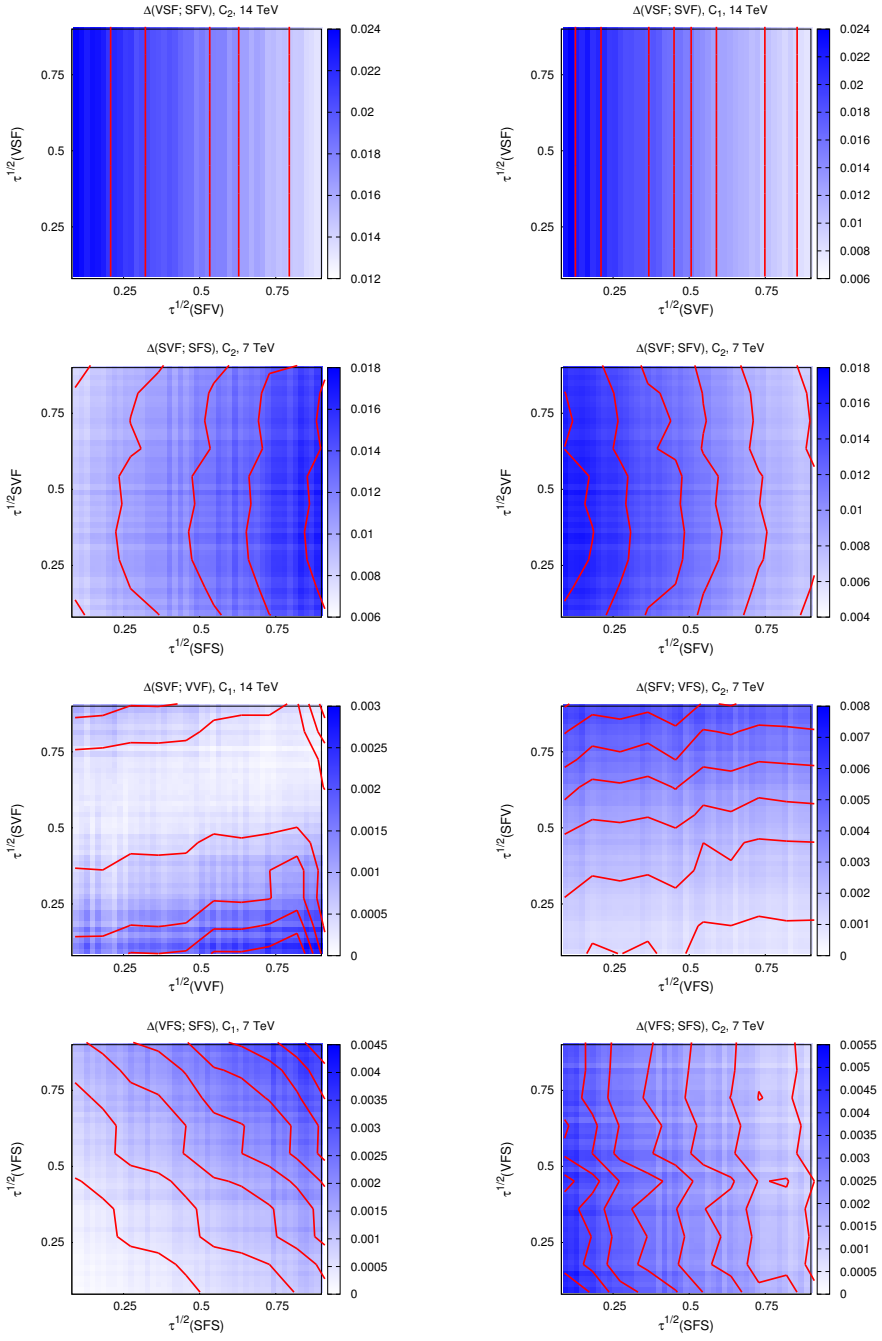

Figure 5.17: Comparison plots for different spin scenarios.

		(SFS;SVF)	**(SFV;SVF)**	**(VFS;SVF)**
7 TeV				
C_1	Min.	(0.12; 0.33; 0.03; 300k)	(0.12; 0.23; 0.05; 150k)	(0.73; 0.93; 0.01; 10^6)
C_1	Max.	(0.96; 0.95; 4.08; 1670)	(0.96; 0.95; 3.97; 1719)	(0.93; 0.12; 3.16; 2198)
C_2	Min.	(0.10; 0.93; 7.5; 902)	(0.96; 0.93; 5.23; 1302)	(0.84; 0.93; 20.8; 325)
C_2	Max.	(0.95; 0.5; 17.9; 376)	(0.10; 0.50; 17.6; 382)	(0.15; 0.50; 27.7; 243)
14 TeV				
C_1	Min.	(0.19; 0.71; 0.01; 10^6)	(0.39; 0.51; 0.06; 122k)	(0.39; 0.86; 0.01; 10^6)
C_1	Max.	(0.10; 0.12; 2.98; 2367)	(0.95; 0.96; 2.37; 2884)	(0.96; 0.12; 7.50; 930)
C_2	Min.	(0.12; 0.12; 3.95; 1712)	(0.96; 0.10; 1.5; 4644)	(0.91; 0.12; 7.48; 905)
C_2	Max.	(0.96; 0.96; 9.5; 713)	(0.10; 0.96; 9.4; 720)	(0.14; 0.96; 15.4; 440)

		(VVF;SVF)	**(SFS;VVF)**	**(VFS;VVF)**
7 TeV				
C_1	Min.	(0.41; 0.26; 0.04; 170k)	(0.66; 0.96; 0.01; 10^6)	(0.12; 0.89; 0.07; 100k)
C_1	Max.	(0.96; 0.95; 3.0; 2256)	(0.96; 0.89; 1.03; 6679)	(0.96; 0.96; 3.35; 2083)
C_2	Min.	(0.96; 0.93; 7.66; 884)	(0.42; 0.19; 0.10; 70k)	(0.84; 0.17; 2.5; 2798)
C_2	Max.	(0.10; 0.50; 12.2; 553)	(0.96; 0.96; 1.6; 4285)	(0.15; 0.96; 5.4; 1269)
14 TeV				
C_1	Min.	(0.78; 0.77; 0.05; 150k)	(0.51; 0.26; 0.02; 500k)	(0.14; 0.89; 0.06; 122k)
C_1	Max.	(0.86; 0.12; 2.90; 2385)	(0.93; 0.86; 0.94; 7365)	(0.96; 0.96; 3.5; 2003)
C_2	Min.	(0.93; 0.10; 1.81; 3744)	(0.10; 0.19; 0.6; 11k)	(0.91; 0.19; 3.0; 2289)
C_2	Max.	(0.35; 0.96; 3.8; 1784)	(0.93; 0.93; 2.9; 2370)	(0.14; 0.93; 6.9; 994)

		(SFS;SFV)	**(VFS;SFV)**	**(VVF;SFV)**
7 TeV				
C_1	Min.	(0.69; 0.59; 0.00; 10^6)	(0.10; 0.12; 0.39; 17k)	(0.15; 0.17; 0.01; 10^6)
C_1	Max.	(0.12; 0.95; 0.85; 8153)	(0.96; 0.96; 4.3; 1617)	(0.89; 0.96; 0.99; 7149)
C_2	Min.	(0.50; 0.42; 0.01; 10^6)	(0.84; 0.10; 0.58; 11k)	(0.50; 0.60; 0.08; 84k)
C_2	Max.	(0.95; 0.95; 2.79; 2456)	(0.15; 0.96; 7.3; 939)	(0.96; 0.10; 1.47; 4726)
14 TeV				
C_1	Min.	(0.59; 0.42; 0.01; 10^6)	(0.10; 0.14; 0.22; 32k)	(0.96; 0.66; 0.01; 10^6)
C_1	Max.	(0.10; 0.95; 1.11; 6263)	(0.96; 0.95; 4.4; 1605)	(0.89; 0.95; 1.01; 6852)
C_2	Min.	(0.48; 0.26; 0.01; 10^6)	(0.91; 0.17; 0.4; 17k)	(0.75; 0.95; 0.17; 41k)
C_2	Max.	(0.96; 0.96; 2.06; 3312)	(0.14; 0.96; 5.3; 1298)	(0.93; 0.10; 2.8; 2504)

		(SFS;VFV)	**(SFV;VFV)**	**(VFS;VFV)**
7 TeV				
C_1	Min.	(0.10; 0.59; 0.12; 57k)	(0.14; 0.59; 0.5; 13k)	(0.24; 0.46; 0.00; 10^6)
C_1	Max.	(0.96; 0.48; 2.14; 3195)	(0.98; 0.48; 2.1; 3301)	(0.98; 0.59; 0.94; 7385)
C_2	Min.	(0.15; 0.35; 0.01; 10^6)	(0.78; 0.39; 0.0; 10^6)	(0.84; 0.10; 0.02; 300k)
C_2	Max.	(0.96; 0.66; 4.27; 1595)	(0.98; 0.10; 5.1; 1358)	(0.15; 0.66; 9.67; 705)
14 TeV				
C_1	Min.	(0.10; 0.11; 0.01; 10^6)	(0.14; 0.73; 0.18; 38k)	(0.15; 0.23; 0.01; 10^6)
C_1	Max.	(0.98; 0.68; 1.4; 4879)	(0.98; 0.67; 1.45; 4700)	(0.96; 0.73; 1.25; 5557)
C_2	Min.	(0.24; 0.26; 0.03; 230k)	(0.86; 0.39; 0.02; 300k)	(0.98; 0.12; 0.03; 200k)
C_2	Max.	(0.96; 0.73; 3.72; 1830)	(0.10; 0.73; 3.64; 1868)	(0.14; 0.73; 7.60; 894)

		(VVF;VFV)	**(VSF;VFV)**	**(SVF;VFV)**
7 TeV				
C_1	Min.	(0.89; 0.93; 0.12; 56k)	(0.10; 0.48; 5.32; 1312)	(0.60; 0.28; 0.01; 10^6)
C_1	Max.	(0.96; 0.48; 1.4; 4874)	(0.10; 0.59; 6.34; 1102)	(0.12; 0.14; 1.29; 5307)
C_2	Min.	(0.50; 0.35; 0.14; 48k)	(0.10; 0.66; 5.56; 1256)	(0.93; 0.66; 3.56; 1961)
C_2	Max.	(0.96; 0.10; 3.63; 1906)	(0.10; 0.10; 25.0; 283)	(0.50; 0.10; 23; 310)
14 TeV				
C_1	Min.	(0.73; 0.44; 0.06; 110k)	(0.10; 0.84; 9.55; 735)	(0.84; 0.24; 0.01; 10^6)
C_1	Max.	(0.96; 0.68; 0.91; 7450)	(0.10; 0.73; 10.6; 660)	(0.12; 0.84; 3.27; 2100)
C_2	Min.	(0.75; 0.48; 0.21; 32k)	(0.10; 0.73; 9.34; 750)	(0.10; 0.73; 0.58; 12k)
C_2	Max.	(0.93; 0.10; 4.37; 1588)	(0.10; 0.10; 27.78; 256)	(0.98; 0.10; 11.80; 595)

Table 5.5: Maximal and minimal Δ for various scenarios. The numbers are $(\sqrt{\tau_c}(X); \sqrt{\tau_c}(Y);\ \Delta \cdot 10^3,\ \#evts)$ of **(X;Y)**

		(SFS;VSF)	(SFV;VSF)	(VFS;VSF)
7 TeV				
C_1	Min.	(0.10; 0.10; 7.99; 852)	(0.10; 0.10; 10.2; 665)	(0.96; 0.10; 2.75; 2484)
C_1	Max.	(0.96; 0.10; 14.10; 481)	(0.96; 0.10; 13.8; 489)	(0.10; 0.10; 6.78; 1006)
C_2	Min.	(0.10; 0.10; 10.34; 658)	(0.96; 0.10; 7.6; 897)	(0.84; 0.10; 25.3; 267)
C_2	Max.	(0.95; 0.10; 19.4; 348)	(0.10; 0.10; 18.9; 356)	(0.15; 0.10; 29.8; 227)
14 TeV				
C_1	Min.	(0.10; 0.10; 10.1; 672)	(0.14; 0.10; 13.01; 521)	(0.96; 0.10; 4.63; 1478)
C_1	Max.	(0.93; 0.10; 17.4; 389)	(0.95; 0.10; 17.8; 380)	(0.10; 0.10; 10.0; 678)
C_2	Min.	(0.10; 0.10; 19.25; 351)	(0.96; 0.10; 12.3; 551)	(0.91; 0.10; 28.2; 239)
C_2	Max.	(0.87; 0.10; 24.16; 279)	(0.10; 0.10; 23.9; 281)	(0.14; 0.10; 33.7; 200)

		(VVF;VSF)	(SVF;VSF)	(SFS;VFS)
7 TeV				
C_1	Min.	(0.89; 0.10; 7.6; 900)	(0.96; 0.10; 3.1; 2200)	(0.10; 0.10; 0.07; 97k)
C_1	Max.	(0.96; 0.10; 12.1; 562)	(0.12; 0.10; 11.7; 581)	(0.96; 0.96; 4.5; 1528)
C_2	Min.	(0.96; 0.10; 10.2; 664)	(0.91; 0.10; 0.13; 53k)	(0.95; 0.84; 0.48; 14k)
C_2	Max.	(0.10; 0.10; 13.0; 520)	(0.19; 0.10; 0.67; 10330)	(0.10; 0.15; 5.07; 1377)
14 TeV				
C_1	Min.	(0.89; 0.10; 10.5; 649)	(0.93; 0.10; 7.37; 924)	(0.10; 0.14; 0.02; 350k)
C_1	Max.	(0.96; 0.10; 16.0; 424)	(0.12; 0.10; 23.9; 283)	(0.93; 0.96; 4.2; 1631)
C_2	Min.	(0.93; 0.10; 10.5; 642)	(0.96; 0.10; 3.7; 1860)	(0.82; 0.59; 0.34; 20k)
C_2	Max.	(0.19; 0.10; 13.7; 493)	(0.12; 0.10; 8.2; 839)	(0.10; 0.14; 2.17; 3191)

Table 5.6: Same as table 5.5.

figure 5.18. The simulation and the fixed $\sqrt{\hat{s}}$ results coincide very well. The deviation from PS is, as discussed and expected, very small since τ_c is close to 1. The Susy example was considered with intermediate $\tilde{e}_R$ and $\tilde{e}_L$ and t-channel squarks. We have chosen a mass point where $m_{\tilde{\chi}_0} = 118$ GeV, $m_{\tilde{e}_L} = 206$ GeV, $m_{\tilde{e}_R} = 119$ GeV. We show the distributions on the right side of figure 5.18 and as in the UED example, the analytic result for fixed $\sqrt{\hat{s}}$. The simulations coincide very well despite the many diagrams beyond the simple antler topology that are included in the CalcHep simulation. Furthermore we see that both shapes are distinguishable although both spin scenarios basically resemble PS, but at different energies. For UED, the fixed δ^2 approach mimics the $\sqrt{\hat{s}}$ distribution of the PDFs at the maximal production as assumed. For Susy, the PS at TH result is also in very good agreement with the CalcHep results. We have used CTEQ5M PDF sets in all simulations.

5.5 Summary

In this chapter we have studied the antler diagram which is the s-channel $2 \to 4$ topology with two visible leptons and two invisible particles in the final state. We have picked a certain variable, a function of the difference of the pseudorapidities of the two visible leptons, $\mathcal{C}_B$, which is discussed in the literature as a tool to discriminate between UED and Susy in this topology. We have studied the phase space distribution of this variable that carries no spin information, and the corresponding deviations from it for the 8 different spin scenarios which can be assigned to this topology. We have addressed the question how the mass and coupling scenario can influence this distribution and hide or reveal the spin

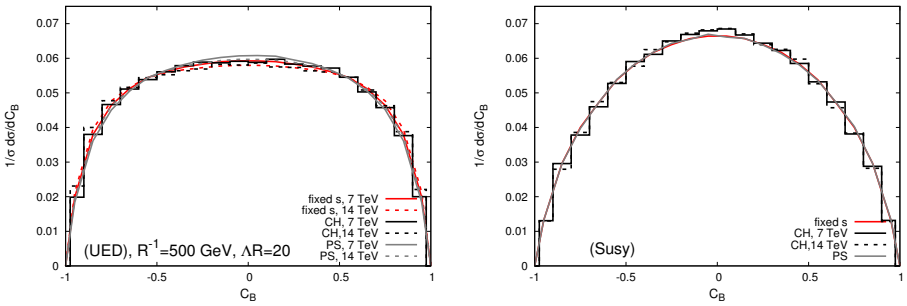

Figure 5.18: Left: Simulated UED distributions for 7 and 14 TeV and in comparison the corresponding distributions for fixed $\sqrt{\hat{s}}$. The simulation and fixed $\sqrt{\hat{s}}$ result coincide but both show only little deviation from PS. Right: Simulated Susy distributions for 7 and 14 TeV. CH denotes the CalcHep simulation with PDFs at 7/14 TeV.

information.
In the limit where the energy is very large in comparison to the intermediate particles' mass, one has the high energy relations given in equation 5.2 between the $\mathcal{C}_B$ distribution for UED and Susy which can thus be discriminated in this case. We have investigated the limit where these relations are not valid. In a first step we have calculated the complete squared matrix elements for the processes for a fixed energy, and then have taken the limit where the intermediate on-shell particles are produced at threshold. We have derived the corresponding differential cross sections in terms of $\mathcal{C}_B$. As a result, we have found that they give simple dependences on the masses and couplings which are however more involved than the high energy limit.
With protons in the initial state, one has to separate the spin effects coming from the matrix elements squared and the energy smearing of the PDFs. We have chosen a fixed $\sqrt{\hat{s}}$ approach which is supposed to disentangle these two effects. In Section 5.3 we have determined a suitable fixed $\sqrt{\hat{s}}$ with which one can mimic the peaking $\sqrt{\hat{s}}$ distribution of the PDFs. This can be done in a region close to the threshold of the two B particles.
In a third step, we investigate for each spin scenario the deviation from phase space and from the other spin scenarios with the help of the full calculation at this fixed $\sqrt{\hat{s}}$. We saw that for specific mass and coupling scenarios, the distributions resemble phase space and no spin effects are present, while for other scenarios the distributions are rather distinct from phase space and carry spin information. We saw that these dependences can be traced back very well to the threshold results which therefore can be used as a first means to decide for which scenario the discrimination is at least possible.
In Section 5.4 we have investigated the pairwise difference of distributions belonging to different spin assignments. As a distance measure we use the symmetrized Kullback-Leibler distance, which also allows to estimate the minimal number of events needed for the discrimination of two models. We found that for some scenarios, there is always good discrimination power between the different sce-

narios, while for others, the distributions resemble phase space and cannot be discriminated from each other. In summary, we have concluded that:

- (SSF) resembles phase space for all scenarios and hence carries no spin information as expected.

- Besides for (VVF) and (SVF), spin effects at threshold only come in via chiral couplings, where pure left or right handed couplings have the largest impact. We saw in Section 5.4 that this is also true for the non-threshold distributions.

- (VSF), which includes the Susy scenario, resembles phase space at threshold for all masses and couplings for a large range of energies. This is due to the fact that the high energy limit of (VSF) and the threshold limit are very similar and one has the characteristic $1 - \cos^2\theta^*$ distribution already close to threshold. Therefore, (VSF) always has a large distance measure to the other scenarios and there is hence a good discrimination power.

- (VFV), which includes the UED scenario, also has spin dependence only for chiral couplings. The deviation between (VFV) and (VSF) for the Susy and UED case comes mainly from the fact that (VFV) resembles phase space, which changes with increasing energy and thus is distinct from the threshold result for (VSF). For degenerate masses where $\sqrt{\tau_c}(VFV) = 1$, the deviation from phase space is minimal.

- (VFS) and (SFS) only have coupling dependence and no mass dependence. They show a deviation from phase space for chiral couplings that does not change with varying mass ratios $\sqrt{\tau_c}$.

The largest discrimination power is that of (VSF) against the other models for almost all couplings and masses. Also notable is (VFS) with spin scenario C_2 which has a constant deviation from phase space and is thus well distinguishable from all other scenarios.
A particularly strong example is given by (VSF) $\leftrightarrow$ (VFS) with $\Delta = 33.7 \cdot 10^{-3}$ corresponding to a minimal number of 200 events needed for discrimination. This is followed by (SVF)$\leftrightarrow$ (SFS), (SFV), (VFS); (VFV)$\leftrightarrow$ (VFS), (VSF), (SVF); (VSF) $\leftrightarrow$ (SFS), (SFV), (VFS), (VVF), (SVF) for specific mass and coupling choices. These scenarios lie between a KL distance of $\Delta = 33.7 \cdot 10^{-3}$ and $5 \cdot 10^{-3}$ (200... 1350 events). Particularly bad examples include (VFS) $\leftrightarrow$ (SFS), (SVF); (VFV)$\leftrightarrow$ (SVF), (VVF), (SFS) ; (VVF)$\leftrightarrow$ (SFS), (SFV); (SFS)$\leftrightarrow$ (SVF), (SFV); (VSF)$\leftrightarrow$ (SVF) where $\Delta \leq 3 \cdot 10^{-3}$ ($>$ 2300 events). This is of course only true in the context of specific coupling and mass choices as discussed in Section 5.4.2. There are some scenarios where the deviation is rather large and constant for all mass scenarios. Those are (VSF)$\leftrightarrow$ (VFV); all (VSF) to the other scenarios besides (SVF) (C_2); (SVF) $\leftrightarrow$ (SFS), (VFS) (C_2); (SVF) $\leftrightarrow$ (VVF).
Of course the deviation between two scenarios can change from e.g. $\Delta = 0.01 \cdot 10^{-3}$ to $\Delta = 7.5 \cdot 10^{-3}$ ((VFS)$\leftrightarrow$ (SVF), corresponding to 10^6 vs. 930 events) within one coupling scenario depending on the mass ratios $\sqrt{\tau_c}$.

There are several issues which we have not covered in this chapter. Since our studies are model independent, we did not take SM backgrounds into account which have to be included in a more detailed study. An interesting topic is also the question to which extend the $\mathcal{C}_B$ distributions change if one includes initial state radiation and cuts. As we have seen in the example of Susy and UED, one can also have t-channel contributions. Simulations have shown that they have only negligible influence on the distributions. However, it would be interesting to see, how t-channel diagrams influence the $\mathcal{C}_B$ distributions and possibly add another uncertainty to spin determination. Although these problems are important and should not be neglected, most of them can only be investigated in the context of a specific model. This is beyond the scope of this work and is left for future studies.

We have seen that, although the variable $\mathcal{C}_B$ works satisfactorily for the discrimination of some models, it is not a variable that can distinguish the spin scenarios uniquely (which it already does not for the high energy limit, cf. equation 5.2). By comparing the threshold matrix element formulas in equation 5.27 and the threshold formulas in equation 5.33 we see that due to the symmetry of the variable $\mathcal{C}_B$, additional information that is originally in the matrix element is sometimes lost after rewriting it as a function of $\mathcal{C}_B$. We have also seen that the spin, mass and coupling dependence can be read off from the threshold formulas we give in equation 5.33. One has to note here, that also some of the full results for the non-threshold formulas in equation 5.26, e.g. (SSF), never show any angular distribution that is distinct from phase space. In such a case one has to take other observables, such as the production cross section, into account. However, this cannot be done for generic spin scenarios since one has to know the total coupling strength.

Chapter 6

Conclusion

> *I have no data yet. It is a capital mistake to theorise before one has data. Insensibly one begins to twist facts to suit theories, instead of theories to suit facts.*
>
> (Sir Arthur Conan Doyle,
> Sherlock Holmes in "The Adventures of Sherlock Holmes")

A new energy scale has become experimentally accessible for the first time as both ATLAS and CMS have recorded about 5 inverse femtobarns of data at 7 TeV by the end of 2011. Great expectations lie in the observations that can be made at these high energies and one hopes that possible discoveries answer some of the most compelling questions of particle physics. In the last decades a lot of effort went into the construction and phenomenology of new physics models. These new models are mostly designed to solve shortcomings of the Standard Model such as the lack of a Dark Matter candidate and the hierarchy problem, while being simultaneously compatible with all known experimental constraints. A challenge that comes with the potential observation of new physics is the determination of its nature. As we have seen, some models can have similar collider signatures due to their gauge quantum numbers and mass spectra. An important consequence of this is that the spin of new particles has to be determined in order to pin down the correct underlying theory. When considering UED and Susy for example, the spin of the particles can be the most significant difference in the accessible energy range and is therefore a powerful but also necessary tool to distinguish between those two models.
This is primarily done with the help of decay chains which are typical in scenarios with a conserved parity. It is possible to fix spins of known particles and vary those of the unknown ones. One then investigates the suitable variables, mostly the invariant masses, which can be constructed from the visible parts of the decay chains. Depending on the couplings and masses, one can assign a specific spin to the particles involved.
However, there are some restrictions to this method which we have investigated in this thesis.
In Chapter 3 we have studied the influence of non-renormalizable couplings on spin determination via the invariant mass distribution. We have seen that ef-

fective dimension 5 operators in principle have no effect on spin determination in decay chains. If one is however interested in detailed parameter determination concerning the couplings, their contributions cannot be neglected. We find that the leading contribution of the anomalous interactions is suppressed by the square of the scale of the dimension 5 operator. We have derived the analytic expressions for the modified differential decay widths which can be used as a basis for further studies of parameter determination.
In Chapter 4 we have turned our interest towards the question what the relation between the spin of the particles and the invariant mass is in the context of a decay that is mediated through a heavy off-shell particle instead of an on-shell subsequent decay. In some scenarios, subsequent two body decays are forbidden and three body decays show up that are normally suppressed by a phase space factor. We have worked out a complete strategy that is capable of determining the spin of the decaying and the invisible particles independently of the couplings and masses. We have shown in a Monte Carlo study how this strategy works and where it has problems. We have also investigated the influence of different topologies and the intermediate particle mass.
In Chapter 5 we have investigated a topology which is called "antler topology", that has short decay chains so that a suitable invariant mass can not be build for use in the conventional approach. We have picked a different variable that can in principle distinguish between Susy and UED in the limit of high energies. We have then turned our interest to a different limit that is appropriate for heavier particles involved. We have derived, analogous to the high energy limit, equations for the threshold limit and discussed how one can choose an appropriate energy that can be used to mimic PDF effects. With the help of this fixed $\sqrt{\hat{s}}$ approach, we have been able to study the influences of masses and couplings. We have seen that some scenarios resemble the phase space distribution and the spin information is lost depending on the specific choice of masses and couplings, while for others the variable works well. We have compared the different spin assignments for varying masses and couplings and used a distance measure to estimate the minimal number of events needed to distinguish between these scenarios. We found that the (VSF) distributions, which contain the Susy case, have a characteristic shape for all masses and a wide energy range that makes them easy to discriminate from the other 7 scenarios. For the other cases, we found that the discrimination power of the variable in question strongly depends on the masses and the couplings. Consequently one does not have a unique discrimination variable, but one that is useful in specific scenarios and regions of parameter space.

Numerous approaches to spin determination were proposed in the literature which work well in selected models and mass scenarios. We have pursued a systematic approach to spin determination that is unbiased and does not restrict itself to the comparison of two or three particular models. We have seen that, although possible in an ideal world, it is mostly only reasonable to exclude rather than to confirm a particular spin assignment if one has to deal with finite statistics. We

have also seen that the masses and couplings can play an important role in the discrimination power of variables and that some models can mimic others. This is a crucial point in spin determination and has to be pursued further.
As soon as new particles are detected at ATLAS and CMS, one has to make sure that the underlying model is not misidentified due to theoretical prejudice. To avoid this, it might be important to investigate further, which approaches are useful for the different topologies, decay channels and kinematical scenarios. It is therefore important to explore the viability of the different observables, combine them and, if necessary, introduce new ones such that different approaches complement each other systematically.

Appendix A

Models for Monte Carlo Generators

Slow I go
And the wait seems to be over

(In Flames, "System")

In this thesis, we have used two different matrix element and Monte Carlo (MC) generators: WHIZARD/O'Mega [56, 57], CalcHep [78, 79] and Madgraph [82] in combination with Feynrules [83] and we have implemented a generic model adapted to the respective problem which we will describe in the following. We have used Madgraph only for cross checks and will not go into this implementation.

A.1 Model for O'Mega/WHIZARD

For the validation and investigation of the decay chains in chapter 4, we have implemented a generic model in O'Mega/WHIZARD which allows to let generic particles decay with the desired couplings without being bound to a specific model. The original version of the two models are for O'Mega/WHIZARD 1.x, but there also exists a later version for WHIZARD 2.x.
WHIZARD is a powerful and multifunctional Monte Carlo generator for arbitrary partonic processes in the Standard Model and beyond. The necessary tree level matrix elements are provided by the Optimized Matrix Element Generator O'Mega or can be interfaced in different ways. O'Mega/WHIZARD can be downloaded at

`http://projects.hepforge.org/whizard/`.

Our generic model file for O'Mega includes generic vector, scalar and fermionic (both Dirac and Majorana) particles with general left and right handed couplings. The model files and detailed installation instructions can be found at

`http://theorie.physik.uni-wuerzburg.de/~ledelhaeuser/lama/lama.html`.

The model file is called LAMA (=Little Arbitrary Model Application) and the implementation comes with the following files

1. LAMAnual.pdf
2. `modelsLAMA.ml` LAMA Model file for O'Mega
3. `f90_LAMA.ml`
4. `parameters.LAMA.omega.f90` LAMA Model/parameter file for WHIZARD
5. `readincoupl.pl, LAMAmake, LAMAraw, LAMA.mdl` Scripts for changing the couplings

Generic interactions and implementation

Here we have summarized some parts of the model file and the parameter file. Our model file provides scalar (generically denoted with S, charged and uncharged), vector (V, charged and uncharged) and fermion (Majorana (M) and Dirac (F)) particles in three types of "flavor" $i = 1, 2, 3$ each,

$$f_i^{\pm}, m_i, v_i, s_i, s_i^{\pm}, v_i^{\pm}. \tag{A.1}$$

This allows for example to have a heavy scalar decaying into two fermions and a light scalar with a very heavy fermion inbetween. The provided couplings including fermion particles are $(i, j, k = 1, 2, 3)$

$$V_i F_j^{\pm} F_k^{\mp}; \qquad S_i F_j^{\pm} F_k^{\mp}; \tag{A.2a}$$

$$M_i V_j^{\pm} F_k^{\mp}; \qquad M_i S_j^{\pm} F_k^{\mp}. \tag{A.2b}$$

The first line contains the vertices which have two charged fermions, in the second line, there is one uncharged fermion and one charged fermion with charged bosons. These are all the vertices which are needed for the first two topologies in Chapter 4. One of the charged fermions plays the role of the SM-fermion in the three body decays. For the third topology, one needs also the following interactions of either three bosons or two uncharged Majorana particles

$$V_i V_j V_k \qquad S_i V_j V_k \qquad V_i V_j V_k \qquad S_i S_j S_k \tag{A.3a}$$

$$M_i S_j M_k; \qquad M_i V_j M_k. \tag{A.3b}$$

The files which had to be changed are:

• `/whizard-1.92/omega-src/bundle/src/models.ml:`

`module LAMA`; Definition of particles:

```
type flavor =
  | PFermion of neuf  | PAFermion of neuf
  | PVector of neuv
  | PVectorPlus of neuvm   | PVectorMinus of neuvm
  | PMajorana of neum
  | PScalar of neus
  | PScalarPlus of neusm    | PScalarMinus of neusm
```

The generic particle types, e.g. for f or v, are denoted with `neuf` or `neuv`. If the particle is charged, then it has the additional letter "m" for minus, e.g. `neuvm`. The coupling constants are now defined as a type depending on the three flavours

```
    type constant = | G_vnfpfm of neuf*neuv*neuf  | G_snfpfm of neuf*neus*neuf
                    | G_vmfpm of neum*neuvm*neuf  | G_spfmm of neum*neusm*neuf
                    | G_smfpm of neum*neusm*neuf  | G_vpfmm of neum*neuvm*neuf
```

after defining the conjugate particle, the Lorentz structure and so on which is quite clear from the context, the vertices have to be defined:

```
let scalarvertices a n f =
   [
 (PAFermion a, PScalar n, PFermion f), FBF (1, Psibar, SLR, Psi),G_snfpfm (a,n,f)
   ]

let vectorvertices a n f =
   [
 (PAFermion a, PVector n, PFermion f), FBF (1, Psibar, VLR, Psi),G_vnfpfm (a,n,f)
   ]

let vectorvertices2 n m f =
   [
 (PMajorana n, PVectorPlus m, PFermion f), FBF (1, Chibar, VLR, Psi), G_vpfmm(n,m,f);
 (PAFermion f, PVectorMinus m, PMajorana n), FBF (1, Psibar, VLR, Chi), G_vmfpm (n,m,f)
   ]

let scalarvertices2 n m f =
   [
 (PMajorana n, PScalarPlus m, PFermion f), FBF (1, Chibar, SLR, Psi), G_spfmm (n,m,f);
 (PAFermion f, PScalarMinus m, PMajorana n), FBF (1, Psibar, SLR, Chi), G_smfpm (n,m,f)
   ]

let vertices () =
   (
 List.flatten (Product.list3 scalarvertices [F1;F2;F3] [S1;S2;S3] [F1;F2;F3]) @
 List.flatten (Product.list3 vectorvertices [F1;F2;F3] [V1;V2;V3] [F1;F2;F3]) @
 List.flatten (Product.list3 vectorvertices2 [M1;M2;M3] [VM1;VM2;VM3] [F1;F2;F3]) @
 List.flatten (Product.list3  scalarvertices2 [M1;M2;M3] [SM1;SM2;SM3] [F1;F2;F3])
   , [], [])
```

This defines e.g. the `scalarvertices` as a function of three arguments a,n,f which are the flavour types. The entry in the first bracket denotes the types of particles which are in the corresponding vertex, the second one, which type of interaction (here: FBF=Fermion-Boson-Fermion) and the last two entries give the interaction (SLR=Scalar-Left-Right) and the constant which is to be put there. The particles/antiparticles are chosen in such a way that:

Ψ: incoming fermion, outgoing antifermion
$\overline{\Psi}$: outgoing fermion, incoming antifermion

In the end, one has to map the O'Caml symbols to the Fortran symbols via

```
 let constant_symbol = function
| G_vnfpfm (a,n,f) -> "v"^string_of_neuv n^"f"^string_of_neuf a^"pf"^string_of_neuf f^"m"
| G_snfpfm (a,n,f) -> "s"^string_of_neus n^"f"^string_of_neuf a^"pf"^string_of_neuf f^"m"
| G_vpfmm (n,m,f)  -> "v"^string_of_neuvm m^"pf"^string_of_neuf f^"mm"^string_of_neum n
| G_vmfpm (n,m,f)  -> "v"^string_of_neuvm m^"mf"^string_of_neuf f^"pm"^string_of_neum n
| G_smfpm (n,m,f)  -> "s"^string_of_neusm m^"mf"^string_of_neuf f^"pm"^string_of_neum n
| G_spfmm (n,m,f)  -> "s"^string_of_neusm m^"pf"^string_of_neuf f^"mm"^string_of_neum n
```

so that the first letter gives either scalar or vector with its flavour number, if followed by a "m" (minus) or "p" (plus) the negative particle, the second entry gives the fermion or antifermion ("fp" or "fm") and the last one gives the third fermion ("fm") or the Majorana particle "m". The number between the particle type ("v") and its charge ("m") is indicating its type $1 \ldots 3$. For example, "s1f1pf2m" is the vertex with an uncharged scalar, an outgoing fermion type 1 and an incoming antifermion. This is a 2-dim. list of entries with the first entry

being the left handed and the second one being the right handed coupling.

• `/whizard-1.92/conf/models/LAMA.mdl`

In this file, the parameters and particles are defined. By default the couplings are all set to zero and the masses to a very large value. In `./readincoupl.pl` one can define the couplings which are needed and run it on `LAMAraw` which converts it into `LAMA.mdl` (which is actually done by the `LAMAmake` script) and sets the corresponding couplings to values which have to be written down in `./readincoupl.pl`. The particles are defined with their type, name, their quantum numbers, the LaTeXcode and its mass name as in this example of a fermion

```
1046 particle F_LEPTON1 11
1047   spin 1/2,  isospin -1/2,  charge  -1
1048   name f1-,          tex:f^-_1
1049   anti omega:f1+,     tex:f^+_1
1050   mass mfermi1
```

which is quite self explaining. In the end of this file there is a list of all possible couplings e.g. for some of the fermions

```
# f 1 m
vertex f1+ f1- v1
vertex f1+ f2- v1
vertex f1+ f3- v1
```

Last, we have the file `parameters.LAMA.omega.f90` which has a definition of all the O'Mega couplings and their corresponding WHIZARD naming. Due to some rule that the names can only have max. 8 characters, some renaming had to be done, in a way that the "fp" is called "a" (for antifermion). This means, that a coupling which looks like this in omega is converted into a WHIZARD name:

```
v1f1pf3m(2) =par%v1a1f32
```

which stands for vector (1), antifermion 1, fermion 3 (minus) and here (2) marks the right-handed component (which gives the last 2).

• Short explanation for `readincoupl.pl`

`readincoupl.pl` is a perl script which copies the `LAMAraw` into `LAMA.mdl` and replaces the values of the couplings and masses noted `readincoupl.pl` :

```
# "couplings"############################
#  g_LR
#
$zeile=~s/v1a1f21 0.0/v1a1f21 0.5/g;
$zeile=~s/v1a1f22 0.0/v1a1f22 0.5/g;
# complex conjugate
#
$zeile=~s/v1a2f11 0.0/v1a2f11 0.5/g;
$zeile=~s/v1a2f12 0.0/v1a2f12 0.5/g;
# second graph
#"coupling (if vector is uncharged)"
# g*_LR
$zeile=~s/v1a2f31 0.0/v1a2f31 0.5/g;
$zeile=~s/v1a2f32 0.0/v1a2f32 0.5/g;
#
# complex conjugate
$zeile=~s/v1a3f21 0.0/v1a3f21 0.5/g;
$zeile=~s/v1a3f22 0.0/v1a3f22 0.5/g;
```

This is just the first coupling. This example shows the decay $v_1 \to f_1, f_2, v_3$, with uncharged v_1, v_3. We have two possible graphs here, and thus four couplings $g_{L/R}$ and $g_{L/R}{}^*$ and $n_{L/R}$ and $n_{L/R}{}^*$.

A.2 Model for CalcHep/CompHep

The implementation in CalcHep/CompHep is specifically adapted for the antler processes in chapter 5.

Implementation of new variables

The variables which are implemented in CalcHep version 3.0 are defined in the file `phys_val.c` in `c_source/num/`. For our simulations in chapter 5, we need the invariant mass squared and $\mathcal{C}_B$ which are implemented with the following code in `phys_val.c` for use in the antler diagram. The invariant mass is

```
case 'V': /* invariant mass squared with two entries   */
     {
        do
          {
           if(lv[i]>nin_int) for(j=0;j<4;j++) pp[j] += V[4*(lv[i]-1)+j];
           else for(j=0;j<4;j++)           pp[j] -= V[4*(lv[i]-1)+j];
          } while(lv[++i]);
          s=pp[0]*pp[0]; for(j=1;j<4;j++) s -=pp[j]*pp[j];
         return s;
            }
```

so that one can call it with `V(P1,P2)` for particle P1 and P2. $\mathcal{C}_B$ is calculated with

```
case 'B':  /* Barr's Angle with two entries   */
{
        double barrangle;
double rap3;
double rap4;
        double p3[4];
        double p4[4];
    int    k;
     for(k=0; k<4; k++)
     {
p3[k] = V[4*(lv[0]-1)+k];
p4[k] = V[4*(lv[1]-1)+k];
              }

rap3 = 0.5 *log((p3[0]+p3[3])/(p3[0]-p3[3]));
rap4 = 0.5 *log((p4[0]+p4[3])/(p4[0]-p4[3]));

 barrangle = tanh(0.5*(rap3-rap4));
   return barrangle;
}
```

and is called by `B(P1,P2)` in CalcHep.

Particles and their notation

The particle naming is as in figure A.1 and we denote the particles in the s-channel collectively with index 1, the particles B with index 2 and the particles C with index 3. They can be either scalar (s), vector (v) or fermion (f). We denoted the SM-leptons with l_3. The masses are then denoted with "m" for mass, then by the particle type, e.g. "f" and the corresponding number, e.g. 3, so `mf3`. The witdh is the same but with w instead of m, e.g. `wf3`. The model file `SM generic` is a generic extension of the SM model file. We have added the particles we need for the investigations of the antler diagram to the SM particles. They are generically called scalar ("s"), vector ("v") or fermion ("f"), each coming with an index $1, 2, 3$ if they are representatives of particles A,B or C respectively. We

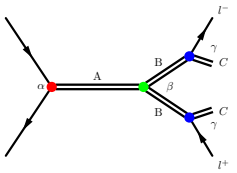

Figure A.1: Feynman diagramm with notation for CalcHep/CompHep.

decided to implement a generic SM-lepton, which plays the role of the observable final state particle later, as l_3, L_3, so that we can be free in choosing the couplings and mass. The particle definition is in `prtcls1.mdl` and is shown here. We have left out the SM particles except for the quarks:

```
SM generic
 Particles
 Full  name  |>A     <|>A <| number |2*spin| mass |width |color|aux|>LaTex(A)<|>LaTeX(A+)   <|
d-quark      |d      |D   |1       |1     |0     |0     |3    |   |d         |\bar{d}
u-quark      |u      |U   |2       |1     |0     |0     |3    |   |u         |\bar{u}
s-quark      |s      |S   |3       |1     |0     |0     |3    |   |s         |\bar{s}
c-quark      |c      |C   |4       |1     |Mc    |0     |3    |   |c         |\bar{c}
b-quark      |b      |B   |5       |1     |Mb    |0     |3    |   |b         |\bar{b}
t-quark      |t      |T   |6       |1     |Mt    |wt    |3    |   |t         |\bar{t}
```

The particles in the s-channel, here denoted by the index 1, are

```
vec-1        |v1     |v1  |10001   |2     |mv1   |wv1   |1    |   |v_1       |v_1
scal-1       |s1     |s1  |100011  |0     |ms1   |ws1   |1    |   |s_1       |s_1
```

The B-particles, denoted by the index 2 are

```
fermi-2      |f2     |F2  |10002   |1     |mf2   |wf2   |1    |-3 |f_2       |\bar{f}_2
scal-2       |s2     |S2  |100021  |0     |ms2   |ws2   |1    |-3 |s_2       |\bar{s}_2
vec-2        |v2     |V2  |100022  |2     |mv2   |wv2   |1    |-3 |v_2       |\bar{v}_2
```

And finally the C-particles, denoted by the index 3 are

```
scal-3       |s3     |s3  |10003   |0     |ms3   |ws3   |1    |   |s_3       |s_3
lepton-3     |l3     |L3  |10004   |1     |ml3   |wl3   |1    |   |l_3       |\bar{l}_3
vec-3        |v3     |v3  |100031  |2     |mv3   |wv3   |1    |   |v_3       |v_3
fermi-3      |f3     |F3  |100032  |1     |mf3   |wf3   |1    |   |f_3       |\bar{f}_3
```

We have also implemented some more particles which were used for generic decays and t-channel simulations, but are not relevant for the antler diagram:

```
I-vec        |VI1    |VI1 |100041  |2     |mvi   |wvi   |1    |   |          |
X-fermi      |x1     |X1  |100042  |1     |mx1   |wv1   |1    |   |          |
y-fermi      |y1     |Y1  |100043  |1     |my1   |wy1   |1    |   |          |
I-scal       |SI1    |SI1 |100044  |0     |msi   |wsi   |1    |   |          |
X-scal       |XS1    |XS1 |100045  |0     |mxs   |wxs   |1    |   |          |
X-vec        |XV1    |XV1 |100046  |2     |mxv   |wxv   |1    |   |          |
Y-scal       |YS1    |YS1 |100047  |0     |mys   |wys   |1    |   |          |
Y-vec        |YV1    |YV1 |100048  |2     |myv   |wyv   |1    |   |          |
F-I          |fI1    |FI1 |100049  |1     |mfi   |wfi   |1    |   |          |
Lepto-Vec    |w1     |W1  |100050  |2     |mw1   |ww1   |3    |   |w_1       |
Lepto-scal   |h1     |H1  |100051  |0     |mh1   |wh1   |3    |   |h_1       |
Lepto-scal   |h3     |H3  |100052  |0     |mh3   |wh3   |1    |   |h_3       |
```

Vertices

The implemented generic model is an extension of the SM, based on the SM model file. We have coupled the s-channel particles A to the quarks so that we can make use of the PDF implementation. The interactions of the particles are determined from the file `lgrng1.mdl` which we show here (without the SM model part). The interaction of the A particles to the quarks is:

```
SM generic
 Vertices
A1   |A2   |A3   |A4   |>        Factor            <|>  Lorentz part     <|
v1   |u    |U    |     |1                            |G(m1)*(Avl*(1-G5)+Avr*(1+G5))
v1   |d    |D    |     |1                            |G(m1)*(Avl*(1-G5)+Avr*(1+G5))
v1   |c    |C    |     |1                            |G(m1)*(Avl*(1-G5)+Avr*(1+G5))
v1   |s    |S    |     |1                            |G(m1)*(Avl*(1-G5)+Avr*(1+G5))
s1   |u    |U    |     |As                           |1
s1   |d    |D    |     |As                           |1
s1   |c    |C    |     |As                           |1
s1   |s    |S    |     |As                           |1
```

The interactions of the A to the B particles is defined here

```
f2   |F2   |v1   |     |1                            |G(m3)*(Bvl*(1-G5)+Bvr*(1+G5))
f2   |F2   |s1   |     |1                            |(Bsl*(1-G5)+Bsr*(1+G5))
s2   |S2   |v1   |     |Bvs                          |m3.(p1-p2)
s2   |S2   |s1   |     |Bss                          |1
v1   |v2   |V2   |     |Bvv                          |m1.m2*(p1-p2).m3+m2.m3*(p2-p3).m1+m3.m1*(p3-p1).m2
s1   |v2   |V2   |     |Bsv                          |m2.m3
```

and the interactions of the B to the C particles are

```
f2   |L3   |s3   |     |1                            |Csl*(1-G5)+Csr*(1+G5)
l3   |F2   |s3   |     |1                            |Csr*(1-G5)+Csl*(1+G5)
f2   |L3   |v3   |     |1                            |G(m3)*(Cvl*(1-G5)+Cvr*(1+G5))
l3   |F2   |v3   |     |1                            |G(m3)*(Cvl*(1-G5)+Cvr*(1+G5))
f3   |L3   |s2   |     |1                            |SCl*(1-G5)+SCr*(1+G5)
l3   |F3   |S2   |     |1                            |SCl*(1+G5)+SCr*(1-G5)
f3   |L3   |v2   |     |1                            |G(m3)*(VCl*(1-G5)+VCr*(1+G5))
l3   |F3   |V2   |     |1                            |G(m3)*(VCl*(1-G5)+VCr*(1+G5))
```

For the simulation of generic decays and t-channel diagrams, we have the following additional vertices, which are not needed for the antler diagram, but are useful anyway:

```
l3   |X1   |VI1  |     |1              |G(m3)*(VXl*(1-G5)+VXr*(1+G5))+A1*(G(m3)*G(p3)-G(p3)*G(m3))*(IxV+Ix5*G5)
x1   |L3   |VI1  |     |1              |G(m3)*(VXl*(1-G5)+VXr*(1+G5))+A1*(G(m3)*G(p3)-G(p3)*G(m3))*(IxV-Ix5*G5)
l3   |Y1   |VI1  |     |1              |G(m3)*(VYl*(1-G5)+VYr*(1+G5))+A2*(G(m3)*G(p3)-G(p3)*G(m3))*(IyV+Iy5*G5)
y1   |L3   |VI1  |     |1              |G(m3)*(VYl*(1-G5)+VYr*(1+G5))+A2*(G(m3)*G(p3)-G(p3)*G(m3))*(IyV-Iy5*G5)
l3   |X1   |SI1  |     |1              |(SXl*(1-G5)+SXr*(1+G5))+A3*G(p3)*(AxSi+AxPi*G5)
x1   |L3   |SI1  |     |1              |(SXl*(1+G5)+SXr*(1-G5))+A3*G(p3)*(AxSi+AxPi*G5)
l3   |Y1   |SI1  |     |1              |(SYl*(1-G5)+SYr*(1+G5))+A4*G(p3)*(AySi+AyPi*G5)
y1   |L3   |SI1  |     |1              |(SYl*(1+G5)+SYr*(1-G5))+A4*G(p3)*(AySi+AyPi*G5)
l3   |FI1  |XS1  |     |1              |(Xsl*(1-G5)+Xsr*(1+G5))+A5*i*G(p3)*(AxS+AxP*G5)
fI1  |L3   |XS1  |     |1              |(Xsl*(1+G5)+Xsr*(1-G5))+A5*i*G(p3)*(AxS+AxP*G5)
l3   |FI1  |YS1  |     |1              |(Ysl*(1-G5)+Ysr*(1+G5))+A6*i*G(p3)*(AyS+AyP*G5)
fI1  |L3   |YS1  |     |1              |(Ysl*(1+G5)+Ysr*(1-G5))+A6*i*G(p3)*(AyS+AyP*G5)
l3   |FI1  |XV1  |     |1              |G(m3)*(Xvl*(1-G5)+Xvr*(1+G5))+A7*(G(m3)*G(p3)-G(p3)*G(m3))*(AxV+Ax5*G5)
fI1  |L3   |XV1  |     |1              |G(m3)*(Xvl*(1-G5)+Xvr*(1+G5))+A7*(G(m3)*G(p3)-G(p3)*G(m3))*(AxV-Ax5*G5)
l3   |FI1  |YV1  |     |1              |G(m3)*(Yvl*(1-G5)+Yvr*(1+G5))+A8*(G(m3)*G(p3)-G(p3)*G(m3))*(AyV+Ay5*G5)
fI1  |L3   |YV1  |     |1              |G(m3)*(Yvl*(1-G5)+Yvr*(1+G5))+A8*(G(m3)*G(p3)-G(p3)*G(m3))*(AyV-Ay5*G5)
f2   |U    |w1   |     |1              |G(m3)*(wl*(1-G5)+wr*(1+G5))
u    |F2   |W1   |     |1              |G(m3)*(wl*(1-G5)+wr*(1+G5))
f2   |U    |h1   |     |1              |hl*(1-G5)+hr*(1+G5)
u    |F2   |H1   |     |1              |hr*(1-G5)+hl*(1+G5)
s2   |s3   |H3   |     |Ch3            |1
S2   |s3   |h3   |     |Ch3            |1
```

Finally one has to define the values of the coupling strengths, the particle masses and widths, which is done in `vars1.mdl`. Since the listing is straightforward, we will only give a short example:

```
SM generic
 Parameters
>Name         <| Value       |> Comment
mv1            |100          |Mvec1
wv1            |3            |width vec1
ms1            |100          |Mscal1
ws1            |3            |width scal1
Avl            |1            |left handed cpl vec
Avr            |1            |right handed cpl vec
Bvl            |1            |left handed B-v
Bvr            |1            |right handed B-v
Bsl            |1            |left handed B-s
Bsr            |1            |right handed B-s
```

Appendix B

Analytic Results

B.1 Appendix to Chapter 3: Anomalous couplings

We give here the analytic results for the decays in chapter 3. We use the following short forms for the couplings from equation 3.14 and 3.15 and the masses

$$\tau_I = \frac{m_I}{m_X}; \qquad \tau_Y = \frac{m_Y}{m_X}; \qquad 1/\Lambda_i = R_i = \frac{R'_i}{m_x};$$
$$g_V = g_r + g_l; \qquad g_A = g_r - g_l; \qquad n_V = n_r + n_l; \qquad n_A = n_r - n_l;$$

and analogous for $a_{l/r}, b_{l/r}, c_{l/r}, x_{l/r}, y_{l/r}, z_{l/r}$. As a complete example we give the decay $S \to f\bar{f}S$. The remaining decays are displayed up to the order of $R'^2 \propto 1/\Lambda^2$ where we have set $R'_x = R'_y = R'_z = R'_a = R'_b = R'_c = R'$. The decays (V,V) is only shown for the couplings $x_{A/V}, a_{A/V}$ since the complete result is very long. The NWA result in terms of these is separated in

$$\frac{d\,\Gamma}{d\,s_{ff}} \propto (A_{D4} + A_{D5}) + (B_{D4} + B_{D5}) \cdot s_{ff} + (C_{D4} + C_{D5}) \cdot s_{ff}^2. \tag{B.1}$$

- (S, S):

$$\begin{aligned}
A_{D4} =& 2m_X^2 \left(1-\tau_I^2\right)(\tau_I-\tau_Y)(\tau_I+\tau_Y)\left(g_A^2\left(n_A^2+n_V^2\right)+4g_Ag_Vn_An_V+g_V^2\left(n_A^2+n_V^2\right)\right)\\
B_{D4} =& -16g_A\ g_V\ n_A\ n_V\ \tau_I^2\\
A_{D5} =& -2m_X^2\tau_I^2\left(\tau_I^2-1\right)(\tau_I-\tau_Y)(\tau_I+\tau_Y)\times\\
&\Big(a_A^2R_a^{'2}\Big(n_A^2+n_V^2+\tau_I^2\Big(R_x^{'2}\left(x_A^2+x_V^2\right)-2R'_xR'_z(x_Az_A+x_Vz_V)+R_z^{'2}\left(z_A^2+z_V^2\right)\Big)\Big)\\
&+2a_AR'_a\left(\tau_I^2\left(2(a_VR'_a-c_VR'_c)(R'_xx_A-R'_zz_A)(R'_xx_V-R'_zz_V)\right.\right.\\
&\left.-c_AR'_c\Big(R_x^{'2}\left(x_A^2+x_V^2\right)-2R'_xR'_z(x_Az_A+x_Vz_V)+R_z^{'2}\left(z_A^2+z_V^2\right)\Big)\right)\\
&+2a_Vn_An_VR'_a-R'_c\left(c_A\left(n_A^2+n_V^2\right)+2c_Vn_An_V\right))\\
&+\tau_I^2\Big(a_V^2R_a^{'2}\Big(R_x^{'2}\left(x_A^2+x_V^2\right)-2R'_xR'_z(x_Az_A+x_Vz_V)+R_z^{'2}\left(z_A^2+z_V^2\right)\Big)\\
&-2a_VR'_aR'_c\left(2c_A(R'_xx_A-R'_zz_A)(R'_xx_V-R'_zz_V)\right.\\
&\left.+c_V\Big(R_x^{'2}\left(x_A^2+x_V^2\right)-2R'_xR'_z(x_Az_A+x_Vz_V)+R_z^{'2}\left(z_A^2+z_V^2\right)\Big)\right)\\
&+R_c^{'2}\Big(c_A^2\Big(R_x^{'2}\left(x_A^2+x_V^2\right)-2R'_xR'_z(x_Az_A+x_Vz_V)+R_z^{'2}\left(z_A^2+z_V^2\right)\Big)\\
&+4c_Ac_V(R'_xx_A-R'_zz_A)(R'_xx_V-R'_zz_V)
\end{aligned}$$

$$
\begin{aligned}
&+c_V^2\left(R_x^{'2}\left(x_A^2+x_V^2\right)-2R'_xR'_z(x_Az_A+x_Vz_V)+R_z^{'2}\left(z_A^2+z_V^2\right)\right)\Big)\Big)\\
&+a_V^2n_A^2R_a^{'2}+a_V^2n_V^2R_a^{'2}-4a_Vc_An_An_VR'_aR'_c-2a_Vc_Vn_A^2R'_aR'_c-2a_Vc_Vn_V^2R'_aR'_c\\
&+c_A^2n_A^2R_c^{'2}+c_A^2n_V^2R_c^{'2}+4c_Ac_Vn_An_VR_c^{'2}+c_V^2n_A^2R_c^{'2}+c_V^2n_V^2R_c^{'2}\\
&+g_A^2\left(R_x^{'2}\left(x_A^2+x_V^2\right)-2R'_xR'_z(x_Az_A+x_Vz_V)+R_z^{'2}\left(z_A^2+z_V^2\right)\right)\\
&+4g_Ag_V(R'_xx_A-R'_zz_A)(R'_xx_V-R'_zz_V)\\
&+g_V^2\left(R_x^{'2}\left(x_A^2+x_V^2\right)-2R'_xR'_z(x_Az_A+x_Vz_V)+R_z^{'2}\left(z_A^2+z_V^2\right)\right)\Big)\\
B_{D5}=&-16\tau_I^4\left((a_AR'_a-c_AR'_c)(a_VR'_a-c_VR'_c)\left(n_An_V\right.\right.\\
&\left.\left.+\tau_I^2(R'_xx_A-R'_zz_A)(R'_xx_V-R'_zz_V)\right)+g_Ag_V(R'_xx_A-R'_zz_A)(R'_xx_V-R'_zz_V)\right)
\end{aligned}
$$

In the following we show the results for the leading order in R'^2.

- (S,S):

$$
\begin{aligned}
A_{D5}=&\,2m_X^2R'^2\tau_I^2\left(1-\tau_I^2\right)(\tau_I-\tau_Y)(\tau_I+\tau_Y)\times\\
&\times\left(n_A^2\left((a_A-c_A)^2+(a_V-c_V)^2\right)+4n_An_V(a_A-c_A)(a_V-c_V)+n_V^2\left((a_A-c_A)^2+(a_V-c_V)^2\right)\right.\\
&\left.+g_A^2\left((x_A-z_A)^2+(x_V-z_V)^2\right)+4g_Ag_V(x_A-z_A)(x_V-z_V)+g_V^2\left((x_A-z_A)^2+(x_V-z_V)^2\right)\right)\\
&+\mathcal{O}(R^{'3})\\
B_{D5}=&-16R'^2\tau_I^4(n_An_V(a_A-c_A)(a_V-c_V)+g_Ag_V(x_A-z_A)(x_V-z_V))+\mathcal{O}(R^{'3})
\end{aligned}
$$

- (S,V):

$$
\begin{aligned}
A_{D4}=&-2m_X^2\left(\tau_I^2-1\right)(\tau_I-\tau_Y)(\tau_I+\tau_Y)\left(g_A^2\left(n_A^2+n_V^2\right)+4g_Ag_Vn_An_V+g_V^2\left(n_A^2+n_V^2\right)\right)\\
B_{D4}=&-16g_Ag_Vn_An_V\tau_I^2\\
A_{D5}=&-\frac{m_X^2R'^2\left(\tau_I^2-1\right)(\tau_I-\tau_Y)(\tau_I+\tau_Y)}{2\tau_Y^2}\times\\
&\left(4a_A^2n_A^2\tau_I^4+4a_A^2n_V^2\tau_I^4+2\tau_I^2\tau_Y^2\left(4\left(n_A^2\left((a_A-c_A)^2+(a_V-c_V)^2\right)-4n_An_V(a_A-c_A)(a_V-c_V)\right.\right.\right.\\
&\left.\left.\left.+n_V^2\left((a_A-c_A)^2+(a_V-c_V)^2\right)\right)+g_A^2\left(16x_A^2+4x_A(y_A-z_A)+16x_V^2+4x_V(y_V-z_V)\right.\right.\right.\\
&\left.\left.\left.-(y_A-z_A)^2-(y_V-z_V)^2\right)+4g_Ag_V(2x_A(8x_V-y_V+z_V)-(y_A-z_A)(2x_V-y_V+z_V))+g_V^2\right.\right.\\
&\left.\left.\left(16x_A^2+4x_A(y_A-z_A)+16x_V^2+4x_V(y_V-z_V)-(y_A-z_A)^2-(y_V-z_V)^2\right)\right)\\
&+16a_Aa_Vn_An_V\tau_I^4-8a_Ac_An_A^2\tau_I^4-8a_Ac_An_V^2\tau_I^4-16a_Ac_Vn_An_V\tau_I^4+4a_V^2n_A^2\tau_I^4+4a_V^2n_V^2\tau_I^4\\
&-16a_Vc_An_An_V\tau_I^4-8a_Vc_Vn_A^2\tau_I^4-8a_Vc_Vn_V^2\tau_I^4+4c_A^2n_A^2\tau_I^4+4c_A^2n_V^2\tau_I^4+16c_Ac_Vn_An_V\tau_I^4\\
&+4c_V^2n_A^2\tau_I^4+4c_V^2n_V^2\tau_I^4+\tau_Y^4\left(g_A^2\left((4x_A-y_A+z_A)^2+(4x_V-y_V+z_V)^2\right)\right.\\
&\left.-4g_Ag_V(4x_A-y_A+z_A)(4x_V-y_V+z_V)+g_V^2\left((4x_A-y_A+z_A)^2+(4x_V-y_V+z_V)^2\right)\right)\\
&+g_A^2y_A^2\tau_I^4-2g_A^2y_Az_A\tau_I^4+g_A^2y_V^2\tau_I^4-2g_A^2y_Vz_V\tau_I^4+g_A^2z_A^2\tau_I^4+g_A^2z_V^2\tau_I^4-4g_Ag_Vy_Ay_V\tau_I^4\\
&+4g_Ag_Vy_Az_V\tau_I^4+4g_Ag_Vy_Vz_A\tau_I^4-4g_Ag_Vz_Az_V\tau_I^4+g_V^2y_A^2\tau_I^4-2g_V^2y_Az_A\tau_I^4+g_V^2y_V^2\tau_I^4\\
&-2g_V^2y_Vz_V\tau_I^4+g_V^2z_A^2\tau_I^4+g_V^2z_V^2\tau_I^4\Big)+\mathcal{O}(R^{'3})\\
B_{D5}=&\,\frac{4R'^2}{\tau_Y^2}\tau_I^2\left(2\tau_I^2\tau_Y^2(4n_An_V(a_A-c_A)(a_V-c_V)+g_Ag_V((y_A-z_A)(2x_V-y_V+z_V)\right.\\
&\left.-2x_A(8x_V-y_V+z_V)))+\tau_I^4(g_Ag_V(y_A-z_A)(y_V-z_V)-4n_An_V(a_A-c_A)(a_V-c_V))\right.\\
&\left.+g_Ag_V\tau_Y^4(4x_A-y_A+z_A)(4x_V-y_V+z_V)\right)+\mathcal{O}(R^{'3})
\end{aligned}
$$

- (V,S)

$$
\begin{aligned}
A_{D4}=&\,2m_X^2\left(1-\tau_I^2\right)(\tau_I-\tau_Y)(\tau_I+\tau_Y)\left(g_A^2\left(\tau_I^2+2\right)\left(n_A^2+n_V^2\right)\right.\\
&\left.+4g_Ag_Vn_An_V\left(\tau_I^2-2\right)+g_V^2\left(\tau_I^2+2\right)\left(n_A^2+n_V^2\right)\right)\\
B_{D4}=&-16g_Ag_Vn_An_V\tau_I^2\left(\tau_I^2-2\right)\\
A_{D5}=&-\frac{1}{2}m_X^2R'^2\left(\tau_I^2-1\right)(\tau_I-\tau_Y)(\tau_I+\tau_Y)\left(16a_A^2\left(2\tau_I^2+1\right)\left(n_A^2+n_V^2\right)\right.
\end{aligned}
$$

$$
\begin{aligned}
&+8a_A\left(2n_An_V\left(\tau_I^2(8a_V+b_V-c_V)-4a_V-b_V+c_V\right)-b_A\left(\tau_I^2-1\right)\left(n_A^2+n_V^2\right)\right.\\
&\left.+c_A\left(\tau_I^2-1\right)\left(n_A^2+n_V^2\right)\right)+2\tau_I^2\left(n_A^2\left(16a_V^2+4a_V(c_V-b_V)-(b_A-c_A)^2-(b_V-c_V)^2\right)\right.\\
&+n_V^2\left(16a_V^2+4a_V(c_V-b_V)-(b_A-c_A)^2-(b_V-c_V)^2\right)+4n_An_V(b_A-c_A)(2a_V+b_V-c_V)\\
&\left.+4\left(g_A^2\left((y_A-z_A)^2+(y_V-z_V)^2\right)-4g_Ag_V(y_A-z_A)(y_V-z_V)+g_V^2\left((y_A-z_A)^2+(y_V-z_V)^2\right)\right)\right)\\
&+16a_V^2n_A^2+16a_V^2n_V^2-16a_Vb_An_An_V+8a_Vb_Vn_A^2+8a_Vb_Vn_V^2+16a_Vc_An_An_V-8a_Vc_Vn_A^2\\
&-8a_Vc_Vn_V^2+b_A^2n_A^2+b_A^2n_V^2+\tau_I^4\left(n_A^2\left((b_A-c_A)^2+(b_V-c_V)^2\right)-4n_An_V(b_A-c_A)(b_V-c_V)\right.\\
&+n_V^2\left((b_A-c_A)^2+(b_V-c_V)^2\right)+4\left(g_A^2\left((y_A-z_A)^2+(y_V-z_V)^2\right)+4g_Ag_V(y_A-z_A)(y_V-z_V)\right.\\
&\left.\left.+g_V^2\left((y_A-z_A)^2+(y_V-z_V)^2\right)\right)\right)-4b_Ab_Vn_An_V-2b_Ac_An_A^2-2b_Ac_An_V^2+4b_Ac_Vn_An_V\\
&+b_V^2n_A^2+b_V^2n_V^2+4b_Vc_An_An_V-2b_Vc_Vn_A^2-2b_Vc_Vn_V^2+c_A^2n_A^2\\
&+c_A^2n_V^2-4c_Ac_Vn_An_V+c_V^2n_A^2+c_V^2n_V^2)+\mathcal{O}(R^{'3})\\
B_{D5}=&-4R'^2\tau_I^2\left(2\tau_I^2(2a_An_An_V(8a_V+b_V-c_V)+n_An_V(b_A-c_A)(2a_V+b_V-c_V)\right.\\
&-4g_Ag_V(y_A-z_A)(y_V-z_V))-n_An_V(4a_A+b_A-c_A)(4a_V+b_V-c_V)\\
&\left.+\tau_I^4(4g_Ag_V(y_A-z_A)(y_V-z_V)-n_An_V(b_A-c_A)(b_V-c_V))\right)+\mathcal{O}(R^{'3})
\end{aligned}
$$

- (V,V): (only terms $\propto a_{V/A}, x_{V/A}$)

$$
\begin{aligned}
A_{D4}=&-\frac{2m_X^2}{\tau_Y^2}\left(\tau_I^2-1\right)(\tau_I-\tau_Y)(\tau_I+\tau_Y)\left(g_A^2\left(\tau_I^2+2\right)\left(n_A^2+n_V^2\right)\left(\tau_I^2+2\tau_Y^2\right)\right.\\
&\left.+4g_Ag_Vn_An_V\left(\tau_I^2-2\right)\left(\tau_I^2-2\tau_Y^2\right)+g_V^2\left(\tau_I^2+2\right)\left(n_A^2+n_V^2\right)\left(\tau_I^2+2\tau_Y^2\right)\right)\\
B_{D4}=&-\frac{16}{\tau_Y^2}g_Ag_Vn_An_V\tau_I^2\left(\tau_I^2-2\right)\left(\tau_I^2-2\tau_Y^2\right)\\
A_{D5}=&-\frac{8m_X^2R'^2}{\tau_Y^2}\left(\tau_I^2-1\right)(\tau_I-\tau_Y)(\tau_I+\tau_Y)\times\\
&\times\left(a_A^2\left(2\tau_I^2+1\right)\left(n_A^2+n_V^2\right)\left(\tau_I^2+2\tau_Y^2\right)+4a_Aa_Vn_An_V\left(2\tau_I^2-1\right)\left(\tau_I^2-2\tau_Y^2\right)\right.\\
&+a_V^2\left(2\tau_I^2+1\right)\left(n_A^2+n_V^2\right)\left(\tau_I^2+2\tau_Y^2\right)+\tau_Y^2\left(g_A^2\left(\tau_I^2+2\right)\left(x_A^2+x_V^2\right)\left(2\tau_I^2+\tau_Y^2\right)\right.\\
&\left.\left.-4g_Ag_Vx_Ax_V\left(\tau_I^2-2\right)\left(2\tau_I^2-\tau_Y^2\right)+g_V^2\left(\tau_I^2+2\right)\left(x_A^2+x_V^2\right)\left(2\tau_I^2+\tau_Y^2\right)\right)\right)+\mathcal{O}(R^{'3})\\
B_{D5}=&\frac{64R'^2}{\tau_Y^2}\tau_I^2\left(g_Ag_Vx_Ax_V\left(\tau_I^2-2\right)\tau_Y^2\left(2\tau_I^2-\tau_Y^2\right)-a_Aa_Vn_An_V\left(2\tau_I^2-1\right)\left(\tau_I^2-2\tau_Y^2\right)\right)+\mathcal{O}(R^{'3})
\end{aligned}
$$

- $(F,F)_V$

$$
\begin{aligned}
A_{D4}=&-\frac{4m_X^2}{\tau_I^4}\left(\tau_I^2-1\right)(\tau_I-\tau_Y)(\tau_I+\tau_Y)\times\\
&\times\left(g_A^2\left(n_A^2+n_V^2\right)\left(2\tau_I^4+\tau_Y^2\right)+8g_Ag_Vn_An_V\tau_I^4+g_V^2\left(n_A^2+n_V^2\right)\left(2\tau_I^4+\tau_Y^2\right)\right)\\
B_{D4}=&-\frac{16}{\tau_I^2}\left(g_A^2\left(\tau_I^2-1\right)\left(n_A^2+n_V^2\right)(\tau_I-\tau_Y)(\tau_I+\tau_Y)\right.\\
&\left.+4g_Ag_Vn_An_V\tau_I^4+g_V^2\left(\tau_I^2-1\right)\left(n_A^2+n_V^2\right)(\tau_I-\tau_Y)(\tau_I+\tau_Y)\right)\\
C_{D4}=&-\frac{16\left(g_A^2+g_V^2\right)\left(n_A^2+n_V^2\right)}{m_X^2}\\
A_{D5}=&-\frac{m_X^2R'^2}{\tau_I^4}\left(\tau_I^2-1\right)(\tau_I-\tau_Y)(\tau_I+\tau_Y)\left(16a_A^2\tau_I^4\left(\tau_Y^2+2\right)\left(n_A^2+n_V^2\right)-128a_Aa_Vn_An_V\tau_I^4\right.\\
&+16a_V^2\tau_I^4\left(\tau_Y^2+2\right)\left(n_A^2+n_V^2\right)+2\tau_I^2\tau_Y^2\left(16\tau_I^2\left(x_A^2\left(g_A^2+g_V^2\right)+x_V^2\left(g_A^2+g_V^2\right)+4g_Ag_Vx_Ax_V\right)\right.\\
&\left.\left.-\left(g_A^2+g_V^2\right)\left((y_A-z_A)(4x_A+y_A-z_A)+(y_V-z_V)(4x_V+y_V-z_V)\right)\right)\right.\\
&+\tau_Y^4\left(g_A^2+g_V^2\right)\left((y_A-z_A)^2+(y_V-z_V)^2\right)+16g_A^2x_A^2\tau_I^4+8g_A^2x_Ay_A\tau_I^4-8g_A^2x_Az_A\tau_I^4+16g_A^2x_V^2\tau_I^4\\
&+8g_A^2x_Vy_V\tau_I^4-8g_A^2x_Vz_V\tau_I^4+g_A^2y_A^2\tau_I^4-2g_A^2y_Az_A\tau_I^4+g_A^2y_V^2\tau_I^4-2g_A^2y_Vz_V\tau_I^4\\
&+g_A^2z_A^2\tau_I^4+g_A^2z_V^2\tau_I^4+16g_V^2x_A^2\tau_I^4+8g_V^2x_Ay_A\tau_I^4-8g_V^2x_Az_A\tau_I^4+16g_V^2x_V^2\tau_I^4+8g_V^2x_Vy_V\tau_I^4\\
&\left.-8g_V^2x_Vz_V\tau_I^4+g_V^2y_A^2\tau_I^4-2g_V^2y_Az_A\tau_I^4+g_V^2y_V^2\tau_I^4-2g_V^2y_Vz_V\tau_I^4+g_V^2z_A^2\tau_I^4+g_V^2z_V^2\tau_I^4\right)+\mathcal{O}(R^{'3})
\end{aligned}
$$

$$
\begin{aligned}
B_{D5} = {} & \frac{4R'^2}{\tau_I^2}\left(16a_A^2\left(\tau_I^2-1\right)\tau_I^2\left(n_A^2+n_V^2\right)(\tau_I-\tau_Y)(\tau_I+\tau_Y)+64a_Aa_Vn_An_V\tau_I^4\right.\\
& -2\tau_I^2\tau_Y^2\left(8a_V^2\left(\tau_I^2-1\right)\left(n_A^2+n_V^2\right)+g_A^2\left(\tau_I^2-1\right)\left(8x_A^2+4x_A(y_A-z_A)+8x_V^2\right.\right.\\
& +4x_V(y_V-z_V)+(y_A-z_A)^2+(y_V-z_V)^2\big)+32g_Ag_Vx_Ax_V\tau_I^2\\
& \left.+g_V^2\left(\tau_I^2-1\right)\left(8x_A^2+4x_A(y_A-z_A)+8x_V^2+4x_V(y_V-z_V)+(y_A-z_A)^2+(y_V-z_V)^2\right)\right)\\
& +16a_V^2n_A^2\tau_I^6-16a_V^2n_A^2\tau_I^4+16a_V^2n_V^2\tau_I^6-16a_V^2n_V^2\tau_I^4\\
& +\left(\tau_I^2-1\right)\tau_Y^4\left(g_A^2+g_V^2\right)\left((y_A-z_A)^2+(y_V-z_V)^2\right)+16g_A^2x_A^2\tau_I^6-16g_A^2x_A^2\tau_I^4+8g_A^2x_Ay_A\tau_I^6\\
& -8g_A^2x_Ay_A\tau_I^4-8g_A^2x_Az_A\tau_I^6+8g_A^2x_Az_A\tau_I^4+16g_A^2x_V^2\tau_I^6-16g_A^2x_V^2\tau_I^4+8g_A^2x_Vy_V\tau_I^6-8g_A^2x_Vy_V\tau_I^4\\
& -8g_A^2x_Vz_V\tau_I^6+8g_A^2x_Vz_V\tau_I^4+g_A^2y_A^2\tau_I^6-g_A^2y_A^2\tau_I^4-2g_A^2y_Az_A\tau_I^6+2g_A^2y_Az_A\tau_I^4+g_A^2y_V^2\tau_I^6-g_A^2y_V^2\tau_I^4\\
& -2g_A^2y_Vz_V\tau_I^6+2g_A^2y_Vz_V\tau_I^4+g_A^2z_A^2\tau_I^6-g_A^2z_A^2\tau_I^4+g_A^2z_V^2\tau_I^6-g_A^2z_V^2\tau_I^4+16g_V^2x_A^2\tau_I^6-16g_V^2x_A^2\tau_I^4\\
& +8g_V^2x_Ay_A\tau_I^6-8g_V^2x_Ay_A\tau_I^4-8g_V^2x_Az_A\tau_I^6+8g_V^2x_Az_A\tau_I^4+16g_V^2x_V^2\tau_I^6-16g_V^2x_V^2\tau_I^4+8g_V^2x_Vy_V\tau_I^6\\
& -8g_V^2x_Vy_V\tau_I^4-8g_V^2x_Vz_V\tau_I^6+8g_V^2x_Vz_V\tau_I^4+g_V^2y_A^2\tau_I^6-g_V^2y_A^2\tau_I^4-2g_V^2y_Az_A\tau_I^6+2g_V^2y_Az_A\tau_I^4\\
& \left.+g_V^2y_V^2\tau_I^6-g_V^2y_V^2\tau_I^4-2g_V^2y_Vz_V\tau_I^6+2g_V^2y_Vz_V\tau_I^4+g_V^2z_A^2\tau_I^6-g_V^2z_A^2\tau_I^4+g_V^2z_V^2\tau_I^6-g_V^2z_V^2\tau_I^4\right)\\
& +\mathcal{O}(R^{'3})\\
C_{D5} = {} & \frac{4R'^2}{m_X^2}\left(16a_A^2\tau_I^2\left(n_A^2+n_V^2\right)+16a_V^2\tau_I^2\left(n_A^2+n_V^2\right)\right.\\
& \left.+\left(g_A^2+g_V^2\right)\left(\tau_I^2\left((4x_A+y_A-z_A)^2+(4x_V+y_V-z_V)^2\right)-\tau_Y^2\left((y_A-z_A)^2+(y_V-z_V)^2\right)\right)\right)\\
& +\mathcal{O}(R^{'3})
\end{aligned}
$$

B.2 Appendix to Chapter 4: Three body decays

The coefficients of the differential decay widths are given below. We restrict ourselves to the case of massless SM-fermions, implying that $Z = A = 0$ and, thus, the differential widths read

$$\frac{d\Gamma}{d\hat{s}} = \frac{PS}{(2\pi)^3\ 256\ m_X}\left(B + C\hat{s} + D\hat{s}^2 + E\hat{s}^3 + F\hat{s}^4\right). \tag{B.2}$$

Decays of new bosons

The coefficients are shown with all possible diagrams and vertices in Table 4.1. For the definition of ϵ and the various τ_i see Eq. (4.2). We give the various orders separately, e.g.

$$B = \sum_{j=2}^{4} B_j\epsilon^j. \tag{B.3}$$

For brevity, we only explicitely write out the higher orders for (S, S).
• $S \to f\overline{f}S$:

$$
\begin{aligned}
B_2 &= 128\epsilon^2(\tau_Y-1)^2(g(r,s)n(l,s)+g(l,s)n(r,s))^2\\
C_2 &= 128\epsilon^2(\tau_Y-1)^2(g(r,s)n(l,s)+g(l,s)n(r,s))^2\\
D_2 &= 0
\end{aligned}
\tag{B.4}
$$

$$
\begin{aligned}
B_3 &= 64\epsilon^3\tau_C(\tau_Y-1)^2c(s)(g(r,s)n(l,s)+g(l,s)n(r,s))(s(l)+s(r))\\
C_3 &= 64\epsilon^3\tau_C(\tau_Y-1)^2c(s)(g(r,s)n(l,s)+g(l,s)n(r,s))(s(l)+s(r))
\end{aligned}
$$

$$D_3 = 0 \tag{B.5}$$

$$\begin{aligned}
B_4 &= \frac{16}{3}\epsilon^4(\tau_Y-1)^2\left(12g(r,s)^2n(l,s)^2(\tau_Y+1)^2+12g(l,s)^2n(r,s)^2(\tau_Y+1)^2\right.\\
&\quad +24g(l,s)g(r,s)n(l,s)n(r,s)(\tau_Y+1)^2+3\tau_C^2c(s)^2s(l)^2+3\tau_C^2c(s)^2s(r)^2\\
&\quad +\tau_Y^2c(v)^2v(l)^2+6\tau_Yc(v)^2v(l)^2+c(v)^2v(l)^2+\tau_Y^2c(v)^2v(r)^2\\
&\quad \left.+6\tau_Yc(v)^2v(r)^2+c(v)^2v(r)^2\right)\\
C_4 &= -\frac{16}{3}\epsilon^4(\tau_Y-1)^2\left(-48\tau_Yg(r,s)^2n(l,s)^2-96\tau_Yg(l,s)g(r,s)n(r,s)n(l,s)\right.\\
&\quad -48\tau_Yg(l,s)^2n(r,s)^2-3\tau_C^2c(s)^2s(l)^2-3\tau_C^2c(s)^2s(r)^2+2\tau_Y^2c(v)^2v(l)^2\\
&\quad +4\tau_Yc(v)^2v(l)^2+2c(v)^2v(l)^2+2\tau_Y^2c(v)^2v(r)^2\\
&\quad \left.+4\tau_Yc(v)^2v(r)^2+2c(v)^2v(r)^2\right)\\
D_4 &= -\frac{16}{3}\epsilon^4(\tau_Y-1)^4\left(-\left(v(l)^2+v(r)^2\right)c(v)^2+12g(r,s)^2n(l,s)^2\right.\\
&\quad \left.+12g(l,s)^2n(r,s)^2+24g(l,s)g(r,s)n(l,s)n(r,s)\right)
\end{aligned} \tag{B.6}$$

Moreover, we get $E_j = 0$ in all orders considered.

- $S \to f\overline{f}V$:

$$\begin{aligned}
B_2 &= \frac{64}{3\tau_Y^2}\left(g(r,s)^2n(l,v)^2+g(l,s)^2n(r,v)^2\right)\epsilon^2(\tau_Y-1)^2\left(25\tau_Y^2+6\tau_Y+1\right)\\
C_2 &= \frac{128}{3\tau_Y^2}\left(g(r,s)^2n(l,v)^2+g(l,s)^2n(r,v)^2\right)\epsilon^2(\tau_Y-1)^2\left(11\tau_Y^2-2\tau_Y-1\right)\\
D_2 &= \frac{64}{3\tau_Y^2}\left(g(r,s)^2n(l,v)^2+g(l,s)^2n(r,v)^2\right)\epsilon^2(\tau_Y-1)^4
\end{aligned} \tag{B.7}$$

- $V \to f\overline{f}S$:

$$\begin{aligned}
B_2 &= \frac{64}{3}\left(g(r,v)^2n(l,s)^2+g(l,v)^2n(r,s)^2\right)\epsilon^2(\tau_Y-1)^2\left(\tau_Y^2+6\tau_Y+25\right)\\
C_2 &= -\frac{128}{3}\left(g(r,v)^2n(l,s)^2+g(l,v)^2n(r,s)^2\right)\epsilon^2(\tau_Y-1)^2\left(\tau_Y^2+2\tau_Y-11\right)\\
D_2 &= \frac{64}{3}\left(g(r,v)^2n(l,s)^2+g(l,v)^2n(r,s)^2\right)\epsilon^2(\tau_Y-1)^4
\end{aligned} \tag{B.8}$$

- $V \to f\overline{f}V$:

$$\begin{aligned}
B_2 &= \frac{32}{3\tau_Y^2}\epsilon^2(\tau_Y-1)^2\left(g(r,v)^2\left(3\tau_Y^4+16\tau_Y^3+54\tau_Y^2+16\tau_Y+3\right)n(l,v)^2\right.\\
&\quad -g(l,v)g(r,v)n(r,v)\left(3\tau_Y^4+20\tau_Y^3-6\tau_Y^2+20\tau_Y+3\right)n(l,v)\\
&\quad \left.+g(l,v)^2n(r,v)^2\left(3\tau_Y^4+16\tau_Y^3+54\tau_Y^2+16\tau_Y+3\right)\right)\\
C_2 &= -\frac{32}{3\tau_Y^2}\epsilon^2(\tau_Y-1)^2\left(g(r,v)^2\left(5\tau_Y^4+4\tau_Y^3-46\tau_Y^2+4\tau_Y+5\right)n(l,v)^2\right.\\
&\quad -g(l,v)g(r,v)n(r,v)\left(7\tau_Y^4+20\tau_Y^3+34\tau_Y^2+20\tau_Y+7\right)n(l,v)\\
&\quad \left.+g(l,v)^2n(r,v)^2\left(5\tau_Y^4+4\tau_Y^3-46\tau_Y^2+4\tau_Y+5\right)\right)\\
D_2 &= \frac{32}{3\tau_Y^2}\epsilon^2(\tau_Y-1)^4\left(g(r,v)^2\left(\tau_Y^2-6\tau_Y+1\right)n(l,v)^2\right.\\
&\quad \left.-g(l,v)g(r,v)n(r,v)\left(5\tau_Y^2+6\tau_Y+5\right)n(l,v)+g(l,v)^2n(r,v)^2\left(\tau_Y^2-6\tau_Y+1\right)\right)\\
E_2 &= \frac{32}{3\tau_Y^2}\left(g(r,v)^2n(l,v)^2+g(l,v)g(r,v)n(r,v)n(l,v)+g(l,v)^2n(r,v)^2\right)\epsilon^2(\tau_Y-1)^6
\end{aligned} \tag{B.9}$$

Decays of new fermions

As noted before, in this case only the 4th order in ϵ contributes. We split the various coefficients according to the different topologies considered, e.g. the scalar contributions to B_4 are

$B_4 = B_s + B'_s + B_{s,m}$
where B_s : top. 1+2 with intermediate scalars
B'_s : top. 3 with intermediate scalars
$B_{s,m}$: interference term of top. (1+2)+3 with intermediate scalars

For intermediate vector bosons the index v is used. For the interference terms between scalars and vector bosons the index (sv) is used in case of topologies 1+2, $(sv1)$ for the scalars of topology 1+2 and vector bosons of topology 3, $(s1v)$ for the scalars of topology 3 and vector bosons of topology 1+2. Moreover we find that the interference vanishes if both, scalars and vector bosons, stem from the third topology because we have $m_f = 0$ for the SM-fermions.
• Intermediate scalars:

$$
\begin{aligned}
B_s &= \frac{64}{3}(\tau_Y-1)^2\left(2\left((\tau_Y(\tau_Y+6)+1)n(l,s)^2+(\tau_Y(\tau_Y+3)+1)n(r,s)^2\right)g(l,s)^2\right.\\
&\quad -(\tau_Y(\tau_Y+6)+1)g(r,s)n(l,s)n(r,s)g(l,s)+2g(r,s)^2\left((\tau_Y(\tau_Y+3)+1)n(l,s)^2\right.\\
&\quad \left.\left.+(\tau_Y(\tau_Y+6)+1)n(r,s)^2\right)\right)\\
C_s &= -\frac{64}{3}(\tau_Y-1)^2\left(-2g(l,s)g(r,s)n(l,s)n(r,s)(\tau_Y+1)^2\right.\\
&\quad +g(r,s)^2\left(((\tau_Y-4)\tau_Y+1)n(l,s)^2+((\tau_Y-10)\tau_Y+1)n(r,s)^2\right)\\
&\quad \left.+g(l,s)^2\left(((\tau_Y-10)\tau_Y+1)n(l,s)^2+((\tau_Y-4)\tau_Y+1)n(r,s)^2\right)\right)\\
D_s &= -\frac{64}{3}(\tau_Y-1)^4\left(\left(n(l,s)^2+n(r,s)^2\right)g(l,s)^2\right.\\
&\quad \left.+g(r,s)n(l,s)n(r,s)g(l,s)+g(r,s)^2\left(n(l,s)^2+n(r,s)^2\right)\right) \qquad \text{(B.10)}\\
B'_s &= 32(\tau_Y-1)^2\left((\tau_Y+1)^2d(l,s)^2\right.\\
&\quad \left.+8\tau_Y d(r,s)d(l,s)+(\tau_Y+1)^2d(r,s)^2\right)\left(s(l)^2+s(r)^2\right)\\
C'_s &= 128(\tau_Y-1)^2\tau_Y(d(l,s)+d(r,s))^2\left(s(l)^2+s(r)^2\right)\\
D'_s &= -32(\tau_Y-1)^4\left(d(l,s)^2+d(r,s)^2\right)\left(s(l)^2+s(r)^2\right) \qquad \text{(B.11)}\\
B_{s,m} &= -32(\tau_Y-1)^2(g(r,s)n(l,s)+g(l,s)n(r,s))\left(d(r,s)\left(s(l)(\tau_Y+1)^2+4\tau_Y s(r)\right)\right.\\
&\quad \left.+d(l,s)\left(s(r)(\tau_Y+1)^2+4\tau_Y s(l)\right)\right)\\
C_{s,m} &= -128(\tau_Y-1)^2\tau_Y(g(r,s)n(l,s)+g(l,s)n(r,s))(d(l,s)+d(r,s))(s(l)+s(r))\\
D_{s,m} &= 32(\tau_Y-1)^4(g(r,s)n(l,s)+g(l,s)n(r,s))(d(r,s)s(l)+d(l,s)s(r)) \qquad \text{(B.12)}
\end{aligned}
$$

• Intermediate vector bosons:

$$
\begin{aligned}
B_v &= \frac{256}{3}(\tau_Y-1)^2\left(6g(l,v)g(r,v)n(l,v)n(r,v)(\tau_Y+1)^2\right.\\
&\quad +g(l,v)^2\left(2(\tau_Y(\tau_Y+6)+1)n(l,v)^2+3(\tau_Y+1)^2n(r,v)^2\right)\\
&\quad \left.+g(r,v)^2\left(3(\tau_Y+1)^2n(l,v)^2+2(\tau_Y(\tau_Y+6)+1)n(r,v)^2\right)\right)\\
C_v &= \frac{256}{3}(\tau_Y-1)^2\left(\left(12\tau_Y n(r,v)^2-((\tau_Y-10)\tau_Y+1)n(l,v)^2\right)g(l,v)^2\right.\\
&\quad \left.+24\tau_Y g(r,v)n(l,v)n(r,v)g(l,v)+g(r,v)^2\left(12\tau_Y n(l,v)^2-((\tau_Y-10)\tau_Y+1)n(r,v)^2\right)\right)\\
D_v &= -\frac{256}{3}(\tau_Y-1)^4\left(\left(n(l,v)^2+3n(r,v)^2\right)g(l,v)^2\right.
\end{aligned}
$$

$$+6g(r,v)n(l,v)n(r,v)g(l,v)+g(r,v)^2\left(3n(l,v)^2+n(r,v)^2\right)\Big) \tag{B.13}$$

$$\begin{aligned}
B'_v &= \frac{256}{3}(\tau_Y-1)^2\left((\tau_Y(\tau_Y+3)+1)d(l,v)^2-6\tau_Y d(r,v)d(l,v)\right.\\
&\quad\left.+(\tau_Y(\tau_Y+3)+1)d(r,v)^2\right)\left(v(l)^2+v(r)^2\right)\\
C'_v &= -\frac{128}{3}(\tau_Y-1)^2\left(((\tau_Y-4)\tau_Y+1)d(l,v)^2\right.\\
&\quad\left.+12\tau_Y d(r,v)d(l,v)+((\tau_Y-4)\tau_Y+1)d(r,v)^2\right)\left(v(l)^2+v(r)^2\right)\\
D'_v &= -\frac{128}{3}(\tau_Y-1)^4\left(d(l,v)^2+d(r,v)^2\right)\left(v(l)^2+v(r)^2\right)
\end{aligned} \tag{B.14}$$

$$\begin{aligned}
B_{v,m} &= \frac{512}{3}(\tau_Y-1)^2(\tau_Y(\tau_Y+6)+1)(d(l,v)-d(r,v))\\
&\quad (g(l,v)n(l,v)v(l)-g(r,v)n(r,v)v(r))\\
C_{v,m} &= -\frac{256}{3}(\tau_Y-1)^2((\tau_Y-10)\tau_Y+1)(d(l,v)-d(r,v))\\
&\quad (g(l,v)n(l,v)v(l)-g(r,v)n(r,v)v(r))\\
D_{v,m} &= -\frac{256}{3}(\tau_Y-1)^4(d(l,v)-d(r,v))(g(l,v)n(l,v)v(l)-g(r,v)n(r,v)v(r))
\end{aligned} \tag{B.15}$$

• Interference terms between scalars and vector bosons:

$$\begin{aligned}
B_{sv} &= -\frac{512}{3}(\tau_Y-1)^2(n(l,v)(3\tau_Y g(l,s)g(r,v)n(r,s)+g(r,s)(3\tau_Y g(r,v)n(l,s)\\
&\quad +(\tau_Y(\tau_Y+6)+1)g(l,v)n(r,s)))+((\tau_Y(\tau_Y+6)+1)g(l,s)g(r,v)n(l,s)\\
&\quad +3\tau_Y g(l,v)(g(r,s)n(l,s)+g(l,s)n(r,s)))n(r,v))\\
C_{sv} &= \frac{256}{3}(\tau_Y-1)^2(n(l,v)(g(r,s)(((\tau_Y-10)\tau_Y+1)g(l,v)n(r,s)\\
&\quad -6\tau_Y g(r,v)n(l,s))-6\tau_Y g(l,s)g(r,v)n(r,s))+(((\tau_Y-10)\tau_Y+1)g(l,s)g(r,v)n(l,s)\\
&\quad -6\tau_Y g(l,v)(g(r,s)n(l,s)+g(l,s)n(r,s)))n(r,v))\\
D_{sv} &= \frac{256}{3}(\tau_Y-1)^4(g(l,v)g(r,s)n(l,v)n(r,s)+g(l,s)g(r,v)n(l,s)n(r,v))
\end{aligned} \tag{B.16}$$

$$\begin{aligned}
B_{sv1} &= -\frac{256}{3}(\tau_Y-1)^2(\tau_Y(\tau_Y+6)+1)(d(l,v)-d(r,v))\\
&\quad (g(r,s)n(r,s)v(l)-g(l,s)n(l,s)v(r))\\
C_{sv1} &= \frac{128}{3}(\tau_Y-1)^2((\tau_Y-10)\tau_Y+1)(d(l,v)-d(r,v))\\
&\quad (g(r,s)n(r,s)v(l)-g(l,s)n(l,s)v(r))\\
D_{sv1} &= \frac{128}{3}(\tau_Y-1)^4(d(l,v)-d(r,v))(g(r,s)n(r,s)v(l)-g(l,s)n(l,s)v(r))
\end{aligned} \tag{B.17}$$

$$\begin{aligned}
B_{s1v} &= 128(\tau_Y-1)^2(g(r,v)n(l,v)+g(l,v)n(r,v))\left(d(l,s)\left(s(l)(\tau_Y+1)^2+4\tau_Y s(r)\right)\right.\\
&\quad \left.+d(r,s)\left(s(r)(\tau_Y+1)^2+4\tau_Y s(l)\right)\right)\\
C_{s1v} &= 512(\tau_Y-1)^2\tau_Y(g(r,v)n(l,v)+g(l,v)n(r,v))\\
&\quad (d(l,s)+d(r,s))(s(l)+s(r))\\
D_{s1v} &= -128(\tau_Y-1)^4(g(r,v)n(l,v)+g(l,v)n(r,v))(d(l,s)s(l)+d(r,s)s(r))
\end{aligned} \tag{B.18}$$

Appendix C

Appendix to Chapter 5

C.1 Explicit helicity spinors

For the calculation of the production and decays we use explicit helicity spinors. We follow [43] [77] and [76] for the calculation. The wave function solution of a free particle with momentum p and spin s is

$$u(p,s) = \sqrt{2m} \begin{pmatrix} \cosh\frac{\xi}{2}\ \chi_s \\ \vec{\sigma}\cdot\hat{\mathbf{p}}\ \sinh\frac{\xi}{2}\ \chi_s \end{pmatrix}; \tag{C.1a}$$

$$v(p,s) = \sqrt{2m}(-1)^{1/2-s} \begin{pmatrix} \vec{\sigma}\cdot\hat{\mathbf{p}}\ \sinh\frac{\xi}{2}\ \chi_{-s} \\ \cosh\frac{\xi}{2}\ \chi_{-s} \end{pmatrix} \tag{C.1b}$$

where the antiparticle wave function is $v(p,s) = C\bar{u}^T(p)$ and C is the charge conjugation matrix. ξ is the rapidity related to energy and three momentum vector by $E = m\cosh\xi$ and $p = m\sinh\xi$. The Dirac helicity spinors for $\hat{p}, \lambda$ are now defined by rotating the state with helicity λ into the $\hat{z}$ direction

$$\chi_\lambda(\hat{p}) = e^{-i\hat{n}\cdot\vec{\sigma}/2}\chi_\lambda(\hat{z}) \tag{C.2}$$

with the vector $\hat{n} = (-sin\phi, \cos\phi, 0)$ and the unit vector

$$\hat{p} = (\sin\theta\cos\phi, \sin\theta\sin\phi, \cos\theta)$$

in the direction of the three momentum $\vec{p}$ of the particle. The resulting helicity spinor for p, λ is

$$u(p,\lambda) = e^{-i\hat{n}\cdot\vec{\sigma}/2}\ u(p, s=\lambda) = \sqrt{2m} \begin{pmatrix} \cosh\frac{\xi}{2}\ \chi_\lambda(\hat{\mathbf{p}}) \\ \vec{\sigma}\cdot\hat{\mathbf{p}}\ \sinh\frac{\xi}{2}\ \chi_\lambda(\hat{\mathbf{p}}) \end{pmatrix}; \tag{C.3a}$$

$$v(p,\lambda) = \sqrt{2m}(-1)^{1/2-\lambda} \begin{pmatrix} \vec{\sigma}\cdot\hat{\mathbf{p}}\ \sinh\frac{\xi}{2}\ \chi_{-\lambda} \\ \cosh\frac{\xi}{2}\ \chi_{-\lambda} \end{pmatrix}. \tag{C.3b}$$

The chiral representation is more useful to perform explicit calculations, and we get the chiral spinors by

$$u(p,\lambda)_{chiral} = \frac{1}{\sqrt{2}} \begin{pmatrix} 1 & -1 \\ 1 & 1 \end{pmatrix} u(p,\lambda)_{Dirac} \tag{C.4}$$

and inserting equations C.3

$$u(p) = \frac{1}{\sqrt{2(E+m)}} \begin{pmatrix} ((m+E) - \vec{p}\cdot\vec{\sigma})\chi \\ ((m+E) + \vec{p}\cdot\vec{\sigma})\chi \end{pmatrix}$$
$$v(p) = \frac{1}{\sqrt{2(E+m)}} \begin{pmatrix} ((m+E) + \vec{p}\cdot\vec{\sigma})\chi \\ -((m+E) - \vec{p}\cdot\vec{\sigma})\chi \end{pmatrix}$$

and the explicit helicity states

$$\chi(1/2) = e^{-I\phi/2\sigma_3} e^{-I\theta/2\sigma_2} \begin{pmatrix} 1 \\ 0 \end{pmatrix} \tag{C.5}$$
$$\chi(-1/2) = e^{-I\phi/2\sigma_3} e^{-I\theta/2\sigma_2} \begin{pmatrix} 0 \\ 1 \end{pmatrix}. \tag{C.6}$$

Here we have used the definition of the rapidities

$$\cosh\frac{\xi}{2} = \sqrt{\frac{E+m}{2m}} \qquad\qquad \sinh\frac{\xi}{2} = \sqrt{\frac{E-m}{2m}}. \tag{C.7}$$

With these explicit spinors in the chiral representation we are able to derive the decays of the particles for each helicity separately.
In the case of a spin-1 particle, we have three helicity vectors for the massive vector boson moving in the $\vec{k}$ direction

$$\begin{aligned}
\epsilon^\mu(1,k) &= \frac{1}{\sqrt{2}} e^{-I\gamma}(0, -\cos\theta\cos\phi + i\sin\phi,\ -i\cos\phi - \cos\theta\sin\phi, \sin\theta); \\
\epsilon^\mu(-1,k) &= \frac{1}{\sqrt{2}} e^{I\gamma}(0, \cos\theta\cos\phi + i\sin\phi,\ -i\cos\phi + \cos\theta\sin\phi, -\sin\theta); \\
\epsilon^\mu(0,k) &= (\frac{\sqrt{E^2-M^2}}{M}, \frac{E}{M}\sin\theta\cos\phi, \frac{E}{M}\sin\theta\sin\phi, \frac{E}{M}\cos\theta).
\end{aligned}$$

In the case of a massless vector boson, the helicity 0-vector does not exist.
For the decays, we work in the parents' rest frame (here the particles B) which means that the momenta are chosen as follows

$$\begin{aligned}
p_1 &= (M, 0, 0, 0) \\
p_2 &= (E_2, E_2\ \sin\theta\ \cos\phi, E_2\ \sin\theta\ \sin\phi, E_2\ \cos\theta) \\
p_3 &= (E_3, \sqrt{E_3^2 - m^2}\ \sin(\pi-\theta)\ \cos(\phi+\pi), \\
&\qquad \sqrt{E_3^2 - m^2}\ \sin(\pi-\theta)\ \sin(\phi+\pi), \sqrt{E_3^2 - m^2}\ \cos(\pi-\theta)).
\end{aligned}$$

For the sake of brevity and clarity we use here the nomenclature of figure C.1. The Euler angle γ can be chosen arbitrarily. There are two common conventions, and we use $\gamma = 0$ in our calculations. We furthermore need the relation

$$\epsilon^\mu(k,\lambda)^* = (-1)^\lambda \epsilon^\mu(k,-\lambda)$$

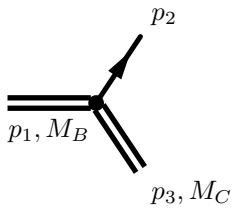

Figure C.1: Short nomenclature for the decays. The momenta are given in the rest frame of the decaying particle. The lepton is massless, the double lines indicate the unknown spin of the particles.

for the polarization vector of the outgoing vector particle. Since we are in the parents' rest frame we can use $\vec{p}_2 = -\vec{p}_3$, which is obtained from $\theta \to \pi - \theta$ and $\phi \to \phi + \pi$ (also in the polarization vectors).
The matrix elements for the different decays involving scalars are

$$\begin{aligned}
s \to l\bar{f} \qquad & \mathcal{N}(\lambda_f, \lambda_l) = \bar{u}(\lambda_l, p_2)\ (a_l\ P_L + a_r\ P_R)\ v(\lambda_f, p_3) \\
s \to \bar{l}f \qquad & \mathcal{N}(\lambda_f, \lambda_{\bar{l}}) = \bar{u}(\lambda_f, p_3)\ (a_r\ P_L + a_l\ P_R)\ v(\lambda_{\bar{l}}, p_2) \\
f \to sl \qquad & \mathcal{N}(\lambda_f, \lambda_l) = \bar{u}(\lambda_l, p_2)\ (a_l\ P_L + a_r\ P_R)\ u(\lambda_f, p_1) \\
\bar{f} \to s\bar{l} \qquad & \mathcal{N}(\lambda_{\bar{f}}, \lambda_{\bar{l}}) = \bar{v}(\lambda_{\bar{f}}, p_1)\ (a_r\ P_L + a_l\ P_R)\ v(\lambda_{\bar{l}}, p_2).
\end{aligned}$$

The matrix elements for the decays involving vector bosons are

$$\begin{aligned}
v \to l\bar{f} \qquad & \mathcal{N}(\lambda_{\bar{f}}, \lambda_l, \lambda_V) = \bar{u}(\lambda_l, p_2)\gamma_\mu(a_l\ P_L + a_r\ P_R)v(\lambda_f, p_3)\epsilon(\lambda_V, p_1) \\
\bar{v} \to \bar{l}f \qquad & \mathcal{N}(\lambda_f, \lambda_{\bar{l}}, \lambda_V) = \bar{u}(\lambda_f, p_3)\gamma_\mu(a_l\ P_L + a_r\ P_R)u(\lambda_{\bar{l}}, p_2)\epsilon(\lambda_V, p_1) \\
f \to lv \qquad & \mathcal{N}(\lambda_f, \lambda_l, \lambda_V) = \bar{u}(\lambda_l, p_2)\gamma^\mu(a_l\ P_L + a_r\ P_R)u(\lambda_f, p_1)\ \epsilon^*_\mu(\lambda_V, p_3) \\
\bar{f} \to \bar{l}v \qquad & \mathcal{N}(\lambda_{\bar{f}}, \lambda_{\bar{l}}, \lambda_V) = \bar{v}(\lambda_{\bar{f}}, p_1)\gamma^\mu(a_l\ P_L + a_r\ P_R)v(\lambda_{\bar{l}}, p_2)\ \epsilon^*_\mu(\lambda_V, p_3).
\end{aligned}$$

C.2 Figures to Section 5.4

Distribution plots for different $\sqrt{\tau_c}$

We show here the $\mathcal{C}_B$ distributions for fixed δ^2 for the different spin scenarios and different mass ratios $\sqrt{\tau_c}$. Each figure shows for C_1 (black) or C_2 (grey) the PS distribution and the distribution for smallest (dashed) and largest (solid) KL distance Δ and thus the smallest or largest deviation from PS that can be achieved in the particular spin scenario.

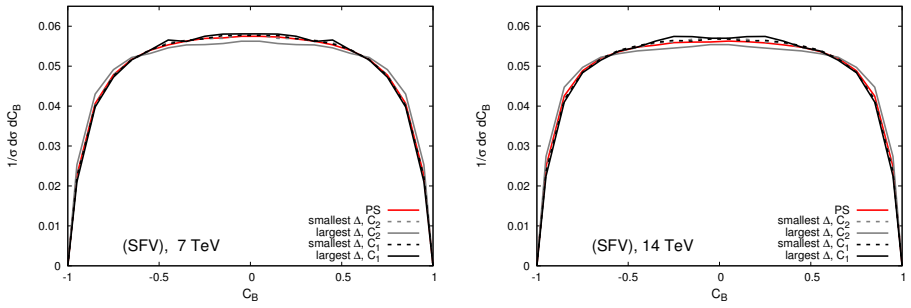

(a) SFV

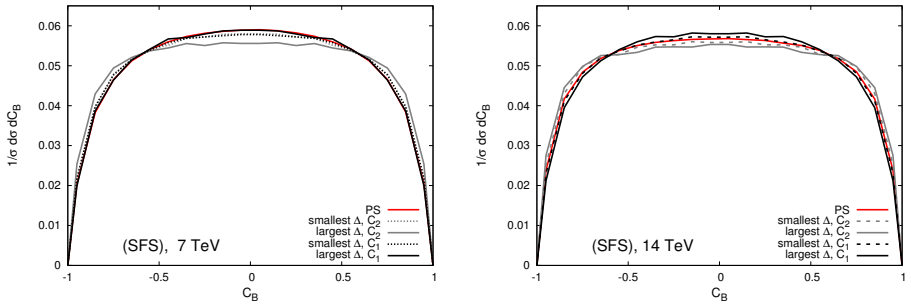

(b) SFS

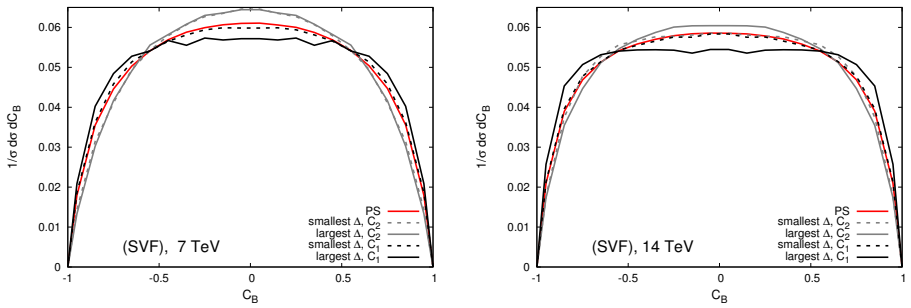

(c) SVF

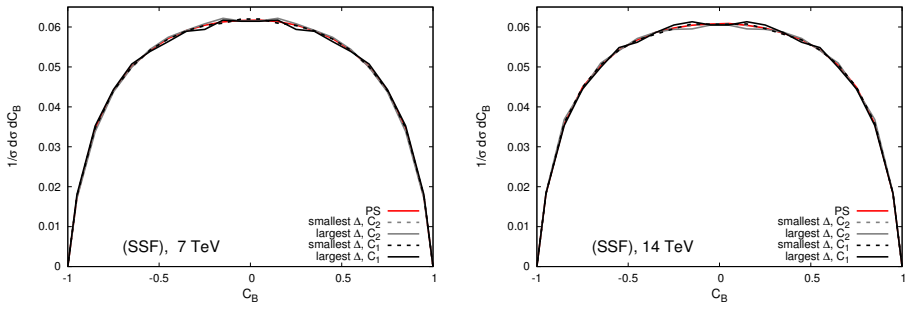

(d) SSF

Figure C.2: Distributions depending on $\sqrt{\tau_c}$ for s-channel scalar

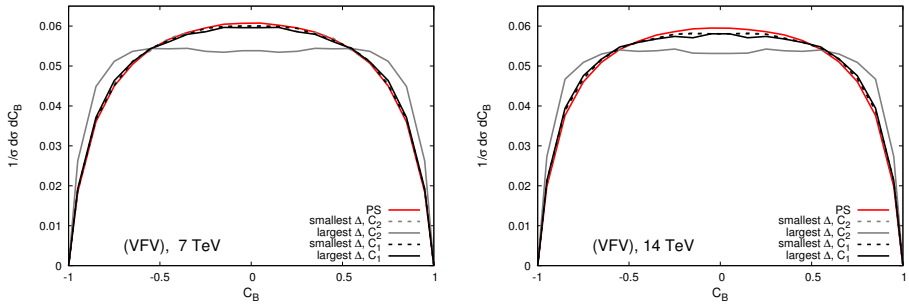

(a) VFV

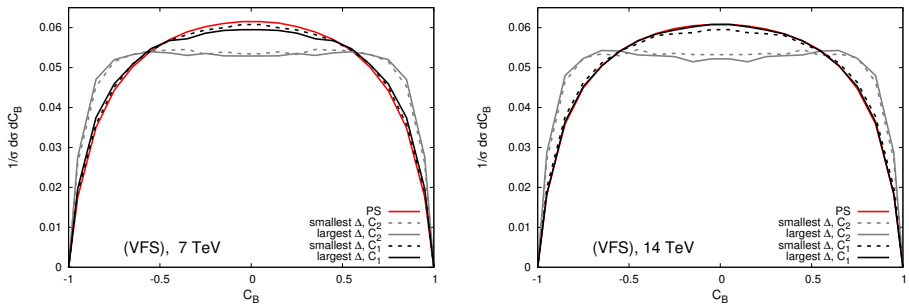

(b) VFS

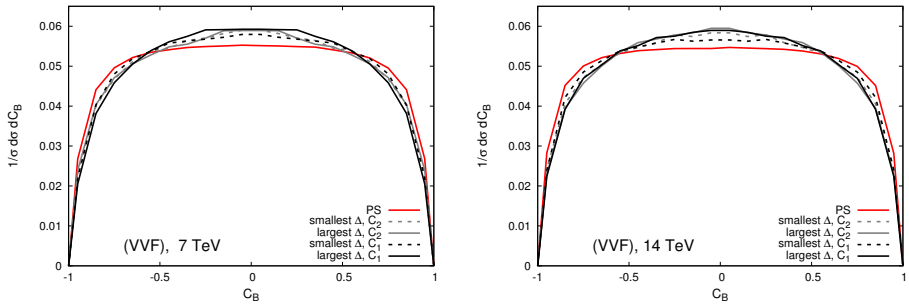

(c) VVF

Figure C.3: Distributions depending on $\sqrt{\tau}_c$ for s-channel vector. (VSF) is TH-PS and already displayed in figure 5.9.

Bibliography

[1] Gordon L. Kane, Alexey A. Petrov, Jing Shao, and Lian-Tao Wang. Initial determination of the spins of the gluino and squarks at LHC. *J.Phys.G*, G37:045004, 2010.

[2] A.J. Barr. Measuring slepton spin at the LHC. *JHEP*, 0602:042, 2006.

[3] J. Wess and J. Bagger. Supersymmetry and supergravity. Princeton, USA: Univ. Pr. (1992) 259 p.

[4] Ian J. R. Aitchison. Supersymmetry and the MSSM: An Elementary introduction. 2005.

[5] M. Drees, R. Godbole, and P. Roy. Theory and phenomenology of sparticles: An account of four-dimensional N=1 supersymmetry in high energy physics. Hackensack, USA: World Scientific (2004) 555 p.

[6] Stephen P. Martin. A Supersymmetry primer. 1997, [hep-ph/9709356].

[7] Sidney R. Coleman and J. Mandula. All possible symmetries of the S matrix. *Phys. Rev.*, 159:1251–1256, 1967.

[8] C. Macesanu, C. D. McMullen, and S. Nandi. Collider implications of universal extra dimensions. *Phys. Rev.*, D66:015009, 2002.

[9] AseshKrishna Datta, Kyoungchul Kong, and Konstantin T. Matchev. Minimal Universal Extra Dimensions in CalcHEP/CompHEP. *New J. Phys.*, 12:075017, 2010.

[10] Cosmin Macesanu. The phenomenology of universal extra dimensions at hadron colliders. *Int. J. Mod. Phys.*, A21:2259–2296, 2006.

[11] Dan Hooper and Stefano Profumo. Dark matter and collider phenomenology of universal extra dimensions. *Phys.Rept.*, 453:29–115, 2007.

[12] Thomas Appelquist, Hsin-Chia Cheng, and Bogdan A. Dobrescu. Bounds on universal extra dimensions. *Phys.Rev.*, D64:035002, 2001.

[13] Thomas Flacke, A. Menon, and Daniel J. Phalen. Non-minimal universal extra dimensions. *Phys.Rev.*, D79:056009, 2009.

[14] Hitoshi Murayama, Mihoko M. Nojiri, and Kohsaku Tobioka. Improved discovery of a nearly degenerate model: MUED using MT2 at the LHC. *Phys.Rev.*, D84:094015, 2011.

[15] Hsin-Chia Cheng, Konstantin T. Matchev, and Martin Schmaltz. Radiative corrections to Kaluza-Klein masses. *Phys.Rev.*, D66:036005, 2002.

[16] G. Belanger, M. Kakizaki, and A. Pukhov. Dark matter in UED: The Role of the second KK level. *JCAP*, 1102:009, 2011.

[17] (Particle Data Group) Nakamura, K. et al. (Particle Data Group). *J. Phys. G 37, 075021*, 2010.

[18] Georges Aad et al. Search for a heavy gauge boson decaying to a charged lepton and a neutrino in 1 fb-1 of pp collisions at sqrt(s) = 7 TeV using the ATLAS detector. *Phys.Lett.*, B705:28–46, 2011.

[19] Georges Aad et al. Search for dilepton resonances in pp collisions at sqrt(s) = 7 TeV with the ATLAS detector. *Phys.Rev.Lett.*, 107:272002, 2011.

[20] Alan J. Barr and Christopher G. Lester. A Review of the Mass Measurement Techniques proposed for the Large Hadron Collider. *J. Phys.*, G37:123001, 2010.

[21] Herbi K. Dreiner, Michael Kramer, Jonas M. Lindert, and Ben O'Leary. SUSY parameter determination at the LHC using cross sections and kinematic edges. *JHEP*, 04:109, 2010.

[22] Jennifer M. Smillie and Bryan R. Webber. Distinguishing Spins in Supersymmetric and Universal Extra Dimension Models at the Large Hadron Collider. *JHEP*, 10:069, 2005.

[23] Christiana Athanasiou, Christopher G. Lester, Jennifer M. Smillie, and Bryan R. Webber. Distinguishing spins in decay chains at the Large Hadron Collider. *JHEP*, 08:055, 2006.

[24] Christiana Athanasiou, Christopher G. Lester, Jennifer M. Smillie, and Bryan R. Webber. Addendum to Distinguishing Spins in Decay Chains at the Large Hadron Collider. 2006, [hep-ph/0606212].

[25] Jennifer M. Smillie. Spin correlations in decay chains involving W bosons. *Eur.Phys.J.*, C51:933–943, 2007.

[26] Lian-Tao Wang and Itay Yavin. Spin Measurements in Cascade Decays at the LHC. *JHEP*, 04:032, 2007.

[27] Patrick Meade and Matthew Reece. Top partners at the LHC: Spin and mass measurement. *Phys.Rev.*, D74:015010, 2006.

[28] Can Kilic, Lian-Tao Wang, and Itay Yavin. On the existence of angular correlations in decays with heavy matter partners. *JHEP*, 0705:052, 2007.

[29] Alexandre Alves and Oscar Eboli. Unravelling the sbottom spin at the CERN LHC. *Phys.Rev.*, D75:115013, 2007.

[30] Arvind Rajaraman and Bryan T. Smith. Determining Spins of Metastable Sleptons at the Large Hadron Collider. *Phys.Rev.*, D76:115004, 2007.

[31] Won Sang Cho, Kiwoon Choi, Yeong Gyun Kim, and Chan Beom Park. M(T2)-assisted on-shell reconstruction of missing momenta and its application to spin measurement at the LHC. *Phys.Rev.*, D79:031701, 2009.

[32] Lian-Tao Wang and Itay Yavin. A Review of Spin Determination at the LHC. *Int. J. Mod. Phys.*, A23:4647–4668, 2008.

[33] Michael Burns, Kyoungchul Kong, Konstantin T. Matchev, and Myeonghun Park. A General Method for Model-Independent Measurements of Particle Spins, Couplings and Mixing Angles in Cascade Decays with Missing Energy at Hadron Colliders. *JHEP*, 0810:081, 2008.

[34] Alexandre Alves, Oscar Eboli, and Tilman Plehn. It's a gluino. *Phys. Rev.*, D74:095010, 2006.

[35] A. J. Barr. Using lepton charge asymmetry to investigate the spin of supersymmetric particles at the LHC. *Phys. Lett.*, B596:205–212, 2004.

[36] B.C. Allanach, C.G. Lester, Michael Andrew Parker, and B.R. Webber. Measuring sparticle masses in nonuniversal string inspired models at the LHC. *JHEP*, 0009:004, 2000.

[37] Cheng-Wei Chiang, Neil D. Christensen, Gui-Jun Ding, and Tao Han. Discovery in Drell-Yan Processes at the LHC. *Phys.Rev.*, D85:015023, 2012.

[38] S.Y. Choi, 2 Miller, D.J., M.M. Muhlleitner, and P.M. Zerwas. Identifying the Higgs spin and parity in decays to Z pairs. *Phys.Lett.*, B553:61–71, 2003.

[39] Alexandre Alves, O.J.P. Eboli, M.C. Gonzalez-Garcia, and J.K. Mizukoshi. Deciphering the spin of new resonances in Higgsless models. *Phys.Rev.*, D79:035009, 2009.

[40] P. Osland, A.A. Pankov, N. Paver, and A.V. Tsytrinov. Spin identification of the Randall-Sundrum resonance in lepton-pair production at the LHC. *Phys.Rev.*, D78:035008, 2008.

[41] P. Osland, A.A. Pankov, A.V. Tsytrinov, and N. Paver. Spin and model identification of Z' bosons at the LHC. *Phys.Rev.*, D79:115021, 2009.

[42] O. J. P. Eboli, Chee Sheng Fong, J. Gonzalez-Fraile, and M. C. Gonzalez-Garcia. Determination of the Spin of New Resonances in Electroweak Gauge Boson Pair Production at the LHC. *Phys. Rev.*, D83:095014, 2011.

[43] Howard E. Haber. Spin formalism and applications to new physics searches. 1994, [hep-ph/9405376].

[44] E. Leader. Spin in particle physics. *Camb. Monogr. Part. Phys. Nucl. Phys. Cosmol.*, 15:1, 2001.

[45] D.M Brink and G.R. Satchler. Angular momentum. *Oxford University Press, London U.K.*, 1968.

[46] M. Jacob and G.C. Wick. On the general theory of collisions for particles with spin. *Annals Phys.*, 7:404–428, 1959.

[47] Fawzi Boudjema and Ritesh K. Singh. A Model independent spin analysis of fundamental particles using azimuthal asymmetries. *JHEP*, 0907:028, 2009.

[48] C.F. Uhlemann and N. Kauer. Narrow-width approximation accuracy. *Nucl.Phys.*, B814:195–211, 2009.

[49] W. Buchmuller and D. Wyler. Effective Lagrangian Analysis of New Interactions and Flavor Conservation. *Nucl. Phys.*, B268:621, 1986.

[50] L Michel. Interaction between four half-spin particles and the decay of the -meson. *Proceedings of the Physical Society. Section A*, 63(5):514, 1950.

[51] Claude Bouchiat and Louis Michel. Theory of μ-meson decay with the hypothesis of nonconservation of parity. *Phys. Rev.*, 106(1):170–172, Apr 1957.

[52] Csaba Csaki, Johannes Heinonen, and Maxim Perelstein. Testing Gluino Spin with Three-Body Decays. *JHEP*, 10:107, 2007.

[53] G.F. Giudice and A. Romanino. Split supersymmetry. *Nucl.Phys.*, B699:65–89, 2004.

[54] Seong Chan Park and Jing Shu. Split Universal Extra Dimensions and Dark Matter. *Phys.Rev.*, D79:091702, 2009.

[55] Alexander Knochel and Thorsten Ohl. Supersymmetric Extensions and Dark Matter in Models of Warped Higgsless EWSB. *Phys.Rev.*, D78:045016, 2008.

[56] Wolfgang Kilian, Thorsten Ohl, and Jurgen Reuter. WHIZARD: Simulating Multi-Particle Processes at LHC and ILC. *Eur.Phys.J.*, C71:1742, 2011.

[57] Mauro Moretti, Thorsten Ohl, and Jurgen Reuter. O'Mega: An Optimizing matrix element generator. 2001, [hep-ph/0102195].

[58] Jose F. Nieves and Palash B. Pal. Generalized Fierz identities. *Am. J. Phys.*, 72:1100–1108, 2004.

[59] G. Weiglein et al. Physics interplay of the LHC and the ILC. *Phys.Rept.*, 426:47–358, 2006.

[60] G.L. Bayatian et al. CMS technical design report, volume II: Physics performance. *J.Phys.G*, G34:995–1579, 2007.

[61] G. Aad et al. Expected Performance of the ATLAS Experiment - Detector, Trigger and Physics. 2009, [arXiv:0901.0512 [hep-ex]].

[62] P. Deuflhard. *Newton Methods for Nonlinear Problems.* Springer, 2004.

[63] B. C. Allanach et al. The Snowmass points and slopes: Benchmarks for SUSY searches. *Eur. Phys. J.*, C25:113–123, 2002.

[64] Tao Han, Ian-Woo Kim, and Jeonghyeon Song. Kinematic Cusps: Determining the Missing Particle Mass at Colliders. *Phys. Lett.*, B693:575–579, 2010.

[65] Won Sang Cho, Kiwoon Choi, Yeong Gyun Kim, and Chan Beom Park. Mass and Spin Measurement with M(T2) and MAOS Momentum. *Nucl.Phys.Proc.Suppl.*, 200-202:103–112, 2010.

[66] Matthew R. Buckley, Hitoshi Murayama, William Klemm, and Vikram Rentala. Discriminating spin through quantum interference. *Phys. Rev.*, D78:014028, 2008.

[67] Alan J. Barr and Claire Gwenlan. The Race for supersymmetry: Using m(T2) for discovery. *Phys.Rev.*, D80:074007, 2009.

[68] Mihoko M. Nojiri, Yasuhiro Shimizu, Shogo Okada, and Kiyotomo Kawagoe. Inclusive transverse mass analysis for squark and gluino mass determination. *JHEP*, 0806:035, 2008.

[69] Tom Melia. Spin before mass at the LHC. *JHEP*, 1201:143, 2012.

[70] C. G. Lester and D. J. Summers. Measuring masses of semiinvisibly decaying particles pair produced at hadron colliders. *Phys. Lett.*, B463:99–103, 1999.

[71] Daniel R. Tovey. On measuring the masses of pair-produced semi-invisibly decaying particles at hadron colliders. *JHEP*, 04:034, 2008.

[72] Konstantin T. Matchev and Myeonghun Park. A General method for determining the masses of semi-invisibly decaying particles at hadron colliders. *Phys.Rev.Lett.*, 107:061801, 2011.

[73] Gudrid Moortgat-Pick, Krzysztof Rolbiecki, and Jamie Tattersall. Early spin determination at the LHC? *Phys. Lett.*, B699:158–163, 2011.

[74] Chien-Yi Chen and A. Freitas. General analysis of signals with two leptons and missing energy at the Large Hadron Collider. *JHEP*, 02:002, 2011.

[75] Alexander Belyaev, Chuan-Ren Chen, Kazuhiro Tobe, and C. P. Yuan. Phenomenology of littlest Higgs model with T-parity: including effects of T-odd fermions. *Phys. Rev.*, D74:115020, 2006.

[76] Herbi K. Dreiner, Howard E. Haber, and Stephen P. Martin. Two-component spinor techniques and Feynman rules for quantum field theory and supersymmetry. *Phys. Rept.*, 494:1–196, 2010.

[77] Peter A. Carruthers. *Spin and Isospin in Particle Physics*. Gordon and Breach, New York, 1971.

[78] A. Pukhov. CalcHEP 2.3: MSSM, structure functions, event generation, batchs, and generation of matrix elements for other packages. 2004, [hep-ph/0412191].

[79] A. Pukhov, E. Boos, M. Dubinin, V. Edneral, V. Ilyin, et al. CompHEP: A Package for evaluation of Feynman diagrams and integration over multiparticle phase space. 1999. User's manual for version 33, [hep-ph/9908288].

[80] S. Kullback and R. A. Leibler. On information and sufficiency. *Ann. Math. Statistics*, 22:79–86, 1951.

[81] Christopher G. Lester, Michael Andrew Parker, and Martin J. White, 2. Determining SUSY model parameters and masses at the LHC using cross-sections, kinematic edges and other observables. *JHEP*, 01:080, 2006.

[82] Johan Alwall, Michel Herquet, Fabio Maltoni, Olivier Mattelaer, and Tim Stelzer. MadGraph 5 : Going Beyond. *JHEP*, 1106:128, 2011.

[83] Neil D. Christensen and Claude Duhr. FeynRules - Feynman rules made easy. *Comput.Phys.Commun.*, 180:1614–1641, 2009.

Dank

An dieser Stelle möchte ich mich bei allen bedanken, die zum Gelingen dieser Arbeit beigetragen haben. Mein Dank gilt insbesonders:

- Prof. Dr. Werner Porod für die Möglichkeit an einem interessanten und aktuellem Thema in seiner Arbeitsgruppe zu arbeiten, für die Betreuung, die hilfreiche Unterstützung und die Möglichkeit eines Auslandsaufenthaltes.
- Dr. Ritesh K. Singh für die gute und interessante Zusammenarbeit und viele hilfreiche Diskussionen.
- Prof. Dr. Reinhold Rückl für die Möglichkeit an seinem Lehrstuhl diese Arbeit anzufangen und Prof. Dr. Ansgar Denner für die Möglichkeit sie an seinem Lehrstuhl fertigzustellen.
- Prof. Dr. Thorsten Ohl für die Hilfsbereitschaft und Diskussionen.
- Prof. Dr. Raimund Ströhmer und Prof. Dr. Thomas Trefzger für Diskussionen bezüglich experimenteller Fragen. Christopher Lester für hilfreiche Tipps und Diskussionen. KC Kong für die Unterstützung bezüglich CalcHep.
- Prof. Dr. Konstantin Matchev für die Möglichkeit, in seiner Arbeitsgruppe an der UF an einem Projekt zu arbeiten und für die vielen hilfreichen und interessanten Diskussionen. Der UF für die Gastfreundschaft und die finanzielle Unterstützung während meines Aufenthaltes.
- Myeonghun Park für die Unterstützung, die Zusammenarbeit und bereichernde Diskussionen. Gaurab Sarangi für die nötige Ablenkung an der UF.
- Brigitte Wehner und Britta Grabsch für ihre Unterstützung und Hilfe in allen bürokratischen Angelegenheiten.
- Elitenetzwerk Bayern für die finanzielle Unterstützung.
- GRK 1147 für die finanzielle Unterstützung und die Ermöglichung und Finanzierung des Auslandsaufenthalts sowie der Besuch der TASI 2011.
- Allen Mitarbeitern der TP2 und Kollegiaten des Graduiertenkollegs GRK 1147 für die bereichernden Diskussionen und Vorträge, für die nette Atmosphäre, insbesondere während der Samerberg-Tage mit Wanderungen und sonstigen Aktivitäten, ebenso für die kurzweiligen Miniworkshops.
- Thomas Flacke, Alex Knochel, Ritesh K. Singh und Christian Speckner für viele Diskussionen in physikalischen Dingen, Barbara Dubanek-Speckner für die Hilfestellung bei "englischen" Haarspaltereien. Christian Speckner für die unglaubliche Hilfsbereitschaft in Bezug auf alle möglichen Computer- und Physikprobleme.
- Martin und Patrick für die schöne Zeit und die nötige Ablenkung.
- Meinen Eltern, Robert und meinen Schwiegereltern für die volle Unterstützung, das Verständnis v.a. in letzter Zeit und nötige Ablenkung mit "normalen" Problemen und lustigen Dingen.
- Zuletzt natürlich Alex für die großartigen Diskussionen zu allen möglichen Dingen, den Rückhalt, die Ablenkung und die Ermunterungen.

Lebenslauf

Persönliche Daten

	Lisa Edelhäuser
	12. Juni 1983 in Rothenburg o.d.T.
Staatsangehörigkeit:	Deutsch
Familienstand:	Verheiratet (05.12.2008), keine Kinder

Ausbildung

10/2007	Doktorandin, Aufnahme als Kollegiatin im Graduiertenkolleg GRK 1147 "Theoretische Astrophysik und Teilchenphysik" in Würzburg
09/2007	Abschluss: Diplom in Physik
2006/2007	Diplomarbeit bei Prof. Dr. W. Porod; Thema: *Mass Factorization of SUSY QCD Processes in DRED*
Sommer 2006	Diplomprüfungen in Physik (Nebenfach: Astrophysik, angewandte Physik: Computational Physics)
10/2002	Beginn des Studiums an der Julius-Maximilians-Universität Würzburg, für Gymnasiallehramt (Mathematik und Physik), Wechsel zu Physik, Diplom
1993-2002	Abitur am Reichsstadtgymnasium Rothenburg o.d.T.
1989-1993	Grundschule (Neusitz)

Lisa Edelhäuser

Liste der Veröffentlichungen

[1] **Lisa Edelhauser**, Werner Porod, and Ritesh K. Singh. Spin Discrimination in Three-Body Decays. *JHEP*, 1008:053, 2010. [arXiv:1005.3720v1 [hep-ph]]

[2] **Lisa Edelhauser**, Werner Porod, and Ritesh K. Singh. Effects of Anomalous Couplings on Spin Determination in Cascade Decays. 2011. [arXiv:1109.3369 [hep-ph]]

[3] **Lisa Edelhäuser**, Konstantin T. Matchev, Myeonghun Park. Spin effects in the antler event topology at hadron colliders. 2012. [arXiv:1205.2054 [hep-ph]]

Erklärung

Diese Doktorarbeit wurde am Lehrstuhl für Theoretische Physik II, Theoretische Elementarteilchenphysik, der Julius-Maximilians-Universität Würzburg angefertigt. Ich erkläre hiermit, dass ich diese Dissertation selbständig verfasst und keine anderen als die angegebenen Quellen und Hilfsmittel benutzt habe. Ich erkläre außerdem, dass diese Dissertation weder in gleicher noch in anderer Form bereits in einem anderen Prüfungsverfahren vorgelegen hat. Ich habe früher außer den mit dem Zulassungsgesuch urkundlich vorgelegten Graden keine weiteren akademischen Grade erworben oder zu erwerben versucht.

Lisa Edelhäuser